Advances in Tunable Diode Laser Spectroscopy for Aero Engine Research

Thomas Benoy

Centre for Microsystems and Photonics

Department of Electronic and Electrical Engineering

University of Strathclyde

This dissertation is submitted for the degree of Doctor of Philosophy

February 2017

T*o my parents,*

& *to my teachers.*

DECLARATION

This thesis is the result of the author's original research. It has been composed by the author and has not been previously submitted for examination which has led to the award of a degree. The copyright of this thesis belongs to the author under the terms of the United Kingdom Copyright Acts as qualified by University of Strathclyde Regulation 3.50.

Due acknowledgement must always be made of the use of any material contained in, or derived from, this thesis.

Signed:_____

Date:_____

Thomas Benoy

ACKNOWLEDGEMENTS

Several people have contributed towards my PhD degree over the past three years. I would like to extend my sincere gratitude to Prof. Walter Johnstone for being my supervisor and the strong pillar, to help me towards the completion of my PhD. His prudent attitude, his guidance and the occasional scolding for getting side tracked with trivial issues, have helped towards the successful completion of my PhD. It has to be said that his role was nothing less than that of a guardian for me in Scotland and has kept my morale up. The conferences and the consortium meetings attended with him were pleasurable with the occasional humour he provides. His belief in my abilities has helped me gain confidence and stride towards the right direction. His insights into the research problems and his grasp of the subject were extremely helpful throughout the project.

Prof. George Stewart has been equally enjoyable to work with. George is one of the most brilliant scientists I have had the pleasure to know and comes up with solutions to the toughest of problems. I would like to thank him for drafting the theory for the wavelength modulation properties of DFB lasers. Our email conversations have led to good quality work. His role complimented that of Walter's during the toughest of times.

Dr. Michael Lengden is an excellent experimentalist and working with him has helped in solving some of the key experimental problems in the project. I would like to thank him for transferring his Matlab skills as well as the one to one discussions which have been extremely useful in solving the important research problems. I thank Dr. David Wilson for significant help in setting up the optics for the aero engine tests at East Kilbride, as well as help with the instrumentation for the FLITES (Fibre Laser Imaging of gas Turbine Exhaust Species) system, setting up the tomographic ring optics etc. Dr. Ian Armstrong was an initial strong influence and his leaving to OptoSci has certainly dragged this project back by a couple of months. Ian has helped me with the initial methodologies for characterising the DFB laser and getting up to speed during the beginning of my PhD. I would like to thank him and Dr. Michael Lengden for building the high temperature (HT) gas cell, Ian in particular for the HT spectral characterisation data.

Dr. James Bain was very helpful during the initial stages and much of the work I have done had strong foundations on his work.

I would like to thank the FLITES consortium for funding this project. Special note of thanks to Prof. Hugh McCann, for his help on all aspects of the FLITES project and for heading the project. Discussions with Dr. Edward Fisher were extremely helpful in clearing certain ideas; his explanation of certain concepts was illuminating. He has been instrumental in designing the electronics and data processing for FLITES. Contributions from Mr. Gordon Humphries have been very significant towards the end of this work, as his expertise in LabVIEW has resulted in the timely execution of the Phantom tests at INTA (*Instituto Nacional de Técnica Aeronáutica*), Madrid. Meetings with Dr. Nick Polydorides have been very useful in understanding key issues in tomography. I would like to thank Dr. Alex Tsenkis for his help with the design and development of the ring mounting plates, electronics, signal processing and the general opto-mechanical aspects of FLITES. The Optoelectronics Research Centre (ORC) group of Southampton, especially Dr. Yutong Feng and Dr. Fuchong have been helpful to get me acquainted with the thulium doped fibre amplifier (TDFA) system built by them, and Prof. Johan Nilsson in supervising the operations on the TDFA and discussions regarding various aspects of FLITES. I thank Mr. Andrea Chigne for designing the field programmable gate array (FPGA) based lock-in amplifiers for FLITES. I would like to thank Mark Johnson of Rolls-Royce for sharing his knowledge on engine diagnostics and Hugh Douglas for facilitating the engine tests at East Kilbride. I would also like to express my sincere gratitude towards the other members of FLITES: Mr. Victor Archilla Prat (INTA), Jorge Roig (INTA), Prof. Krikor B. Ozanyan, John Black (Rolls-Royce - R-R), Philip Ronson (Aggelia), Dan Hewak, Paul Bastock, David Richardson (Soton), Corin Gawith (Covesion), Douglas Walsh, Iain Mauchline, Dr. Ian Armstrong (OptoSci), Dr. Paul Wright, Joanna Bauldreay (Shell), John Mark and Dr. David McCormick (Univ. of Manchester) for their help in various aspects of the project and the constructive FLITES consortium meetings.

I am thankful to Dr. Walter Lubeigt for convening my first year viva and his advice on various aspects of my PhD, Dr. Gordon Flockhart for his help in general matters, sharing his wisdom and the fruitful discussions. The CMP group head, Prof. Deepak Uttamchandani was ever helpful and his constant and gentle pecking helped keep my

foot affirm. Ms. Josephine Hamilton was very supportive with office matters. Mr. Abhishek Upadhyay was fun to be with in Glasgow as well as in Florence and his insights into TDLS-WMS were very useful. I express my warm gratitude to the other members of the group; Ms. Barbara Schilt, Ms. Kay McMillan, Ms. Theresa Christ, Mrs. Carlota Albuquerque, Mr. Cameron Henry Hawkins, Dr. Ralf Bauer, Mr. Alan Paterson, Dr. Michele Zagnoni, Dr. Ran Li, Dr. Li Li, Mr. Jonas Kuch, Dr. Graham Robertson and Dr. Robert Blue for providing a stimulating environment and the interesting lunch times.

The professors at the International School of Photonics (ISP), Cochin University of Science of Technology (CUSAT) deserve special credit for providing me with the opportunity of learning the wonderful subject of Photonics. Pioneers such as Prof. V.P.N. Nampoori, Prof. C.P.G. Vallabhan and Prof. P. Radhakrishnan deserve special mention as they were instrumental in my success. A very special mention should be given to Prof. Sheenu Thomas for her efforts to bring the best out of me. I thank the other teachers, staff and professors at ISP for their help. I pause in the fond remembrance of Prof. Annie Joseph Vallamattom.

I owe a lot to Rajagiri Public School; the teachers and all my friends for instilling good values in me and enriching my talents.

I acknowledge the Engineering and Physical Sciences Research Council (EPSRC) and the engineering faculty for funding this work.

ABSTRACT

Tunable diode laser spectroscopy (TDLS) is a widely used technique for the measurement of gas species and offers *in-situ* operation, accuracy and faster response time compared to other optical and non-optical gas sensing techniques.

The work in this thesis focusses on the measurement of CO_2 in the harsh environment of a gas turbine engine (GTE). The work is part of a much larger initiative called Fibre Laser Imaging of gas Turbine Exhaust Species (FLITES) aimed at obtaining concentration distributions of gas species such as CO_2 and NO, unburnt hydrocarbons, and soot in a gas turbine exhaust plume using optical tomography. In the FLITES system, a thulium doped fibre amplifier (TDFA) is used to boost the optical power output from a 2 mW, 1997 nm, multi-quantum well distributed feedback (DFB-MQW) laser to feed 126 measurement channels arranged in dodecagon geometry for optical tomography. Hence, agile TDLS techniques need to be developed which can be scaled up to the multi-channel measurement system.

Attributed by the interference from noise in the measurement environment of a GTE, phase sensitive detection using a lock-in amplifier (LIA) has to be employed where an additional current modulation is applied to the DFB laser, creating an instantaneous intensity modulated output and a delayed wavelength modulation (WM) output. This technique falls under a metrology branch known as wavelength modulation spectroscopy (WMS).

The unknown measurement conditions expected in a GTE engine necessitates the use of calibration-free WMS techniques for the simultaneous measurement of gas concentration and temperature. Calibration-free techniques in WMS have been developed at the Centre for Microsystems and Photonics (CMP) of Strathclyde University. These are known as the phasor decomposition method (PDM) and the residual amplitude modulation (RAM) technique. They employ the signals obtained using the first harmonic demodulation of the WMS signals, followed by post processing to recover the gas absorption line shape. It was known in the CMP group that the accuracy of these techniques was limited by the variation in the laser modulation parameters such as the phase of the wavelength modulation relative to the intensity modulation (WM-IM phase lag) and the wavelength modulation amplitude across the laser current scan.

The solutions to two problems are addressed in this thesis, viz. the implementation of correction procedures to account for the variation in the laser modulation parameters across the current scan and the need for a calibration-free technique for the measurement of CO_2 in a GTE exhaust plume scalable to a multi-channel measurement system.

Accurate measurements of the wavelength modulation parameters were made across the current scan and correction algorithms were implemented to compensate for its effects on the recovered gas absorption line shape.

The gas spectral parameters were measured in the lab for the R48 absorption line of CO_2 near 1997.2 nm at the higher temperatures (up to 500°C) expected in a GTE exhaust plume, using a heated gas cell. A Fourier expansion model was developed for the WMS signals which employ the measured laser modulation and gas spectral parameters. *1f* normalised *2f* WMS technique was chosen as the calibration-free measurement approach due to the advantages of cancellation of the transmission fluctuations as well as signal normalisation. The *2f/1f* measurement technique was validated in the lab at higher temperatures for the simultaneous recovery of the CO_2 concentration and temperature with an accuracy of 3.39 % and 3.72 %, respectively. Subsequently, field campaigns were conducted at the Rolls-Royce test facility at East Kilbride, yielding concentration and temperature values having good correlation to the engine operating conditions such as the throttle and core temperature.

Multi-channel tomographic measurements were conducted on the test phantoms at INTA, Madrid, using TFLAS-WMS (tunable fibre laser absorption spectroscopy). Accurate concentration images could be recovered using tomographic reconstruction algorithms.

CONTENTS

List of Abbreviations

1D	One dimensional
2D	Two dimensional
AC	Alternating current
ADC	Analog to digital converter
AM	Amplitude modulation
BNC	Bayonet Neill-Concelman connector
CDSD	Carbon dioxide spectral database
CEAS	Cavity enhanced absorption spectroscopy
CFD	Computational fluid dynamics
CMP	Centre for Microsystems and Photonics
CST	Chemical species tomography
CUSAT	Cochin University of Science and Technology
DAC	Digital to analog converter
DAQ	Data acquisition
DAS	Differential absorption spectroscopy
DC	Direct current
DDS	Dynamic digital synthesizer
DFB	Distributed feedback
DFG	Difference frequency generation
DIP	Dual in-line package
DR	Dynamic reserve
DS	Direct spectroscopy
EFE	Environmentally friendly engine
EK	East Kilbride
EPSRC	Engineering and Physical Sciences Research Council
FC-APC	Ferrule connector with angled physical contact
FFT	Fast Fourier transform
FLITES	Fibre Laser Imaging of gas Turbine Exhaust Species
FM	Frequency modulation
FMS	Frequency modulation spectroscopy
FPGA	Field programmable gate array

List of Abbreviations

FRR	Fibre ring resonator
FSR	Free spectral range
FTIR	Fourier transform infrared
FWHM	Full width at half maximum
GC	Gas chromatography
GEISA	Gestion et Etude des Informations Spectroscopiques Atmosphériques
GPIB	General purpose interface bus
GRIN	Graded index
GTE	Gas turbine engine
HCl	Hydrogen chloride
HITEMP	High-temperature molecular spectroscopic database
HITRAN	High-resolution transmission molecular absorption database
HT	High temperature
HWHM	Half width at half maximum
IM	Intensity modulation
InGaAsP	Indium gallium arsenide phosphide
InP	Indium phosphide
INTA	Instituto Nacional de Técnica Aeronáutica
IR	Infrared
ISP	International School of Photonics
I-V	Current-voltage
I-λ	Current-wavelength
LDC	Laser diode controller
L-I	Light-current
LIA	Lock-in amplifier
LIDAR	Light detection and ranging
LII	Laser induced incandescence
LOS	Line of sight
MATLAB	Matrix laboratory
MCT	Mercury cadmium telluride
MQW	Multi-quantum well
NEA	Noise equivalent absorption
NIR	Near-infrared
ORC	Optoelectronics Research Centre

List of Abbreviations

PAS	Photoacoustic
PDM	Phasor decomposition method
PID	Proportional-Integral-Derivative
PNNL	Pacific Northwest National Laboratory
PSD	Phase sensitive detection
PXI-e	PCI eXtensions for instrumentation-express
QCL	Quantum cascade laser
RAM	Residual amplitude modulation
RC	Resistor, capacitor
RIN	Relative intensity noise
RLC	Resistor, inductor, capacitor
RMS	Root mean square
RT	Ratio thermometry
RTP	Room temperature and pressure
SHM	Simple harmonic motion
SM 2000	Single mode 2000(Thorlabs)
SMF	Single mode fibre
SNR	Signal-to-noise ratio
SPIE	Society of photo-optical instrumentation engineers
TDFA	Thulium doped fibre amplifier
TDLS	Tunable diode laser spectroscopy
TEC	Thermoelectric controller
TFLAS	Tunable fibre laser absorption spectroscopy
TTL	Transistor-transistor logic
UV	Ultraviolet
VCSEL	Vertical cavity surface emitting laser
WM	Wavelength modulation
WMS	Wavelength modulation spectroscopy
XWB	Extra wide body

Chapter 1

Introduction

1.1 Background

The work presented in this thesis concerns the measurement of chemical species concentration in extremely harsh environments such as the exhaust plume of a gas turbine engine (GTE). Many techniques are available for the measurement of gas concentration, however, most require transducers that could not survive the environment of a GTE exhaust plume. The chosen technique must be non-intrusive (no disruption of the exhaust flow) and be totally immune to degradation in the harsh conditions. In the work presented here, tunable diode laser spectroscopy with wavelength modulation spectroscopy (TDLS-WMS) was proposed for investigation as the preferred choice. In addition to meeting the above requirements, it was proposed that the technique can be scaled up to provide multiple path measurements across the plume, yielding 2D real-time concentration and temperature distributions (through tomography imaging) of CO_2 gas in the exhaust plume of a gas turbine engine. Such measurements of emissions are required to optimise engine operation and design, enable engine diagnostics and to undertake research into alternative fuels and engines. The work is part of a much larger project called FLITES (Fibre Laser Imaging of gas Turbine Exhaust Species) which will be briefly introduced in Section 1.4. Apart from monitoring CO_2 emissions, 2D concentration images can give significant information to the test engineer for engine condition monitoring. For example, an asymmetry in the concentration image indicates non-optimal operation of the aero engine.

In traditional combustion measurements, the measurement gas samples are extracted *in-situ* using intrusive multiple sampling point rakes [1]. The samples are later analysed using laboratory techniques such as gas chromatography (GC) or other optical techniques such as Fourier transform infrared (FTIR) spectroscopy, cavity enhanced

absorption spectroscopy (CEAS) or photoacoustic spectroscopy (PAS). However, the rake perturbs the combustion flow which is not an ideal measurement scenario. Also, for 2D measurements, the rake has to be moved, and hence it is not possible to generate real-time concentration images of the plume. The cavity enhanced techniques have been used for detection of gases in flames to study the combustion processes, but are extremely sensitive to alignment and losses from dust as well as other issues such as thermo-mechanical stability. PAS is limited due to the high acoustic noise levels in harsh environments. GC is a very slow measurement process where the gas is flown through liquid columns and is useful mostly as an analytical laboratory technique.

In contrast to the traditional techniques, tunable diode laser spectroscopy with wavelength modulation offers the advantages of calibration-free, rapid, in-situ, non-intrusive measurement of concentration and temperature or pressure in an aero engine exhaust plume. In addition, it can potentially be scaled up to achieve simultaneous multi-path measurements to yield quasi real-time images through tomographic techniques. As such, TDLS is the favoured technique for investigation in this work. Other applications of tunable diode laser spectroscopy include remote sensing, LIDAR, laser cooling and trapping of atoms, frequency standards, length standards, trace gas detection, fuel cells, biological sensing applications (breath analysis using gases as biomarkers) and henceforth.

1.2 Tunable Diode Laser Spectroscopy / Wavelength Modulation Spectroscopy

Tunable diode laser spectroscopy is a technique which scans the emission wavelength of a narrow line width diode laser across closely spaced rotational-vibrational transitions of a gas molecule. The light, when passed through the gas sample is attenuated by it at the characteristic wavelengths corresponding to the energy level transitions in the gas molecules. Then, the attenuated light is detected by a photodiode and subsequently the signal at the photodiode is analysed in the wavelength/frequency domain to gain information about the state of the gas such as its concentration, temperature and pressure. In applications with high noise levels, the technique is used in conjunction with phase sensitive detection by a lock-in amplifier where an additional modulation of

the laser output frequency (or wavelength) is applied. The technique is known as wavelength modulation spectroscopy or frequency modulation spectroscopy (FMS) depending on the frequency of the applied modulation relative to the width of the gas absorption line.

TDLS techniques provide the following advantages compared to the other optical gas sensing techniques: (A) it is non-intrusive (only the laser beam passes through the measurement zone), (B) immune to degradation in harsh environments, (C) the potential to be calibration-free, (D) *in-situ* measurement, (E) faster sensor response times (several tens of kHz), (F) sensitive comparable to the other techniques (NEA~10^{-6} cm^{-1} $Hz^{-1/2}$), (G) gas specific, (H) repeatable, (I) measurement of concentration and temperature or pressure, (J) miniaturisation, (K) larger dynamic range of concentration measurements, etc.

TDLS also has certain disadvantages. For example, accuracy over a much wider temperature range is difficult; calibration can be difficult in some circumstances especially at very low concentrations and at very high temperatures; the spectral modelling, especially at higher pressures and/or temperatures, can be challenging (mathematically complex).

In TDLS, a linear current sweep scans the laser wavelength across the absorption line and the laser output intensity is attenuated at the wavelengths corresponding to the bandgap of the rotational-vibrational transitions. When a current modulation is applied to the DFB laser, it creates an instantaneous intensity modulation (IM) output and a time delayed wavelength modulation (WM) output, both of which interact with the gas absorption line. The phase lag between the IM and WM is referred to as the WM-IM phase lag. In addition to a very strong IM signal at the modulation frequency, referred to as the *1f* IM signal, successively weaker IM signals occur in the laser output at higher harmonics of the modulation frequency due to the nonlinearity of the IM-current characteristics. These signals are referred to as the *2f, 3f….nf* IM signals. All of these IM components are attenuated by the gas absorption line and they generate amplitude modulated voltage signals at the detector output referred to as residual amplitude modulation (RAM) signals. The interaction of the wavelength modulated laser output and the gas absorption line results in further IM signals proportional to the laser

intensity at the fundamental modulation frequency and its harmonics i.e. at *1f*, *2f* …., etc. These are phase delayed relative to the RAM signals due to the WM-IM phase lag in the laser output. At the detector output the voltage signals generated by the latter are referred to as the WMS signals at the various harmonics of the modulation frequency. A full explanation of how the WMS signals are generated and mathematically modelled will be given in Chapter 2.

A lock-in amplifier is used to demodulate all of these signals at the various harmonics of the modulation frequency and output signals that are proportional to the amplitudes of these harmonics. Demodulation at the first harmonic frequency is known as *1f* detection, demodulation at the second harmonic frequency is termed *2f* detection and so on. The demodulated signals at each harmonic frequency consist of components arising from the RAM signals and the WM signals. The WMS signals arising at any of the harmonics can be used to measure gas parameters, although the *1f* and *2f* signals are the ones most commonly used. Also, the *1f*-RAM signal phase separated from the *1f*- WMS signal may be used to measure the gas absorption line shape from which the gas parameters may be extracted (the higher harmonics of the RAM are too small to be useful).

The design challenges in any TDLS-WMS sensor systems can be classified into:

(1) noise reduction, (2) calibration, (3) signal normalisation or obtaining a zero baseline, (3) ease of implementation, (4) cost, (5) availability of source, detector and optics at the given wavelength, (6) multi-parameter detection (example, concentration and temperature [2] or pressure [3]), (7) accuracy, (8) species specificity, (9) sensitivity, (10) safety, (11) temperature range of operation (for example in ratio thermometry (RT) [4]), (12) very small path lengths (of the order of μm), (13) high pressure modelling etc.

The traditional approach in WMS is to calibrate the measurements to a reference cell containing a known gas concentration. This method is not feasible in high enthalpy combustion flow measurements, and hence calibration-free techniques are required to measure the gas concentration and temperature or pressure. Calibration-free measurements mean that the gas concentration and temperature or pressure can be determined without referencing to a known gas mixture. The most useful approach to achieving this is to do a least-squares curve fit of theoretical WMS signals modelled using the measured laser modulation and the gas spectral parameters, to the

experimentally measured WMS signals, with the gas thermodynamic state variables such as concentration and temperature or pressure as the fitting parameters. It is not possible to determine all the three thermodynamic state variables simultaneously as the least-squares fitting algorithm has a proper solution for only two of the thermodynamic state variables.

Calibration-free techniques can be broadly classified into *2f* and *1f* detection schemes depending on the harmonic signal being demodulated by the LIA. One of the major disadvantages of *1f* detection is the presence of the high background RAM signal on the WMS signals. This high background limits the minimum detectable sensitivity. The RAM background is much smaller for *2f* detection compared to *1f* detection. Also, the *2f* signal is more sensitive to the gas absorption line shape (spectral parameters) and offers better separation of the dense gas lines. The nonlinear *2f*-RAM is usually very small for most DFB lasers and could be neglected in the analysis [3]. Hence, *2f* detection is preferred to *1f* detection in the majority of the gas sensing applications requiring very high sensitivities.

In environments with rapidly changing transmission, it has been found that the first harmonic signal can be used to normalise higher order harmonic signals [5–7]. This method cancels the dependence on the instantaneous intensity (transmissivity fluctuations) of the laser and could improve the signal-to-noise ratio (SNR) up to two orders in magnitude compared to *2f* detection [8]. This method is especially useful when a baseline is not available for the probed species transmission, due to blending of neighbouring absorption lines, even at atmospheric pressures. This is the case for many molecules such as CO_2 in the near-infrared. Hence, it was proposed to investigate this method for the measurement of CO_2 in the combustion plume. More specifically, it was proposed to develop it for simultaneous measurement of the concentration and temperature of CO_2 across the aero engine plume by a spectral fitting routine based on the nonlinear least-squares curve fit method i.e. fitting of theoretical WMS models to experimentally obtained WMS signals.

The key component in a TDLS system is the laser. In this work a single mode DFB laser was used emitting at 1997 nm, with a multi-quantum well (MQW) gain region. It has been known within the CMP group since 2009 [9] that the variation in the

wavelength modulation characteristics across the current scan causes a distortion in the recovery of the gas absorption line shape using *1f* demodulation techniques such as the phasor decomposition method. This was further supported by X. Chao et al. [10]. Hence, it is important to include the laser modulation parameters across the current scan, such as the WM-IM phase lag, tuning coefficient and IM characteristics for accurately modelling the experimental WMS signals. These characteristics are laser specific, and depend on the applied modulation frequency, diode temperature and bias current.

1.3 Gas Turbine Engine Measurements

The gas turbine engine consists of four parts: the propeller, the compressor, the ignition chamber and the gas turbine, all of which are connected by a common shaft. Gas turbine engines can be classified into turbojet and turbofan engines. Turbofan engines have a propeller behind the compressor stage and are high air bypass engines. Turbojets are low air bypass engines and use the pressure of the exiting gases for thrust and are generally fuel inefficient.

Figure 1-1 is a schematic diagram of a high bypass gas turbine engine. The air is sucked into the engine and is divided into two parts, about 20 % passes through the compressor and the rest is bypassed around it. The bypass duct decreases in area further increasing the air pressure which provides increased thrust. The air is compressed by means of rotating compressor shafts to very high pressures for ignition. In the combustion/ignition chamber the pressurised air is mixed with atomised fuel to cause an explosive reaction which causes the pressure to increase even further. These high pressure exhaust gases drive the gas turbines which rotate. The gas turbine which is connected to the compressor blades and the propeller through a common shaft also starts to rotate drawing more air through the bypass. The bypassed air provides 75 % of the thrust. The high pressure exhaust gases mix with bypass air, which exits the exhaust nozzles. Commercial aircraft use turbofan engines due to the high fuel efficiency, while military aircraft which need large thrusts use the less fuel efficient turbojet engines. Hybrid aircraft have an afterburner, which is a perforated tube through which fuel is injected for increased thrust. The modern experimental engines such as the scramjet engines do not have any moving parts and only use the fuel combustion in a supersonic flow to reach very high velocities of the order of Mach 10.

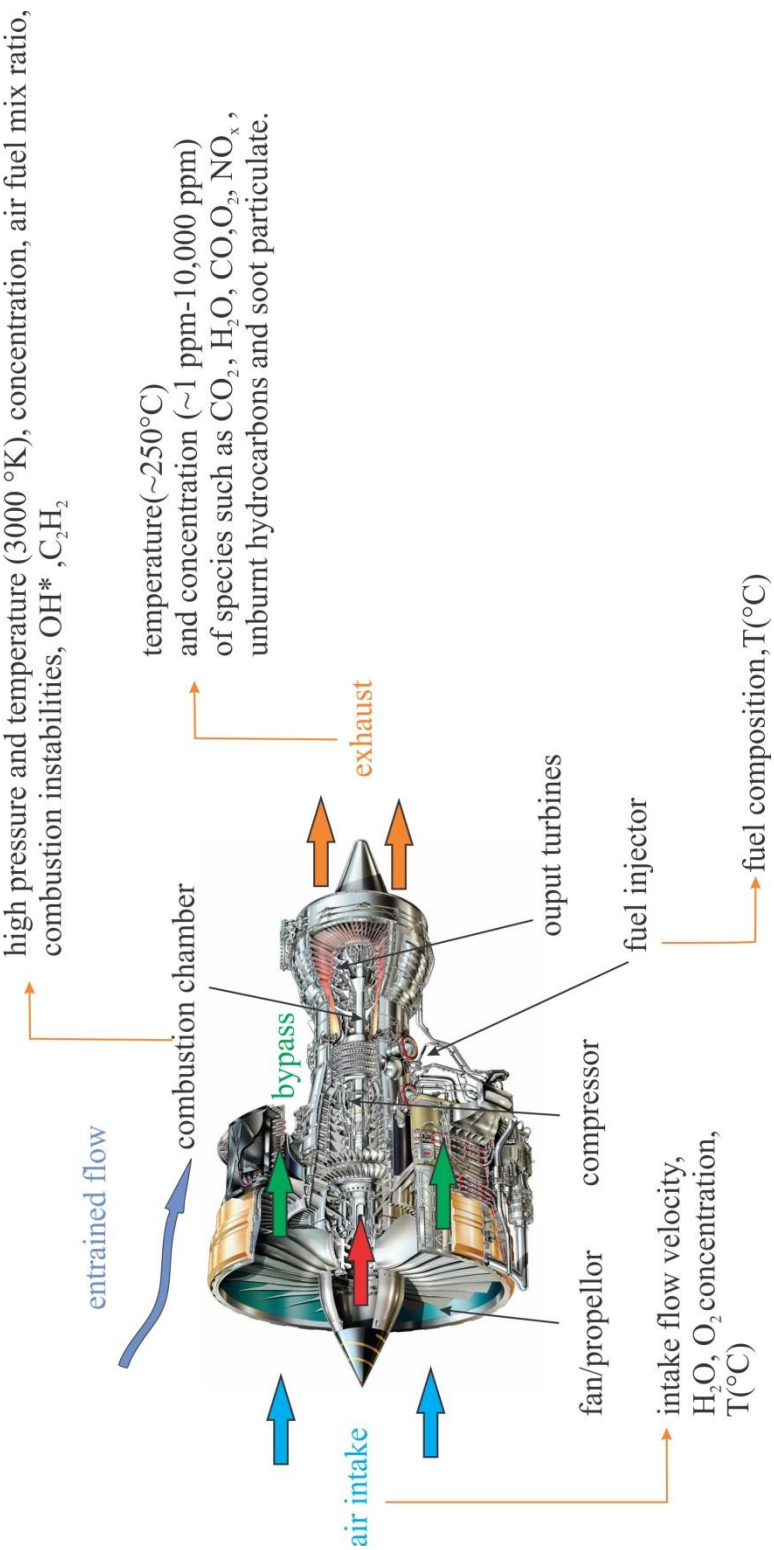

Figure 1-1. Optical sensing in an aero engine (Rolls-Royce Trent 700 [11]).

EFEs (environmentally friendly engines) have multiple gas turbines in an annular geometry. The measurement quantities of interest are the concentration, temperature, pressure, flow velocity and mass flux [12] as shown in Figure 1-1.

The work reported here focusses on the measurement of path integrated concentration of carbon dioxide and plume temperature across the aero engine exhaust.

A major issue in optical probing of combustion environments is keeping the optics and windows clean. Periodic cleaning of the optics is necessary as either they get eroded due to the harsh environment or they become covered in oil or dust. Other issues include beam divergence and wandering effects [13] due to the plume turbulence. Customised optical launch and receive optics are required to mitigate these problems to some extent. These problems in combustion system measurements can be addressed by the *1f* normalised WMS technique [8, 14, 15] as will be shown.

1.4 FLITES

This work is part of a much larger research programme entitled Fibre Laser Imaging of gas Turbine Exhaust Species (FLITES) which is a joint venture between the Universities of Strathclyde, Manchester, Edinburgh and Southampton to obtain time resolved 2D concentration distributions (tomographic images) of gas and particulate species such as CO_2, hydrocarbon species, NO, unburnt hydrocarbons and soot in the exhaust plume of a GTE.

CO_2 is an important gas to monitor especially from an environmental point of view. The Clean Sky 2 [16] European consortium aims to develop technologies for the reduction in the total global aircraft emissions of CO_2 by 50 % towards the end of 2020. FLITES aims to achieve very accurate measurement of chemical species distribution with state of the art spatial and temporal resolution for engine performance testing, emissions measurement, evaluation of bio-derived fuels, engine diagnostics and control of engine operations. The major objectives of the project are:

A. Development of TDLS techniques and instrumentation for near and mid-infrared optical sensing of species such as CO_2 and NO_x (responsibility of Strathclyde).
B. Development of a 2 μm thulium doped fibre amplifier for CO_2 measurements, mid-IR fibre lasers and novel mid-IRoptical fibres for generation and delivery of light

for the measurement of unburnt hydrocarbons and NO (responsibility of Southampton).

C. Chemical species tomography (CST) for obtaining spatio-temporal concentration distributions of CO_2 and unburnt hydrocarbons (University of Edinburgh).
D. Construction and development of a fibre delivery system in order to realise multiple laser projection across the plume to achieve optical tomography. (Universities of Strathclyde and Manchester).
E. Electronics and signal processing (University of Edinburgh).
F. Imaging of soot particulates using laser induced incandescence (LII). (University of Manchester).
G. Measurement of unburnt hydrocarbons using differential absorption spectroscopy (DAS) (University of Manchester and University of Stanford).

The measurement system for CO_2 is shown in Figure 1-2. To obtain accurate tomographic images of concentration and temperature using a single wavelength, it was required to have a 126 beam projection across the plume as sets of 21 beams at 6 different projection angles. For this, a dodecagon mounting ring was placed behind the engine near the detuner structure. The launch and receive optics will be mounted alternately on each side of the dodecagon ring assembly. Figures 1-3 and 1-4 show schematics of the ring system as it will appear *in-situ*.

The source (2 mW, 1997 nm DFB-MQW) laser is mounted in an OptoSci laser control module, which facilitates for laser current and temperature control. Since the power output of the DFB laser is insufficient to feed the 126 beam projection channels, a TDFA is used to amplify the output of the DFB laser up to 2.5 W. The TDFA output feeds the splitter network which delivers the light into the 126 measurement channels across the GTE exhaust plume (Figure 1-2). The signals will subsequently be detected by 126 optical detectors and demodulated by 126 LIAs divided among six demodulation hubs placed on the ring.

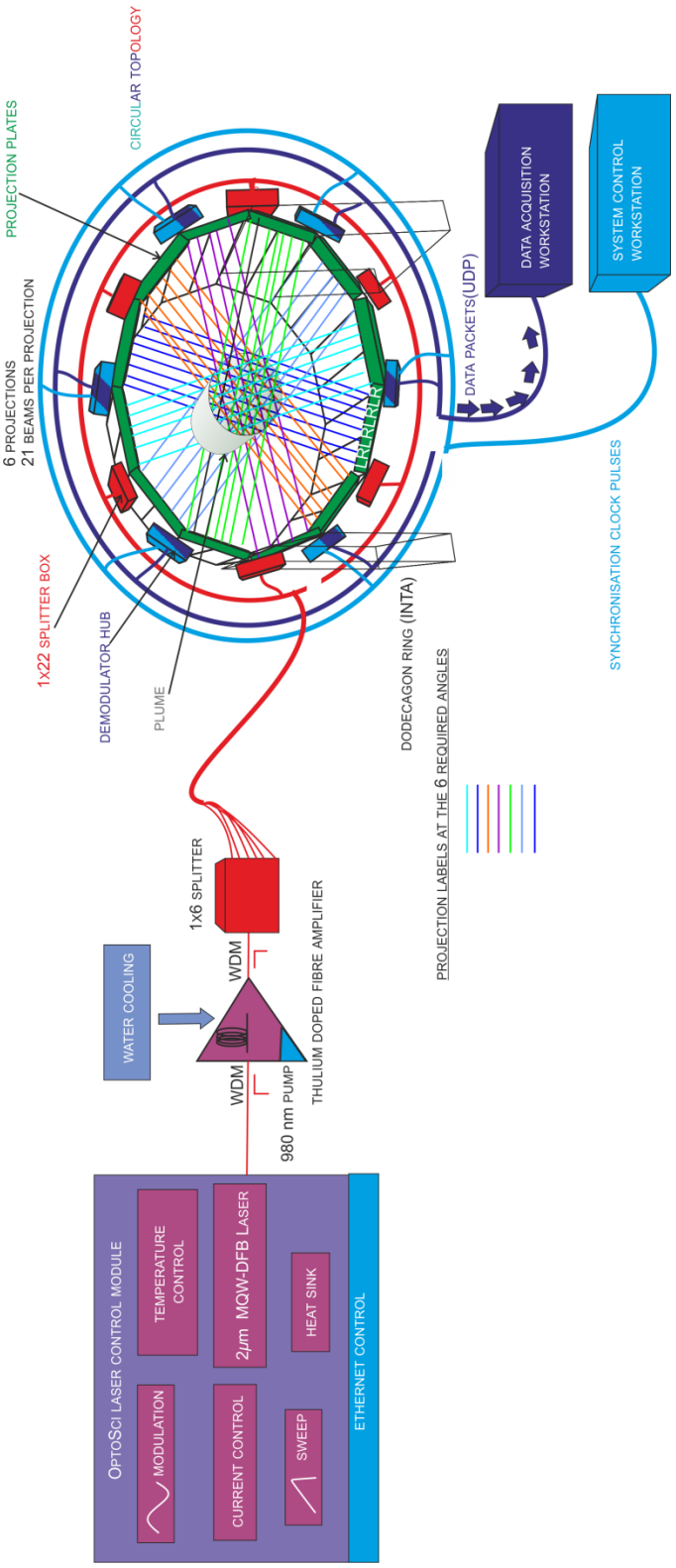

Figure 1-2. The experimental setup for chemical species tomography at INTA, Madrid [17].

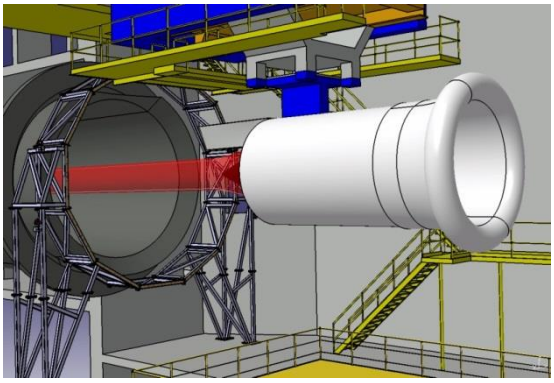

Figure 1-3. The dodecagon ring near the detuner and the GTE exhaust plume (image obtained from INTA, Madrid).

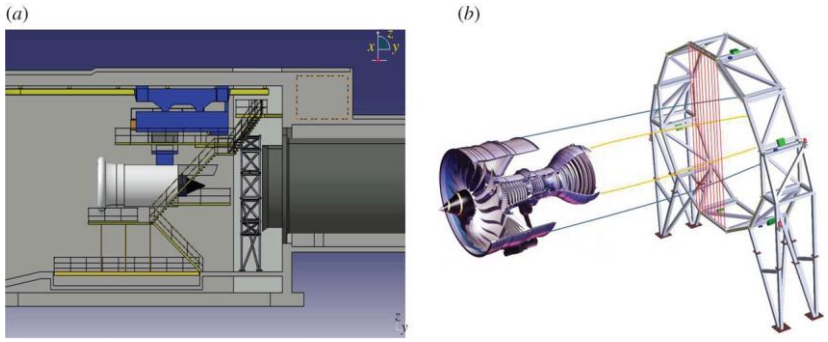

Figure 1-4. Figure showing the engine placed in front of the dodecagon mounting ring. 126 beams dissect the plume cross-section for tomographic imaging of concentration and temperature (figure courtesy of the FLITES consortium).

1.5 Aims and Objectives

The aim of this research is to develop a technique for the measurement of gaseous chemical species concentration, particularly CO_2, scalable to multi-path measurements to enable tomographic imaging in the exhaust plume of a gas turbine engine. The objectives and sub-objectives to achieve this can be broadly classified into:

1. Develop and validate an accurate model of TDLS-WMS signals using
   - Precise measurement and understanding of the laser modulation parameters.
   - Development of a CO_2 gas spectral database.
2. Develop a measurement strategy for the accurate extraction of concentration and temperature or pressure using the *1f*-WMS line shape recovery techniques.

- Investigate the effect of the laser modulation characteristics on the WMS signals and determine if they need to be accounted for in the model.
- Laboratory validation of concentration and temperature measurements using *1f* measurement techniques.

3. Develop a calibration-free WMS methodology for the extraction of CO_2 gas concentration and temperature for optical tomography.
    - Validate the technique in the laboratory and in a gas turbine exhaust plume environment.
    - For accurate tomographic reconstruction the targeted requirement is a 4% error in concentration.
    - The technique should also be suitable for a TFLAS (tunable fibre laser absorption spectroscopy) - WMS measurement system using the thulium doped fibre amplifier.

1.6 Summary

This chapter gives a brief introduction to the non-intrusive optical sensing techniques used to measure gas species concentration in harsh environments such as an aero engine exhaust plume. In this project tunable diode laser spectroscopy with wavelength modulation will be used for the simultaneous measurement of gas concentration and temperature in an aero engine exhaust plume. TDLS-WMS sensors have the advantage of faster response times combined with accuracy in comparison to other optical and non-optical gas sensing techniques. The principle of calibration-free metrology is introduced. This is a collaborative work as part of the FLITES project, and hence a brief introduction is given on this project and its capabilities.

Chapter 2 gives an introduction of the theory of gas absorption in the near and mid-IR caused by the rotational-vibrational motion of the gas molecules. It is used in the development of analytical models for calibration-free measurements. The spectral databases such as HITRAN are introduced which are important for the calibration-free measurements.

Chapter 3 introduces the different WMS techniques wherein phase sensitive detection is performed at frequencies away from the *1/f* noise band. The Fourier formalism of WMS is introduced. The RAM technique and phasor decomposition method are also

introduced. The theory of *1f* normalised *2f* spectroscopy is explained which will be used for the measurements in a GTE plume.

Chapter 4 explains the experimental techniques used for characterisation of the DFB laser as well as measurement of the WMS signals. *In-situ* characterisation approaches are briefly introduced.

In Chapter 5, the measured modulation parameters of the 2 μm DFB laser used for high resolution CO_2 spectroscopy are presented. An analytical semiconductor heat transfer model was developed to explain these modulation characteristics and to gain understanding into the wavelength modulation properties of DFB lasers at the sub-MHz frequencies used in WMS. The effect of the laser modulation parameters on the *1f* line shape recovery techniques have been investigated and correction algorithms applied to compensate for effects such as the phase and tuning coefficient walk-off (variation) across the laser current scan. A *1f*-WMS line shape recovery technique is described which is independent of the phase of the LIA reference signal, useful in field as well as laboratory applications.

Chapter 6 focusses on the development of a high temperature TDLS-WMS sensor using the *1f* normalised *2f* WMS technique for simultaneous measurement of the concentration of CO_2 and temperature in a GTE exhaust plume. The sensor was initially validated in the laboratory and subsequently field campaigns were conducted in aero engine test beds.

Chapter 2

Fundamentals of Molecular Spectroscopy

2.1 Overview

The aim of this chapter is to give a practitioner's introduction to molecular spectroscopy with emphasis on high temperature spectroscopy. Initially, the vibrational spectra of molecules are described followed by the rotational fine structure of vibrational transitions. The main aim of this project is to measure CO_2 transitions in the NIR, hence, most of these concepts have been explained from the perspective of the targeted CO_2 molecular spectra. Nevertheless, the theory applies to any gas molecule.

Calibration-free approaches to spectroscopic measurements involve least-squares curve fitting of theoretical models to experimental gas absorption spectra applying the gas spectral parameters such as the line width and line strength (proportional to the area under the absorption curve) to obtain the thermodynamic state variables such as concentration and temperature or pressure. Although the relationship between the spectral line shape and thermodynamic state variables is not trivial, assumptions can be used to simplify the problem. Spectral databases are available such as HITRAN [18], GEISA [19] etc. which give the values for gas spectral parameters for modelling the gas absorption profile.

The line strength is obtained from the area under the absorption feature (with known values for the pressure, concentration and path length) and depends on the difference in the energy levels for the transition and also on the temperature (population density). Line broadening originates from two mechanisms viz. the thermal and collisional broadening. Collisional broadening or pressure broadening is a homogeneous broadening mechanism represented by a Lorentzian line shape function and occurs as

the naturally broadened (Heisenberg's uncertainty principle) energy levels are further broadened by collisions with other molecules. Thermal broadening is a consequence of the Doppler shift due to the thermal motion of gas molecules and is an inhomogeneous broadening mechanism represented by a Gaussian line shape function. It becomes important only at higher temperatures (for atmospheric pressure), whereas at room temperature and atmospheric pressure, the broadening is mainly collisional. The resultant gas absorption line shape is a convolution of the Lorentzian and Gaussian line shape functions and mathematically represented by a Voigt function. Several implementations of the Voigt function exist in literature such as using the complex error function or other numerical approximations. In this work, the Voigt function has been implemented using the error function [20] method and McLean's approximation [21] (Appendix B).

2.2 Light Molecule Interactions

From the perspective of high resolution spectroscopy, a molecule possesses three forms of energy: electronic, vibrational and rotational.

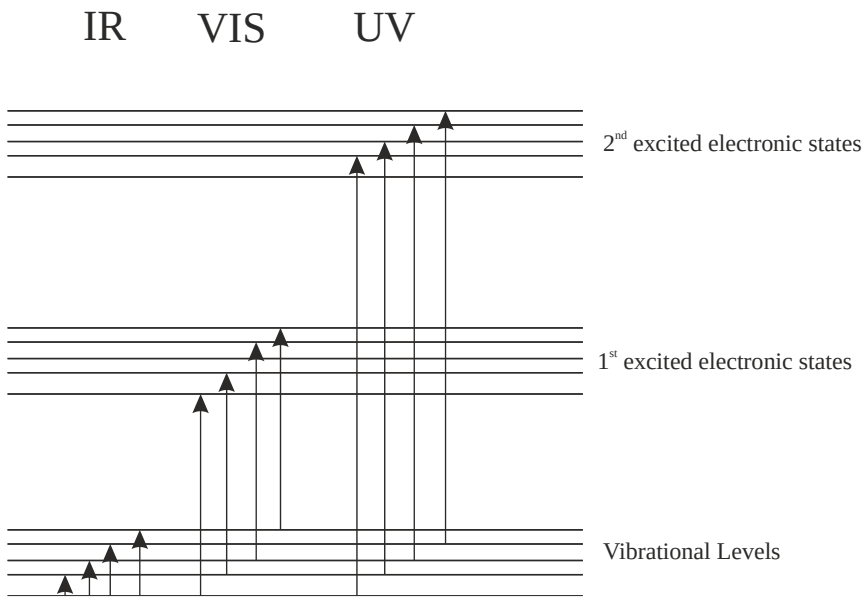

Figure 2-1. Molecular energy levels and their interaction with incoming electromagnetic radiation.

The approximate energy level differences are such that $\Delta E_{\text{electronic}} = \Delta E_{\text{vibrational}} \times 10^3 = \Delta E_{\text{rotational}} \times 10^6$ and the total energy of the molecule is the sum of the three, i.e. $E_{total} = E_{electronic} + E_{vibrational} + E_{rotational}$. The interaction of external radiation with the molecular energy levels is illustrated in Figure 2-1.

The high energy X-ray or UV-vis-NIR absorption occurs when the incident light field has energy corresponding to the electronic energy level transitions. Transitions in the near-IR to far-IR occur due to vibrational motion. Microwave spectra are a result of the rotational transitions. It is to be noted that the rotational and vibrational transitions result owing to a change in electronic dipole moment of the molecule.

2.3 A Vibrating Diatomic Molecule

Initially, the simple case of a linear diatomic molecule is considered. The atoms of the molecule are attached via a chemical bond.

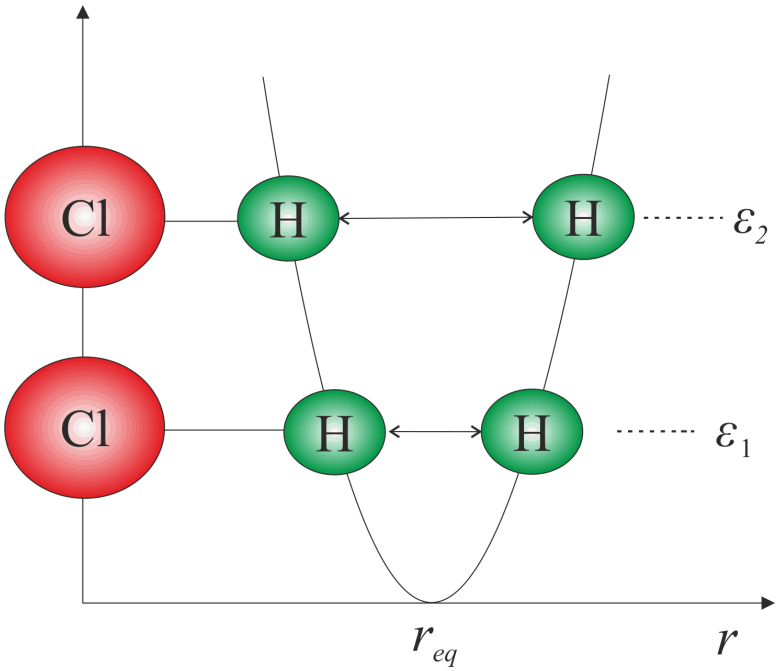

Figure 2-2. Example of HCl molecule executing simple harmonic motion (SHM). Different vibrational amplitudes correspond to different energy levels.

There will be repulsion between the positively charged nuclei and the negatively charged electron clouds of the atoms, which will tend to tear them apart. On the other hand, there is also an attraction between the positively charged nucleus of one atom and the negatively charged electron cloud of the other atom and vice versa. The two atoms settle at a mean internuclear distance so that these two opposing forces are balanced. Energy that distorts this bond length causes vibrations as these forces try to bring the atoms back to the equilibrium position as shown in Figure 2-2.

The energy of the molecule is minimal at the equilibrium internuclear distance (r_{eq}) and when disturbed to a distance r oscillates with its energy governed by the Hooke's law as $E = \frac{1}{2}k_s(r - r_{eq})^2$, assuming the chemical bond to be a mechanical spring with a characteristic spring constant k_s.

Solving the equation of motion for the simple harmonic spring oscillator gives the oscillation frequency as,

$$\bar{\omega}_{osc} = \frac{1}{2\pi c}\sqrt{\frac{k_s}{\mu}}\ \text{cm}^{-1} \tag{2.1}$$

where c is the speed of light in vacuum and μ is the effective mass of the two body system. From a quantum mechanical perspective, solving the Schrodinger's equation for a simple harmonic oscillator, gives the energy as:

$$E_v = \left(v + \frac{1}{2}\right)\bar{\omega}_{osc}\ cm^{-1}\ \ (v = 0,1,2 \ldots\ldots\ldots) \tag{2.2}$$

Equation (2.2) states that the energy levels are discretised in terms of the vibrational quantum number v.

The above equation also implies that a molecule can never have zero energy. Hence, the lowest possible energy of a molecule, known as its zero point energy is given as $E = \frac{1}{2}\bar{\omega}_{osc}$, in contrast to the result obtained from the classical mechanics.

Following quantum mechanics, the transition selection rule is written as:

$$\Delta v = \mp 1 \tag{2.3}$$

The spacing between successive energy levels is $\bar{\omega}_{osc}$ as shown in Figure 2-3.

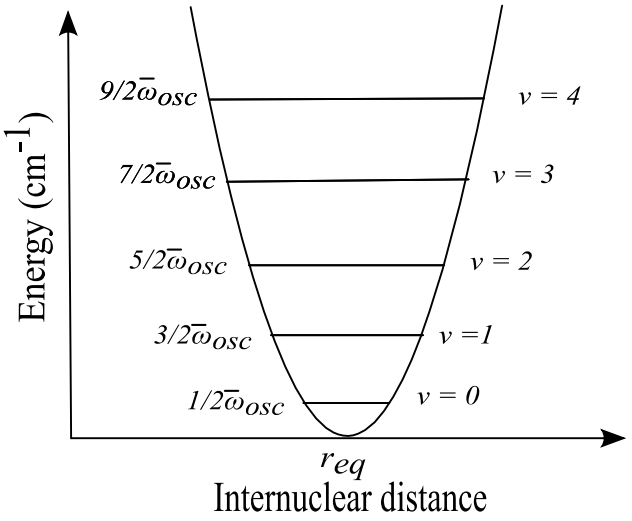

Figure 2-3. The vibrational energy levels of a quantum simple harmonic oscillator.

2.4 The Anharmonic Oscillator

A simple harmonic model is an ideal assumption for a molecule where the displacement is proportional to the restoring force. In real molecules (or mechanical springs) the restoring force is not directly proportional to the displacement due to a damping force. An anharmonic oscillator model is characteristic of a real molecule and the expression for its energy is derived from the Morse function [22, 23] as,

$$E = D_{eq}\left[1 - \exp\{a(r_{eq} - r)\}\right]^2 \tag{2.4}$$

where a is a constant for a given molecule and D_{eq} is the dissociation energy, the expression for energy becomes (using (2.4) in Schrodinger's equation):

$$E_v = \left(v + \frac{1}{2}\right)\bar{\omega}_e - \left(v + \frac{1}{2}\right)^2 \bar{\omega}_e \chi_e \tag{2.5}$$

where $\bar{\omega}_e$ is the oscillation frequency and χ_e is the anharmonicity constant. Equation (2.5) can be rewritten as:

$$E_v = \bar{\omega}_e \left[1 - \chi_e \left(v + \frac{1}{2}\right)\right]\left(v + \frac{1}{2}\right) \tag{2.6}$$

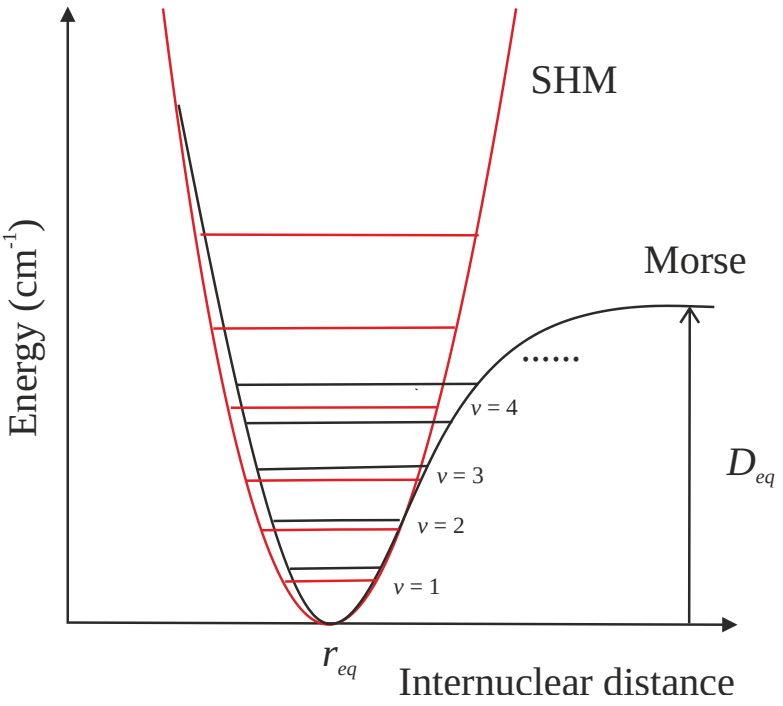

Figure 2-4. Anharmonic oscillator model for a diatomic molecule.

Comparing equation (2.6) with equation (2.2):

$$\bar{\omega}_{osc} = \bar{\omega}_e \left(1 - \chi_e \left(v + \frac{1}{2}\right)\right) \tag{2.7}$$

Thus the anharmonic oscillator behaves similarly to a harmonic oscillator but with decreasing energy spacing with increasing vibrational quantum number or energy. $\bar{\omega}_e$ is defined as the equilibrium oscillation frequency ($E = 0$, hypothetically). The selection rule for the anharmonic oscillator is given as:

$$\Delta v = \mp 1, \mp 2, \mp 3 \ldots \ldots \tag{2.8}$$

Here $\Delta v = \mp 1$ is known as the fundamental band. $\Delta v = \mp 2, \mp 3 \ldots$ etc. are referred to as the overtone bands.

2.5 The Diatomic Vibrating Rotator

From the Born-Oppenheimer approximation it follows that the diatomic molecule can execute rotations and vibrations independently of each other. Therefore, the total energy can be written as a combination of rotational and vibrational energies:

$$E = E_{rot} + E_{vib} \text{ cm}^{-1} \tag{2.9}$$

A diatomic molecule can rotate about three directions: a) about the bond axis, b) end-over-end rotations in the plane of the paper and c) end-over-end rotations at right angles to the plane of paper. The rotational moments of inertia for these motions are termed I_A, I_B and I_C, respectively. For a linear diatomic molecule $I_B = I_C$ and $I_A = 0$. It will be different for other shapes such as a symmetric top molecule. A detailed discussion of this topic can be found in the standard spectroscopy textbooks [22].

It is now stated without proof [22] that the rotational energy for a linear diatomic molecule is, by solving Schrodinger's equation for a non-rigid rotator,

$$E_{rot} = BJ(J+1) - DJ^2(J+1)^2 + \cdots. \tag{2.10}$$

where J is the rotational quantum number, B is the rotational constant given by $B = h/8\pi^2 I_B c$ and D is the centrifugal distortion constant. It is noted from equation (2.10) that the spacing between successive rotational energy levels increases with the rotational quantum number.

Ignoring the higher order terms as they only have a very small effect, the total energy can be written as:

$$E_{total} = BJ(J+1) + \left(v + \frac{1}{2}\right)\bar{\omega}_e - \left(v + \frac{1}{2}\right)^2 \bar{\omega}_e \chi_e \tag{2.11}$$

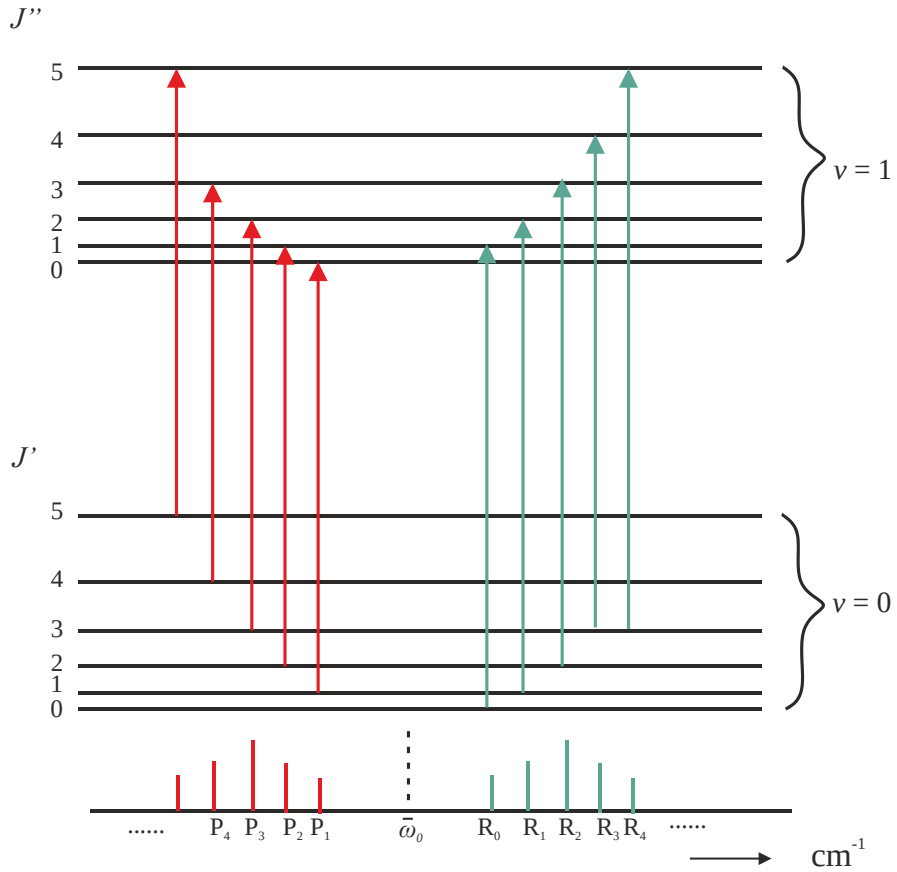

Figure 2-5. The vibrational energy levels with the P and R rotational fine structure [22]. In the diagram $\bar{\omega}_0 = \bar{\omega}_e(1 - 2\chi_e)$.

The selection rule for transitions between rotational energy levels with the corresponding rotational quantum numbers can be written as:

$$\Delta J = 0, \mp 1 \tag{2.12}$$

Figure 2-5 shows the rotational fine structure of vibrational transitions from the v = 0 $\rightarrow v$ = 1 energy level. Rotational absorption lines at the low frequency side with $\Delta J = -1$ are referred to as the P branch, lines with $\Delta J = 0$ is referred to as the Q branch and the spectra corresponding to $\Delta J = +1$ are referred to as the R branch. The Q branch can only be observed in diatomic and polyatomic molecules with appreciable angular momentum in the electronic ground states such as nitric oxide (NO). Most diatomic molecules such as O_2 only have a very small moment of inertia, and hence a very small

angular momentum; consequently the Q branch is not observed in such diatomic molecules.

2.6 Vibrational Spectra of Polyatomic Molecules

So far only the simplest case of a linear diatomic molecule was discussed. This analysis shall now be extended to the general case of polyatomic molecules in order to understand their rotational and vibrational motion, using the fundamental degrees of freedom and symmetry.

2.6.1 Fundamental Vibrations and Symmetry Considerations

Polyatomic molecules with $\mathcal{N}$ atoms, where each atom can move in the X, Y or Z direction has $3\mathcal{N}$ degrees of freedom. The molecule as a whole can translate in space, and hence translational movement accounts for 3 degrees of freedom. The remaining $3\mathcal{N}$-3 degrees of freedom arise from the rotational and vibrational motion. A molecule has 3 degrees of freedom for rotational motion in the X, Y and Z directions. Therefore, vibrational motion has $3\mathcal{N}$-6 degrees of freedom. For a linear molecule, rotation about the bond axis is redundant, and hence only 2 degrees of rotational motion are possible. Consequently, a linear triatomic molecule such as CO_2 will have $3\mathcal{N}$-5 fundamental vibrational modes.

The fundamental vibrational modes of CO_2 are shown in Figure 2-6. These are classified into symmetric or asymmetric modes. The CO_2 molecule has two axes of symmetry. One is the two fold axis (C_2) passing through the bond centre and the other is the ∞-fold axis (C_∞) passing through the bond axis. In order for a molecule to be infrared active, there must be a change in its dipole moment with vibration or rotation. It is seen that the vibrational symmetric stretching mode for CO_2 produces no net change in the dipole moment. Hence, this fundamental mode is not infrared active.

It is expected that CO_2 will have four fundamental modes ($3\mathcal{N}$-5) of vibration. In fact, the v_2 mode is doubly degenerate since it includes two equivalent bending modes, one in the plane of the paper and the other perpendicular to the plane of paper. It is observed

that the rotational selection rules change for molecules undergoing perpendicular or parallel vibrations.

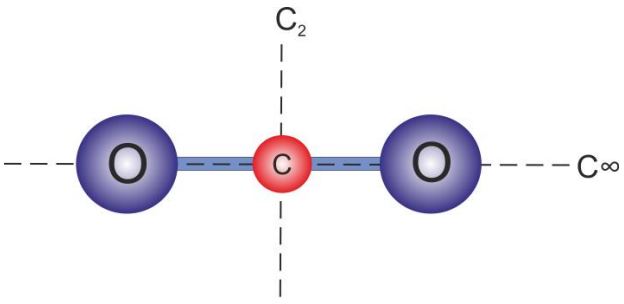

(a) Symmetry axes of CO_2.

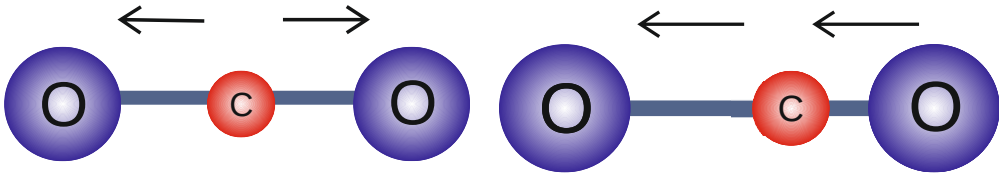

(b) Symmetric stretching mode (1330 cm^{-1}, ν_1 ||)

(c) Asymmetric stretching mode (2349 cm^{-1}, ν_3 ||)

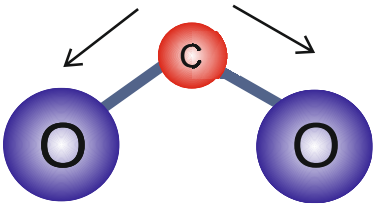

(d) Bending mode (667.3 cm^{-1}, $\nu_2\perp$)

Figure 2-6. The fundamental vibrational modes of CO_2 [22].

In the case of CO_2, alternate lines of the P and R branch have zero intensity (i.e. R48 exists, however, the next line is R50). This is a consequence of the nuclear spin [22]. Therefore, the separation between successive rotational lines (Figure 2-5) will be 4B instead of 2B.

2.6.2 Combination Bands, Overtones and Fermi Resonance

The fundamental bands by themselves do not explain all the lines observed in the vibrational spectra of a molecule. Combination bands, overtones and hot bands are the other types of excitations that can occur in a molecule.

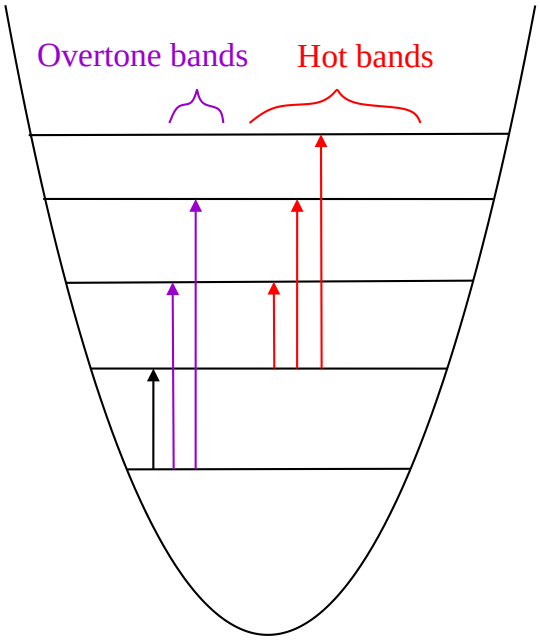

Figure 2-7. The fundamental, overtone and hot band transitions.

These transitions are represented in Figure 2-7 .The transition from 0→ 1 is referred to as the fundamental transition; 0→2 the first overtone; 0→n+1 the n^{th} overtone and henceforth; the intensity rapidly diminishes from the fundamental to the n^{th} overtone. For n > 1, the transition from m→n for m ≠ 0 is a hot band, i.e. hot bands are the transitions which take place from already excited vibrational energy levels. The strength (intensity) of hot band transitions increases with temperature because the population of the excited state increases exponentially as a function of temperature. Hence, the name 'hot bands' because high temperature is one of the conditions for their existence. These hot bands are not usually visible in room temperature spectra. As the spacing between successive energy levels decreases with increasing vibrational quantum number (v), these hot bands occur at lower frequencies with respect to the nearby fundamental and overtone transitions. Hot bands are important in high temperature spectroscopic analysis.

The vibrational spectra of a molecule result from the fundamental mode or overtones as shown in Figure 2-7. However, it can also consist of bands arising from the superposition of the various vibrational modes. These are known as combination bands where two or more fundamental vibrational modes or their overtones are excited simultaneously. Transitions arising from combinations such as $v_1 + v_2$, $2v_1 + v_2$ etc. are examples. Combination bands generally mean addition of two modes; however, difference bands such as $v_1 - v_2, 2v_1 - v_2$ etc. are also possible. The intensity of combination bands is again considerably less compared to that of the fundamental bands.

In certain situations, it is possible that the intensities of the combination bands or overtones can be enhanced by resonance with strong, usually fundamental vibrational modes having similar energy. This phenomenon is termed as Fermi resonance.

Fermi resonance occurs between vibrational bands with nearly the same energy and symmetry. Fermi resonance occurs in CO_2 between the fundamental mode v_1 (at 1330 cm^{-1}) and the overtone $2v_2$ (at 1334 cm^{-1}). These two bands interfere such that the higher is lowered in energy and the lower is raised in energy, the result is two bands with similar intensities at 1280 cm^{-1} and 1388 cm^{-1}. This is because of resonance energy transfer from the fundamental to the overtone band. Fermi resonance can be considered analogous to two pendulums connected by a common bar. When the pendulums oscillate at different frequencies, there is no transfer of energy. However, when they oscillate at similar frequencies (energies), the probability of energy transfer increases.

2.7 The Beer Lambert Law

The Beer Lambert law gives the relation between the light intensity incident on a medium and the light intensity transmitted through the medium and for a uniform medium is given as,

$$I_t = I_{in} \exp\big(-\alpha(v)\big) \tag{2.13}$$

where $\alpha(\nu)$ is called the spectral absorbance or optical depth of the medium, ν is the laser frequency, I_t is the transmitted intensity and I_{in} is the incident intensity. For an optically thin medium, $\alpha(\nu) < 0.05$ and an optically thick medium, $\alpha(\nu) > 0.1$.

The spectral absorbance $\alpha(\nu)$ is written as,

$$\alpha(\nu) = \sigma(\nu) N_g l \tag{2.14}$$

$\sigma(\nu)$ is the absorption cross-section, N_g is the number of gas molecules per unit volume (number density) and l is the optical path length through the medium.

Equation (2.14) can be expanded as,

$$\alpha(\nu) = S(T)\, \phi(\nu, T, P, \chi) N_g l \tag{2.15}$$

where $S(T)$ is the line strength per molecule which is a function of the temperature (T), ϕ is the line shape function which can be calculated mathematically using the line width which is a function of the temperature (T), pressure (P) and gas mole fraction (χ).

The line width and the line strength values can be obtained from databases such as HITRAN or characterised experimentally using a heated low pressure gas cell. This will be explained in Section 6.8. Experimental data is preferred especially at higher temperatures (~ 500 °C) where hot bands may start to appear, and hence have to be accounted for. Subsequent sections explain these important spectral parameters.

2.8 Line Width

The previous sections laid the foundations of IR rotational-vibrational spectroscopy. Spectral lines at a given wavelength are not strictly monochromatic. Even with low resolution spectrometers it was observed that these transitions were broadened in wavelength and have a finite line width. This is because of the broadening of the energy levels due to different mechanisms. There are three major line broadening mechanisms:

A. Natural broadening
B. Collisional broadening
C. Doppler broadening

These broadening mechanisms are briefly discussed.

2.8.1 Natural Broadening

Heisenberg's uncertainty principle states that energy of a quantum level cannot be precisely determined because of its finite lifetime. This is mathematically represented as:

$$\Delta E \Delta t \approx \hbar \tag{2.16}$$

The broadening due to this uncertainty is referred to as natural broadening and has a Lorentzian line shape (homogeneous broadening mechanism) given as,

$$f_{L-N}(\nu) = \frac{1}{\pi \gamma_N}\left[\frac{1}{1+\left(\frac{\nu-\nu_0)}{\gamma_N}\right)^2}\right] \tag{2.17}$$

where $\gamma_N = \sum A_{kl}$ is the half width at half maximum (HWHM) of the line shape function equal to the sum of the decay rates of the excited level *k* into all lower states l and ν_0 is the line centre frequency. A_{kl} can be found in spectral databases such as HITRAN.

2.8.2 Collisional (Lorentzian) Broadening

The naturally broadened rotational-vibrational energy level is further broadened by collisions with other molecules of the same or different species. Collisional broadening or pressure broadening depends on the temperature and density of the gas. This mechanism broadens the line shape in the same way for each molecule, and therefore is a homogenous broadening mechanism represented by a Lorentzian functional distribution:

$$f_L(\nu) = \frac{1}{\pi \gamma_L}\left[\frac{1}{1+\left(\frac{\nu-\nu_0)}{\gamma_L}\right)^2}\right] \tag{2.18}$$

where γ_L is the collisional line width represented as a half width at half maximum of the collissionally broadened Lorentzian lineshape.

The magnitude of collisional broadening is much greater than natural broadening (a constant), and thus Lorentzian broadening refers primarily to collisional broadening.

The collisional line width γ_L at a pressure *P* and temperature *T* is given by the empirical relationship,

$$\gamma_L = \gamma_0 \left(\frac{P}{P_0}\right)\left(\frac{T_0}{T}\right)^{\Delta} \tag{2.19}$$

where Δ is the temperature broadening coefficient and γ_0 is the collisional line width at a temperature T_0 (= 296 K) and pressure P_0 (= 1 atm).When there is more than one molecular species in the gas mixture, the collisional line width is given by,

$$\gamma_{L,i} = \gamma_L^{ii}\chi_i + \sum\nolimits_j \gamma_L^{ij}\chi_j \tag{2.20}$$

where γ_L^{ii} is the self-broadening coefficient for the target gas *i*, γ_L^{ij} is the cross-broadening coefficient for each colliding gas *j* with the target gas *i* and $\chi_{i,j}$ are the gas concentrations in mole fraction.

2.8.3 Doppler Broadening

Doppler (thermal) broadening of absorption lines occurs due to the random thermal motion of gas molecules relative to the incoming radiation. From the frame of reference of the molecule, if a molecule is moving towards the source of radiation, the incoming radiation is blue shifted, and similarly, if the molecule is moving away from the source, the photons are red shifted in energy. Consequently, the absorption or emission spectrum is broadened.

Molecular thermal velocities follow the Maxwell's statistical distribution with the line shape represented by a Gaussian distribution function as [20]:

$$f_G(\nu) = \frac{1}{\gamma_G}\sqrt{\frac{\ln(2)}{\pi}}\exp(-\ln(2)\left(\frac{\nu-\nu_0}{\gamma_G}\right)^2) \tag{2.21}$$

where γ_G is the Gaussian (Doppler) half width at half maximum given as [20],

$$\gamma_G = \nu_0\sqrt{\frac{2\ ln2\ k_B T}{Mc^2}} \tag{2.22}$$

ν_0 is the line centre frequency, M is the molecular mass, k_B the Boltzmann constant, c is the speed of light and T is the temperature (in Kelvin).

2.9 The Generalised Voigt Line Shape

Section 2.8 discussed the mechanisms which broaden the absorption line shape, viz. the collisional and Doppler mechanisms represented by Gaussian and Lorentzian line shape functional profiles [24], respectively. The resultant absorption line shape is given by a convolution of the Lorentzian and Gaussian line shape functions, called the Voigt line shape function. This is mathematically represented as:

$$f_{Voigt} = f_{Lorentzian} \otimes f_{Gaussian} \tag{2.23}$$

Therefore, Voigt line shape function is represented by the convolution integral which has a solution of the form,

$$f_v(\nu) = \int_{-\alpha}^{\alpha} d\nu' f_L(\nu - \nu', \gamma_L) f_G(\nu - \nu_0, \gamma_G)$$

$$= \frac{\sqrt{ln2/\pi}}{\gamma_G} K(x, y) \tag{2.24}$$

where $K(x, y)$ is the Voigt function normalised to $\sqrt{\pi}$ [20] given as,

$$K(x, y) = \frac{y}{\pi} \int_{-\alpha}^{\alpha} \frac{e^{-t^2}}{(x - t)^2 + y^2} dt \tag{2.25}$$

where $x = \sqrt{ln2}\,\frac{(\nu - \nu_0)}{\gamma_G}$, $y = \sqrt{ln2}\,\frac{\gamma_L}{\gamma_G}$ and t is an arbritrary variable.

There are several mathematical methods to compute $K(x, y)$. It is the real part of the complex error function represented in the form,

$$w(z) = K(x, y) + iW(x, y) \tag{2.26}$$

$$= \frac{i}{\pi} \int_{-\alpha}^{\alpha} \frac{e^{-t^2}}{(z-t)} dt \; ; \qquad z = x + iy$$

$K(x, y)$ can also be implemented using numerical approximations such as the McLean's method. The complex error function method is found to be approximately four times faster. These two methods are not discussed here but the interested reader may consult references [20] and [21], respectively.

2.10 Line Strength

The strength/intensity of a molecular absorption is attributed by two major factors:

1. Probability of the molecular transition.
2. Population of the lower state energy level.

The transition probability is given by Einstein's *A* and *B* coefficients. The population distribution of rotational-vibrational quanta in the energy levels is governed by Boltzmann statistics as discussed further.

2.10.1 Boltzmann Statistics

For a thermodynamic system in equilibrium the population density of upper energy level n_i with an energyE_i, relative to the overall population density n_t, can be written as,

$$\frac{n_i}{n_t} = g_i exp \frac{-E_i/k_B T}{Q(T)} \tag{2.27}$$

where g_i is the degeneracy of level i, $k_B T$ is the Boltzmann constant times the temperature and $Q(T)$ is the partition function defined as $\sum_i g_i \exp(-E_i/k_B T)$. The population of the lower state energy level is $n_t - n_i$.

2.10.2 Einstein's *A* and *B* Coefficients

The major processes that affect the population of a molecular energy level are the stimulated and spontaneous emission or absorption. When a molecule is illuminated by light quanta of energy equal to the transition energy between two states, there are two possibilities. It can absorb the photon and go to an excited energy state, or it can cause

stimulated emission of multiple photons if there is a population inversion. For a two level system with the lower state energy level denoted by 1 and the upper state denoted by 2, ratio of stimulated emission to stimulated absorption is given as:

$$\frac{B_{21}}{B_{12}}\frac{g_2\exp(-E_2/k_BT)}{g_1\exp(-E_1/k_BT)} = \exp(-hc\bar{\nu}_0/k_BT) \tag{2.28}$$

Here, B_{12} and B_{21} are the Einstein's B coefficients for absorption and stimulated emission, and $\bar{\nu}_0$ is the wave number. The wave number representation is used here for consistency with earlier works. The probability of absorption is one minus the probability of stimulated emission and can be written as (assuming non-degenerate energy levels):

$$1 - \exp(-(hc\bar{\nu}_0)/k_BT) \tag{2.29}$$

The absorption strength of a given energy level can now be written as:

$$S \propto \zeta\,|R_t|^2\, n_L/n_t\{1 - \exp(-(hc\bar{\nu}_0)/k_BT)\} \tag{2.30}$$

ζ is the isotopic abundance, $|R_t|^2$ is the probability of transition (Einstein's A Coefficient) and n_L is the population density of the lower energy state.

Using equation (2.27) for the lower level population density and (2.29) for the absorption probability, this can be re-written as:

$$S_i \propto \zeta\,|R_t|^2 \left\{\frac{exp(-hcE"/k_BT)}{Q(T)}\right\}\{1 - exp(-(hc\bar{\nu}_0)/k_BT)\} \tag{2.31}$$

Here $Q(T)$ is the total internal partition function which is a product of the rotational partition function and the vibrational partition function (when the interaction between vibrations and rotations is ignored). An approximate formulation of $Q(T)$ is used in this work:

$$Q(T) = a + bT + cT^2 + dT^3 \tag{2.32}$$

a, b, c and d are constants for a given temperature range and are available from literature [25].

$Q(T)$ depends on the molecule/isotope and the temperature range. Most spectroscopic databases define line strength relative to a reference temperature T_0:

$$S(T) = S(T_0)\frac{Q(T_0)}{Q(T)}\frac{\exp(-hcE"/k_BT)\{1-\exp(-(hc\bar{\nu}_0)/k_BT)\}}{\exp(-hcE"/k_BT_0)\{1-\exp(-(hc\bar{\nu}_0)/k_BT_0)\}} \quad (2.33)$$

The partition function values can be obtained from spectroscopic databases such as HITRAN or HITEMP discussed in the next section.

2.11 Molecular Spectral Databases

Spectral databases are available which contain the molecular spectral parameters discussed above such as the line strength and line broadening parameters. These values are used to theoretically model the direct or WMS absorption spectra based on equation (2.13). Two such databases are of interest in this work namely the HITRAN and the HITEMP.

HITRAN (HIgh resolution TRANsmission database) contains the line by line spectral parameters for modelling the high resolution absorption/transmission profiles of various gas molecules at temperatures close to the ambient. All these parameters are referenced with respect to room temperature and atmospheric pressure. The latest HITRAN 2012 database encompasses the spectral information of about 47 molecules and 120 isotopes, from microwave to visible region of the electromagnetic spectrum.

Table 2-1 shows the order in which the spectral parameters are stored in the HITRAN 2012 database. HITRAN is useful for the measurement of gas thermodynamic state variables such as temperature (close to ambient), concentration and pressure from experimental signals by comparing the theoretically modelled spectra against the experimental signals. It is an indispensable tool for spectral survey as it serves to identify the potentially well isolated lines having absorption and temperature dependencies that match the sensor requirements (Chapter 6).

Parameter	Meaning	Units
$\mathcal{M}$	Molecule ID	
$\mathcal{I}$	Isotopologue number	
$\bar{\nu}$	Wavenumber	cm^{-1}
S	Line strength per molecule	$cm^{-1}/(molecule\ cm^{-2})$ at 296 K
$\|R_t\|^2$	Probability (Einstein's *A* coefficient)	s^{-1}
γ_{air}	Air-broadened half width	HWHM at 296K($cm^{-1}atm^{-1}$)
γ_{self}	Self-broadened half width	HWHM at 296K($cm^{-1}atm^{-1}$)
E"	Lower state energy	cm^{-1}
n	Temperature dependent coefficient	of γ_{air}
δ	Pressure induced line shift	$cm^{-1}\ atm^{-1}$
V'	Upper state vibrational level	
V"	Lower state vibrational level	
Q'	Upper state local quanta	
Q"	Lower local quanta	
lerr	Error	
lref	Reference	
*	Float	
g'	Upper state degeneracy	
g"	Lower state degeneracy	

Table 2-1. The HITRAN 2012 format[18].

It has been found that there are inaccuracies in this database and it may not always be suitable for calibration-free measurements. Hence, it was required that the spectral parameters available in the HITRAN database be validated, by comparing the theoretically modelled spectrum using these parameters against the experimentally measured spectrum, at a given path length, temperature, concentration and pressure. Moreover, HITRAN is not suitable for modelling the gas spectra for temperatures significantly different from the ambient because it does not take account of the transitions that occur from excited energy levels (hot bands) and as it does not contain the high temperature partition functions. The HITEMP database [26] (High Temperature Molecular Spectral Database) complements HITRAN at higher temperatures (> 1000 K).

The temperatures expected in a GTE exhaust plume (~50-500 °C) are at the higher end for HITRAN database and towards the lower end for the HITEMP database. Hence, in

this work, extensive experimental high temperature laboratory characterisation was necessary to obtain the CO_2 spectral parameters.

2.12 Extracting the Concentration, Temperature and Pressure

Equations (2.13) to (2.15) are not by themselves useful in extracting the required information about the target gas species. The key parameters of interest in optical gas sensing applications are the concentration, pressure and temperature. An alternate definition for gas concentration in terms of pressure and temperature is derived from the ideal gas law ($PV = n_t\mathcal{R}T$) as,

$$N_g = \frac{n_g N_A}{V} = \left(\frac{n_g}{n_t}\right)\left(\frac{n_t}{V}\right)N_A = \chi\left(\frac{P}{\mathcal{R}T}\right)N_A \tag{2.34}$$

where N_g is the number density of the gas molecule, n_g is the number of moles of the gas, n_t is the total number of moles, N_A is the Avogadro's number, $\mathcal{R}$ is the ideal gas constant, χ is the mole fraction, P is the pressure in atm, V is the volume occupied by the gas and T is the temperature in Kelvin.

Hence, the absorbance (for a uniform medium) (equation (2.15)) can be rewritten as,

$$\alpha(\nu) = [SN_A/\mathcal{R}T\,]\phi(\nu)\chi Pl = S'(T)\phi(\nu)\chi Pl \tag{2.35}$$

Equation (2.35) is much more useful and relates the thermodynamic state variables of pressure, temperature and mole fraction to the molecular absorbance [27]. It has to be borne in mind that an area normalised line shape function is employed.

It is indicated by equation (2.35) that the concentration, pressure and temperature influence the gas absorption signal. The line strength is mostly a function of temperature only (Equation (2.20)). This is made use of in ratio thermometry applications. Once the temperature, pressure and path length are known, concentration can be determined from the depth of the absorption feature.

In majority of the gas sensing applications the two unknown variables are the temperature and concentration as the pressure is near atmospheric as in the case of a GTE exhaust plume. Over and above, the least-squares curve fitting algorithm has a unique solution for only two of the thermodynamic state variables of pressure, concentration and temperature, but not all the three. Hence, a least-squares curve fitting technique was implemented, which subtracts the theoretical absorption line shape (equation (2.13)) from experimental spectra to extract the gas concentration and temperature, assuming a known pressure, by minimising the squared and rooted residuals. The curve fit is verified to have a unique solution (minima for the residual plot) from the theoretical simulations. In view of the fact of the relatively closely spaced residual values and owing to the inadequacies in signal modelling, noise etc., the algorithm can sometimes converge to the wrong solution for concentration and temperature. Applying a finite range to the temperature and concentration values, close to the expected values in the fitting routine can be used to mitigate this problem to some extent. The initial measurement strategy was to fit for the concentration with the temperature known/measured, assuming a top hat distribution profile across the plume. Since the temperature in the GTE plume was continuously changing, for obtaining concentration measurements satisfying the accuracy requirement for tomographic imaging, it was necessary to fit for the temperature as well.

2.13 Summary

This chapter gives the introductory theory of molecular absorption of light in the infrared region of the electromagnetic spectrum. It begins by considering the molecule as vibrating and then includes the rotational motion of the gas molecule to explain the fine structure of the vibrational transitions. The quantum anharmonic oscillator model for vibrational motion explains the existence of overtone bands through relaxation of the selection rule. Combination bands and Fermi resonance are introduced to explain the bands which are not fundamental or overtones. The absorption bands which become visible at high temperatures known as the hot bands are also discussed. This chapter also introduces the analytical models used to extract gas thermodynamic variables from the experimental absorption spectra. Accurate tomographic imaging of the spatial distribution of CO_2 requires the concentration values to be known within an accuracy of

below 4 % [28]. This is only possible with an accurate knowledge of the temperature which is expected to change continuously with the engine operating conditions. Consequently, a least-squares curve fit algorithm will be implemented with the theoretical absorption signals compared against the experimental signals to simultaneously infer the gas concentration and temperature.

Chapter 3

Spectroscopic Techniques for Harsh Environments

3.1 Introduction

This chapter introduces the theory of spectroscopic techniques for harsh environmental sensing in a gas turbine exhaust plume.

A hostile or harsh environment in electronics or photonics is defined as an environmental condition in which survival of physical sensing devices is difficult. The temperatures outside the range of -40 °C to 125 °C is usually considered harsh. Further contributors to harsh environments are moisture, fuels, noxious gases, electromagnetic interference, gamma rays, vibrations, shock waves etc. The exhaust plume of an aero engine is exemplary of a harsh environment.

The simplest and widely used TDLS technique is direct spectroscopy. In direct spectroscopy a linear current sweep is applied to the laser which creates an instantaneous intensity sweep and a corresponding wavelength sweep. The swept intensity when passed through the analyte gas is attenuated at the wavelengths corresponding to molecular transitions in the gas. This is normalised with a baseline intensity signal with no gas. In situations where a background signal is not available for normalisation, the background signal is obtained from the non-absorbing regions traversed by wavelength scan, using a polynomial fit of the baseline or advanced baseline fitting algorithms [29]. Though easier to implement and analyse, it has limitations in harsh environments where the gas absorption measurement signal is buried

in noise. Digital fast scanning (DFS) of the laser (equivalent to applying a comb filter) [7] typically at tens of kilohertz, can be used to filter the noise from fast transmissivity fluctuations. However, low frequency transmission noise at multiples of the scan frequency is not filtered.

As direct spectroscopy is limited by noise, wavelength modulation techniques were used. Wavelength modulation spectroscopy puts to use a phase sensitive detection by the lock-in amplifier and is a very effective technique used in harsh environmental metrology. The laser intensity and wavelength/frequency are repetitively scanned across the absorption line using a linear current sweep, simultaneously, a sinusoidal injection current modulation is added to it, which generates an instantaneous intensity modulation output and a delayed frequency modulation output. The laser output signal with the scan, IM and FM, interacts with the gas signal to give a strong signal proportional to the derivative of the absorption line shape and additional components from the interaction of the IM signals with the gas absorption line shape. This signal at the detector output is demodulated using a lock-in amplifier at the various multiples (harmonics) of the modulation frequency. Analytical models are then used to recover the gas parameters such as the concentration and temperature (or pressure) from the WMS signals.

Approaches such as the PDM and the RAM technique are used for the recovery of direct absorption line shapes from the first harmonic WMS signals. Owing to their relative simplicity, these techniques are a good starting point for understanding and validation of the spectroscopic model based on a Fourier series expansion of the WMS signal (Chapter 6). In this work, these techniques have been adapted to account for the variation in the laser modulation characteristics such as the WM-IM phase lag and tuning coefficient across the laser scan for accurate line shape recovery. A methodology is also introduced which enables the recovery of the gas absorption line shapes using these techniques, independent of the relative phase of the LIA reference signal with respect to the WMS signals. This methodology is very useful in practical sensing applications as will be explained.

Transmission fluctuations (additive and multiplicative) [30] due to optical beam propagation through the medium with a time varying refractive index (from turbulence in a gas turbine exhaust plume), as well as scattering from soot particles, is one of the major factors adding noise to the WMS signals in a GTE exhaust plume. During the

course of this work it was realised that the *1f* WMS signals drifted severely for the aero engine measurements. Moreover, because of the absence of a non-absorption baseline for the chosen CO_2 absorption line, it was necessary to have a time-multiplexed background signal for normalisation of the gas signals. Due to the signal drift and noise, it was considered impossible to obtain this normalisation background signal. Normalisation with the first harmonic WMS signal is a technique used for cancelling the transmission noise along the optical line of sight. This is introduced in Section 3.9 referred to as the *1f* normalised *2f* WMS technique. The chapter begins by introducing the origin of the derivative line shapes for the WMS signal detected at various harmonics of the modulation frequency.

3.2 Wavelength Modulation Spectroscopy

In harsh environments, wavelength modulation spectroscopy has a significant improvement in signal-to-noise ratio compared to direct spectroscopy, as the signals are measured at a frequency band away from the *1/f* noise spectral bands. The laser is modulated using a slow current ramp of frequency less than few tens of kHz, which repetitively scans the laser wavelength across the absorption line and a fast sinusoidal current modulation of much smaller amplitude, having modulation frequencies in the tens to hundreds of kHz.

The intensity output of the laser is given by,

$$I_l(\nu) = I(\nu) + \Delta I(\nu)cos(\omega t) + \Delta I_2(\nu)\cos(2\omega t + \psi_2) \tag{3.1}$$

where ω is the frequency of the sinusoidal modulation, $I(\nu)$ is the instantaneous intensity of laser, $\Delta I(\nu)$ and $\Delta I_2(\nu)$ are the amplitudes of linear and nonlinear intensity modulations respectively, and ψ_2 is the phase of the nonlinear IM relative to the linear FM.

The frequency output of the laser is given as,

$$\nu = \nu_1 + \Delta\nu\cos(\omega t - \psi_1) \tag{3.2}$$

where ν_1 is the central frequency of the laser, $\Delta\nu$ is the frequency modulation amplitude and ψ_1 is the phase of the FM relative to the linear IM. The second order frequency

modulation amplitude is calculated to be very small for most DFB lasers, and hence ignored in the analysis.

Intensity of the light transmitted through the gas (I_{out}) is given by the Beer Lambert law,

$$T = \frac{I_{out}}{I_l} = \exp[-\alpha(\nu_1 + \Delta\nu\cos(\theta))] \tag{3.3}$$

where $\alpha(\nu)$ is spectral absorbance, I_l is the incident laser intensity and $\theta = \omega t - \psi_1$.

The optical gas transfer function (T) can be expressed as a Fourier series expansion [8][31],

$$T = \sum_{n=0}^{\alpha} a_n(\nu_1 + \Delta\nu\cos(\theta))\cos n\omega t \tag{3.4}$$

where a_n are the Fourier coefficients given by,

$$a_n = \frac{1}{2\pi}\int_{-\pi}^{\pi} \exp\left(\sum\nolimits_j S_j'(T)\phi_j(T, P, \chi, \Delta\nu, \gamma_L, \nu_0, \nu, \gamma_G)\right) P\chi_i l\cos n\theta \; d\theta \tag{3.5}$$

$S_j'(T)$ is the line strength of the j^{th} absorption line and ϕ_j is its line shape function.

The LIA multiplies the transmitted signal with $\cos(n\omega t + \theta_L)$ and $\sin(n\omega t + \theta_L)$ and extracts the DC components by low pass filtering the resultant signals. The output of the lock-in amplifier has the characteristic shape of the n^{th} derivative of the absorption line shape. This is pictorially explained in the Figure 3-1. The interaction of the input sinusoidal signal with the nonlinear absorption transfer function generates outputs at the various harmonic frequencies. The maximum amplitude of the first harmonic component of the resultant signal occurs at the full width at half maximum (FWHM) where the slope is the most linear. The maximum *2f* signal arise from the peak which is the most nonlinear. The first harmonic signal reverses in magnitude at the peak where it has zero amplitude. The *2f* signal on the contrary goes to zero when the signal is linear, i.e., has no higher harmonic components. Consequently, the *1f* signal has the characteristic shape

of the first derivative of the absorption line shape and the *2f* signal has the shape of its second derivative and henceforth. The process is similar to FM to AM conversion, i.e. the AM and FM modulated signal interacts with a gas absorption line, which consequently gives rise to secondary AM components at different harmonics which are then selectively demodulated by the LIA.

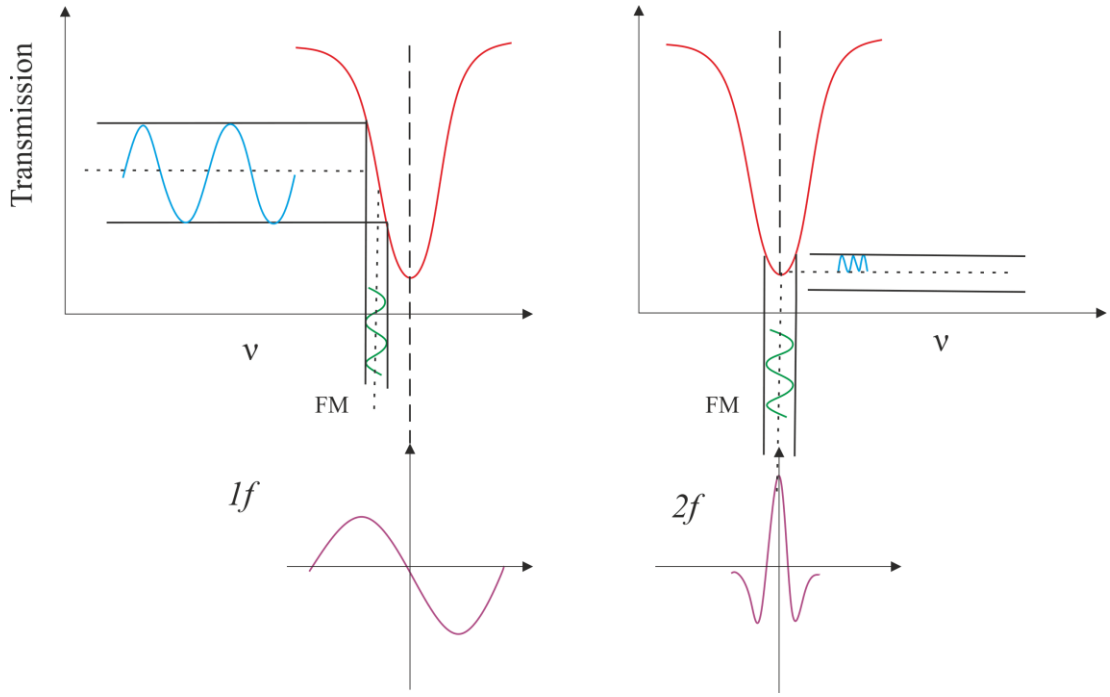

Figure 3-1. FM to AM conversion due to a gas absorption line.

3.3 Calibration-free Phase Sensitive Detection

The lock-in amplifier performs *nf* demodulation of the input signal by multiplying with $\sin(n\omega t + \theta_L)$ and $\cos(n\omega t + \theta_L)$ to generate the two orthogonal (X and Y channels) lock-in amplifier signals. The WMS signals on the X and Y channels of the LIA are sensitive to phase shifts induced by the launch and receive electronics, and the lock-in amplifier reference phase (θ_L). Therefore, these techniques are referred to as phase sensitive and needs knowledge of the reference phase(θ_L) of the lock-in amplifier.

The commonly used methodology to obtain an unknown gas concentration or temperature is to standardise against a known gas mixture [30]. Calibration-free measurements assume that the gas parameters can be measured without comparison to a known gas concentration or mixture. For these calibration-free techniques, the WMS

models are least-squares curve fit to the measured WMS gas signals to obtain the gas thermodynamic state variables such as the mole fraction (concentration) and temperature or pressure. This work focusses on three calibration-free techniques. These include the RAM [32] technique and the phasor decomposition method [33], both of which are phase sensitive first harmonic detection techniques. Section 3.9 of this chapter focusses on the third technique known as first harmonic normalised *2f* detection (*2f/1f*).

An alternative form of equation (3.4) for optically thin media is given as,

$$T(\nu) = 1 - \alpha(\nu) \tag{3.6}$$

The absorbance $\alpha(\nu)$ is now expanded as a Fourier series,

$$-\alpha(\nu) = \sum_{n=0}^{\infty} a_n(\nu) \cos(n\omega t) \tag{3.7}$$

The detector output signal is now given as (ignoring the nonlinear IM and assuming an optically thin sample ($\alpha(\nu) < 0.05$)),

$$I_{det} = \{I + \Delta I \cos \omega t\} \left\{1 + \sum_{n} a_n \cos(n\omega t - n\psi_1)\right\} \tag{3.8}$$

Generally, for nf (or $n\omega$) detection, the output of the lock-in amplifier consists of the unwanted *nf* residual amplitude modulation which is simply the nth order IM at frequency $n\omega$, plus three additional components which originate from the interaction with the gas line. These components are:

1. The primary derivative component proportional to $a_n I(\nu)$ at a phase of $-n\psi_1$ relative to the IM signal (This component is known in the literature [34, 35] as the FM component because it is the prominent component having the shape of the nth derivative as shown in Figure 3-1).
2. Contributions from the linear RAM proportional to $0.5a_{n-1}\Delta I(\nu)$ at a phase of $-(n-1)\psi_1$, and
3. $0.5a_{n+1}\Delta I(\nu)$ at a phase of $-(n+1)\psi_1$.

For $n = 2$ (*2f* detection) these three components are represented in the following phasor diagram (Figure 3-2),

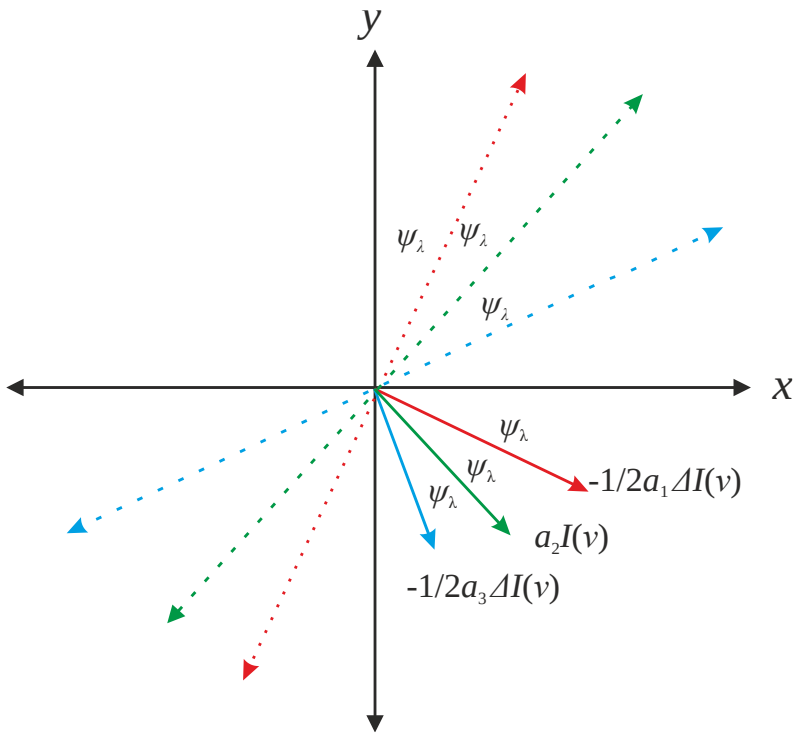

Figure 3-2. Signals at $n = 2$. The dashed lines represent the orientation of the lock-in reference signal to cancel each of these components. The nonlinear RAM component is not shown.

In Figure 3-2, $\psi_\lambda = \psi_1 - \pi$ is known as the phase difference between intensity modulation (IM) and wavelength modulation (WM), where ψ_1 is the phase of the *1f*-FM signal w.r.t. the *1f*-IM signal. WM is π radians out of phase with FM. Here the signals are only shown in the 4th quadrant. In reality, the signals are both in the 2nd and 4th quadrants as they have both positive and negative values. For example, the *1f* signal changes from positive to negative at the origin (i.e. at the absorption line centre). This also highlights the difference between WM and FM. i.e. FM goes from positive to negative at the origin; while the WM is 180 degrees out of phase to the FM and goes from negative to positive.

From Figure 3-2, it can be inferred that by changing the phase of the lock-in amplifier reference signal to align it orthogonally with a particular signal component; it was possible to cancel that component. This forms the basis of the PDM and the RAM technique discussed in Sections 3.4 and 3.5, respectively.

3.4 RAM Technique

As indicated in the previous section, the RAM technique isolates a projection of the *1f* RAM signal, with the absorption signal superimposed in it, to one of the orthogonal lock-in amplifier channels.

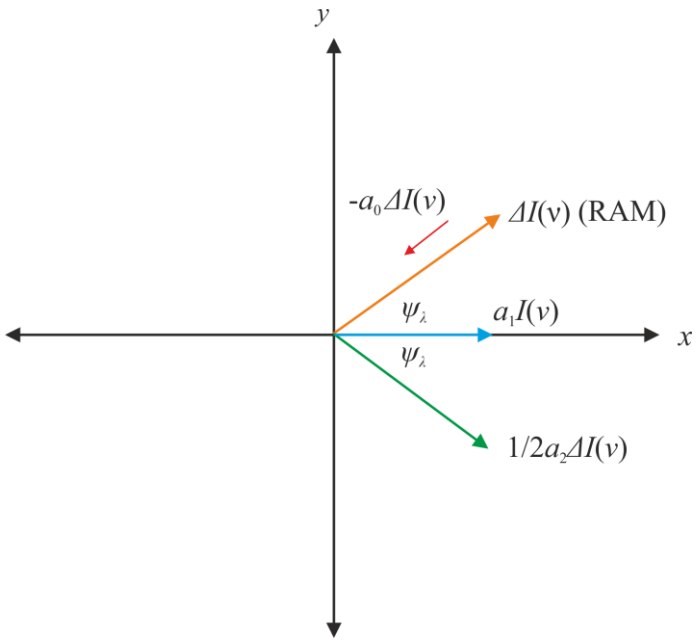

Figure 3-3. The RAM technique.

The signal at the input end of the lock-in amplifier at detection frequency 1ω is:

$$I_{det}^{\omega} = \Delta I(\nu)\cos(\omega t) + a_0(\nu)\Delta I(\nu)\cos(\omega t) + a_1(\nu)I(\nu_1)\cos(\omega t - \psi_1) + 0.5\, a_2(\nu)\Delta I(\nu)\cos(2\omega t - 2\psi_1) \quad (3.9)$$

These are represented in the phasor diagram of Figure 3-3.

The phase of the lock-in amplifier reference is adjusted such that the Y-channel contains a projection of the RAM absorption signal and no FM contribution [36] (hence the name RAM isolation). The X-channel now has an orthogonal projection of the RAM absorption signal and the entire FM component.

The RAM absorption signal isolated on the LIA Y-channel is given as:

$$RAM = \Delta I(\nu)\{1 + a_0 - 0.5a_2\}\sin(\psi_\lambda) \quad (3.10)$$

Normalising this with a non-absorbing background signal or a signal obtained from the baseline fit of the non-absorbing regions of the signal which is proportional to the RAM signal ($\Delta I sin(\psi_\lambda)$) removes the contribution of the background RAM signal, thus recovering the gas absorption line shape. It is important to notice that the signal amplitude is reduced by a factor of $\sin(\psi_\lambda)$.

As evident from Figure 3-3, the RAM absorption signal on the Y-channel contains the projection of a distorting *2f* component ($0.5\Delta I a_2 \sin(\psi_\lambda)$). Considering its magnitude as negligible for smaller modulation amplitudes, this term is often ignored. Yet, at higher wavelength modulation amplitudes this distorting component tends to flatten the recovered RAM absorption signal. In general, distortion of any WMS signal is quantified using a dimensionless parameter known as the modulation index, which is the ratio of the frequency modulation amplitude to the half width at half maximum of the probed absorption line shape. The modulation index will be further examined in Section 3.6.

3.5 Phasor Decomposition Method

It was noted in the case of the RAM technique that only a fraction of the RAM absorption signal is recovered (on one of the orthogonal lock-in amplifier channels). This drawback is overcome using the phasor decomposition method which uses both the X and Y channels of the LIA to extract the entire RAM absorption signal. In the PDM the phase of the lock-in amplifier reference signal is adjusted such that a pure FM signal with its non- absorbing wings going to zero is isolated on the LIA Y-channel.

The Y-channel now contains the projection of the FM signal with no RAM contribution. The signal at the Y-channel of the LIA is given by,

$$M_y = a_1 I(\nu) \sin(\psi_\lambda) - 0.5 a_2 \Delta I(\nu) \sin(2\psi_\lambda) \tag{3.11}$$

i.e., the FM component ($a_1 I(\nu) \sin(\psi_\lambda)$) and additionally a small *2f* line shape component (negligible at small modulation indices).

The X-channel now has the entire RAM absorption on it and the orthogonal projections of the signals on the Y-channel,

$$M_x = \Delta I(\nu)\{1 + a_0\} - a_1 I(\nu)\cos(\psi_\lambda) + 0.5a_2\Delta I(\nu)\cos(2\psi_\lambda) \quad (3.12)$$

The RAM signal with the absorption line shape superimposed on it is recovered using the mathematical relation:

$$M_x + \frac{M_y}{\tan(\psi_\lambda)} = \Delta I(\nu)\{1 + a_0 - 0.5a_2\} \quad (3.13)$$

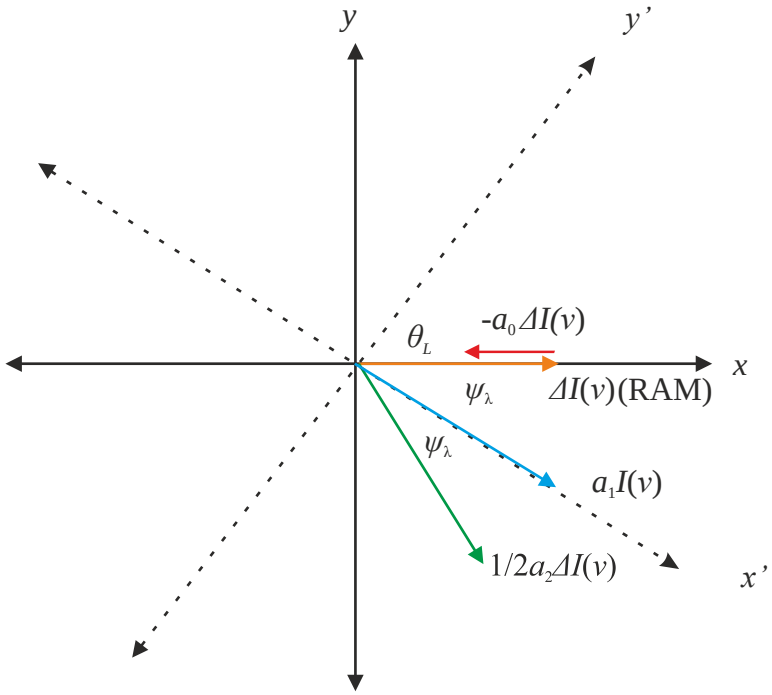

Figure 3-4. Figure shows the phasor decomposition method where the lock-in amplifier X-channel is oriented to the *1f* RAM component.

The distorting component, $a_2\Delta I$, is very small at lower modulation amplitudes characterised by smaller modulation index (< 0.2) which is a very important parameter in WMS and will be discussed in detail in Section 3.6.

In is noted that in both the RAM technique and the PDM, the knowledge of the WM-IM phase (ψ_λ) is required to measure the gas absorption. The WM-IM phase (ψ_λ) is usually measured experimentally. Alternately, a vector method proposed by A. McGettrick [35] could be used to obtain the WM-IM phase from the LIA signals shown in Figure 3-4. This method as well as other methods to experimentally measure ψ_λ are explained in Section 4.7. Each of these methods has its own advantages and disadvantages which will be discussed in this work.

The signal-to-noise ratio of the PDM is higher than the RAM technique because the entire RAM absorption signal is recovered (owing to the absence of the $\sin(\psi_\lambda)$ term). The signal is normalised by dividing (3.13) by a background time multiplexed signal (or the signal obtained from the baseline fit) obtained by the purging gas cell to create a vacuum or by filling it with a buffer gas such as N_2 , the background signal only having the IM term (ΔI), thereby recovering the gas absorption line shape.

3.6 Modulation Index

It is observed that as the modulation amplitude increases the distorting *2f* line shape component ($\Delta I 0.5 a_2$) also increases in magnitude and tends to broaden the absorption line shape recovered using the PDM or RAM technique.

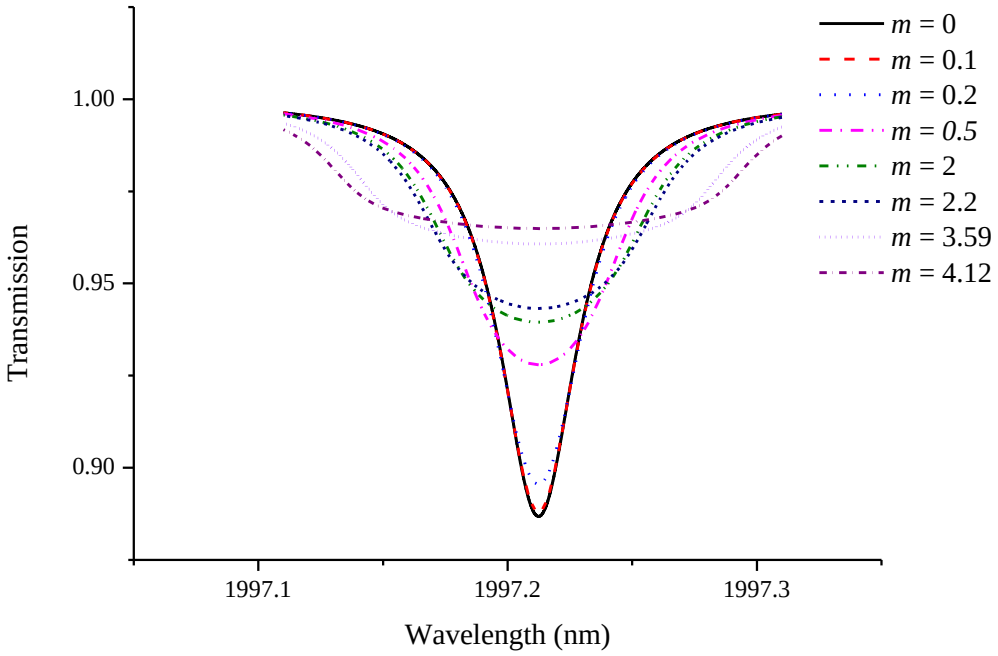

Figure 3-5. Distortion in the recovered gas absorption line shape with an increase in the modulation index. It is observed that the signal starts to distort significantly at m > 0.2.

In general, the distortion of any WMS line shape signal can be quantified by using a very important dimensionless quantity known as the modulation index, which is defined

as the ratio of the frequency modulation amplitude ($\Delta\nu$) to the half width at half maximum of the probed absorption feature, i.e.,

$$m = \frac{\Delta\nu}{\gamma_{HWHM}} = \frac{di * \in}{\gamma_{HWHM}} \tag{3.14}$$

where $\in$ is the tuning coefficient of the laser in $\mathrm{GHz/mA}$ or ($\mathrm{cm^{-1}/mA}$) and *di* is the amplitude of the current modulation applied to the laser.

Absorption line shapes recovered using the PDM at different m values are shown in Figure 3-5. The characteristic values; 2, 2.2, 3.59 and 4.12, correspond to the modulation indices to obtain the maximum amplitude for the *1f, 2f, 3f* and *4f* harmonic signals, respectively. As can be seen, the recovered absorption line shape tends to be broadened for $m > 0.2$. The aforementioned distortion due to the second harmonic line shape component was compensated for by multiplying the recovered absorption line shape by a correction function [34]. An equivalent approach is presented in Section 6.4 of this thesis.

3.7 Phase Independent PDM

As discussed in Sections 3.4 and 3.5, the phasor decomposition method and RAM technique are phase sensitive. These two methods require careful alignment of the phase of the LIA reference signal. The above mentioned methodology is considered difficult to implement especially in the field. It was observed that the above stated techniques were sensitive to phase changes less than a degree. Consequently, it would be an added advantage if these techniques were made independent of the orientation of the lock-in amplifier reference signal with respect to the WMS signals at the detector.

Let θ_L be any arbitrary orientation angle of the lock-in reference channel. This is depicted in Figure 3-4.

The signals on the X and Y channels are now given by [37],

$$M_x = \Delta I(\nu)(1 + a_0)\sin(\theta_L) + a_1 I(\nu)\sin(\theta_L + \psi_\lambda) + 0.5a_2\Delta I(\nu)\sin(\theta_L + 2\psi_\lambda) \tag{3.15}$$

$$M_y = -\Delta I(1 + a_0)\cos(\theta_L) - a_1 I(\nu)\cos(\theta_L + \psi_\lambda) - 0.5a_2\Delta I(\nu)\cos(\theta_L + 2\psi_\lambda) \quad (3.16)$$

The value of θ_L in the above equation is iterated from 0 to π till no FM contribution is obtained on the absorption line shape recovered using equation (3.13). This condition is satisfied when the depth of the recovered absorption signal is minimal [37].

This method is particularly useful in applications such as optical tomography where multiple measurement paths are employed (in a ring fibre network topology). The relative reference phase alignment along each of these arms will be different due to the different fibre lengths along the ring (changing the IM phase), varying response of the transmitter and receiver side electronics, synchronisation issues etc.; rendering it difficult to individually align the lock-in amplifier reference phase for each of the measurement arms.

3.8 Drawbacks of the PDM and RAM Technique

It was observed that the PDM and RAM technique are not suitable for measurement in harsh environments with rapidly changing transmission conditions [7], such as in a GTE exhaust plume.

Due to the random fluctuations in the RAM during the field measurements, it is not possible to normalise this signal using a time multiplexed background signal. The transmission noise on the signal also makes it unsuitable for baseline fitting routines to obtain accurate measurements. Under such circumstances, *2f* detection techniques seem to be the preferred choice because the signal at *2f* detection has only a very small nonlinear RAM component of magnitude at least two orders less than the linear RAM. That being the case, signals at *2f* detection also have a near zero background and are easier to calibrate. A *2f*-PDM technique was proposed by Chakraborty et al. [38] to extract the primary *2f* derivative line shape signal as well as to null the nonlinear RAM using optical techniques. A dual beam electronic technique to null the nonlinear *2f*-RAM was also proposed by Zhu and Cassidy [39] using the Hobbs auto-balanced noise-cancelling circuit [40]. This method was implemented by Bain et al. [41] for the water vapour lines at 1430 nm in the exhaust of an aero engine to obtain *2f* WMS signals with the *2f*-RAM signal cancelled. Another method was proposed by Liu et al. [42] by

applying an additional second harmonic current modulation to the DFB laser using a summing amplifier and adjusting its phase and magnitude so as to cancel the *2f*-RAM signal. In this work, the *2f*-RAM signal is cancelled by a background subtraction method.

3.9 Calibration-free *1f* Normalised *2f* WMS Technique

Reid et al. [43] implemented a method based on the analytical expressions developed by Arndt et al. [44] for a Lorentzian line shape under the influence of wavelength modulation, for the lock-in amplifier output signals at *2f* detection, and could extract the pressure or line width from the ratio of the peak to trough of the *2f* signal. This was similar to the methodology by Henningson et al. [45], to determine the gas parameters from the peak to trough ratios and the apparent widths of the *2f* line shape signal. However, these techniques considered only the pure FM signal component and did not take RAM component into account, as it was an unwanted signal that made analysis difficult at the time. Thus, the DFB lasers were assumed to have a linear current-intensity response and the nonlinear IM was considered negligible.

For the CO_2 absorption feature, it will be shown (Chapters 5,6) that non-absorbing wings are not available within the wavelength scan range of the DFB laser, which made it difficult to extract a RAM baseline signal for in-line normalisation of the RAM absorption signals, from a polynomial fit of wings of the absorption feature. Hence, the only method to normalise the absorption signal was with a time multiplexed background gas signal containing the RAM signal with no absorption. On the other hand, in measurements where the transmission conditions are fluctuating over time, the RAM signal would have changed by the time the background is recorded. Hence, these techniques cannot be used in environments where the intensity is fluctuating due to vibrating optics, varying refractive index, physical obstruction of the beam etc.

Even supposing the *2f* detection was used, the signal was observed to be buried in noise arising from fluctuations in the transmissivity as well as etalons. This is explained in Chapter 6.

It was reported by a former member of the CMP group (Arup Lal Chakraborty [46]) as well as other works [6, 8, 30] that for a given DFB laser, the ratio of IM to instantaneous intensity remains a constant for a given laser temperature, bias current and modulation frequency, at every point along the measurement path. Hence, equation (3.1) was rewritten as,

$$I_l(\nu) = I(\nu)\{1 + i_0(\nu)\cos(\omega t + \psi_1) + i_2(\nu)\cos(\omega t + \psi_2)\} \tag{3.17}$$

where,

$$i_0 = \frac{\Delta I(\nu)}{I(\nu)}, i_2 = \frac{\Delta I_2(\nu)}{I(\nu)} \tag{3.18}$$

are constants for a given DFB laser.

For an optically thick sample, assuming the *2f* signal is aligned with the X-channel of the LIA, the *2f* signals on the X and Y channels of the lock-in amplifier are derived as, from equations (3.3) to (3.5),

$$X_{2f} = \frac{\mathcal{G}I}{2}\left[a_2 + \frac{i_0}{2}(a_1 + a_3)\cos(\psi_1) + i_2\left(a_0 + \frac{a_4}{2}\right)\cos(\psi_2)\right] \tag{3.19}$$

$$Y_{2f} = -\frac{\mathcal{G}I}{2}\left[\frac{i_0}{2}(a_1 - a_3)\sin(\psi_1) + i_2\left(a_0 - \frac{a_4}{2}\right)\sin(\psi_2)\right] \tag{3.20}$$

where the constant $\mathcal{G}$ accounts for the channel gain for the LIA.

The parameters i_0, i_2, ψ_1, ψ_2 are expected to be constants for a given DFB laser, chip temperature and laser bias current. a_0, a_1, a_2, a_3 and a_4 are the Fourier coefficients with the characteristic derivative line shape at various harmonics (Figure 3-1) from the zeroth to the 4th order; calculated using equation (3.5). The magnitudes of higher order Fourier coefficients are small enough and may be neglected in the analysis. It can be observed that the RAM term is absent in equation (3.19); however, it is embedded in the exponential in equation (3.3).

These signals are represented by the phasor diagram in Figure 3-6. As seen, at *2f* detection; the second harmonic line shape signal (Ia_2) has the largest magnitude but is mainly distorted by the *1f* line shape signal (ΔIa_1) and a residual amplitude modulation signal ($\Delta I_2(1 + a_0)$). As mentioned previously, Chakraborty et al. had developed a strategy to cancel the *1f* line shape signal using a *2f* - PDM method [38] and cancel the

nonlinear *2f* - RAM using an optical nulling technique. However, this method suffers from the difficulty in aligning the *2f* line shape signal to a given lock-in amplifier channel as in Figure 3-6, because of the projections of the *1f* line shape signal ($\Delta I a_1$) and a small *3f* line shape signal on it ($\Delta I a_3$).

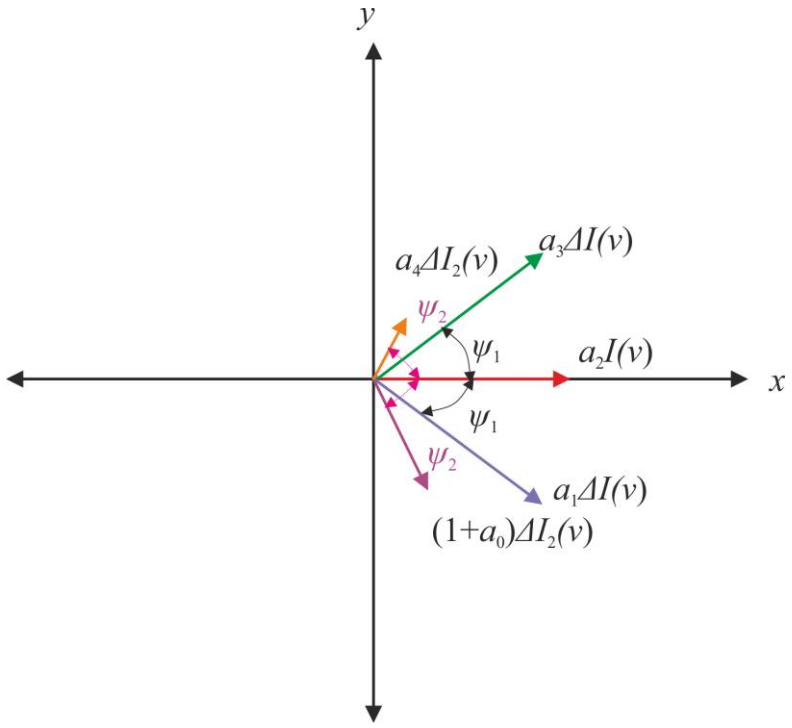

Figure 3-6. Alignment of the prominent component signals at *2f* detection. Not drawn to scale.

Since it is difficult to align the signals, it is considered advantageous to take the magnitude of the *2f* signal, i.e. $R_{2f} = \sqrt{\mathrm{X}_{2f}^2 + \mathrm{Y}_{2f}^2}$.

All the parameters in the *2f* WMS signal are constants for a given laser except the instantaneous laser intensity $I_l(\nu)$ which is affected by the transmissivity noise expected in harsh environments. Several different approaches could be used to calibrate out the instantaneous laser intensity. For example, a reference intensity signal from the laser was used to normalise the instantaneous laser intensity through the measurement arm, to get a suitable scaling factor. The scaling factor is required to be a constant over time. However, any change in the transmission characteristics either through the reference arm or the measurement arm will cause a change in this scaling factor. Hence, for field

applications in harsh environments with rapidly changing transmission conditions, such an approach is not possible.

It was pointed out by Ebert et al. [7] that the first harmonic WMS signal can be used as a "transmission probe" to cancel the effects of transmission fluctuations. This technique was further developed by Rieker et al. [8].

The magnitude of the *1f* signal is given by (assuming the same configuration as the RAM technique):

$$X_{1f} = \frac{\mathcal{G}I}{2}[a_1 + i_0(a_0 + 0.5\,a_2)\cos\psi_1 + i_2(a_1 + a_3)\cos\psi_2] \tag{3.21}$$

$$Y_{1f} = -\frac{\mathcal{G}I}{2}[i_0(a_0 - 0.5\,a_2)\,sin\,\psi_1 + i_2(a_1 - a_3)\sin\psi_1] \tag{3.22}$$

$$R_{1f} = \sqrt{X_{1f}^2 + Y_{1f}^2} \tag{3.23}$$

Dividing the magnitude of the *2f* signal with the magnitude of the *1f* signal cancels the multiplicative transmission fluctuations as follows:

$$\frac{R_{2f}}{R_{1f}} = \frac{\sqrt{(X_{2f}^2 + Y_{2f}^2)}}{\sqrt{X_{1f}^2 + Y_{1f}^2}} = \mathrm{F}\{i_0, i_2, \psi_1, \psi_2, \Delta\nu, \gamma_{HWHM}(\chi, T, P), \nu_0(P), S'(T)\} \tag{3.24}$$

From the above equation is can be elucidated that the *2f*/*1f* signal is only a function of the constant laser and spectral parameters. Even though equation (3.24) cancels out the instantaneous intensity, it was necessary to subtract the nonlinear RAM background in equation (3.19), which can be significant at high *m* values. The recovered line shape signals also tend to be severely affected by etalons in the system, non-ideal filtering effects as well as background absorption. Etalons which can induce spurious *2f* signals are difficult to avoid in most measurement systems. Spurious *2f* signals can also be induced by background absorption signals.

The background signals in the absence of absorption or etalons, for *2f* detection, are given as:

$$X_{2f}^{bk} = \frac{1}{2}\mathcal{G}Ii_2\cos\psi_1 \tag{3.25}$$

$$Y_{2f}^{bk} = -\frac{1}{2}\mathcal{G}Ii_2\sin\psi_1 \tag{3.26}$$

$$R_{2f}^{bk} = \frac{1}{2}\mathcal{G}Ii_2 \tag{3.27}$$

Similarly, for *1f* detection:

$$R_{1f}^{bk} = \frac{1}{2}\mathcal{G}Ii_0 \tag{3.28}$$

To cancel out the effect of the nonlinear RAM, the spurious *2f* signals generated by wavelength dependent transmission effects not accounted for in the model and the background absorption signals, the background signal is vector subtracted [47] as follows (Figure 3-7):

$$2f/1f = \sqrt{\left(\frac{X_{2f}}{R_{1f}} - \frac{X_{2f}^{bk}}{R_{1f}^{bk}}\right)^2 + \left(\frac{Y_{2f}}{R_{1f}} - \frac{Y_{2f}^{bk}}{R_{1f}^{bk}}\right)^2} \tag{3.29}$$

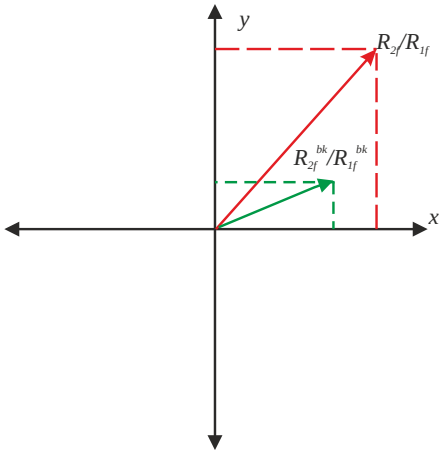

Figure 3-7. Phasor plot representation of the vector background subtraction procedure to null the RAM component of the WMS signal. As the signal resultant and the background resultant are not in phase they are projected onto the X and Y channels for vector subtraction.

This form is useful to cancel the *2f*-nonlinear RAM, background absorption signals, non-ideal filtering effects of the LIA and reduces the effects of temporally stable etalons. Equation (3.29) is valid for any optical depth [48] and modulation index.

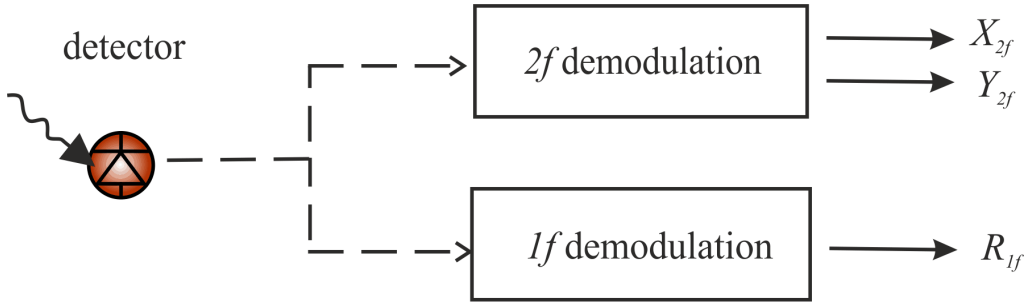

Figure 3-8. The figure shows the block diagram of the first harmonic normalised WMS technique.

Practically any n^{th} harmonic WMS signal can be normalised by the *1f* WMS signal. Higher harmonic detection can be advantageous because the nonlinear RAM decreases (at least by two orders in magnitude) with increasing harmonic order of detection and for this reason the background subtraction may not be necessary. It is also seen that the sensitivity to the curvature of the line shape is greater for higher harmonics. However, all this comes at the cost of reduced signal level and the requirement of higher sampling frequencies. This topic is dealt with in detail by Sun et al. [49].

3.10 Summary

This chapter introduces the important TDLS techniques used in harsh environmental sensing. The drawbacks of direct spectroscopy in harsh environmental applications were briefly discussed. Phase sensitive detection using a lock-in amplifier is considered as a solution for recovery of gas absorption signals submerged in *1/f* noise. These techniques are grouped under a branch of spectroscopy known as wavelength modulation spectroscopy. The Fourier model of wavelength modulation spectroscopy was described. Phase sensitive LIA techniques such as the RAM technique and the phasor decomposition method were discussed. As these techniques are extremely sensitive to the phase of the WMS signals relative to the phase of the LIA reference signal, a phase independent version of the PDM was also implemented for application in FLITES

system where the phase locking can be difficult to achieve. These techniques were used for validating the Fourier model for WMS as will be shown in Chapter 6.

These techniques have limitations in harsh environmental applications owing to changing transmission conditions along the beam path. Hence, a *1f* normalised *2f* WMS technique was proposed to cancel the effects of transmissivity fluctuations with the advantages of second harmonic detection. The results for these techniques tested in the harsh environment of a GTE exhaust plume are presented in Chapter 6.

Chapter 4

Experimental Methodology

4.1 Introduction

In this chapter, the experimental measurement systems and the characterisation approaches for direct and wavelength modulation spectroscopy are presented. The aim of this work is to implement spectroscopic techniques for gas measurements in harsh environments, gas turbine (aero) engine exhaust plumes in particular. Wavelength modulation spectroscopy is the preferred technique which achieves a good signal-to-noise ratio under harsh measurement conditions. Wavelength modulation spectroscopy is similar to direct spectroscopy (DS) except that phase sensitive detection is used. Hence, the equipment used for both techniques are very similar except for additional equipment in WMS to modulate the laser, a bias-T and a signal generator, and to demodulate the signal, i.e. a lock-in amplifier.

Extensive characterisation of the IM and WM is necessary to quantify the LIA signals using WMS models. In direct detection, a low frequency (typically less than 1 kHz) current sweep is applied to the laser which creates an intensity scan and a corresponding wavelength scan. The intensity is attenuated at the wavelengths corresponding to the gas energy level transitions. Wavelength referencing the current sweep is necessary (DC wavelength response) to assign the wavelengths to each of the absorption features traversed by the scanned laser wavelength. The wavelength referencing scheme is discussed in Section 4.6.1.

In wavelength modulation spectroscopy an additional high frequency (AC) current modulation (tens to hundreds of kHz) is applied to the DFB laser which creates an instantaneous intensity modulation and a time delayed frequency modulation. The high

frequency response of the modulation and demodulation electronics is important as it is specific to a particular hardware.

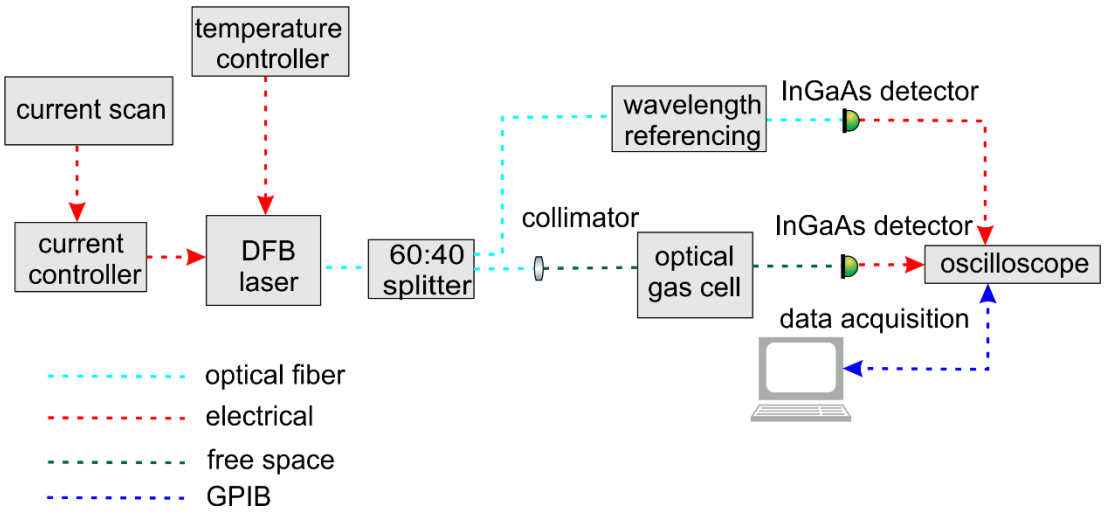

Figure 4-1. The experimental setup for direct detection.

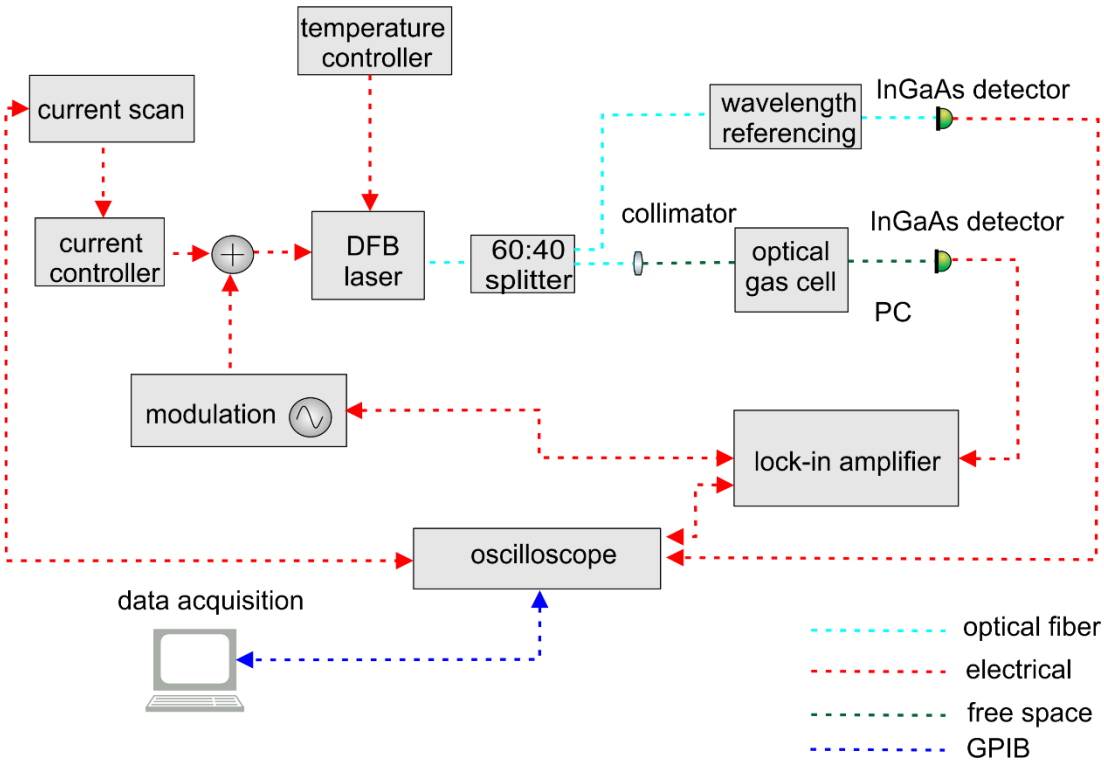

Figure 4-2. Experimental setup for wavelength modulation spectroscopy.

Therefore, it is necessary to characterise the AM and WM response of the laser system as a function of the modulation frequency to accurately quantify the WMS signals using spectroscopic models. For example, this approach is employed in photoacoustic WMS as the magnitude of the signal depends on the system parameters such as the resonance of the acoustic cavity. The signal magnitude in WMS depends on the AC (dynamic) IM and WM response of the system. The DC wavelength response and intensity are equally important in the WMS spectral models.

Much of the work presented in this thesis have been done using a heated optical gas cell to measure the spectral parameters at higher temperatures of the order of 500 °C and to validate the WMS concentration and temperature sensor at the higher temperatures expected in a GTE exhaust plume. The details of this cell will be briefly discussed in Section 4.4. Figures 4-1 and 4-2 depict the experimental arrangement for the direct and WMS detection schemes. Each component of the direct and WMS detection schemes will be explained in detail.

The absorption feature at 1997.2 nm was identified as the target feature, accessible with a DFB-MQW InGaAsP laser. The output power of DFB lasers is very small (< 50 mW), however, tomographic imaging needs multiple optical measurement paths. In optical tomography using a single wavelength, the optimum number of measurement paths to dissect the plume was identified as 126; to accurately reconstruct the 2D concentration and temperature distributions [50–52]. A single DFB laser cannot feed enough power into all the measurement paths (~2 mW each). Hence, a silica fibre amplifier doped with the rare-earth element thulium (to modify the crystal band energy to the 2 μm region) was used to amplify the output power of the DFB-MQW laser. Introducing a laser seeded fibre amplifier alters the IM response of the system. This technique has been termed tunable fibre laser absorption spectroscopy. The tunable diode laser seeded fibre amplifier system will be presented in a different publication.

4.2 Laser and Drive Electronics

The optical source used in this work to probe the CO_2 absorption at 1997.2 nm is a DFB (Eblana Photonics) laser with a MQW gain region. It is packaged in a 14 pin butterfly DIP and mounted on a Thorlabs LM-14S2 butterfly mount with in-built heat sink. The DFB laser was later transferred to an OptoSci laser control module for the FLITES

measurement system. Other lasers used are: (1) a DFB laser at 1650 nm for accessing the methane R4 line and (2) a 1430 nm DFB-MQW laser used for experimental study of the wavelength modulation characteristics of semiconductor DFB lasers explained in the next chapter.

The central wavelengths for the 1650 nm and 1430 nm DFB lasers were confirmed using an optical spectrum analyser. The 2 μm wavelength region could not be accessed using the available spectrum analysers designed for telecom wavelengths. Therefore, the central wavelength of this DFB-MQW laser was confirmed using a grating spectrometer (attached to a photomultiplier tube detector).

Figure 4-3 shows the optical spectrum of the 1650 nm DFB laser at varying diode temperatures. Increasing the diode temperature causes a red shift in the wavelength output. This is a consequence of the change in the Bragg length of the grating structure of the DFB laser due to thermal expansion. The temperature of the laser diode is controlled by an integrated thermoelectric Peltier cooling element.

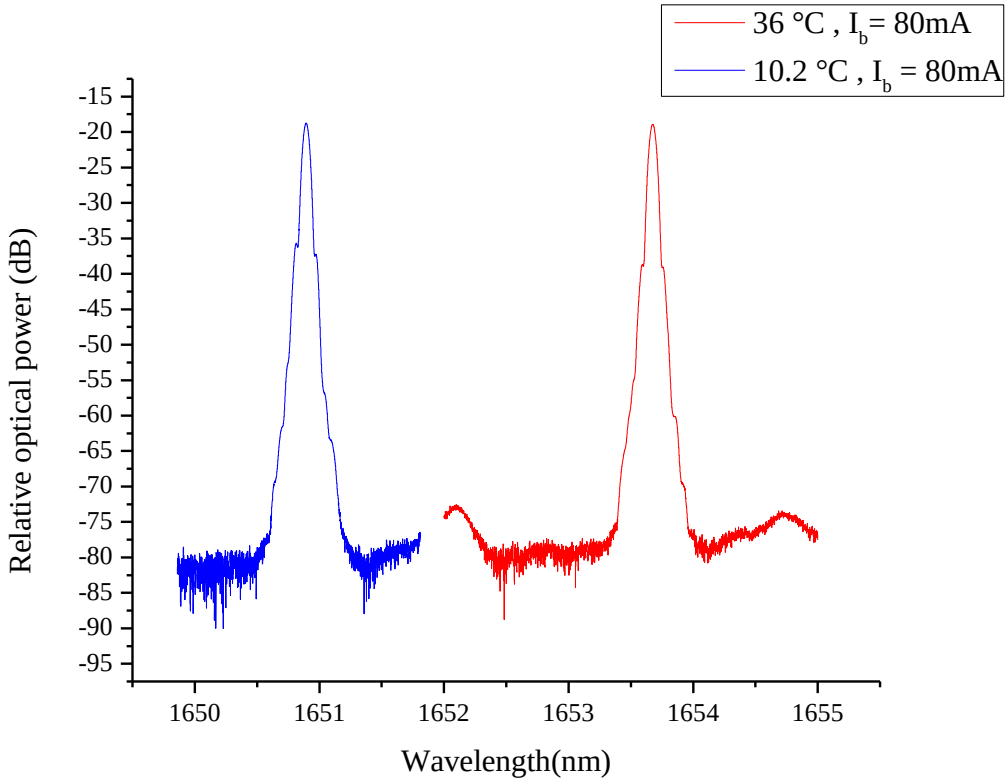

Figure 4-3. The 1650 nm DFB laser output at two different diode temperatures (measurement taken from an optical spectrum analyser). It shows the principle of temperature induced wavelength chirp.

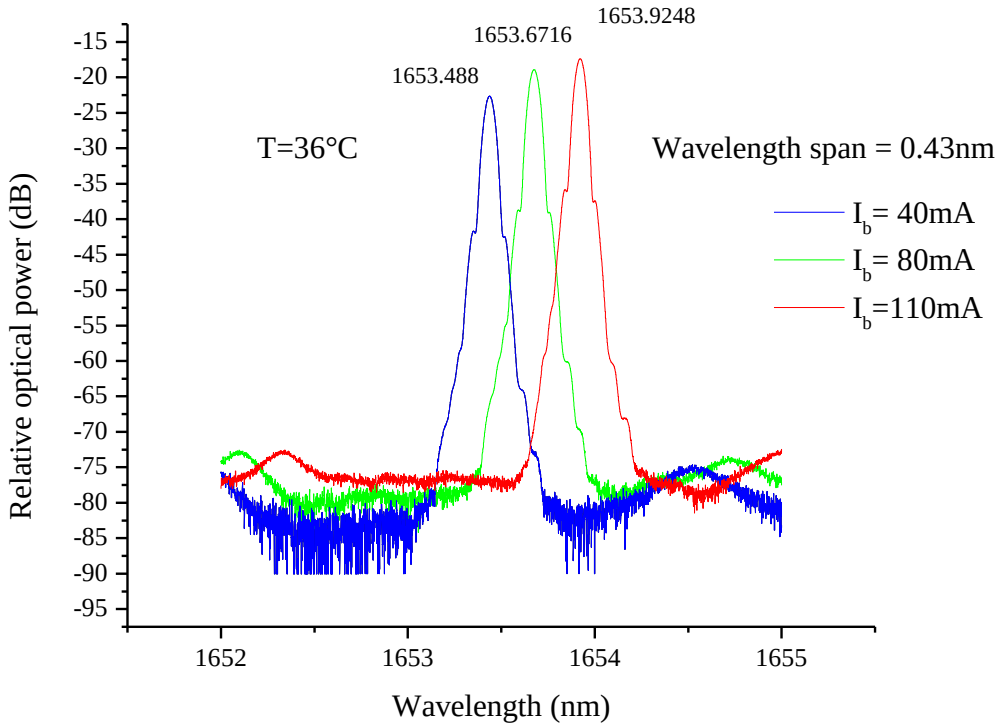

Figure 4-4. Illustration of fine tuning of the DFB laser wavelength by changing the drive current (measurement taken from an optical spectrum analyser).

The temperature of the integrated Peltier cooling element is adjusted using a Proportional-Integral-Derivative (PID) servo controller (TED 2000) by monitoring the temperature of a thermistor near the laser chip, to maintain a constant temperature, and hence wavelength. The resistance of the thermistor is displayed on the front panel of the TED 2000 thermoelectric controller (TEC) and indicates the temperature of the laser using the following equation:

$$T_{heat\ sink} = \frac{3892}{\ln\left(\frac{R_{thermistor}}{2.142 \times 10^{-5}}\right)} - 273.15 \tag{4.1}$$

Here $R_{thermistor}$ is the resistance (in kΩ) of the thermistor displayed on the TEC.

Temperature is used for coarse tuning because of its slow response. The temperature of the TEC is adjusted so that the laser output wavelength matches a particular gas absorption wavelength.

Fine tuning the DFB laser wavelength across the absorption feature is achieved by applying a linear current sweep. Fine tuning the wavelength by varying the bias current is illustrated in Figure 4-4. A slow 5 Hz current ramp is applied to the 1997 nm DFB-MQW laser using an Agilent signal generator (33250A) connected to the summing amplifier of an LDC 202x current controller biased at 80 mA, which repetitively scans the laser wavelength across the absorption feature without any mode-hop.

The output resistance of the Agilent signal generator is always set to high impedance so that all the voltage drops across the load (~50 Ω). A 50 Ω output impedance setting of the signal generator would cause only half the voltage to drop across the load.

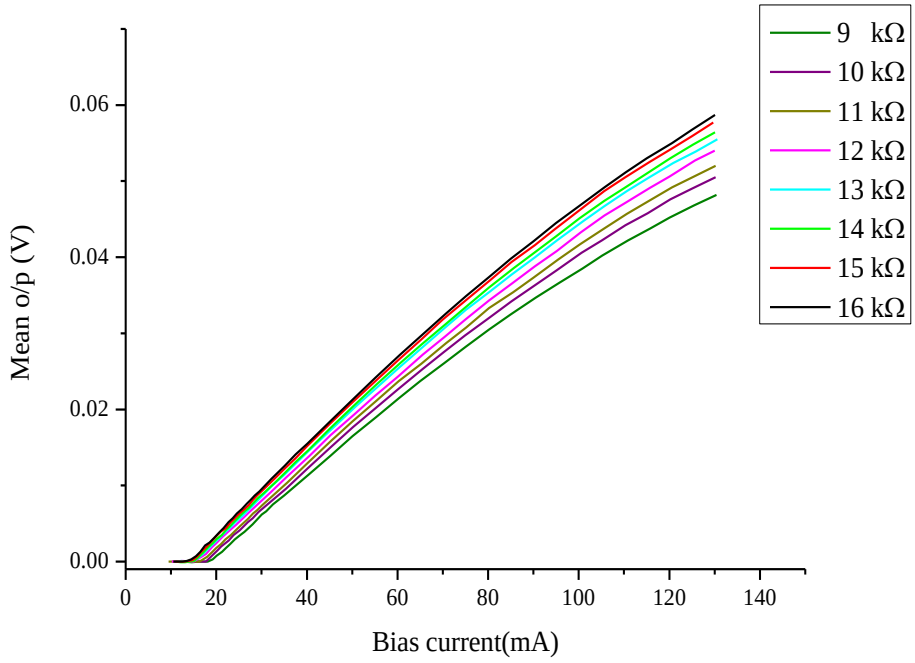

Figure 4-5. Power-current characteristics of the 1997 nm laser at different temperatures indicated by the resistance of the thermistor in kΩ.

The transconductance values for LDC 201x is 100 mA/V and for LDC 202x it is 20 mA/V. LDC 201x is used in most of the experiments. The bandwidth of LDC 201x is

approximately 25 kHz. To achieve a higher modulation frequency operation, LDC 202x is used, having a 250 kHz bandwidth.

The maximum current limit for the 1997 nm DFB-MQW laser is 135 mA. Hence, for accessing a single CO_2 transition at 1997.2 nm, the temperature of the laser is adjusted to 21.96 °C, the LDC is biased at 80 mA and a 70 mA_{p-p}(700 mV_{p-p}) current ramp is applied to it. This scans the laser from 45 mA to 115 mA within the safe region of operation, without negative biasing the laser. For accessing the two spectrally close transitions of CO_2 a larger current sweep of 115 mA(p-p) was applied at 70 mA and a diode temperature of 20.52 °C (12.2 kΩ). Part of the current scan was below the threshold current of the 1997 nm DFB laser (~20 mA). This is shown by the power-current characteristics of 1997 nm DFB laser (Figure 4-5) at various laser temperatures.

The high frequency current dither (typically 10 kHz-500 kHz) and the 5 Hz current ramp biased at 80 mA via the constant current source, are applied simultaneously to the DFB laser diode using a bias-T network as shown in Figure 4-6. Knowledge of the frequency response characteristics of the bias-T is important to quantify the WMS signals and is discussed in the following section.

4.3 The Bias-T

As shown in Figure 4-2, a bias-T network was used to apply a high frequency current modulation to the laser simultaneously with the applied low frequency current ramp. The bias-T is a passive RLC circuit as shown in Figure 4-6.

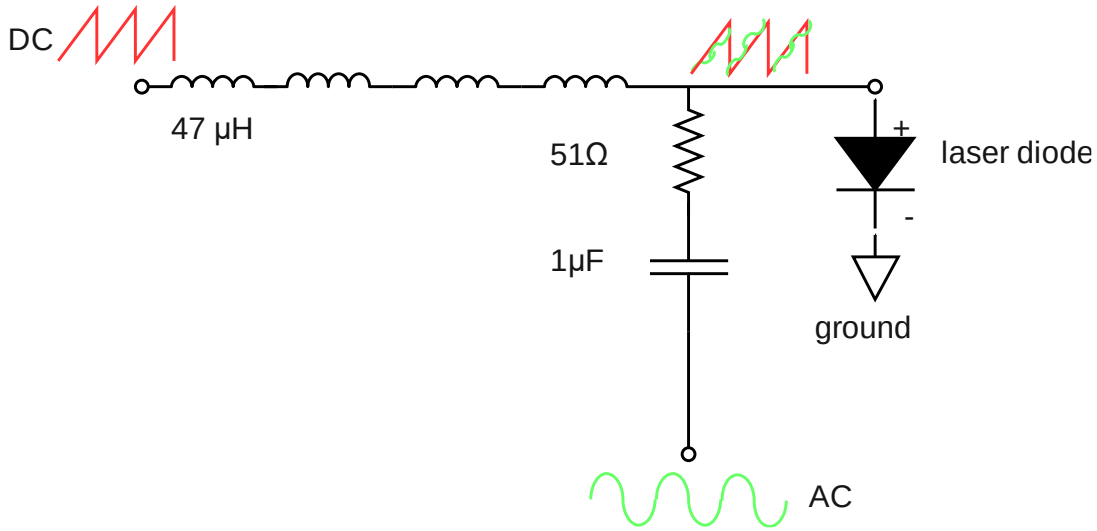

Figure 4-6. Bias-T circuit diagram.

The DC arm consists of an inductor in series with the laser diode. The AC arm contains a capacitor in series with a 50 Ω load resistor, parallel to the laser diode. The circuit is self-explanatory. The DC arm will act as a low pass filter ($X_L = 2\pi fL$) passing only the lower frequencies of the current ramp. The capacitor acts as a high pass filter ($X_C = 1/2\pi fC$), passing only the higher frequencies of the dither above the high pass cut-off frequency. The 50 Ω resistor is for impedance matching to the BNC connectors and the signal generator output.

Considering the DC arm open, the low frequency cut-off of the bias-T is given as:

$$f_L = \frac{1}{2\pi R_{AC} C} \tag{4.2}$$

R_{AC} is the impedance as seen from the AC arm, which is the impedance of the 1997 nm DFB-MQW laser chip measured as approximately 5.2 ∓ 0.2 Ω using digital multimeter. This gives a lower cut-off frequency of approximately 3 kHz for the AC arm.

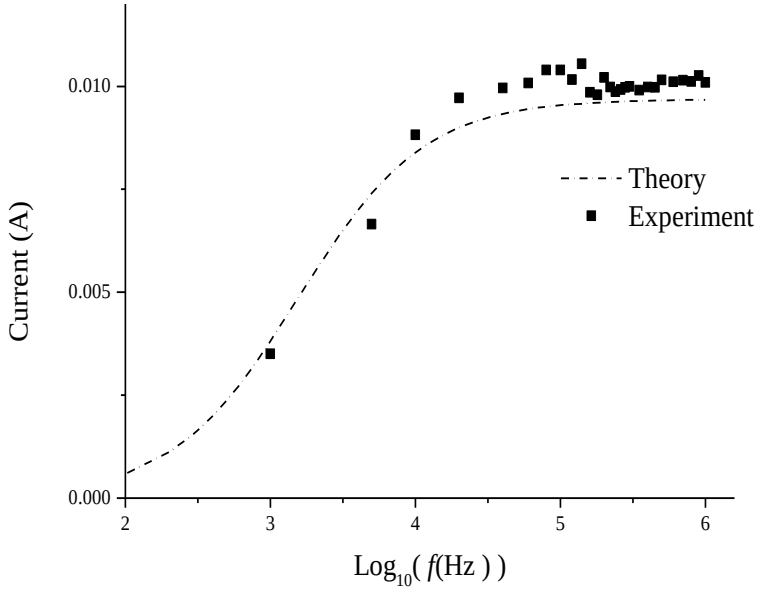

Figure 4-7. Figure shows the experimentally and theoretically calculated amplitude response of the bias-T circuit.

For the DC arm, assuming the AC arm is open, the upper cut-off frequency is given by,

$$f_H = \frac{R_{DC}}{2\pi L} \tag{4.3}$$

where R_{DC} is the sum of the impedance of the biasing constant current source and the input impedance of the load (the laser diode). The upper cut-off frequency for the DC arm is approximately equal to 4 kHz. The AC frequency response of the bias-T was theoretically modelled and compared against the experimental measurements as shown in Figures 4-7 and 4-8. Phase is calculated using the relation $\Phi = \tan^{-1}\left(\frac{X_c}{R}\right)$.

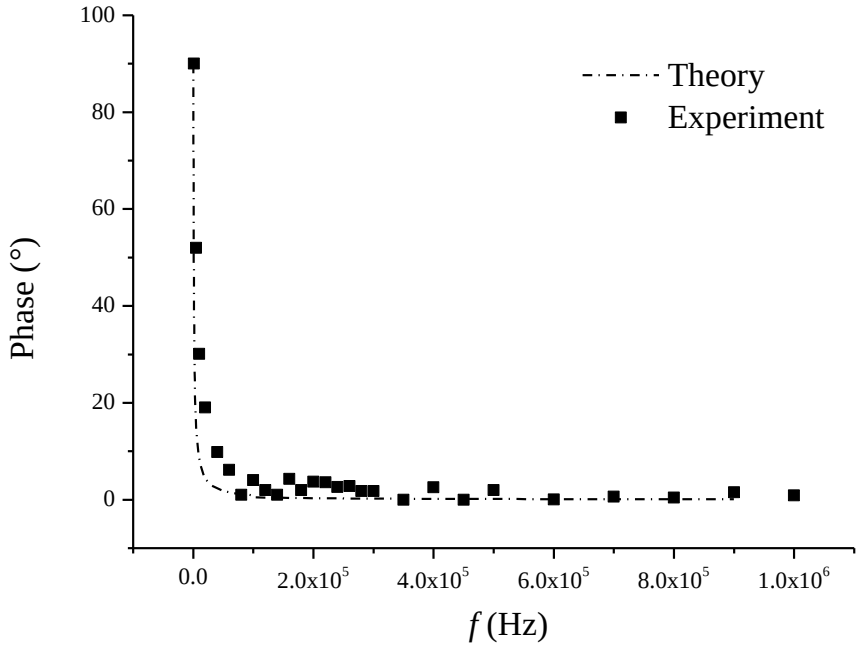

Figure 4-8. Experimental and theoretically calculated phase response of the bias-T.

As expected, the response of the bias-T is frequency dependant as shown in Figure 4-8. The bias-T has a flat amplitude and phase response at frequencies above 100 kHz, and hence was suitable for measurements above that value. The trans-impedance factor of the bias-T is calculated as 10 mA/V. The measured standard deviation for the trans-impedance was found to be approximately equal to ∓ 0.19 mA/V over frequencies greater than 100 kHz. The standard deviation of phase over the flat response region was calculated as approximately 3°.

Other approaches used to apply an external current modulation to the laser diode include using a wide bandwidth summing amplifier to add both the AC and the DC

waveforms or by synthesizing the waveforms in the digital domain (LabVIEW). These approaches have the advantage of flatter amplitude and phase responses, over a larger frequency range, without having to replace the passive circuit elements.

4.4 High Temperature Optical Gas Cell

The optical gas cell is the next component to be discussed. It was necessary that the gas cell be heated to higher temperatures of the order of 600°C to perform measurements at conditions closer to that expected in an aero engine exhaust plume. Other design considerations were that the gas temperature be a constant along the optical path length of the cell. Taking all this into account a specialised HT optical gas cell was built at Strathclyde [53].

A cross-sectional view of the HT gas cell is depicted in Figure 4-9. The various parts labelled as A to G will be described.

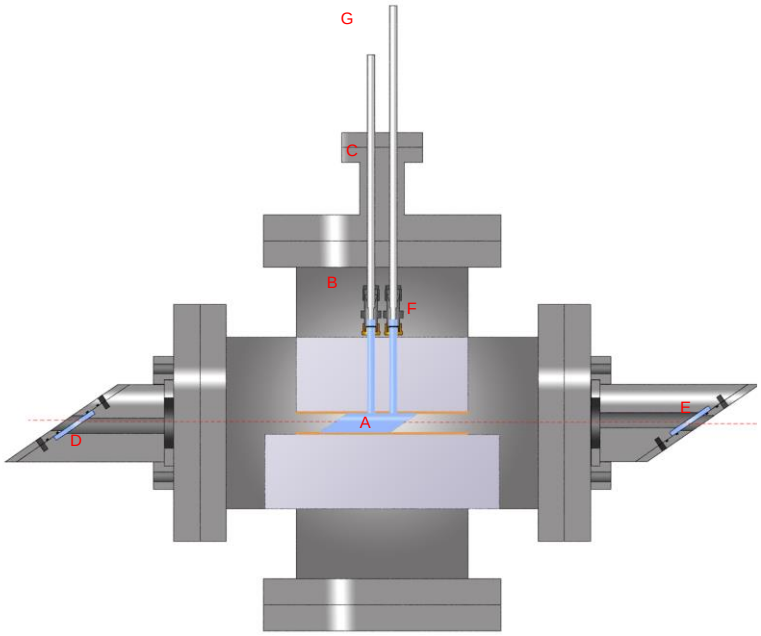

Figure 4-9. Cross-sectional view of a high temperature optical gas cell built at Strathclyde.

A is the glass optical cell made of quartz which is transparent in the visible and near-IR. D and E are the input and output cell windows made of CaF_2. The glass windows and the end faces of the glass cell are wedged to prevent etalon formation. C and G are the gas inlet and the outlet valves (Swagelok). The gas is flown into the cell using ¼ inch steel tubing, through a mass flow controller (Bronkhorst) which regulates the gas flow

rate. The steel tubing is attached to the optical cell using a steel to ceramic curing agent (as shown in (F)).

The volume outside the glass cell is bound by a vacuum sealed stainless steel vessel which constitutes the outer cell. It is usually filled with buffer gas (usually N_2) at a pressure slightly (~50 mbar) greater than the inner cell. This is to prevent gas leakage from the inner cell to the outer cell.

Coils of thermal resistance wire are wound around the glass cell to heat it to the desired temperature. The inner gas cell is surrounded by an insulator material (fibreglass) to prevent the heat from conducting out of the gas cell and heating the outer enclosure.

The temperature of the gas cell is monitored by four K-type thermocouples, two at the top and two along the side windows. These thermocouples are used to calibrate the temperature corresponding to a given current flowing through the thermal resistance wire, as well as to continuously monitor the gas temperature.

The pressure of the inner and outer cell are monitored using two pressure gauges connected to the quarter inch steel tubing G and the tubing attached to the external cell inlet valve (not shown).

The output of the inner gas cell is either connected to a vacuum pump for creating a near vacuum condition (1-5 mbar (barometric standard)) inside the cell, or to the fume hood for atmospheric pressure measurements. A particular pressure is achieved inside the gas cells by slowly (10-50 ml/min) flowing gas in with the exit valve closed and closing the input valve when the desired pressure reading is obtained on the manometer. The pressure in the outer cell is always maintained to be slightly higher than the inner cell by approximately 50 mbar to prevent leakage of the inner cell test gas to the outer cell.

To achieve a given concentration value, the test gas is mixed with a buffer gas similar to N_2 to achieve the desired mole fraction. During the measurements, flowing the gas through the inner cell was found to aid in maintaining a uniform temperature across the optical path through the gas.

It takes approximately 45 minutes to an hour for the gas spectra to stabilise at a given temperature (this is due to the time taken to achieve a uniform temperature across the cell). It was found that a moderate gas flow rate has negligible effect on the gas concentration, though, the temperature takes a long time to reach a steady value under

higher flow rates. Typical flow rates used while measuring at higher temperatures were under 100 ml/minute.

The actual optical path length through the cell is unknown because the light beam is not parallel to the optical axis of the gas cell. The optical path length through the cell was measured as 5.5 cm by a least-squares curve fit of the standard absorption feature of methane at 1650 nm to a Voigt line shape model, using the verified HITRAN spectral parameters, the path length being the only unknown.

Even though the inner gas cell was constructed to be leak-proof, it was not seen to be the case. The ceramic to steel junction is subject to stress due to different values of the coefficient of thermal expansions for ceramic and steel. Consequently, a small amount of gas leak is always expected during operation. Procedures were followed such as to purge the inner cell after each measurement and to regularly flow buffer gas through the external cell, to remove any test gas that may have leaked into it.

4.5 Receiver Electronics

The receiver side consists of an extended InGaAs detector (Thorlabs) (PDA-10D) with a detector surface area of 3 mm^2 ($diameter^2$) connected to a preamplifier. The output of the detector is either connected to an oscilloscope in case of direct detection or to a lock-in amplifier for phase sensitive detection (PSD). The lock-in amplifier [54] is the most important part of the receiver system and will be thoroughly discussed in this section. Three lock-in amplifiers were used for this work; the Stanford Research 830, Perkin Elmer 7280 and a LIA implemented in the software domain using the LabVIEW PXIe board. The hardware lock-in amplifiers provide real-time measurements and are based on FPGA (field programmable gate array) boards, while the software LIA implementation is just a signal processing strategy. The functionality of a LIA is explained with the PE 7280 LIA as the example, however, generally the principle applies to any LIA.

The block diagram of a lock-in amplifier is shown in Figure 4-10. The input signal is amplified before converting into the digital domain. The input gain is adjusted to give the maximum possible signal amplitude at the analog to digital converters (ADC). The total gain of the lock-in amplifier is a combination of the input AC gain and the demodulator gain. The demodulator gain and the resolution of the ADC set the

maximum input signal to the lock-in amplifier. If the input signal is above the limit set by the input gain (not to exceed the ADC voltage range), a lock-in amplifier overload warning is generated.

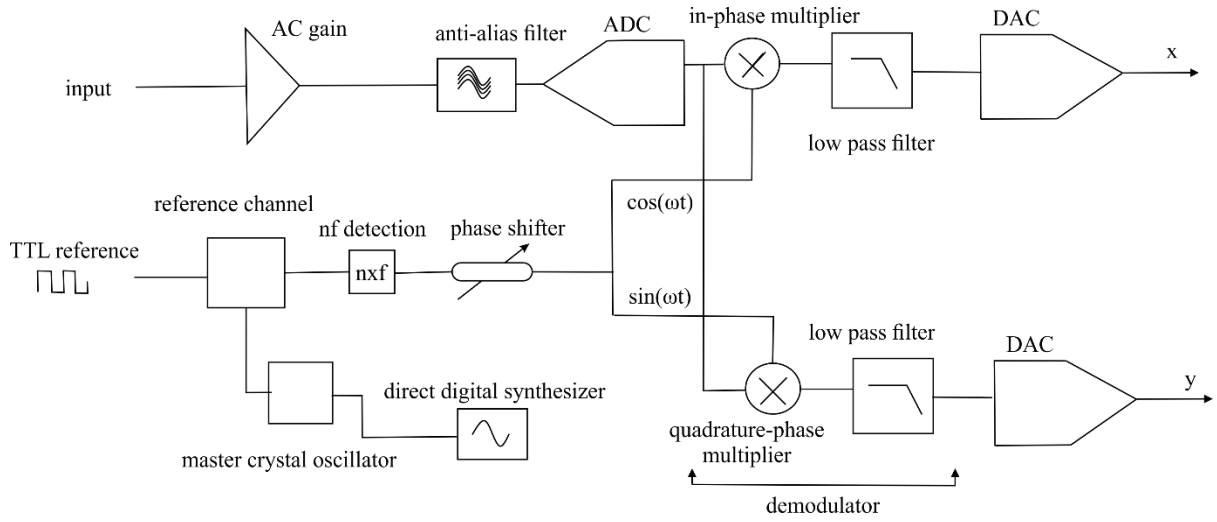

Figure 4-10. A simplified functional block diagram of the lock-in amplifier.

The signal after passing through the input filter is passed through an anti-alias filter which removes any unwanted signals that would have resulted from the sampling process at the input ADC. The full scale sensitivity (net gain) is set by a combination of the AC input gain and the demodulator gain. When the full scale sensitivity is decreased to a value less than the maximum input signal permitted by the AC input gain, an output overload warning is displayed on the lock-in amplifier. On the other hand, if the full scale sensitivity is set to a value that exceeds the maximum input signal set by the AC gain, the AC gain is automatically shifted to the nearest allowed value.

The lock-in amplifier outputs the RMS value of the input signal i.e. if the input signal is 1 V, the output is 0.707 V.

The dynamic reserve (DR) is a very important parameter for a lock-in amplifier to achieve a given signal-to-noise ratio and is given as:

$$DR = 0.7\,\frac{Input\ limit}{Full\ scale\ sensitivity} \tag{4.4}$$

The factor of 0.7 is because of the RMS value. DR is usually described in decibels as:

$$DR(dB) = 20 \times \log_{10}\{DR(ratio)\} \tag{4.5}$$

For example, if the maximum input signal set by the AC gain is 800 mV and the full scale sensitivity is 10 nV, the dynamic reserve is about 154 dB. For acceptable performance DR<100 is usually the standard norm.

The input output relation for the Perkin Elmer 7280 lock-in amplifier is given as percentage (*X, Y, R* %) of full scale sensitivity times 2.5 V i.e. if the input is 20 mV_{rms}, the sensitivity 20 mV; the output will be 2.5 V. Hence, the gain is unity. Now if the full scale sensitivity is decreased to 10 mV, the output will be 1.25 V, i.e. the output gain is reduced to half. However, this does not imply that the signal is reduced in accuracy as only the output voltage is reduced.

The phase of the reference signal of the lock-in amplifier is obtained from the signal generator TTL trigger pulse (triggered by the sinusoidal current modulation applied to the DFB laser). The Perkin Elmer 7280 LIA generates a sinusoidal reference signal from the TTL trigger using a dynamic digital synthesizer (DDS) board and a master crystal oscillator. The phase of the LIA reference signal can be shifted relative to the TTL trigger pulse. The input signal is multiplied by the in-phase and quadrature-phase reference signals and followed by low pass filtering to generate the X and Y channels (axes) of the lock-in amplifier. If the input signal is given as $V_{Sig}sin(\omega t)$, it is then multiplied by two signals $V_{LIA}\sin(\omega t + \emptyset)$ and $V_{LIA}\cos(\omega t + \emptyset)$ and low pass filtered to extract the DC components, i.e.,

$$V_{Sig}sin(\omega t)V_{LIA}\sin(\omega t + \emptyset) = \frac{V_{Sig}V_{LIA}}{2}\{\cos(\emptyset) - \cos(2\omega t + \emptyset)\}..DC\ filt \approx \frac{V_{Sig}V_{LIA}}{2}\cos(\emptyset) \tag{4.6}$$

Equation (4.6) describes the action of the demodulator. V_{LIA} is usually unity for most LIAs, and hence the RMS value of the input signal amplitude is obtained when the signal is completely aligned to one of the LIA channels. The frequency roll-off rate of the low pass filter is preferably set to 12 dB/octave (second order filter) for acceptable noise performance. Its bandwidth (time constant) should encompass all the frequency

components of the ramp signal with the gas absorption multiplied to it. The output of the demodulator is converted back into the analog domain using a digital to analog converter (DAC).

4.6 Characterisation

This section describes the characterisation approaches for direct spectroscopy and wavelength modulation spectroscopy. The parameters of interest in calibration-free WMS are the WM-IM phase, the wavelength modulation amplitude or the tuning coefficient and the laser intensity modulation characteristics. Their measurement approaches are described in Section 4.7.

Assigning wavelengths for each bias point along the laser current scan by referencing to the peak wavelength of a known absorption feature is important both in direct spectroscopy as well as wavelength modulation spectroscopy, and hence the wavelength referencing technique is discussed as follows.

4.6.1 Wavelength Referencing

The gas spectral measurements recorded on most oscilloscopes as well as data acquisition boards are time indexed. The nonlinear nature of the current to wavelength dependence of the lasers makes it necessary to have a referencing method to assign wavelength to the time indices of the measured gas absorption spectra. In some of the earlier approaches, the data points were used as counters for wavelength between two absorption peaks at known wavelengths. However, this will result in errors in the modelled spectra, especially when the current-wavelength relationship is not linear. Hence, methods were devised for assigning wavelengths to the spectral absorption measurements. These include using diffraction gratings, optical ring resonators, solid-state Fabry-Perot etalons or high precision-long term stable measurements using optical frequency combs [55, 56]. Fibre ring resonators (FRRs) [34] are easy to build, cheaper, suitable for field measurements and require no alignment, compared with solid-state Fabry-Perot cavities, and hence was the preferred wavelength-selective component for wavelength referencing. Solid-state Fabry-Perot cavities are suitable at the mid-IR wavelengths due to the fibre losses being too great which results in insufficient transmission (lower finesse), and improved temperature stability of the solid state

etalons compared to FRRs. In the mid-IR wavelength region, solid-state germanium etalons are used [10].

The optical setup of a fibre ring resonator is shown in Figure 4-11. The choice of 80:20 couplers or 60:40 couplers depends on the required finesse of the optical ring cavity. The 80:20 couplers give a larger finesse as more light is coupled into the ring cavity and less of the light is coupled out to the detector. Hence, a trade-off exists between the finesse and contrast of the resonator trace.

The free spectral range (FSR) of the fibre ring resonator is calculated as,

$$FSR = \frac{c}{2n_e L_{ring}} \tag{4.7}$$

where n_e is the effective refractive index of the single mode optical fibre, c is the speed of light and L_{ring} the length of the ring cavity.

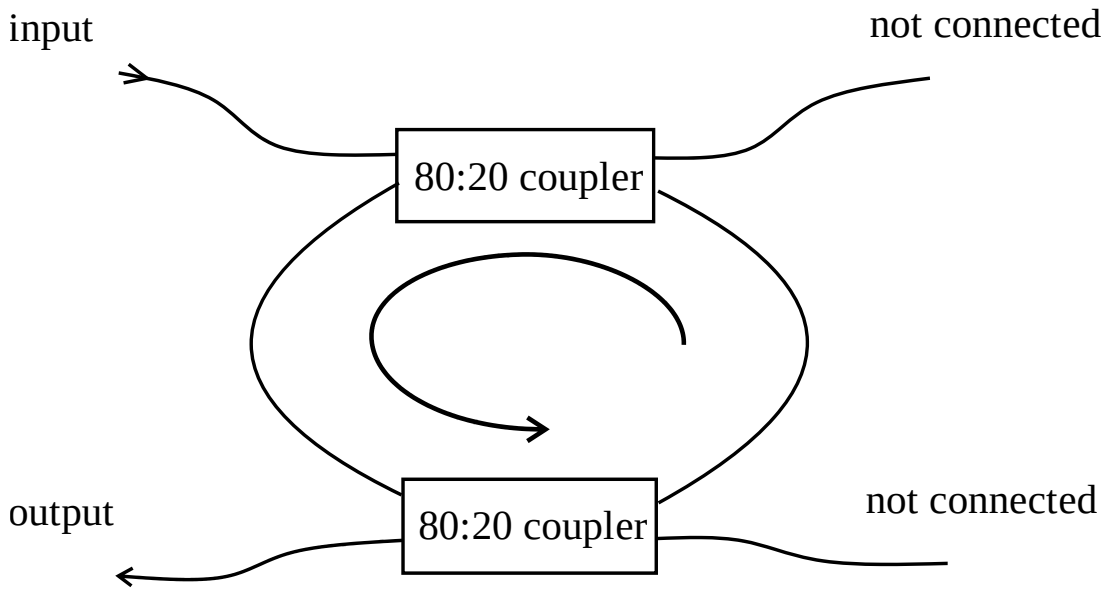

Figure 4-11. Diagram of an optical fibre ring resonator.

To assign the proper wavelength to each of the resonator peaks, it is required to accurately measure the FSR of the fibre resonator. The guide values for the effective refractive index and fibre length are not sufficient to accurately calculate the FSR using equation (4.7).

The FSR of the fibre ring resonator was accurately measured using two known absorption features as shown in Figure 4-12. FSR times the number of resonator peaks (n_{peak}) is the total wavelength traversed between two successive absorption lines of CO_2. With the wavelength of the two absorption peaks known, the FSR can be obtained by dividing the wavelength difference by n_{peak}-1. Here, the R48 and R50 transitions of CO_2 are used to measure the FSR at 2 μm. The standard deviation of FSR measurements was 0.8 %. It is to be noted that this method also accounts for the nonlinear nature of the wavelength-current curve.

An alternate method for finding an unknown FSR at a given wavelength is to calibrate it against another resonator with a larger known (measured) FSR at that wavelength. The FSR at 2 μm is measured to be 0.124 GHz using the traditional method. This value gives sufficient resolution for wavelength referencing, and more importantly the measurement of the WM characteristics, limited only at higher modulation frequencies (> 500 kHz) as will be further explained in Section 4.7.3.

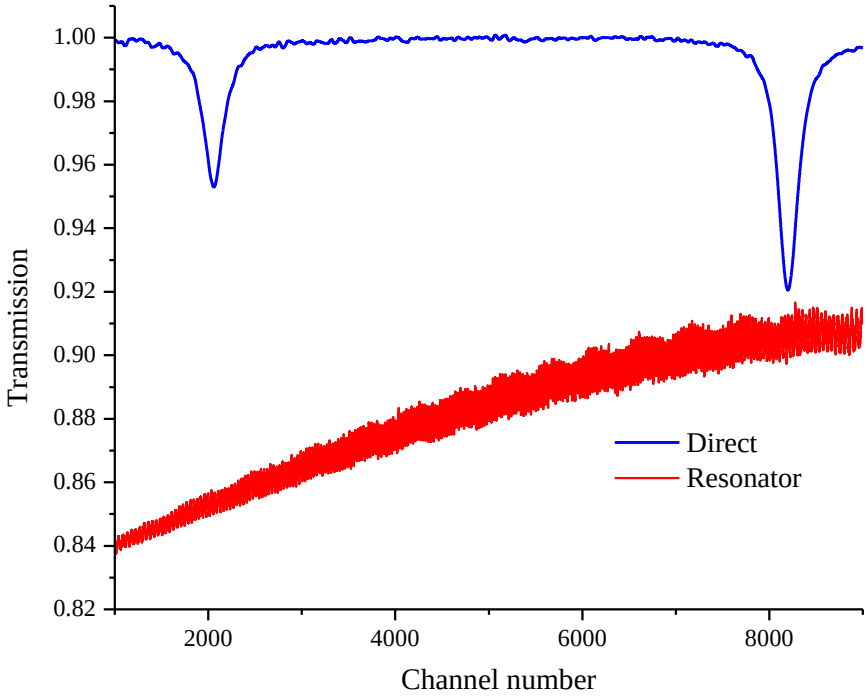

Figure 4-12. Measurement of the resonator FSR using peak wavelengths of two known absorption lines.

4.7 Measurement of Laser Modulation Parameters

Direct spectroscopy requires measurement of the scanned laser wavelength. While in wavelength modulation spectroscopy, the laser is additionally modulated with a high frequency sinusoidal injection current. The injection current modulation has two important consequences, viz. modulation of the laser intensity (IM) and a delayed modulation of the laser wavelength (WM). The instantaneous intensity modulation is caused by stimulated emission in the active region of the DFB laser. The modulation in the laser wavelength is caused by a change in the length of the Bragg grating of the laser due to the thermal heating as well as due to variations in the refractive index because of the thermo-optic effect and carrier induced change (from the Kramer's Kronig relations), the latter being the main contributor in DFB laser structures. The thermal expansion of the Bragg length is not instantaneous and is delayed in time. As a result, the wavelength modulation is delayed in time relative to the intensity modulation.

In WMS, it is important to accurately measure the laser modulation characteristics. As explained in Chapter 3, the important laser modulation parameters are the linear IM, the nonlinear IM (due to nonlinear power-current response of the laser diode), the wavelength modulation amplitude, and the phase shifts between the linear IM signal, the nonlinear IM signal and the WM signal. The measurement setup for the characterisation of laser modulation parameters is similar to the one for direct spectroscopy (Figure 4-1). The resonator arm is used for measuring the WM amplitude (tuning coefficient) and phase, and the measurement arm with an empty gas cell is used for measuring the IM parameters such as its phase and amplitude. The phase difference due to varied path lengths along the two arms was negligible (~ 0.05 °). Instead of a low frequency current sweep, a high frequency current modulation is applied to the DFB laser either using a summing amplifier or a bias-T with the DC arm disconnected. The detector outputs of the resonator arm and the measurement arm are connected to an oscilloscope which is triggered by the high frequency sinusoidal injection current signal. The laser is characterised at each bias point by changing the DC bias level on the LDC (constant current source). This section discusses the different techniques used for measuring the laser modulation characteristics of the DFB laser such as the WM-IM phase lag, tuning coefficient, and the linear and nonlinear IM amplitudes.

4.7.1 WM-IM Phase

The WM-IM phase at a given bias current, modulation frequency and diode temperature could be measured using the centre of the non-responsive region of the resonator output as it corresponds to the maxima or minima of the WM signal.

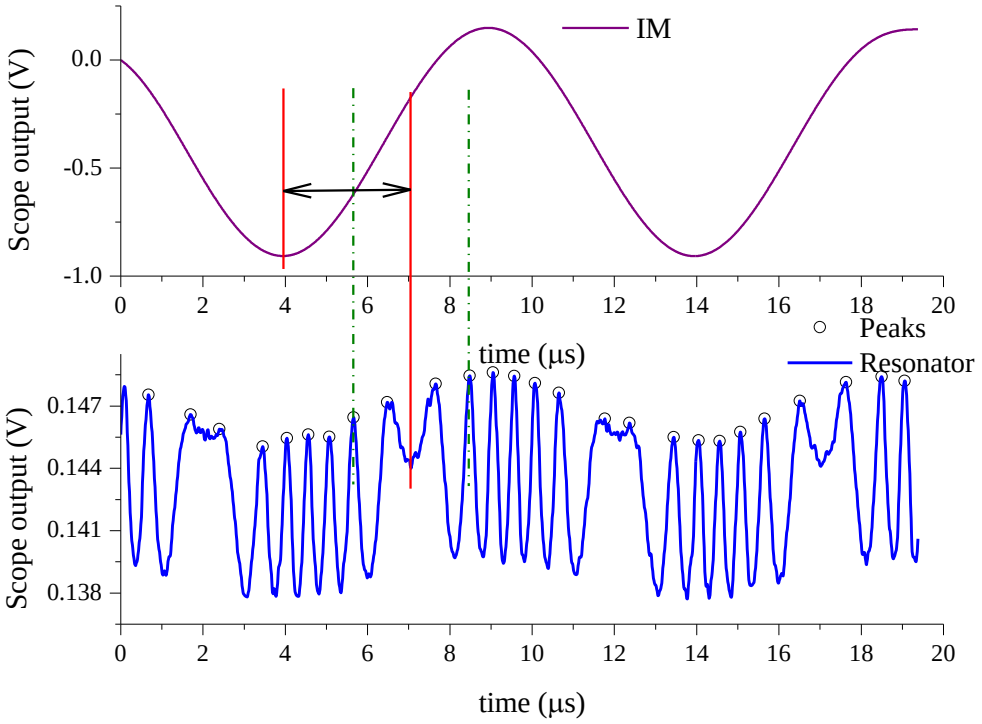

Figure 4-13. The intensity modulation signal and corresponding resonator output, for a modulation amplitude of 10 mA, at a bias point of 115 mA and modulation frequency of 100 kHz.

A typical scope output of the resonator and the measurement arms is shown in Figure 4-13 for a 10 mA, 100 kHz injection current modulation at a bias current of 115 mA and chip temperature of 20.5 °C for the 1997 nm DFB-MQW laser. The selected extrema for the IM and WM signals are also shown (vertical red lines). Near the peak or trough of the applied injection current modulation signal, the magnitude of current is changing very slowly that the laser wavelength is also changing very slowly, and thus no peaks are traversed near this region. Hence, the region is known as the non-responsive region [57] of the resonator.

An interesting fact about the non-responsive region is that the peaks on its either side are symmetric and their midpoint i.e. the centre of non-responsive region corresponds

to the peak or trough of the wavelength modulation.

Subtracting in time the centre of the non-responsive region from the peak or trough of the IM signal (Δt) gives the phase of FM signal relative to IM signal using the relation $\psi = 2\pi f \Delta t$, where f is the frequency of the applied current modulation.

4.7.2 Nonlinear Least-squares Curve Fit

The commonly used method to measure the laser IM and WM characteristics is to perform a least-squares curve fit of the WM signal (after converting the temporal peaks in the resonator signal output to a wavelength scale using the resonator FSR) and the IM signal, to a nonlinear sinusoidal function [8, 10]. This approach is very accurate, and thus used in the measurements presented throughout this thesis unless specified otherwise.

The amplitude of the frequency modulation and its phase relative to the current modulation (the scope reading is synchronised with the current modulation applied to the DFB laser) can be obtained from fitting the peaks of the resonator trace (translated to a frequency scale through the FSR)), to an equation of the form;

$$y_{FM} = \nu_c + \Delta\nu cos(\omega t + \phi_{FM}) + \Delta\nu_2 \cos(\omega t + \phi_{2FM}) \qquad (4.8)$$

where ν_c is the unmodulated laser frequency (arbitrary in the fitting routine), $\Delta\nu$ and $\Delta\nu_2$ are the linear and nonlinear frequency modulation amplitudes (GHz), and ϕ_{FM} and ϕ_{2FM} are their phases with respect to the current modulation. Figure 4-14 shows the resonator peaks fit to a sinusoidal function. The amplitude of the nonlinear FM ($\Delta\nu_2$) is usually very small and can be neglected in the analysis.

The output of the measurement arm (with an empty gas cell) is the intensity modulated signal, which can be fit to a similar nonlinear equation:

$$y_{IM} = I + \Delta I\ cos(\omega t + \phi_{IM}) + \Delta I_2 \cos(\omega t + \phi_{2IM}) \qquad (4.9)$$

where ϕ_{IM} and ϕ_{2IM} are the phases of the linear and nonlinear IM relative to the current modulation. This is shown in Figure 4-15 which also shows the nonlinear *2f* residual signal when an IM signal is fit to a first harmonic sinusoidal signal. The nonlinear curve fit algorithm is implemented in Matlab using the *lsqnonlin()* function.

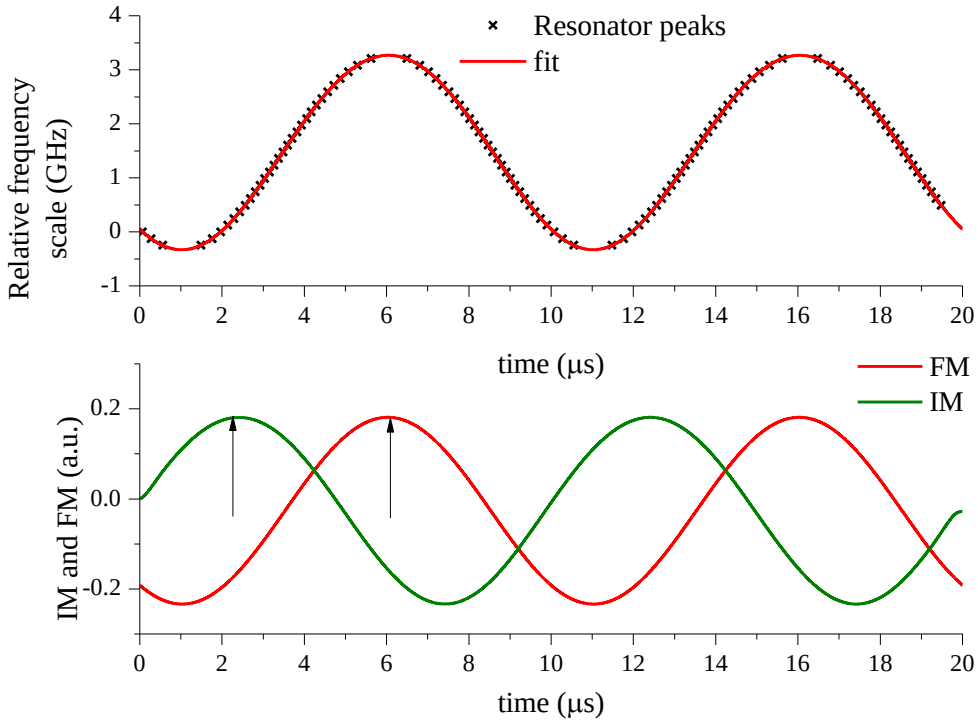

Figure 4-14. Measurement of the FM-IM phase and amplitude using the nonlinear least-squares fit method.

The IM-FM phase is then given as,

$$\psi = \phi_{IM} - \phi_{FM} \tag{4.10}$$

As stated before, due to convention, wavelength modulation is used which is simply the frequency modulation, 180° out of phase. The WM-IM (ψ_λ) phase is calculated using the relationship:

$$\psi = \psi_\lambda - \pi \tag{4.11}$$

It is known that the intensity modulation amplitude normalised by the instantaneous laser intensity is a constant for a given DFB laser, bias current, chip temperature and frequency, and hence can be obtained from the nonlinear fit , i.e. $i_0 = \Delta I/I$ and $i_2 = \Delta I_2/I$.

The nonlinear curve fitting approach gave more accurate and repeatable measurements for WM-IM phase lag values compared to the method using the centre of the non-

responsive region. The curve fit algorithm also accurately measured the wavelength modulation amplitude. The WM phase and amplitude measurements using this technique are given in Chapters 5 and 6.

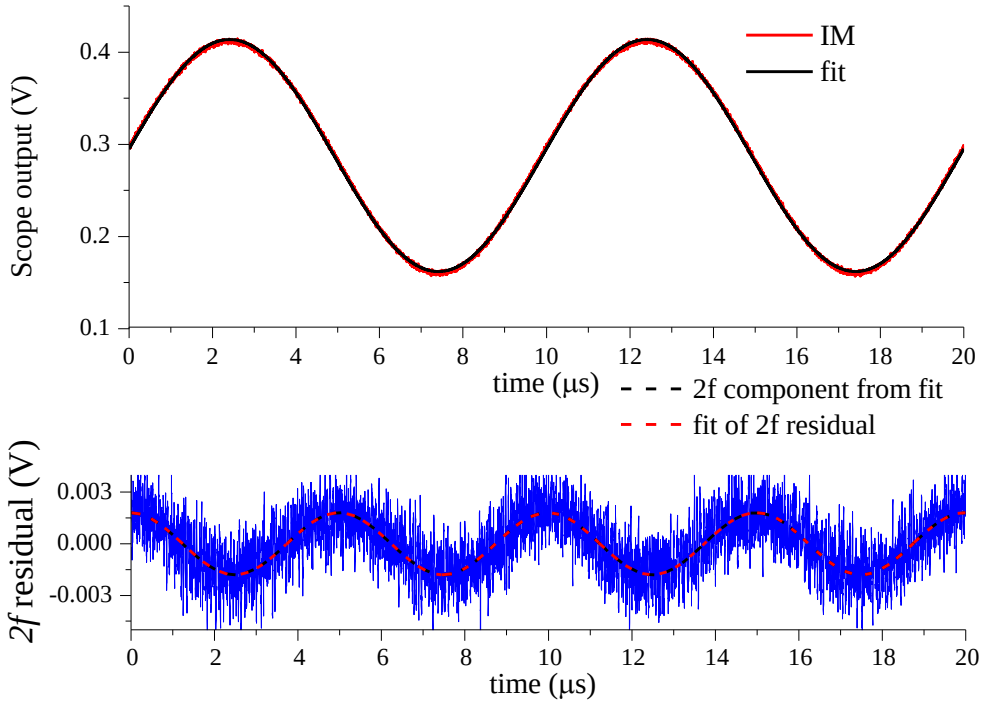

Figure 4-15. The linear and nonlinear IM measured using a nonlinear least-squares curve fit.

A small supressed peak may sometimes begin to appear in the non-responsive region which makes analysis difficult due to loss of the symmetry. Moreover, noise in the resonator trace can cause spurious peaks to be selected by the peak finding algorithm. Hence, the peaks are selected graphically by carefully excluding these unwanted peaks. Computational algorithms were implemented towards the final stage of this work to exclude such peaks. These algorithms used noise filtering and the information in the widths and heights of the peaks for the rejection of spurious peaks. It was then used in a control loop with the frequency of the first order sine functional fit to the resonator peaks being used to verify for a good fit of a second order sinusoid to the resonator peaks. This method, when combined with an automation system to change the laser bias current, could be used for *in-situ* characterisation of the wavelength modulation characteristics to compensate for long term drifts, in future applications.

4.7.3 Measurements Using the LIA

The simplest way to measure the linear and nonlinear IM amplitude and phases is to maximise the IM signal by changing the lock-in amplifier reference signal phase angle at *1f* and *2f* detection. The difference in the lock-in amplifier reference phase angles for the *1f* and the *2f* detection schemes gives the phase difference between the linear and nonlinear IM. The signals R_{1f} and R_{2f}, mentioned in Section 3.9 are equal to the linear and nonlinear IM signals in the absence of gas absorption.

Another method used to measure the WM-IM phase is to successively isolate a pure WM signal and a pure RAM signal to one of the orthogonal lock-in amplifier channels. The difference in the lock-in amplifier reference signal phase angle corresponding to each of these configurations will give the phase difference between the WM and the IM signals. The drawback of this technique is that, if the WM-IM phase is varying significantly across the scan, it would be impossible to isolate the FM and the RAM components onto one of the lock-in channels for each scan point. Hence, this method is useful only if the WM-IM phase is nearly a constant across the current scan. On the other hand, this method is advantageous for measuring the WM-IM phase at high modulation frequencies because the resonator trace quality deteriorates due to the reduced round trip distance travelled by the photons through the ring cavity. In addition, for most conventional DFB lasers, the tuning coefficient reduces at higher modulation frequencies so that sufficient resonator peaks are not traversed due to the resonator FSR not being small enough. It was difficult to fabricate fibre ring resonators with a smaller FSR due to issues such as temperature stability, losses from fibre bending etc. Moreover, careful splicing was necessary to fuse long fibre lengths to the coupler arms. Expensive fibre coupled optical isolators were also necessary for the stable operation of such ring resonators.

Yet another way to measure the WM-IM phase is to use the vector LIA [53] method with same signal phase configuration as the PDM (Figure 4-16). In this method the phase of the lock-in amplifier reference signal is adjusted so that a pure WM signal is isolated onto one of the orthogonal LIA channels. When a non-absorbing region is not available in the spectrum traversed by the scanned laser wavelength, the technique described in Section 5.8 was used.

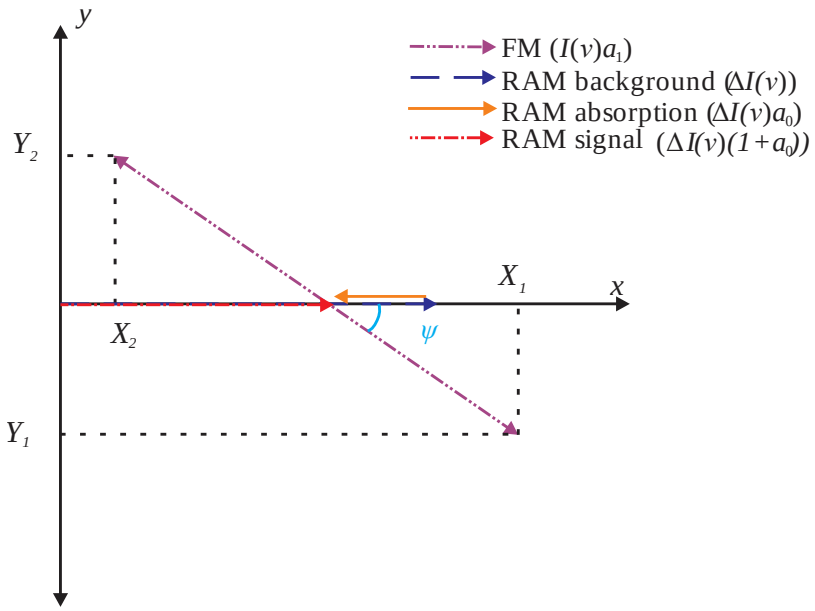

Figure 4-16. Vector lock-in method for measuring the WM-IM phase. The phase configuration of the FM and RAM signals is identical to the phasor decomposition method.

From Figure 4-16 , the WM-IM phase can be obtained from the magnitude of the WM signal as,

$$\psi_\lambda = \tan^{-1}\left\{\frac{|Y_1| + |Y_2|}{X_1 - X_2}\right\} \tag{4.12}$$

where X_1 and X_2, and Y_1 and Y_2 are the maximum and the minimum values of the WM signal projections on the X and Y lock-in amplifier channels, respectively. Figure 4-17 shows the measured WM-IM phase using this method compared against the laser WM-IM phase measured using the nonlinear curve fit.

The WM-IM phase angle obtained using this method closely matches the WM-IM phase from the curve fit method near the line centre for the absorption feature on the right.

Figure 4-17 shows that the vector lock-in method is useful in cases where the WM-IM phase is not changing with a steep gradient across the current scan as is the case for the phase variation at higher bias currents (wavelengths) for the 1997 nm DFB-MQW laser (Figure 4.17).

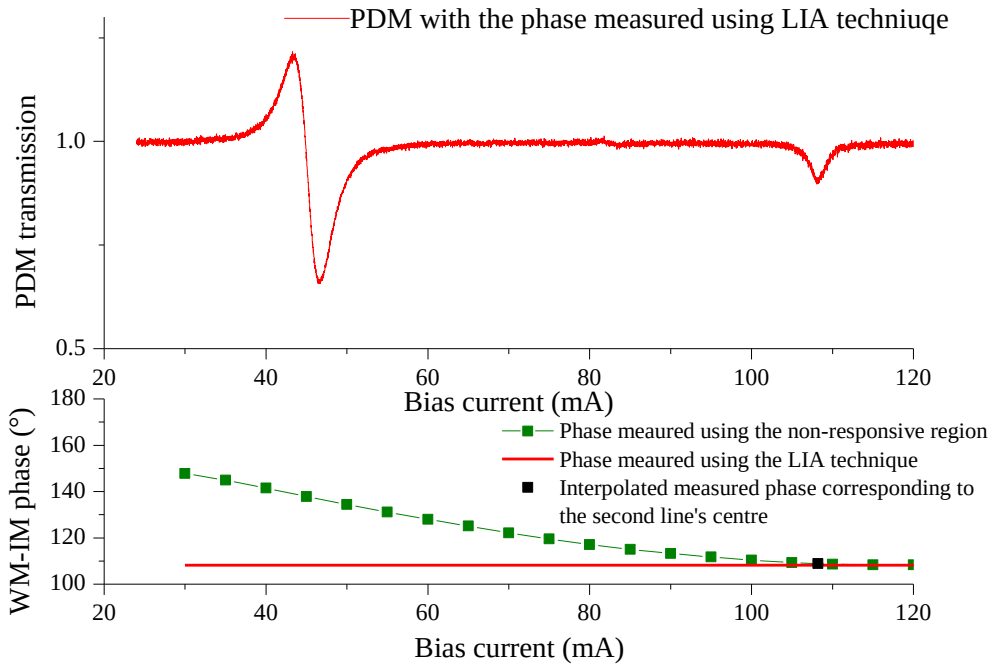

Figure 4-17. Comparison of phase measured using the vector-lock-in method to the nonlinear curve fit method. It was observed that the vector lock-in method calculated the WM-IM phase lag correctly for the absorption feature on the right.

4.8 *In-situ* Characterisation of IM

In-situ characterisation of the laser IM parameters could be advantageous in systems with long term DFB laser drift or other factors such as temporally stable etalons, dark current fluctuations or in systems with a changing nonlinearity of the IM characteristics such as the TDFA. The WM parameters on the other hand are less susceptible to changes in the transmission or the measurement system. Therefore, a provision was made for *in-situ* measurement of laser IM modulation parameters. The intensity modulation parameters; ΔI and ΔI_2, can be measured by subtracting the original WMS signal from the low pass filtered raw intensity signal at the detector or performing a digital PSD measurement on it. The instantaneous intensity (I) is obtained from the low pass filtered signal. A low- pass filter cut-off frequency of 500 Hz should be sufficient so as to include all the frequency components of the ramp. The i_0 values obtained for the 1997 nm DFB-MQW laser by applying this method to the detector signal recorded using an Agilent scope (higher sampling rates) at a sampling frequency of

10 MSamples/s and the i_0 values obtained using the curve fit method described in Section 4.7.2 is shown in Figure 4-18.

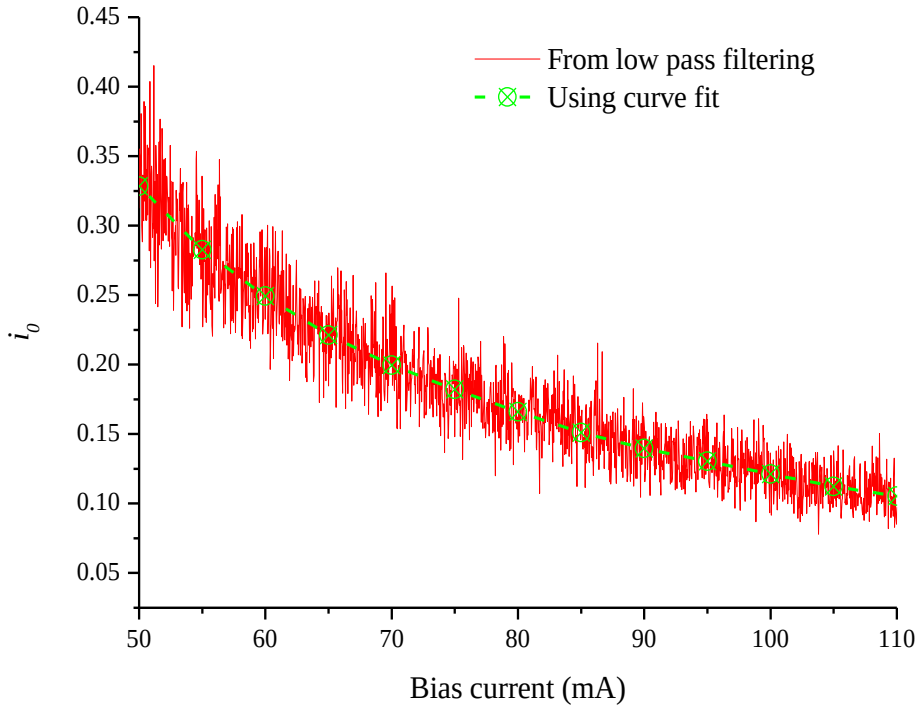

Figure 4-18. i_0 values measured *in-situ* by lock-in detection and low pass filtering a no-gas detector signal compared to i_0 values measured using the curve fit method described in Section 4.7.2. Current modulation amplitude = 10 mA, modulation frequency = 200 kHz and diode temperature = 21.96 °C.

Subsequently, measurements were conducted using signals acquired with a LabVIEW PXIe board. The sampling rate was limited to 2 MSamples/s, and thus the maximum modulation frequency for *2f* demodulation was limited to 100 kHz. A LabVIEW based LIA was used in some of the initial measurements at INTA due to a delay in the implementation of FPGA based LIAs.

4.9 Summary

The experimental measurement techniques have been briefly introduced in this chapter. The experimental measurement setups for direct and WMS detection schemes are described. The individual components of a WMS measurement system are explained

such as the laser drive electronics, bias-T and the lock-in amplifier. Design of a high temperature optical gas cell has been described which was used for a significant part of the work done for measurement of HT gas spectral parameters and validation of the measured spectral parameters by curve fitting the *2f/1f* WMS model to HT *2f/1f* signals measured in the lab.

WMS and direct spectroscopy require accurate assignment of wavelength value to each DC scan point across the current scan of the DFB laser. A wavelength referencing technique is described where a known gas line is used to assign the absolute wavelength and an interferometer to assign wavelength values to each measured scan point.

Measurement of the IM and WM parameters of the laser is important for constructing theoretical WMS signals for fitting to the experimentally measured signals to obtain the thermodynamic state variables of the gas, viz. the concentration and temperature. Different techniques are described for this purpose such as using the non-responsive region of resonator output to measure the WM-IM phase lag or by a least-squares curve fit technique. This is followed by a brief discussion on the techniques to measure the laser intensity modulation parameters *in-situ*.

Chapter 5

Analytical Treatment of Laser Modulation for WMS Applications

5.1 Introduction

Distributed feedback lasers are the tunable sources that are commonly used in WMS sensor systems. This chapter presents an analytical model for the wavelength modulation characteristics of semiconductor DFB lasers and techniques for the recovery of the gas absorption line shape from the first harmonic detection signals such as the phasor decomposition method, compensated for the effects of these characteristics.

As described in Chapter 2, for wavelength modulation spectroscopy, when a current modulation is applied to a DFB laser, it gives an instantaneous intensity modulation output and a time delayed wavelength modulation output. The amplitude and phase of IM output of DFB lasers have a flat response at the modulation frequencies less than the relaxation oscillation frequency (which lies in the GHz frequency range [58, 59]). Hence, the IM response is assumed to be a constant for the modulation frequencies used in WMS (< 1 MHz) and is not considered in this analysis. It is well documented in literature that the wavelength modulation output in DFB lasers is caused by the slow thermal and the fast carrier effects [34]. The majority of the earlier studies on the wavelength modulation properties of DFB lasers have been for optical communication systems where the modulation frequencies used are in the GHz range, and hence the

WM is dominated by the fast carrier effects (with the thermal effect dying off at high modulation frequencies). However, at the modulation frequencies (< 1MHz) used in WMS, the total frequency chirp is caused by a contribution from the carrier effects and the slow thermal effects.

An analytical model has been derived to explain the WM amplitude and phase response DFB lasers based on a thermal heat conduction model and semiconductor carrier dynamics. Section 4.7 discussed how these WM parameters were measured using a least-squares curve fitting procedure; in Section 5.5, the wavelength modulation properties of a 1997 nm DFB-MQW (Eblana Photonics) laser will be presented and explained using the analytical model developed. The wavelength modulation properties of another DFB-MQW laser at 1430 nm is also measured and compared with the model to validate the analytical model for different DFB laser types.

Section 5.6 discusses the effect of the DFB laser WM parameters in the recovery of the absorption line shape using RAM based techniques such as the phasor decomposition method. In majority of the calibration-free WMS techniques mentioned in literature [8, 60], laser modulation parameters and spectral parameters of the absorption feature were used to theoretically model the lock-in amplifier output signals, which are least-squares fitted to the experimental signals to infer gas thermodynamic state variables such as concentration and temperature or pressure. For example, Duffin et al. [35] used a calibration-free *1f*-WMS technique (PDM) to extract the gas concentration by the least-squares fit of a recovered WMS line centre absorption value to that obtained from a Voigt profile model for direct spectra. Li et al. [8] had used a *1f* normalised *2f* WMS signal to recover the gas concentration from an absorption feature with the gas temperature measured *a-priori* using ratio thermometry [8]. In vast majority of these techniques, the wavelength modulation parameters are assumed to be constant across the DFB laser current scan. Besides, only the line centre values of the laser modulation parameters were important to recover the peak absorption. For the simultaneous measurement of gas concentration and temperature using a single absorption feature, information from the entire gas absorption line shape (width and height) had to be utilised in the fitting algorithm. In the case of a 1997 nm DFB-MWQ laser used in this work, the WM-IM phase was observed to vary significantly as a function of the current

scan. On the contrary, the measured WM parameters were observed to vary less significantly for some of the other DFB lasers.

It was noted by previous members in the group that accurate recovery of the entire gas absorption line shape was not possible without compensating for this variation in the DFB laser modulation characteristics across the current scan. Hence, in this work these laser modulation parameters were measured across the current scan and applied to the line shape recovery models to recover the complete gas absorption line shape. This has implications in various measurement strategies used in WMS such as ratio thermometry or the simultaneous recovery of gas concentration and temperature.

Twin line absorption thermometry (also known as ratio thermometry) [14, 31, 41], uses the ratio of the peak absorbance of two transitions with dissimilar temperature dependence, but similar pressure and concentration dependence, to infer the temperature of the targeted species. Accurate measurements at a wider range of temperatures using RT demands the use of two nearby absorption features due to their similar dependence on pressure and concentration [47]. Using a single laser source is also advantageous in ratio thermometry as it simplifies the transmission and reception hardware requirements. Therefore, in ratio thermometry, it is preferable to use a larger current scan from a single laser source to access two nearby absorption features. Due to the large current scan, the change in the wavelength modulation parameters such as the WM-IM phase and tuning coefficient can be significant. A case study is presented in Section 5.7 for the 1997 nm DFB-MQW laser; it will be shown that correction for change in DFB laser modulation characteristics such as WM-IM phase is absolutely essential for the PDM to recover two nearby gas absorption line shapes using current scan from a single laser source.

The *1f* demodulation techniques such as the phasor decomposition method discussed in Section 3.5 requires pre-set adjustment of the lock- in amplifier reference signal phase to isolate the RAM component to one of the orthogonal measurement channels of the LIA. In Section 5.8, it will be shown that, owing to the varying WM-IM laser phase across the current scan, it becomes impossible to isolate the RAM component at each bias point across the full current scan. A phase insensitive variant of the PDM has been introduced in Section 5.9, which is of use in such situations. This method already introduced in

Section 3.7 is useful in multi-channel measurement using optical tomography, as well as in field applications.

5.2 Wavelength Modulation in DFB Lasers

Given the significance of WM characterisation of DFB lasers used in TDLS-WMS as discussed above; it was considered important to develop an understanding of these WM characteristics. Hence, an analytical model of wavelength modulation is presented in this section which calculates the wavelength modulation properties such as the WM-IM phase and WM amplitude as a function of the applied modulation frequency, current scan and henceforth.

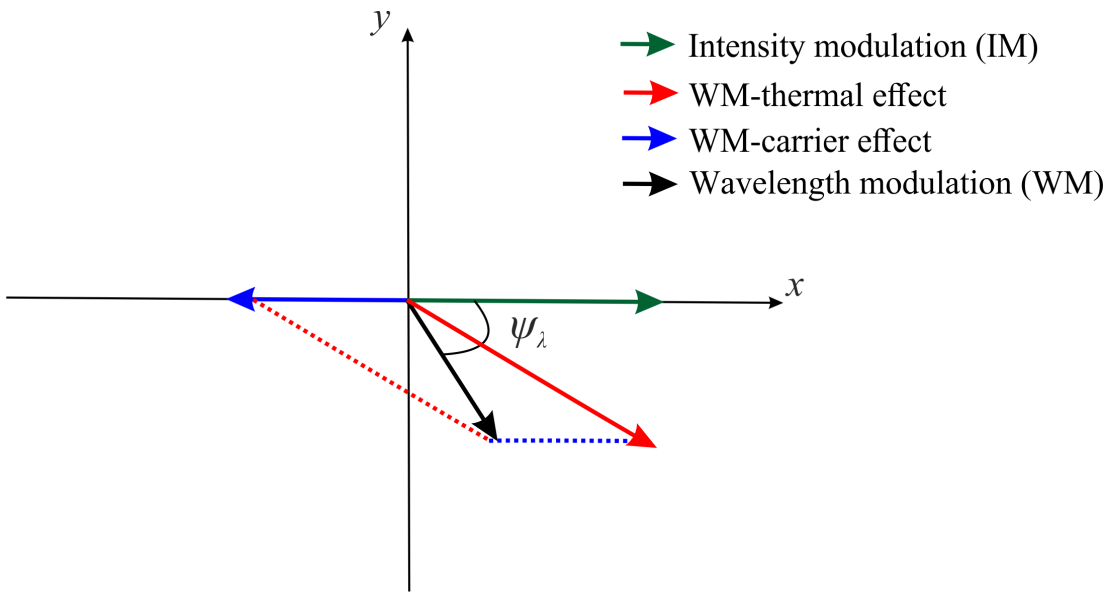

Figure 5-1. Phasor diagram representing the carrier and thermal contributions to wavelength modulation.

As mentioned before, when a sinusoidal current modulation is applied to a DFB laser; it generates an instantaneous intensity modulated output with a time delayed wavelength modulation. The instantaneous intensity modulation output is caused by stimulated emission of photons in the active region. The wavelength modulation output from the DFB laser is caused by the change in the effective length of the laser diffraction grating period due to thermal heating and change in the refractive index from the carrier (and small thermal) effects. The carrier induced wavelength modulation is usually assumed to be a constant and 180° out of phase with the applied current modulation. The thermally

induced WM lags with respect to the applied current modulation due to the low pass filter response of heat conduction and decreases in magnitude with increasing modulation frequencies and was expected to approach a phase of $\pi/2$. The resultant WM is a vector sum of the WM caused by the thermal and carrier effects as indicated by the phasor diagram of Figure 5-1. In this section a brief discussion is given on both these effects.

5.2.1 Carrier Contribution to Wavelength Modulation

The study of carrier contribution to the frequency (wavelength) chirp in the optical communications frequency regime (several GHz) is well documented in literature [58, 59]. This is because at higher modulation frequencies, the thermal contribution to WM is negligible and WM is caused by purely the carrier effects. The carrier induced WM is assumed to be constant at the sub-optical modulation frequencies (< 1 MHz) [58]. Rate equations are formulated to approximately calculate the perturbation in carrier density with an applied current modulation.

The carrier and the photon dynamics, when a constant current is injected into the DFB laser is summarised in Figure 5-2.

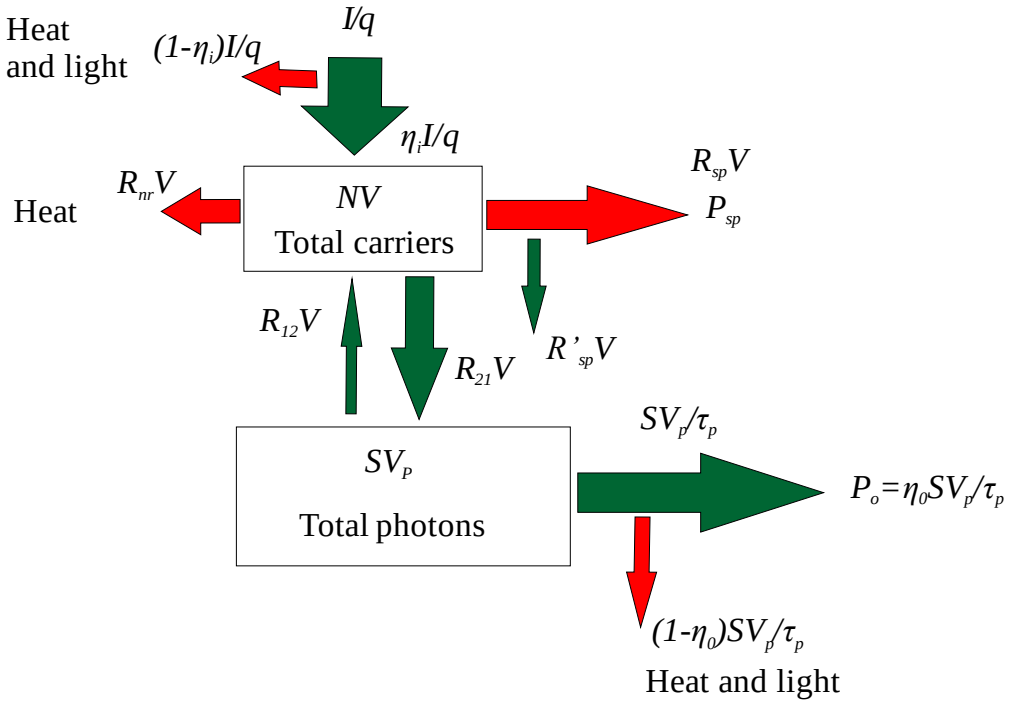

Figure 5-2. Carrier and photon dynamics in a semiconductor laser [59].

The total number of charge carriers injected per second into the gain region is $\eta_i I/q$, where I is the current applied to the diode laser, q is the charge in coulombs and η_i is the injection/internal efficiency for the DFB laser. The total number of charge carriers in the active region is given by NV, where N is the carrier density (assuming a uniform carrier distribution) and V is volume of the active region. S is the photon density. A small portion of the carriers in the active region is lost by nonradiative recombination ($R_{nr}V$) via surface imperfections and defects, to generate lattice vibrations (phonons), which is given out as heat. R_{nr} is the number of electrons lost per unit volume per second by nonradiative processes. The majority of the charge carriers in the active region will undergo stimulated emission as photons; the number of coherent photons emitted per second per unit volume is given by the stimulated emission rate $R_{21}(s^{-1})$. A small portion of the charge carriers are emitted as photons with a random phase through spontaneous emission ($R_{sp}V$). Some of these spontaneously emitted photons couple to the laser mode given by $R_{sp}'V$. A small fraction of the charge carriers in the active region is replenished by stimulated absorption given as $R_{21}V$.

Similarly, photons generated in the mode volume V_p, that satisfy the Bragg condition are coupled out of the cavity through lossy partially reflective surfaces (cleaved surfaces with anti-reflective coatings). Some of these photons are lost as either heat or light via free carrier absorption, scattering at rough surfaces or are absorbed outside the active region [59]. The optical power coupled out of the cavity is given by $\eta_o SV_p/\tau_p$, where η_0 represents the output coupling efficiency and τ_p represents the photon cavity lifetime. Photons emitting into the other modes are ignored [59].

The carrier rate equation is written as,

$$\frac{VdN}{dt} = \frac{\eta_i I}{q} - \left(R_{sp} + R_{nr}\right)V - (R_{21} - R_{12})V \tag{5.1}$$

i.e., the rate of change of carriers in the active region is given by the carriers injected by the applied current and carriers replenished by stimulated absorption less the carriers lost through spontaneous, stimulated and nonradiative emissions.

In an analogous fashion, the rate equation for the photons can be written as:

$$\frac{V_p dS}{dt} = (R_{21} - R_{12})V - \frac{SV_p}{\tau_p} + R'_{sp}V \tag{5.2}$$

The first term in the RHS is from the stimulated emission and stimulated absorption, the second term is from the cavity losses represented by the photon lifetime (τ_p) and the third term represents the coupling of the spontaneous emission to the laser mode.

From the expression for the gain [59] , the equation for the change in carrier density can be rewritten as,

$$\frac{dN}{dt} = \frac{\eta_i I}{q} - \frac{N}{\tau_N} - v_g G(N,S)S \tag{5.3}$$

where τ_N is the carrier lifetime, v_g is the group velocity (converts the gain per unit length to gain per unit time), and $G(N,S)$ is the gain which depends on the carrier density as well as the photon density (hole burning).

Similarly, equation (5.2) is rewritten as,

$$\frac{dS}{dt} = \left(\Gamma v_g G(N,S) - \frac{1}{\tau_p}\right)S + \Gamma\beta'_{sp}N/\tau_N \tag{5.4}$$

where $\Gamma = \frac{V}{Vp}$ is the optical confinement factor and β'_{sp} is the small fraction of the spontaneously emitted photons that are coupled back into the laser mode.

Calculation of gain for a strained MQW laser is not trivial and needs extensive use of quantum mechanics [5].

The gain vs. carrier density is seen to have an empirical logarithmic relation as shown in Figure 5-3. Gain can be represented using an empirical equation of the form [59],

$$G = G_{0N}\ln(\frac{N}{N_{tr}}) \tag{5.5}$$

where, G_{0N} is an empirical factor and N_{tr} is known as the transparency carrier density, i.e carrier density when there is no gain (or stimulated emission).

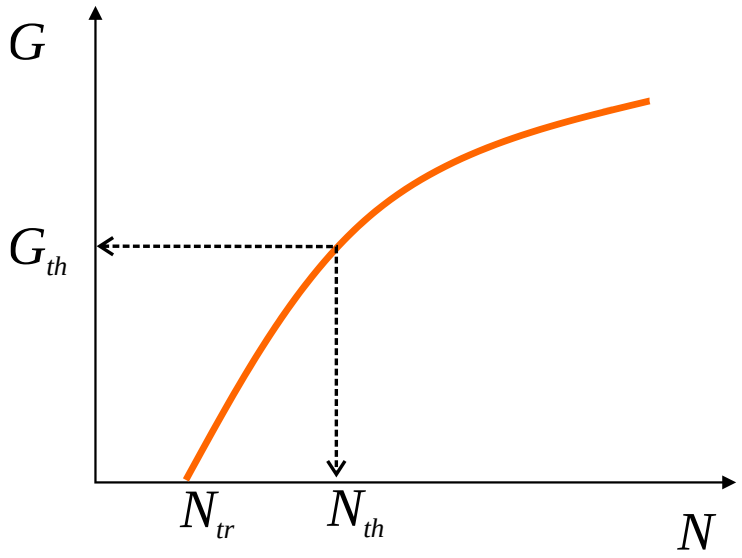

Figure 5-3. Gain as a function of carrier density. The gain, and hence the carrier density gets clamped at threshold.

An empirical formula obtained from the fit of the gain curve is given as [59],

$$G(N,S) = \frac{\varrho}{1+\epsilon S}(N_{tr}+N_s)\ln\left(\frac{N+N_s}{N_{tr}+N_s}\right) \tag{5.6}$$

ϵ is known as the gain compression factor, ϱ is known as the differential gain and N_s is a curve fitting parameter. The additional factor $(1+\epsilon S)$ accounts for the saturation of the gain at high photon densities due to hole burning effects [59]. Another important parameter is the differential gain (change in gain with carrier density),

$$\frac{dG}{dN} = \varrho = \frac{G_{0N}}{N} \tag{5.7}$$

which is important in describing laser modulation. At low photon densities, $\epsilon \ll 1$ and $N - N_{tr} \ll N_{tr} + N_s$, equation (5.6) reduces to a linear form:

$$G(N,S) = \varrho(1-\epsilon S)(N-N_{tr}) \tag{5.8}$$

Once the rate equations for the DFB diode laser have been derived which gives the carrier and photon density due to an applied DC current, the next step is to consider the

change in carrier density as a result of the current modulation. A small AC current modulation is applied to the laser as follows:

$$I = I_0 + \delta I e^{j\omega_m t} \tag{5.9}$$

where I_0 is the applied DC bias current[1] above the threshold, δI is the AC current modulation amplitude and ω_m is the angular modulation frequency.

The carrier density, the photon density, and hence the gain, also oscillate about their steady state values [59],

$$N = N_0 + \delta N e^{j\omega_m t} \tag{5.10}$$

$$S = S_0 + \delta S e^{j\omega_m t} \tag{5.11}$$

$$G = G_0 + \delta G e^{j\omega_m t} \tag{5.12}$$

where N_0, S_0 and G_0 are the steady state values, and δN, δS and δG are the perturbation amplitudes of carrier density, photon density and gain about their steady state values.

For steady state DFB laser operation, the photon and carrier densities gets clamped ($\frac{dS}{dt} = 0, \frac{dN}{dt} = 0$) above threshold, and therefore it follows from equation (5.4):

$$\left(\Gamma v_g G_0 - \frac{1}{\tau_p}\right) S_0 + \Gamma \beta'_{sp} N_0 = 0 \tag{5.13}$$

Taking the differential of equation (5.4),

$$d\left(\frac{dS}{dt}\right) = \left(\Gamma v_g G - \frac{1}{\tau_p}\right) dS + S\Gamma v_g dG + \Gamma \beta'_{sp} dN \tag{5.14}$$

After substitution, ignoring the second order terms, the relationship between the gain perturbation (δG) and the photon density change (δS) is written as,

[1] *The symbol I is used in the previous chapter to define the intensity. It has been used here to define current to maintain consistency with literature.*

$$\delta G = \left\{ \frac{j\omega_m}{\Gamma v_g S_0} + \frac{\beta'_{sp} N_0}{\tau_N v_g S_0^2} \right\} \delta S \tag{5.15}$$

The first term in equation (5.15) is due to the relaxation oscillations and the second term results from the coupling of spontaneous emission to the lasing mode, which only becomes important near the lasing threshold.

Including the spectral hole burning effects, which depends on the photon density, the change in gain due to the carrier and photon density perturbation is given as:

$$\delta G = \frac{\partial G}{\partial N} \delta N + \frac{\partial G}{\partial S} \delta S \tag{5.16}$$

Using equations (5.15) and (5.16), the net carrier density perturbation is written as,

$$\delta N = \frac{1}{\partial G / \partial N} \left\{ \frac{j\omega_m}{\Gamma v_g S_0} + \frac{\beta'_{sp} N_0}{\tau_N v_g S_0^2} - \frac{\partial G}{\partial S} \right\} \delta S \tag{5.17}$$

The change in carrier density results in a change of the refractive index (Kramers-Kronig relation), the cavity losses, as well as the round trip phase for DFB lasers [61].

From the cavity mode condition, the laser frequency ($\not{f}$) is given by the relation,

$$\not{f} n_r L_c = \bar{m} c / 2 \tag{5.18}$$

where n_r denotes the real part of the refractive index, $\bar{m}$ the cavity mode number, L_c is the cavity length and c is the speed of light in vacuum.

The change in the laser frequency (or wavelength) due to a carrier density perturbation is written as [59] :

$$\frac{\delta \not{f}}{\not{f}} = -\frac{\Gamma \delta n_r}{n_{gr}} = -\frac{\Gamma v_g}{c} \frac{\partial n_r}{\partial N} dN \tag{5.19}$$

where n_r is the real part of the refractive index and n_{gr} is the group refractive index.

Equating (5.19) and (5.17) the frequency chirp due to an applied current modulation is given by,

$$\delta f = \frac{\bar{\alpha}}{4\pi}\left\{\frac{j\omega_m}{S_0} + \frac{\Gamma\beta'_{sp}N_0}{\tau_N S_0^2} - \Gamma v_g \frac{\partial G}{\partial S}\right\}\delta S \tag{5.20}$$

where $\bar{\alpha}$ is known as the line width enhancement factor. The line width enhancement factor [62] is defined as the change in real part of the refractive index to the imaginary part of the refractive index due to a change in carrier density [62–65]:

$$\bar{\alpha} = \frac{\partial n_r}{dN} \Big/ \frac{\partial n_i}{\partial N} = -\frac{4\pi f}{c}\frac{\partial n_r}{\partial N} \Big/ \frac{\partial G}{\partial N} \tag{5.21}$$

The line width enhancement factor represents the fluctuations in carrier density which results in a refractive index change (the plasma effect). The typical values of the parameters in equations (5.20) and (5.21) are given in Table 5-1.

.

Important physical constants for a semiconductor laser diode				
Linewidth enhancement factor $\bar{\alpha}$	Spontaneous emission coupling ratio β'_{sp}	Cavity photon lifetime τ_p(ps)	Threshold current I_{th} (mA)	Laser bias current I_{bias}(mA)
4	10^{-5}	1	20	70

Table 5-1. Typical values of the physical constants used in this analysis for InP.

From equation (5.20), it can be summarised that the total frequency chirp due to carrier density change from an applied current modulation arises from three effects:

a. The relaxation oscillation effect.

This effect originates due to the delay in the photon density change with respect to the current density change, which results in relaxation oscillations with a time period of approximately 1 ns. Its value depends on the line width enhancement factor for the DFB laser.

b. Coupling of spontaneous emission to the lasing mode.

This becomes significant only near the threshold.

c. Gain compression due to spectral hole burning.

Gain compression in semiconductor lasers is caused by spectral and spatial hole burning [61, 66, 67].

The contribution to the dynamic frequency chirp from each of these components is now analysed.

A. Relaxation oscillation effect

The relaxation oscillations generally limit the maximum current modulation frequency that can be applied to a laser in the optical communications regime. The frequency chirp due to the relaxation oscillation effect is given, from equation (5.20) as,

$$|\delta\nu| = \frac{\frac{\bar{\alpha}}{2} f_m}{S_0}(\delta S) = f_m \frac{\bar{\alpha}}{2[I_0 - I_{th}]}\delta I \tag{5.22}$$

where f_m is the applied current modulation frequency .

Applying the values in equation (5.22),

$$\delta\nu/\delta I \ = 0.04\ f_m/\text{mA} \tag{5.23}$$

The relaxation oscillation frequency for DFB lasers is usually in the gigahertz range, and hence the contribution to WM from the relaxation oscillation effect is negligible at the modulation frequencies used in wavelength modulation spectroscopy (< 1 MHz).

B. Spontaneous emission

Contribution to WM from spontaneous emissions is written as, using the steady state rate equations;

$$|\delta\nu| = \frac{\bar{\alpha}\beta'_{sp}}{4\pi\tau_p}\frac{I_{th}}{[I_0 - I_{th}]^2}\delta I \tag{5.24}$$

This is calculated as approximately 30 kHz/mA which only become significant near the lasing threshold.

C. Gain compression

For a two level laser system, the gain compression from spectral hole burning effects can be approximated using the equation,

$$\frac{\partial G}{\partial S} = -\frac{\varepsilon G}{(1+\varepsilon S)} \approx -\varepsilon G \tag{5.25}$$

Under steady state operation (ignoring the spontaneous emission), the gain is equal to the cavity losses, i.e.,

$$\Gamma v_g G_0 \cong 1/\tau_p \tag{5.26}$$

which gives the frequency tuning coefficient as:

$$\delta f \cong \frac{\bar{\alpha}\varepsilon S_0}{4\pi\tau_p}\left(\frac{\delta S}{S_0}\right) = \frac{\bar{\alpha}\varepsilon S_0}{4\pi\tau_p[I_0 - I_{th}]}\delta I = \frac{\Gamma\bar{\alpha}\varepsilon}{4\pi h f \eta_o V}\delta P \tag{5.27}$$

For a small gain compression effect, $\epsilon S = 1\%$ and $\delta f/\delta i$ is calculated as 60 MHz/mA.

At low modulation frequencies, the carrier effect is assumed to be a constant and majorly due to the gain compression from the spectral hole burning effects. In some lasers, the carrier effect was observed to be significantly higher. It was proposed by Kobyashi et al. [58] that diffusion and non-uniform carrier distribution (spatial hole burning) could be a reason for this. However, this could not explain the high carrier induced WM in devices with a strong current confinement. Koch and Bowers [68] explain the carrier induced FM at lower modulation frequencies. This is in contrast to the gain compression model developed by Tucker et al. [63] who include a contribution from the spatial hole burning effects, rolling off at higher modulation frequencies.

Moreover, the spatial hole burning effects and spectral hole burning effects are not in phase. In DFB lasers the spatial hole burning affects the round trip phase and the feedback losses, and therefore the gain and the carrier density. The spatial hole burning

effect is also a function of the bias current [69, 70], and hence much more complex. Due to this, the spatial hole burning effects are neglected in this study, none-the less it is expected to contribute significantly to the carrier induced frequency chirp especially at sub-MHz modulation frequencies in devices with a higher carrier confinement as was the case with the 1997 nm DFB-MQW laser used in this work [61, 71, 72].

5.2.2 Thermal Contribution to Wavelength Modulation

One method to analyse the temperature dynamics in a laser diode is to use an electrical equivalent circuit model. A simple RC circuit model of heat conduction for a laser diode is shown in Figure 5-4 with the laser assumed to have a thermal resistance (R_T) and thermal capacitance (C_T).

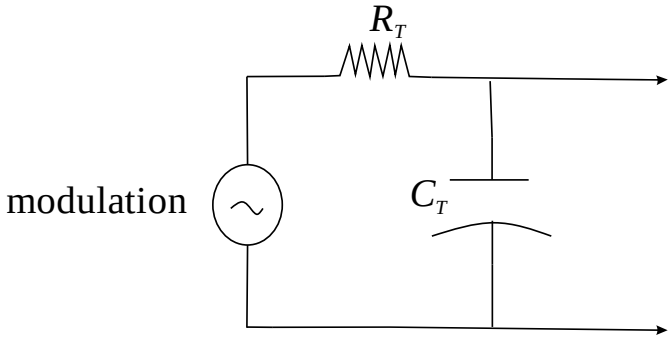

Figure 5-4. An equivalent RC circuit model for thermal conduction in a semiconductor laser diode. An actual representation would include multiple thermal resistances[2] and capacitances for each of the different layers of the DFB laser such as the solder, heat sink etc.

An improved electrical equivalent model based on a three layer laser structure will be discussed in Section 5.4, which shows better concurrence with the measured WM characteristics of the DFB lasers presented in this work and reported in literature.

5.3 RC Equivalent Circuit for Heat Conduction

In the RC thermal equivalent model, the DFB laser is assumed to have a thermal resistance ${}^2R_T$ and thermal capacitance ${}^2C_T$, mounted on a heat sink at a temperature T_0. From the electrical analogue model of heat [73–75] the following equation is written:

[2] From the Fourier's law, the thermal resistance for 1D heat flow is calculated as $R_T = \frac{d_s}{KA}$, where d_s is the thickness of the substrate (the entire laser chip) ,K is the thermal conductivity and A is the area perpendicular to the heat flow. It can be observed that this equation is analogous to electrical resistance. The thermal capacitance of a material quantifies its ability to store or release heat.

$$C_T \frac{dT}{dt} + \frac{T - T_0}{R_T} = P_{el} \tag{5.28}$$

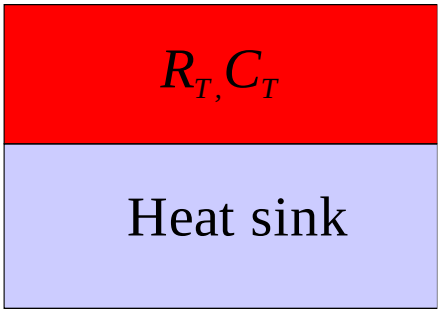

Figure 5-5. RC equivalent heat transfer model.

where P_{el} is the electrical heat dissipated in the laser chip. Equation (5.28) means that the electrical heat dissipated in a laser chip is used to increase the laser temperature to T and the laser dissipates heat at a rate depending on its thermal capacitance.

The electrical heat dissipated in the chip is given by the electrical power input less the optical power output:

$$P_{el} = v_f i_f - P_{opt} = \left[V_j i_f - P_{opt}\right] + i_f^2 r_s \tag{5.29}$$

where, V_j is the junction voltage, i_f is the forward current, r_s is the series resistance of the laser diode and $v_f (= V_j + i_f r_s)$ is the forward voltage.

The optical power output above threshold for the DFB laser is given as,

$$P_{opt} = \eta (I_{bias} - I_{th}) \qquad (I_{bias} > I_{th}) \tag{5.30}$$

where η is the slope of the power-current curve (slope efficiency), I_{bias} is the biased current and I_{th} is the threshold current.

Applying a current modulation above threshold, the forward current in the laser diode is given by,

$$i_f = I_{bias} + i_m \cos(\omega_m t) \tag{5.31}$$

Substituting equation (5.31) into (5.29), the electrical heat dissipated in the laser chip has a form (ignoring the second harmonic term),

$$P_{el} = P_{DC} + A_1 \cos(\omega_m t) \tag{5.32}$$

where P_{DC} represents the DC electrical heat dissipated given as;

$$P_{DC} = \left[V_j I_{bias} - \eta \cdot (I_{bias} - I_{th})\right] \tag{5.33}$$

and $A_1 \cos(\omega_m t)$ represents the first order AC component of the heat generated with a magnitude given by,

$$A_1 = \left(V_j - \eta\right) \cdot i_m \tag{5.34}$$

Equating the thermal output model to the electrical power input, from equations (5.28) and (5.32), and solving for the temperature,

$$T = T_0 + R_T \left\{ P_{DC} + \frac{A_1 cos(\omega_m t - \varphi_1)}{\sqrt{1 + \omega_m^2 \tau_{th}^2}} \right\} \tag{5.35}$$

where $\tau_{th} = R_T C_T$ is defined as the thermal time constant and φ_1 is the phase lag of the thermal effect given by $\varphi_1 = \tan^{-1}(\omega_m \tau_{th})$. From equation (5.35) it can be observed that the temperature response is analogous to that of a RC low pass filter.

The change in the wavelength($\Delta\lambda$) of the DFB laser for a change in temperature (ΔT), assuming a linear relationship is given as,

$$\lambda = \lambda_0 + \frac{\Delta\lambda}{\Delta T} \Delta T \tag{5.36}$$

where, $\frac{\Delta\lambda}{\Delta T} = (\alpha_l + \alpha_n)\lambda$; α_l and α_n are the temperature expansion and refractive index coefficients of wavelength, i.e. the change in laser wavelength with temperature is assumed to arise from a linear contribution of the thermal expansion of the Bragg grating period and the change in its refractive index due to heating (thermo-optic effect).

Substituting equation (5.35) into equation (5.36):

$$\lambda = \lambda_0 + \frac{\Delta\lambda}{\Delta T} R_T \left\{ P_{DC} + \frac{A_1 cos(\omega_m t - \varphi_1)}{\sqrt{1 + \omega_m^2 \tau_{th}^2}} \right\} \tag{5.37}$$

In equation (5.37), $\Delta\lambda/\Delta T$ was calculated for the DFB lasers using the DC wavelength tuning characteristics. A_1 (equation (5.34)) and P_{DC} (equation (5.33)) are calculated from the power-current (*L-I*) and current-voltage (*I-V*) characteristics of the DFB laser. For instance, A_1 can be determined once the forward junction voltage (V_j) and series resistance (r_s) are calculated from the X-intercept and slope of the *V-I* curve, respectively, and the quantum efficiency from the slope of the *L-I* curve.

5.3.1 Nonlinear Heating of the Laser Diode

Inclusion of the nonlinear contribution $i_f^2 r_s$ in equation (5.29) adds a second harmonic component to the electrical heat dissipated:

$$P_{el} = P_{DC} + A_1 \cos(\omega_m t) + A_2 \cos(2\omega_m t) \tag{5.38}$$

The expressions for the DC and AC electrical heating amplitudes (P_{DC}, A_1 and A_2) now become:

$$P_{DC} = \left[V_j I_{bias} - \eta \cdot (I_{bias} - I_{th}) \right] + \left[r_s I_{bias}^2 + \frac{r_s i_m^2}{2} \right] \tag{5.39}$$

$$A_1 = \left(V_j - \eta \right) \cdot i_m + 2 r_s I_{bias} i_m \tag{5.40}$$

$$A_2 = \frac{r_s i_m^2}{2} \tag{5.41}$$

The wavelength tuning is now given as:

$$\lambda = \lambda_0 + \frac{\Delta\lambda}{\Delta T} R_T \left\{ P_{DC} + \frac{A_1 cos(\omega_m t - \varphi_1) + A_2 \cos(2\omega_m t)}{\sqrt{1 + \omega_m^2 \tau_{th}^2}} \right\} \tag{5.42}$$

From the above equations the following conclusions are drawn [37]:

a. The direct-scanning wavelength has a nonlinear dependence on the bias current, plus a small offset due to the current modulation.
b. The amplitude of thermal WM increases with the bias current. Hence, the thermal contribution to wavelength modulation increases across the current scan. This causes the WM-IM phase to change across the current scan, due to the increasing thermal contribution being vectorially added to the carrier contribution (assumed to be at constant phase and magnitude).
c. There is a small wavelength modulation at the second harmonic frequency.

It is interesting that all the nonlinear effects originate from the series resistance of the laser diode which will vary from one laser to another.

5.3.2 Tuning Coefficient and Phase from RC Thermal Model

From equations (5.42), adding a constant carrier contribution (C_f) (the carrier effect is assumed to be a constant at low modulation [37, 76]) gives,

$$\left|\frac{\Delta \not{\nu}}{\Delta i}\right|^2 = \frac{H_0^2 - 2C_f H_0}{1 + (\omega_m/\omega_c)^2} + C_f^2 \tag{5.43}$$

Equation (5.43) represents the thermal tuning in GHz/mA.

Here,

$$H_0 = \left(\frac{c}{\lambda^2}\right)\left(\frac{\Delta\lambda}{\Delta T}\right) R_T\{(V_j - \eta) + 2r_s I_{bias}\} \tag{5.44}$$

is the magnitude of the thermal tuning when $\omega_m \to 0$ and ω_c is the thermal cut-off frequency given by $\omega_c = \kappa/d_s^2$. κ is the thermal diffusivity and d_s is the substrate thickness.

The parameters R_T and C_λ in the above equation can be measured from the *I*-λ curve as follows:

$$\Delta\lambda_{DC} = \left\{\left(\frac{\Delta\lambda}{\Delta T}\right) R_T(V_j - \eta) - C_\lambda\right\} I_{bias} + \left(\frac{\Delta\lambda}{\Delta T}\right) R_T r_s I_{bias}^2 \tag{5.45}$$

where $C_\lambda = (\lambda^2/c)C_f$. V_j and r_s can be calculated from the *I*-*V* curve of the laser diode. The slope efficiency η can be calculated from the *L*-*I* characteristics. $\Delta\lambda/\Delta T$ can be

obtained from the DC wavelength scan measured at two different temperatures. C_λ is estimated from the high modulation frequency tuning coefficient values (~ 1 MHz) where the thermal contribution is negligible. The thermal resistance R_T is calculated theoretically using the dimensions of the laser [59] or using equation (5.45) with all the other parameters obtained as described above.

The WM phase lag is given by the angular component of the complex equation (5.43) as,

$$\psi_\lambda = \tan^{-1} \frac{(\omega_m/\omega_c)H_0}{H_0 - C_f\{1 + (\omega_m/\omega_c)^2\}} \tag{5.46}$$

From equation (5.43), it can be inferred that the RC equivalent thermal model predicts a first order low pass filter response $1/(1 + \left(\frac{\omega_m}{\omega_c}\right)^2)$ for wavelength modulation. It also predicts that the thermal WM-IM phase lag approaches 90° at high modulation frequencies (typically in the hundreds of kHz).

When $H_0 > 2C_f$, the tuning coefficient is expected to increase as a function of the modulation frequency. For $H_0 < 2C_f$, the magnitude of the tuning coefficient decreases with modulation frequency. For $H_0 = 2C_f$, the magnitude of tuning coefficient is independent of the current modulation frequency.

This model has been presented as it provides a simple theoretical understanding of the thermal characteristics of semiconductor laser diodes based on an electrical analogue model of thermal heat conduction.

Several authors have reported that the thermal WM follows a $1/(\omega_m/\omega_c)^{\frac{1}{2}}$ relationship [63, 68, 76]. As a result, at high modulation frequencies, the thermal WM-IM phase lag approaches 45° rather than 90°. Hence, it was obvious that this model is inadequate in explaining the wavelength modulation properties of DFB laser diodes. It serves as a foundation for the advanced thermal model which accurately predicts the WM behaviour of DFB lasers.

5.4 Improved Thermal Model

Many authors have reported that the thermal WM follows a $1/(\omega_m/\omega_c)^{\frac{1}{2}}$ response [63, 68, 76]. Moreover, the thermal WM-IM phase lag was observed to approach a phase angle close to 45° at high modulation frequencies, rather than the 90° phase angle predicted by the RC equivalent circuit model. These characteristics are predicted by the improved thermal model discussed in this section which assumes that the temperature is not uniform across the laser diode.

It is reported that most of the electrical heat (> 90 %) is dissipated in the active region of the DFB laser [76, 77]. The DFB laser is approximated as a three layer structure (Figure 5-6) with the heat flowing out of the active layer to the top buffer layer and the bottom substrate layer. In this model, it is assumed that only the temperature of the active region contributes to the frequency chirp. This is a valid assumption as the grating structure on the laser waveguide is close to the active region. This model is apt, as only the temperature of the active region contributes to the lasing mode (assuming that the majority of the laser mode profile overlaps with the active region). Dilwali et al. [78, 79] had developed an analogous thermal model, where an average temperature over the entire laser structure was used.

The heat dissipated in the active region is written from (5.32) as,

$$P_{el} = P_{DC} + A_1 e^{j\omega_m t} \tag{5.47}$$

Following a similar methodology as in Section 5.3 to find the temperature, equating (5.47) and (5.23), gives the temperature of the active region as,

$$T = T_a(t) + T_{ss} \tag{5.48}$$

where,

$$T_a(t) = \tilde{T}_a e^{j(\omega_m t + \varphi)} \tag{5.49}$$

and,

$$T_{ss} = R_T P_{DC} + T_0 \tag{5.50}$$

$T_a(t)$ is the active layer temperature with an amplitude $\tilde{T}_a$, modulated at a frequency ω_m and has a phase lag φ , T_{ss} is the uniform steady state temperature of the active region and [3]T_0 is the heat sink temperature.

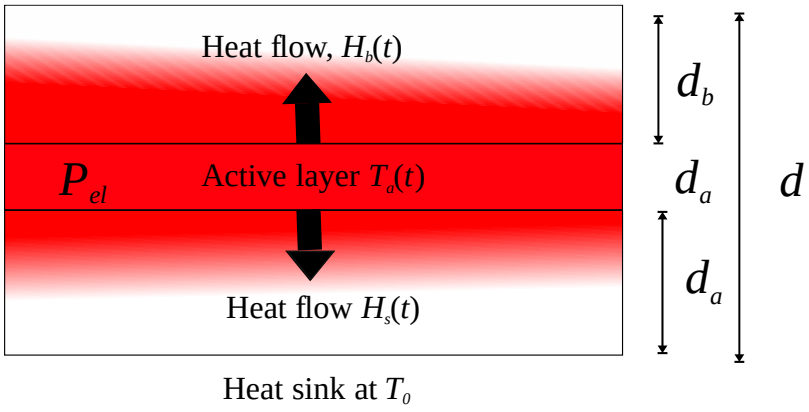

Figure 5-6. A three layer, 1D heat flow model for the DFB laser.

A 1D heat flow model using constraints and boundary conditions will be employed to obtain the temperature of the active region.

Heat flowing out of an enclosed surface is given as [75, 80],

$$\iiint_V \frac{\partial E}{\partial T} dV = \iiint_V Q dV - \oiint_S \vec{q} dS \tag{5.51}$$

where [4]E is the heat energy, [4]Q is heat generation rate from a distribution of heat sources in a given material of volume [4]V and $\vec{q}$ is the heat flux (W/cm^2) vector pointed outward perpendicular to the surface [4]S.

Applying the Gauss's divergence theorem, equation (5.51) can be rewritten as,

$$\frac{\partial E}{dt} = Q - \nabla\vec{q} \tag{5.52}$$

where $E = c_h T = \rho c_p T$ and $\vec{q} = -K\nabla T$. c_h is the heat capacity, c_p is the specific heat capacity, ρ is the material density and K the thermal conductivity. Substituting these values in (5.52), gives a more general form [37]:

[3] Not to be confused with definitions in previous chapters.
[4] Not to be confused with definitions in previous chapters.

$$\frac{\partial T}{\partial t} = -\frac{K}{\rho c_p}\nabla^2 T \tag{5.53}$$

Thermal constants for the DFB laser		
Density ρ (g/cm^3)	Specific heat capacity c_p (J/g °K)	Thermal diffusivity κ (cm^2/s)
4.81	~0.31	0.46

Table 5-2. Density, specific heat capacity and thermal diffusivity for bulk InP. It is known that for group III-IV materials the thermal diffusivity values can drop by one to two orders of magnitude compared to the bulk semiconductor materials [76].

Assuming a 1D heat flow, the heat conduction equation (equation (5.53)) can be written as:

$$\frac{\partial T}{\partial t} = -\kappa\frac{\partial^2 T}{\partial x^2} \tag{5.54}$$

The relationship between thermal diffusivity and thermal conductivity goes as $\kappa = K/(\rho c_p)$. The values of the thermal constants for bulk InP are given in Table 5-2. For the semiconductor DFB laser, the following boundary conditions were imposed:

a. The heat sink is at a temperature T_0 at x = 0.
b. $\frac{\partial T}{\partial x} = 0$, at x = d (the total chip length), which means that there is no heat lost from the top buffer layer.
c. There is no heat generation in the substrate and the buffer layers.

Using these boundary conditions and solving equation (5.54), give the temperature distribution in the substrate and buffer layers as,

$$T(x,t) = T_a(t)\left[\frac{e^{qx} - e^{-qx}}{e^{qd_s} - e^{-qd_s}}\right], \qquad 0 \le x \le d_s \tag{5.55}$$

and,

$$T(x,t) = T_a(t)\left[\frac{e^{q(x-d)} + e^{-q(x-d)}}{e^{qd_b} + e^{-qd_b}}\right], \qquad (d_s + d_a) \le x \le d \tag{5.56}$$

where [5] $q = \sqrt{j\omega_m/\kappa}$.

The heat flow along the vertical direction (assumed to be in the direction of the x axis) from an infinitely thin active layer having an area [6] A is represented by a general thermodynamic relation:

$$H = -KA\frac{\partial T(x,t)}{\partial x} \tag{5.57}$$

The heat flowing from the active region to the substrate and buffer layers is represented by $H_s(t)$ and $H_b(t)$, respectively. Using equations (5.55), (5.56) and (5.57), the heat flowing out of the active layer into the substrate and buffer layers is given as,

$$H_s(t) = KAqT_a(t)\coth(qd_s) \tag{5.58}$$

$$H_b(t) = KAqT_a(t)\tanh(qd_b) \tag{5.59}$$

Now, considering the heat flow out of the active layer to surrounding layers, the following equation is valid (equating the time varying parts):

$$C_a\frac{dT_a(t)}{dt} + H_s(t) + H_b(t) = P_{el}(t) \tag{5.60}$$

where C_a is the thermal capacity of the active layer.

From equations (5.58), (5.59), (5.60) and (5.47) the time varying temperature of the active layer is,

[5] Not to be confused with charge
[6] Not to be confused with integrated absorbance

$$T_a(t) = \frac{A_1 e^{j\omega_m t}}{j\omega_m C_a + KAq\left[\coth(qd_s) + \tanh(qd_{b)}\right]} \tag{5.61}$$

Substituting this in equations (5.48) and (5.50), the total active layer temperature becomes,

$$T = T_0 + R_T\left\{P_{DC} + \frac{A_1 e^{j\omega_m t}}{j\omega_m R_T C_a + qd_s[\coth(qd_s) + \tanh(qd_b)]}\right\} \tag{5.62}$$

For $qd_s << 1$ and $qd_b << 1$, $\coth qd_b \to 1$ and $\tanh(qd_b) \to 0$, the equation reduces to the simple RC thermal model given as,

$$T = T_0 + R_T\left\{P_{DC} + \frac{A_1 e^{j\omega_m t}}{1 + j\omega_m R_T C_T}\right\} \tag{5.63}$$

where $C_T = C_a + C_b + \frac{1}{2}C_s$.

Now, the wavelength tuning can be written as:

$$\lambda = \lambda_0 + \frac{\Delta\lambda}{\Delta T}R_T\left\{P_{DC} + \frac{A_1 e^{j\omega_m t}}{j\omega_m R_T C_a + qd_s\left[\coth(qd_s) + \tanh(qd_{b)}\right]}\right\} \tag{5.64}$$

Defining the thermal cut-off frequencies associated with the substrate, buffer and active layers as [37] $\omega_{cs} = \kappa/d_s^2$,$\omega_{cb} = \kappa/d_b^2$ and $\omega_{ca} = \left(\frac{d_s}{d_a}\right)\omega_{cs}$, equation (5.64) becomes:

$$\lambda = \lambda_0 + \left(\frac{\Delta\lambda}{\Delta T}\right)R_T\left\{\frac{P_{DC}A_1 e^{j\omega_m t}}{j\,\omega_m/\omega_{ca} + (j\,\omega_m/\omega_{cs})^{\frac{1}{2}}\left[\coth(j\,\omega_m/\omega_{cs})^{\frac{1}{2}} + \tanh(j\,\omega_m/\omega_{cb})^{\frac{1}{2}}\right]}\right\} \tag{5.65}$$

Typically, d_s is at least three orders of magnitude greater than d_a, and hence $\omega_{ca} \gg \omega_{cs}$; the first term in the denominator of equation (5.65) goes to zero. The expression for the tuning coefficient can be written as,

$$\frac{\Delta f}{\Delta i} \cong C_f - \left\{ \frac{H_0}{(j\,\omega_m/\omega_{cs})^{\frac{1}{2}}\left[\coth(j\,\omega_m/\omega_{cs})^{\frac{1}{2}} + \tanh(j\,\omega_m/\omega_{cb})^{\frac{1}{2}}\right]} \right\} \quad (5.66)$$

where H_0 is the contribution to WM from purely the thermal effects as discussed in Section 5.3. The dynamic wavelength tuning behaviour depends on three thermal cut-off frequencies; ω_{cs}, ω_{cb} and ω_{ca}.

Equation (5.66) predicts that the WM amplitude has a $1/(\omega_m/\omega_c)^{0.5}$ relationship which showed better concurrence to the experimental data as reported in earlier works [76, 78, 79]. It also predicts the presence of a dip in the tuning coefficient vs. modulation frequency curve because of the slow decrease in thermal wavelength tuning magnitude and that the thermal WM-IM phase approaches a phase angle close to 45° [79] at higher modulation frequencies rather than the 90° phase angle predicted by the RC circuit equivalent model.

5.5 Limitations of this Analysis

The aim of the improved heat conduction model was to explain the wavelength modulation response characteristics which could not be predicted for the DFB laser using the RC equivalent model described in Section 5.3. It cannot be used to accurately calculate the WM characteristics such as the thermal WM phase or amplitude as numerous factors are not taken into account in this model. For example, a one dimensional (1D) heat flow is assumed, whereas, heat flow in a real DFB laser diode is best represented by a two dimensional (2D) model [76]. The thermal capacitance and resistance would also be two dimensional (2D) [59]. For example, as a step closer, the thermal resistance has been calculated using an improved quasi-2D model in [59], with the active region assumed to be a linear strip of thickness d_w, length ℓ, at a distance of d_s from the heat sink as;

$$R_T = \ln(4d_s/d_w)\ /\pi K\ell \quad (5.67)$$

In the three-layer model, the specific heat capacities and thermal diffusivities are assumed to be the same for the buffer, the substrate and the active layer regions. This three-layer heat flow model is an oversimplification. Depending on the DFB laser design

technology which is application specific, the active, substrate and the buffer layers will contain multiple sub-layers. For example, in the DFB-MQW laser structure the active region has several sub-layers of alternating bandgap materials as well as carrier confinement layers [81], the buffer and the substrate layers are also comprised of numerous sub-layers with different thicknesses. Heat flow is further affected by the thermal characteristics of the packaging and the surrounding medium. This model assumes that there is no loss of heat from the laser to the surroundings. This assumption is not true as convective heat flow occurs from the DFB laser to the surrounding medium (the packaging, the heat sink, solder etc.). The model also assumes that all the electrical heat is dissipated in the active region. This could be the case if the laser series resistance is assumed to be negligible and only the junction voltage contributes to the temperature. For more accurate results, numerical computation using 2D heat flow equations taking into account the 2D isotropic thermal properties of the different layers of the DFB laser and surrounding media (packaging) is necessary [76].

The contribution to wavelength tuning from carrier effects is assumed to be a constant at low modulation frequencies (<1MHz). The spatial hole burning effect was reported to contribute significantly to the WM response especially in DFB lasers with an increased carrier confinement, rolling off at higher modulation frequencies [61,66, 67]. Spatial hole burning effects are complex [61, 66, 67, 82] and thus not dealt with in this study.

5.6 Case Studies - Comparison of the Three Layer DFB Laser Model to Experimental Data

The wavelength modulation characteristics, such as the tuning coefficient and WM-IM phase lag, of two DFB lasers were measured experimentally. The first laser is a 1997 nm multi-quantum well DFB laser used for the vast majority of this work for probing the CO_2 absorption features in the near-IR band and the second a 1430 nm DFB-MQW laser previously used by Bain et al. [14] for measuring the aero engine exhaust water vapour concentration and temperature. The tuning coefficient and WM-IM phase lag were theoretically calculated using the three layer laser model for the DFB laser described in Section 5.4. The experimentally measured tuning coefficient and WM-

IM phase values are then compared against the calculated values from the analytical model.

5.6.1 Results for the 1430 nm DFB-MQW Laser

The laser was manufactured by NTT electronics (NEL), Japan (model: NLK1E5GAAA) and has a strained InGaAsP/InP MQW gain (active) region. In order to theoretically model the wavelength modulation characteristics, the laser parameters mentioned in Section 5.4 have to be obtained from the *I-V* characteristics and the *L-I* characteristics. The laser forward junction voltage (V_j) and the series thermal resistance (r_s), were calculated from the *I-V* characteristics shown in Figure 5-7.

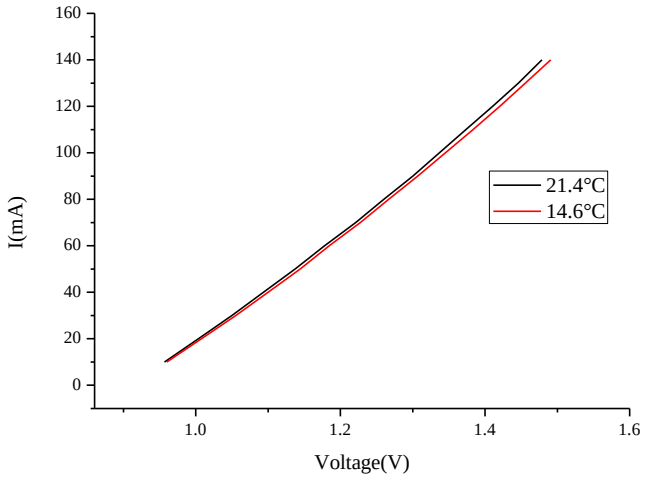

Figure 5-7. Calculation of r_s and V_j from the *I-V* characteristics of the 1430 nm DFB-MQW laser.

Here, the current was measured from the laser diode controller (LDC-202x) and the voltage was measured using a T-piece connector across the bias-T output to the laser. The slope of the *I-V* curve gives the series resistance (r_s) of the laser diode and the forward junction voltage (V_j) is given by the X-intercept. The forward junction voltage and series resistance of the DFB laser were calculated as, V_j = 0.93 V and $r_s = 4\ \Omega$, respectively.

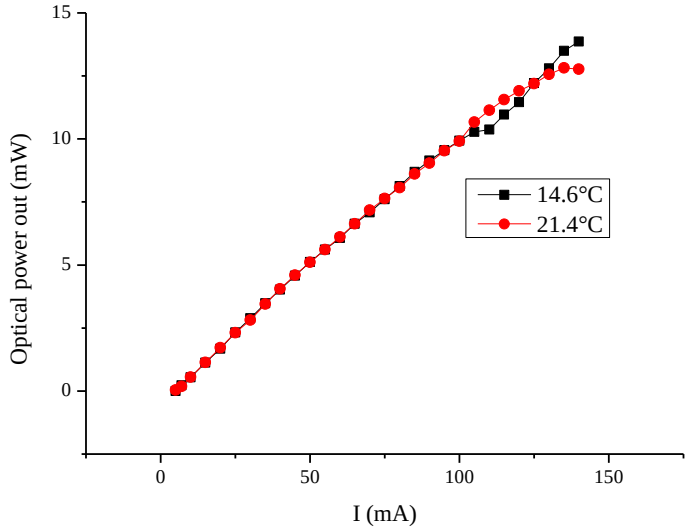

Figure 5-8. *L-I* (power-current) curve for the 1430 nm DFB laser. The quantum efficiency (η) is calculated from the slope as 0.1 W/A.

Figure 5-8 shows the *L-I* characteristics of the DFB laser, the slope of the graph gives the quantum efficiency as η = 0.1 W/A.

The DC (static) thermal tuning ($\Delta\lambda/\Delta T$) is calculated from the direct wavelength scan (using the wavelength referencing technique described in Section 4.6.1) at two different temperatures as shown in Figure 5-9. Its value is found to be 0.11 nm/ ° C.

The carrier induced WM amplitude (C_f) has been approximated as 0.05 GHz/mA from the high modulation frequency tuning coefficient values shown in Figure 5-10, as the thermal effect is negligible at high modulation frequencies (~ 1 MHz). The thermal resistance, R_T is calculated as 36 °C/W from the fit of one of the direct wavelength scans in Figure 5-9 using equation (5.45), with known values of V_j, r_s, η, $\Delta\lambda/\Delta T$ and C_f. A MATLAB code was written to model the amplitude and phase response of the WM. Comparison of the model and experimental results are shown in Figures 5-10 to 5-13. Figure 5-10 shows the tuning coefficient (GHz/mA) measured at different modulation frequencies for a constant bias current of 70 mA. The theoretically calculated tuning coefficient values are also shown, using the improved three layer thermal model (equation (5.66)).

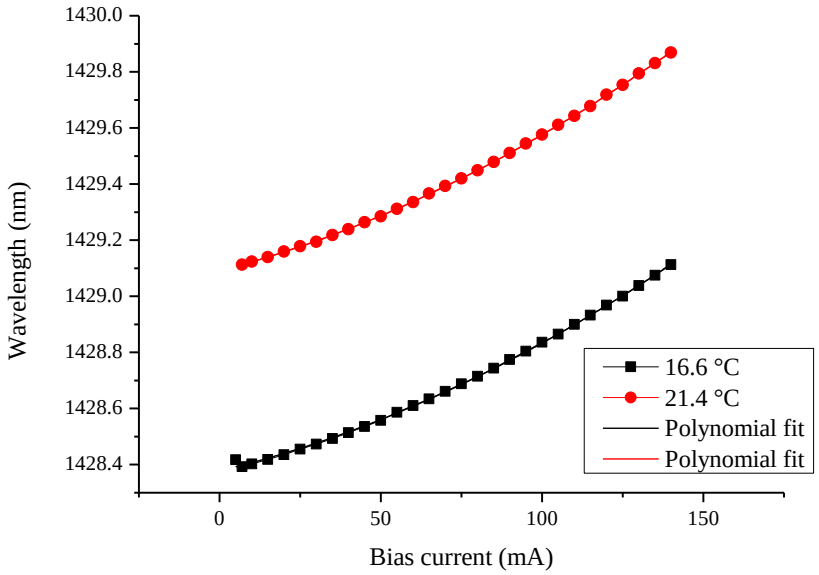

Figure 5-9. Wavelength measured as a function of the applied bias current for the 1430 nm DFB-MQW laser by wavelength referencing to a known absorption line.

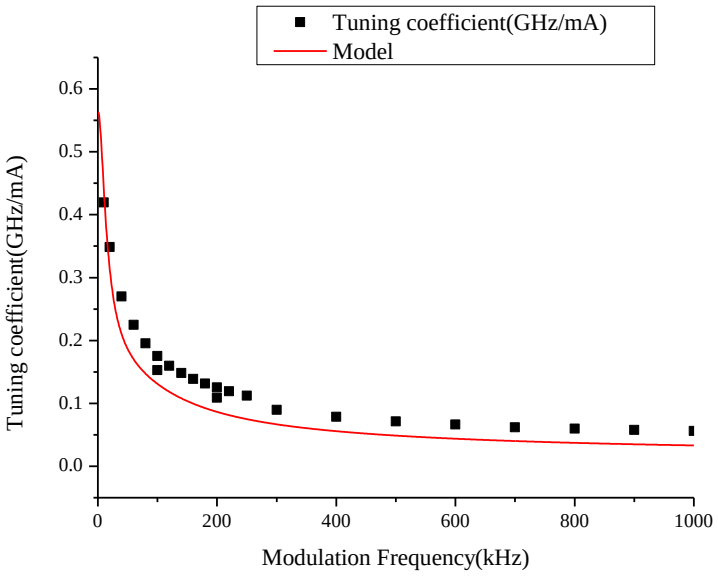

Figure 5-10. Tuning coefficient of the 1430 nm DFB-MQW laser plotted as a function of the applied current modulation frequency, comparison of experiment and theory (equation 5.66).

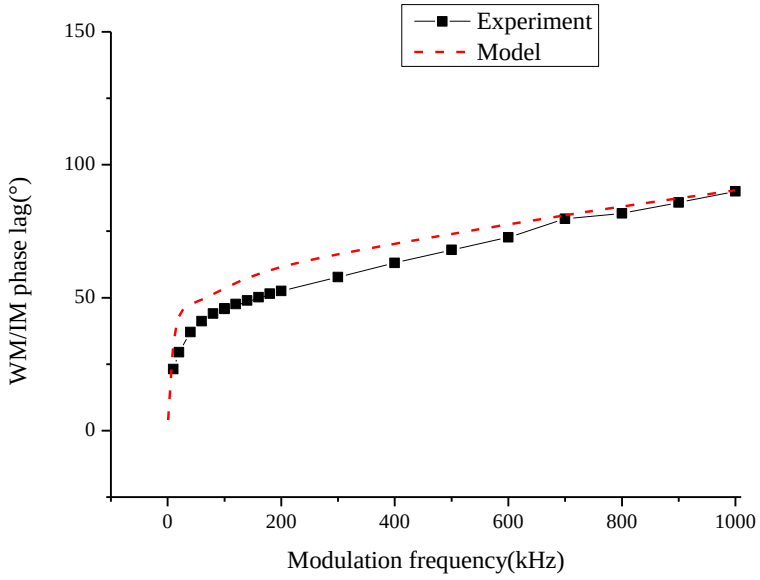

Figure 5-11. WM-IM phase lag of the 1430 nm DFB-MQW laser as a function of modulation frequency, comparison of experiment and theory (equation 5.66). It can be observed that the phase approaches an angle close to 90 °. This is because the thermal effect is more prominent for this laser.

The theoretical value of WM-IM phase lag is calculated from the argument of the complex number given by equation (5.66). Figure 5-11 shows these values compared against the experimentally measured WM-IM phase values, as a function of the applied current modulation frequency, at a given bias current level.

In Figure 5-12, the measured and the theoretically calculated tuning coefficient is plotted as a function of bias current. It can be seen that there is a significant variation in tuning coefficient across the current scan for this particular DFB laser.

Similarly, Figure 5-13 shows the measured and theoretically predicted WM-IM phase values across the current scan. It is observed that the WM-IM phase is nearly a constant across the current scan. These characteristics affect the signal recovery and analysis using the calibration-free models for WMS (Chapter 3).

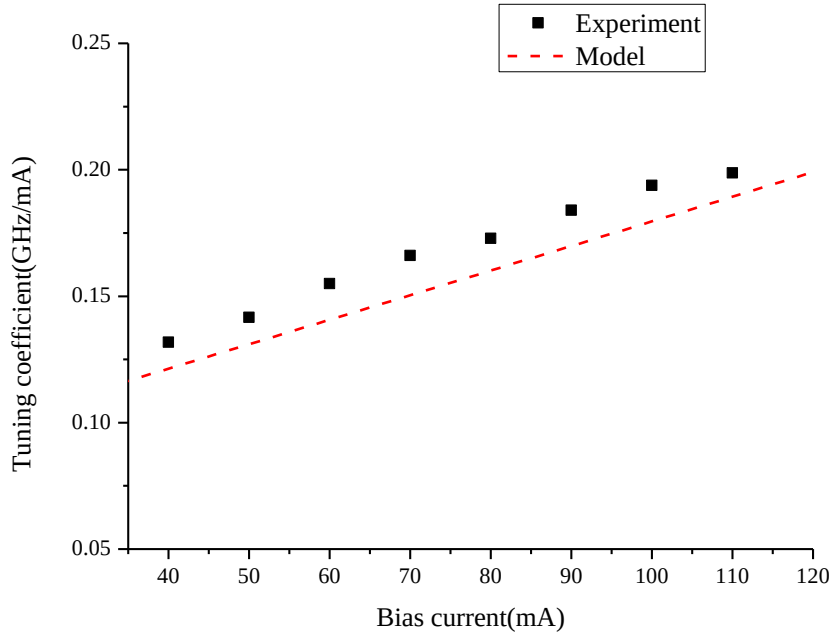

Figure 5-12. Tuning coefficient plotted as a function of bias current for the 1430 nm DFB-MQW laser at a modulation frequency of 100 kHz.

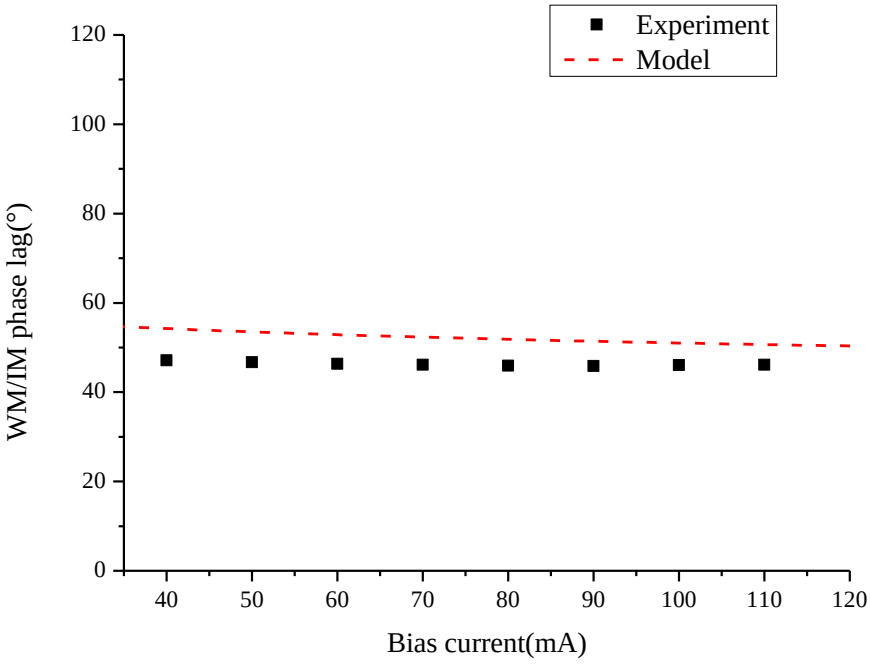

Figure 5-13. WM-IM phase lag as a function of bias current for the 1430 nm DFB-MQW laser at a given current modulation frequency (100 kHz).

From these results the important conclusions are as follows:

a. Due to the small carrier effects, the dynamic wavelength tuning amplitude showed an initial gradual decrease with the applied current modulation frequency, and thereafter was observed to be almost a constant at modulation frequencies in the hundreds of kHz.
b. The WM-IM phase does not approach the 180° phase angle because the thermal component having a higher magnitude compared to the carrier induced WM, approaches a phase angle close to 45°, instead of 90° as predicted by the RC thermal equivalent model described in Section 5.3. So the improved thermal equivalent model predicts the WM characteristics accurately.
c. The qualitative model predicts the change in WM amplitude and phase across the current scan within a reasonable level of accuracy. This could be owing to the carrier effects being negligible and the WM response for this laser attributed primarily by the thermal effects.

5.6.2 Results for the 1997 nm DFB-MQW Laser

The 1997 nm DFB-MQW laser was used for vast majority of the work outlined in this thesis (Sections 5.7, 5.8, 5.9 and the whole of Chapter 6). The structure of the 1997 nm DFB-MQW (Eblana Photonics) laser is shown in Figure 5-14 [81].

The active region of this DFB laser consists of three 8 nm thick quantum wells and four 15 nm thick barrier layers, sandwiched between two 250 nm confinement regions.

The top buffer layer is a 2 μm thick layer of *p*-InP and the bottom substrate is a 117 μm thick layer of *n*-InP. A 3 μm wide ridge of 600 μm in length forms the wave-guiding region. The grating structure (1.8 μm) is etched on top of the active region and occupies most of the buffer layer.

The 2D thermal resistance R_T is calculated as $40\ °\mathrm{C/W}$ using equation (5.67) (d_s is 117 μm and d_w is 3 μm, ℓ is 600 μm and thermal conductivity (K) for InP is 0.68 W/cm °K).

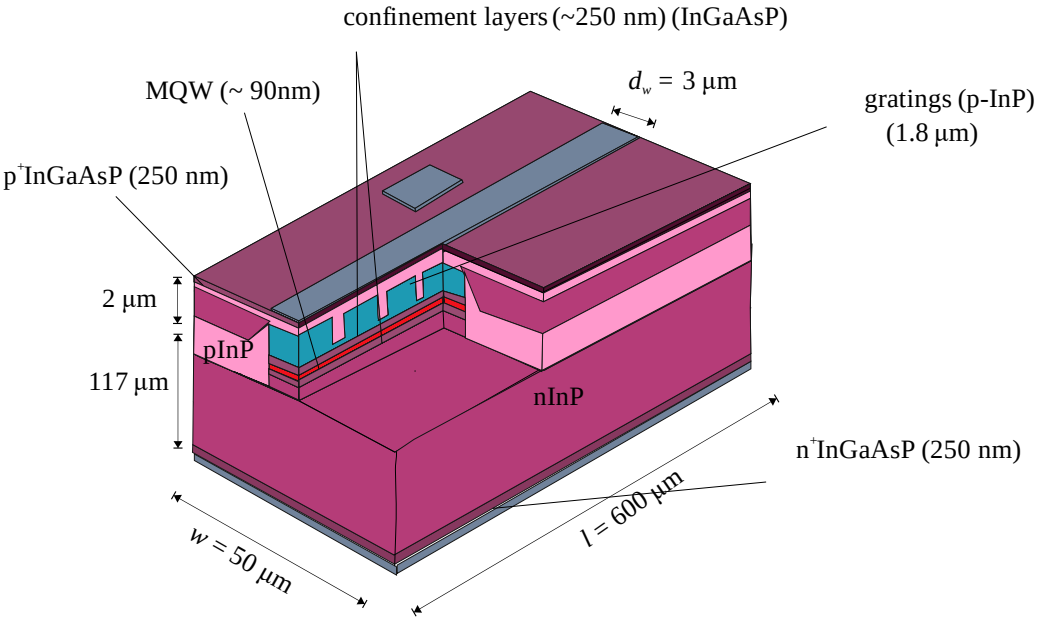

Figure 5-14. Structure of the of the 1997 nm DFB-MQW laser (not drawn to scale).

As for the 1430 nm laser, the optical slope efficiency is measured from the *L-I* characteristics (Figure 5-15) as 0.046 W/A for $T = 20$ °C. The series resistance and the forward junction voltage are calculated from the *I-V* characteristics (Figure 5-16) as $r_s = 5.3\ \Omega$ and $V_j = 0.76$ V, respectively.

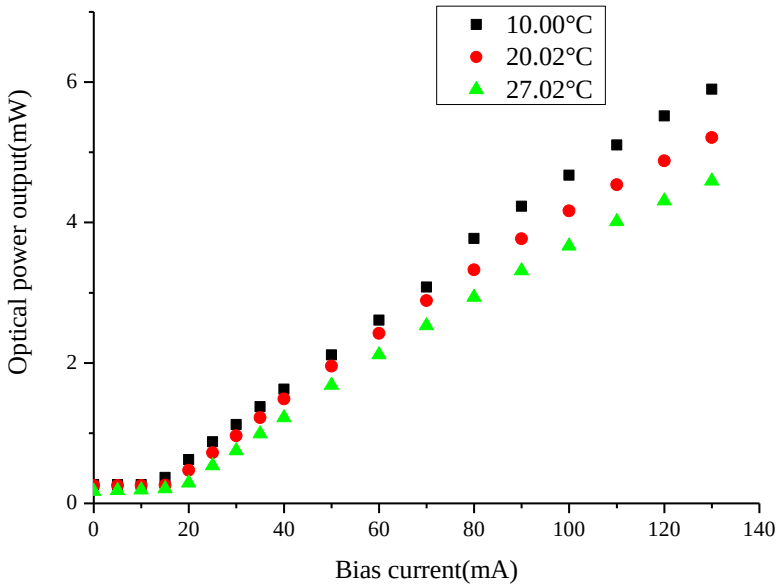

Figure 5-15. *L-I* characteristics of the 1997 nm DFB-MQW laser.

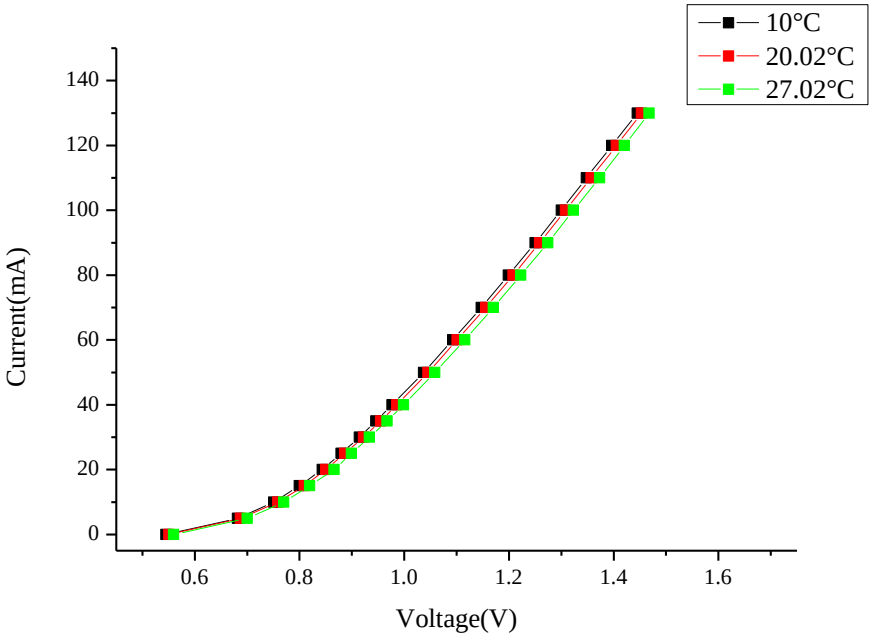

Figure 5-16. *I-V* characteristics of the 1997 nm DFB-MQW laser at diode temperatures of 10 °C, 20 °C and 27 °C.

The DC thermal wavelength tuning ($\Delta\lambda/\Delta T$) is calculated as 0.11 nm/°C (Figure 5-17). The carrier induced WM amplitude is estimated as ~ 0.27 GHz/mA from the WM amplitude response at high modulation frequencies (Figure 5-18). The high value of carrier induced WM amplitude could be due to increased carrier confinement for this laser.

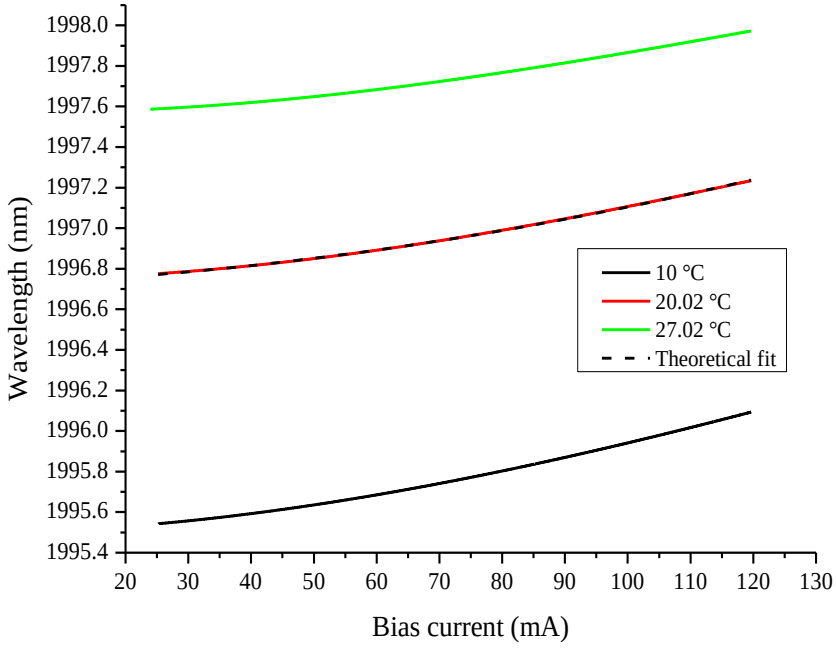

Figure 5-17. DC wavelength scan at various temperatures using the 1997 nm DFB-MQW laser at diode temperatures of 10 ° C, 20 ° C and 27 ° C. Theoretical fit to the DC wavelength scan can be used to determine the thermal resistance (R_T).

The contribution to WM from the thermal effect (at zero modulation frequency), H_0 , is calculated as 0.6 GHz/mA. The thermal cut-off frequencies for the substrate, the buffer and the active layers are calculated as $\omega_{cs} = 70$ kHz, $\omega_{cb} = 5$ kHz and $\omega_{ca} = 1$ MHz, respectively. Applying these values to equation (5.66), the amplitude and phase response of wavelength modulation are calculated.

Figures 5-18 and 5-19 show the experimentally measured tuning coefficient and the WM-IM phase lag for the 1997 nm DFB-MQW laser diode as a function of modulation frequency at a bias current of 70 mA and diode temperature of 21.74 °C. A similar behaviour was observed for similar multi-quantum well laser structures as mentioned in literature [71, 72, 79, 83]. For measurement of the WM parameters below a modulation frequency of 100 kHz, a summing amplifier was used prior to the current controller (LDC 202B), having a low pass filter response (with a cut-off frequency of 250 kHz). For measurements above the 100 kHz modulation frequency the bias-T is used due to its

flat amplitude response above 100 kHz. The theoretically calculated WM-IM phase and tuning coefficient values using the thermal heat conduction model (equation (5.66)) are also shown.

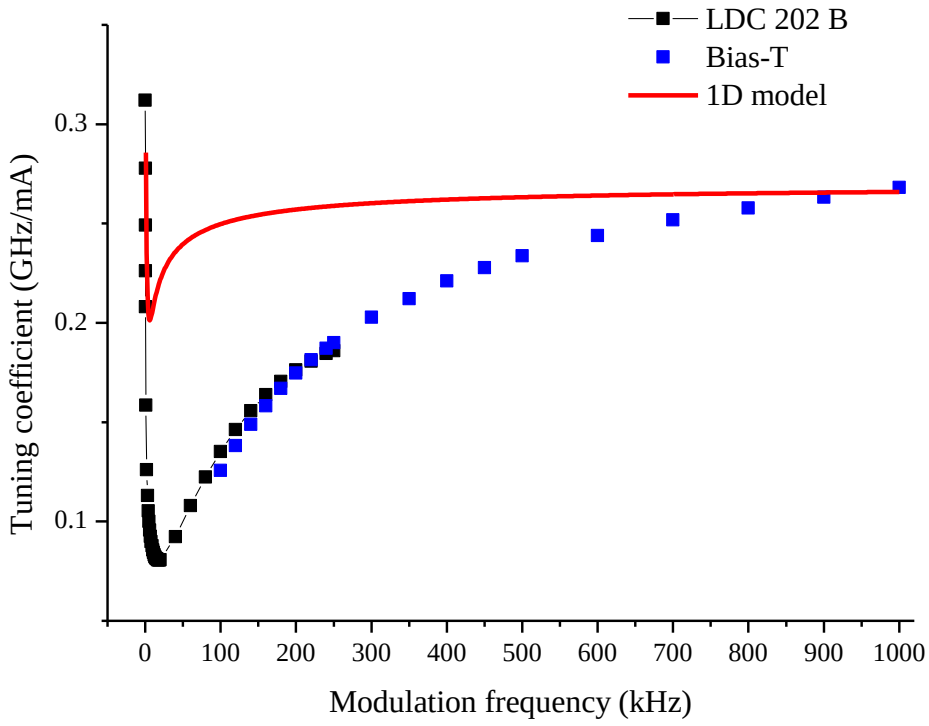

Figure 5-18. Measured tuning coefficient values vs. the frequency of the applied current modulation, compared against the values calculated using the analytical model (red curve) for the 1997 nm DFB-MQW laser.

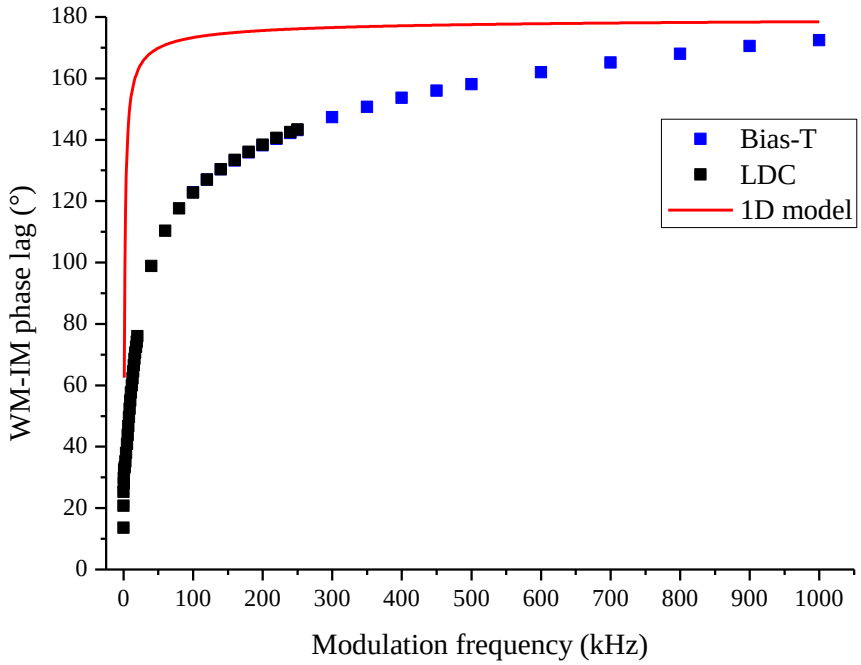

Figure 5-19. WM-IM phase values measured as a function of the frequency of the applied current modulation compared with the theoretical values predicted by the model (red curve) for the 1997 nm DFB-MQW laser.

The following important observations are made:

a. The wavelength modulation amplitude initially decreases with the applied modulation frequency, reaching a minimum value around 6 kHz, thereafter, it increases steadily, saturating at high modulation frequencies. Consequently, a characteristic dip is observed in the WM amplitude vs. modulation frequency curve.

b. The WM-IM phase lag now approaches 180° at high modulation frequencies.

These characteristics are explained using the phasor diagrams shown in Figure 5-20. The amplitudes and phases of thermal and carrier contributions to WM are shown, for three characteristic modulation frequencies of 1 kHz, 6 kHz and 50 kHz, respectively.

The 6 kHz modulation frequency corresponds to the characteristic dip and 1 kHz and 50 kHz are the two modulation frequencies selected on either side of the characteristic dip.

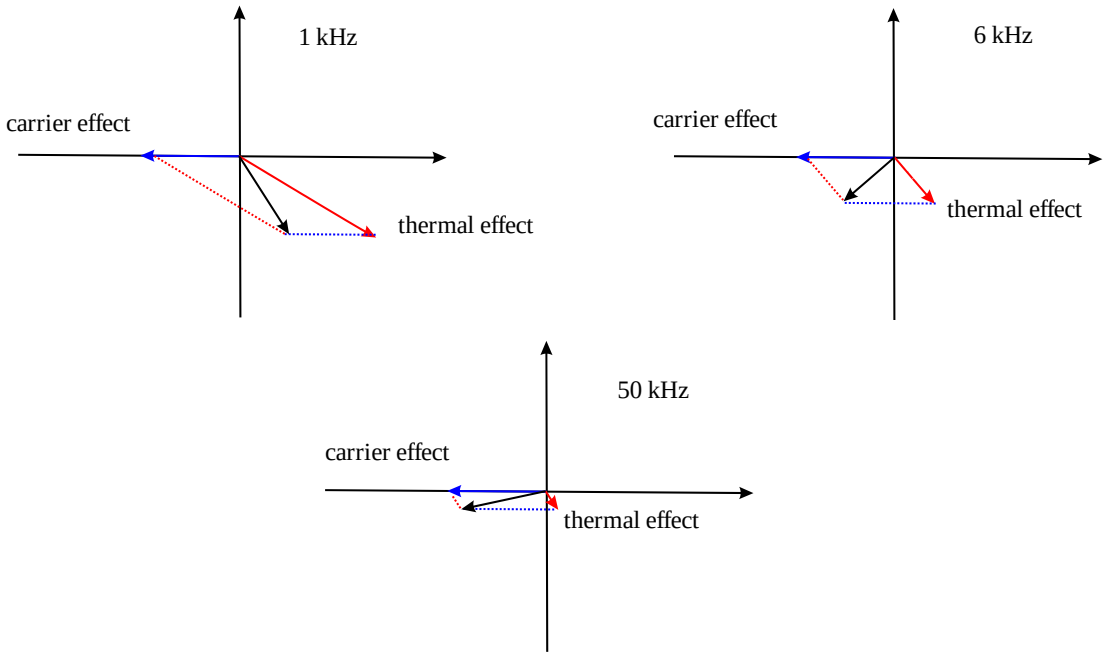

Figure 5-20. Phasor diagrams representing the amplitude and phase of wavelength modulation at three distinct modulation frequencies.

At a modulation frequency of 1 kHz the contribution to WM from the thermal effects is larger than the contribution from the carrier effects. Thereafter, the resultant WM decreases in magnitude due to the reduced thermal WM. A minimum (dip) of WM curve occurs at 6 kHz because the phase of the thermal effect goes to nearly 45 ° and the magnitude of the thermal effect decreases. At 50 kHz, the thermal effect is only one-fifth of the carrier effect, however, the phase does not change significantly. Hence, the net wavelength modulation amplitude starts to increase and the net phase of WM approaches 180 °, closer to the WM component from carrier effects.

The thermal tuning at zero modulation frequency is calculated as $H_0 = 2.25C_f$. From the RC thermal model, since $H_0 > 2C_f$, the tuning coefficient should decrease with increasing modulation frequency. Even though this is initially the case, as the thermal

WM slowly approaches 45 ° its magnitude drops, and hence the thermal effect reduces resulting in the condition $H_0 > 2C_f$, and consequently the WM amplitude increases.

Figures 5-18 and 5-19, show that the theoretical model fails to accurately calculate the phase and amplitude of wavelength modulation because of the shortcomings of the model outlined in Section 5.5, especially since the contribution from spatial hole burning effects have been neglected in this analysis [61, 66, 67]. However, the thermal model is successful in identifying the important features and trends in laser WM characteristics useful for WMS applications.

For theoretical modelling of experimental WMS signals, it is desirable to have only a small variation in the wavelength modulation amplitude and WM-IM phase lag across the laser current scan. From the thermal heat conduction model, it is possible to predict the laser operating conditions and design considerations for this. For instance, by tailoring a laser to have a small ohmic resistance, it should in principle, be possible to reduce the variation in tuning coefficient and WM-IM phase lag across the laser scan.

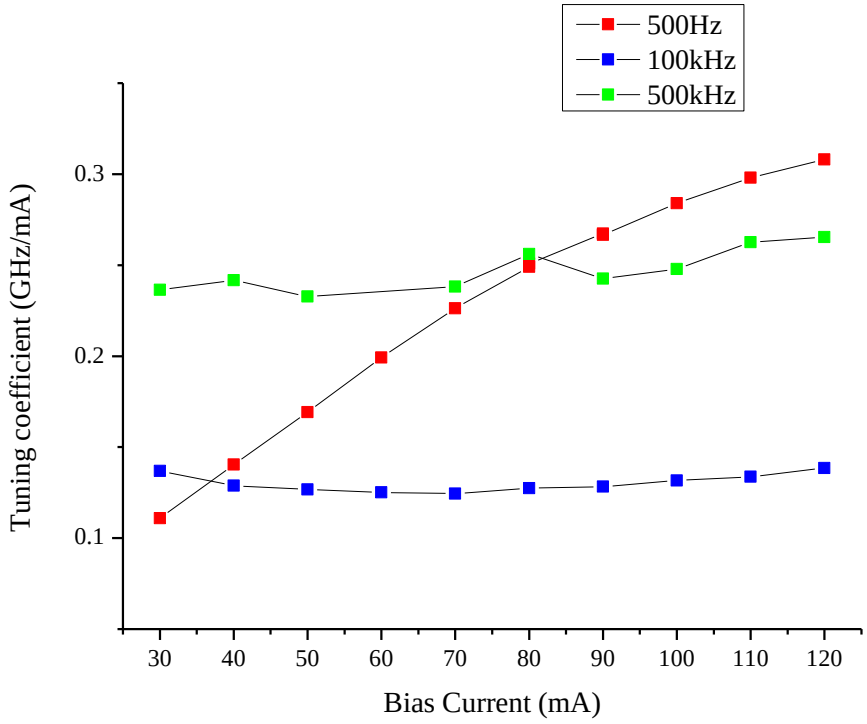

Figure 5-21. The tuning coefficient measured across the current scan for the 1997 nm DFB-MQW laser at modulation frequencies of 500 Hz, 100 kHz and 500 kHz.

Figure 5-23 shows the measured variation in tuning coefficient and WM-IM phase lag across the laser scan for a diode temperature of 21.4 °C, at modulation frequencies of 500 Hz, 100 kHz and 500 kHz, which belong to the low, medium and high modulation frequency regimes for wavelength modulation spectroscopy. Also, Figures 5-23 and 5-24 show the theoretical predictions using the thermal model assuming these DFB laser operating conditions. Figures 5-21 to 5-24 show that the theoretical model for wavelength modulation described in this work successfully predicts the important trends in the wavelength modulation characteristics for the 1997 nm DFB-MQW laser. It can be understood from the model that, in order to work with WMS signals having a smaller measured variation in tuning coefficient across the current scan range, it is desirable to operate at higher modulation frequencies (several hundreds of kHz).

Similarly, Figures 5-23 and 5-24 provide the experimentally measured and theoretically modelled WM-IM phase lag across the current scan at the three modulation frequency regimes. Once more, it is instinctive to operate at very low or very high modulation frequencies to obtain significantly smaller variation in WM-IM phase across the current scan range for the WMS signal.

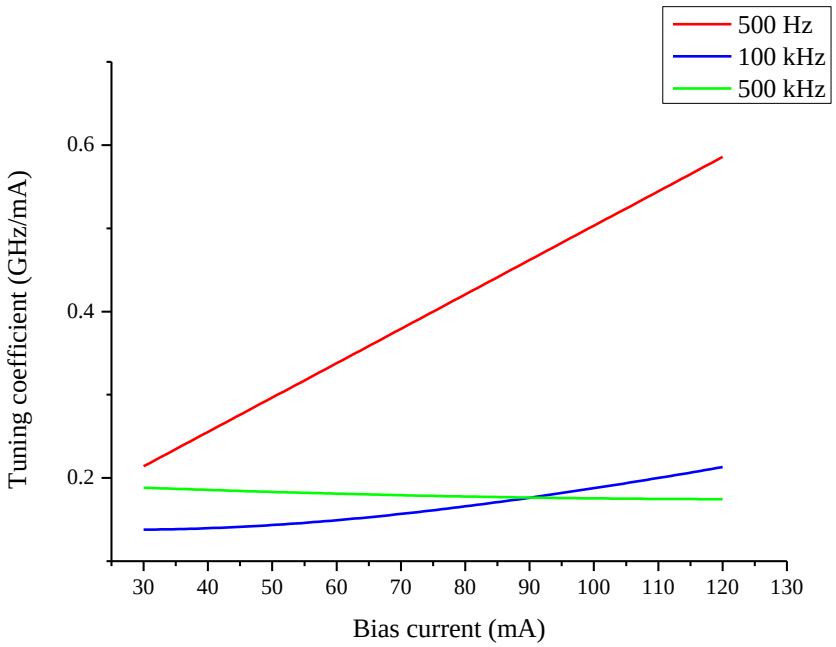

Figure 5-22. Graph of the tuning coefficient vs. bias current predicted by the thermal model for the 1997 nm DFB-MQW laser.

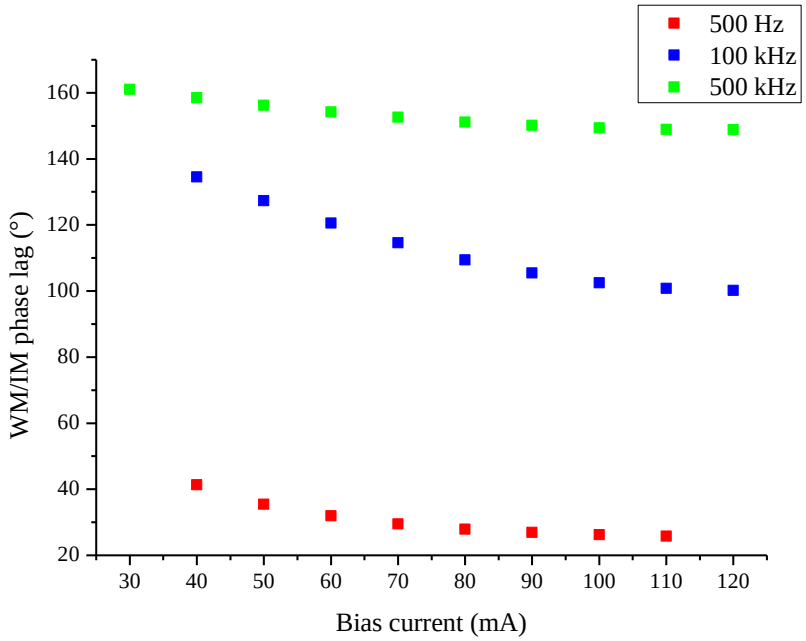

Figure 5-23. Graph provides the measured WM-IM phase lag vs. bias current for the 1997 nm DFB-MQW laser at the three distinctive modulation frequency regimes of WMS.

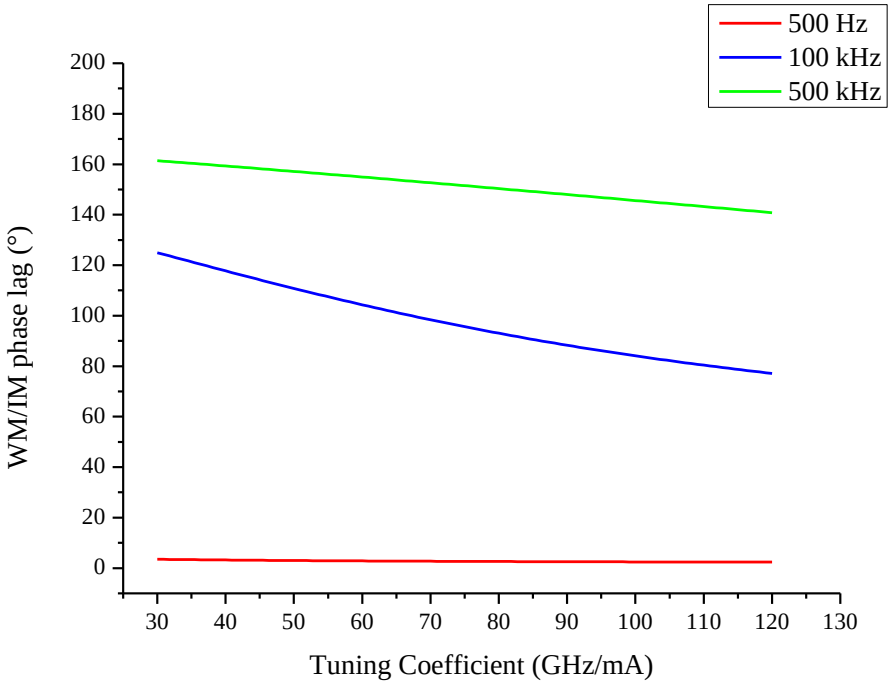

Figure 5-24. WM-IM phase lag vs. bias current for the 1997 nm DFB-MQW laser predicted by the thermal model for the three distinctive modulation frequencies.

This case is furthered by Figure 5-25, which shows the experimentally measured WM-IM phase lag as a function of the applied modulation frequency at different bias currents across the entire current scan range.

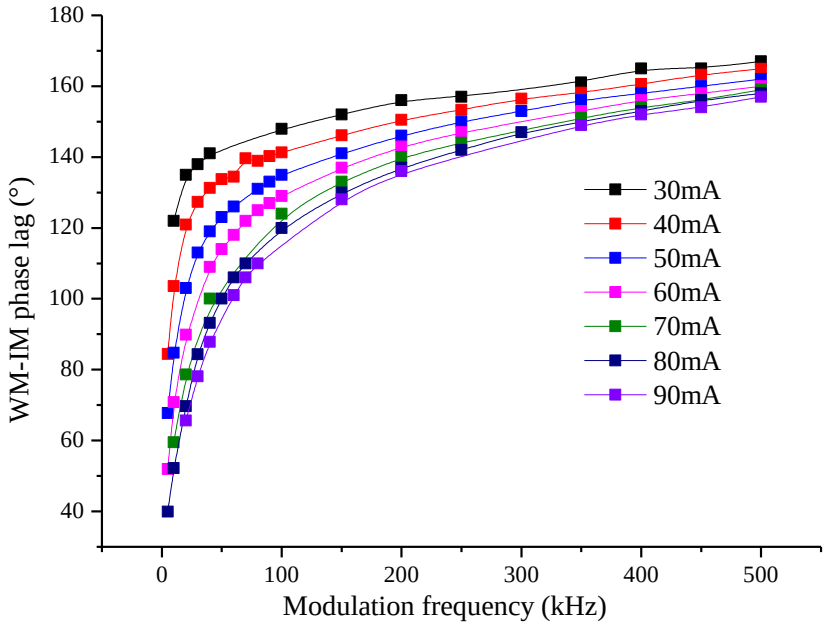

Figure 5-25. Measured WM-IM phase lag as a function of modulation frequency at different bias currents for the 1997 nm DFB-MQW laser, at a laser diode temperature of 21.4 °C.

It is observed that the variation in the WM-IM phase across the current scan range is small at very low and very large modulation frequencies. Figure 5-26 shows the theoretically predicted WM-IM phase lag as a function of the applied current modulation frequency at different bias currents. It can be observed that the theoretical values successfully estimate the trends observed in the experimental data.

In conclusion, from this study on the WM characteristics for the 1997 nm DFB-MQW laser using the theoretical model, supported by the experimental results, it was considered advantageous to measure the WMS signals at higher modulation frequencies due to a relatively smaller variation in wavelength modulation amplitude across the current scan. This is intuitive as the thermal effect is small at higher modulation frequencies (assuming that the carrier effect is independent of the bias current).

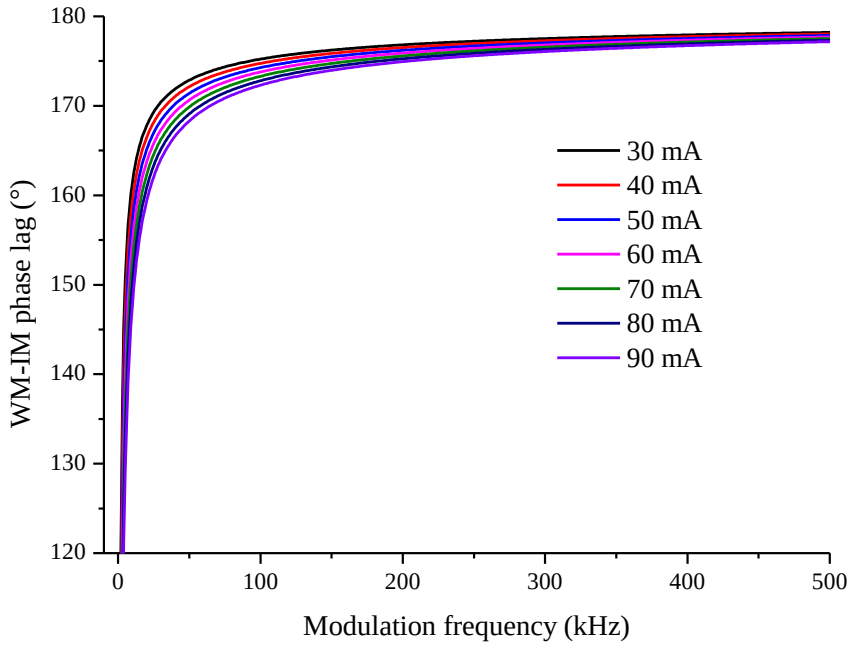

Figure 5-26. Graph shows the theoretically predicted WM-IM phase lag as a function of the current modulation frequency for various bias current values.

It was observed in the initial experiments that a variation in WM parameters across the current scan, such as the WM-IM phase lag, distorted the recovered absorption line shape using the *1f*-WMS techniques such as the PDM or the RAM technique. This reduced the accuracy of the concentration and temperature values measured from the least-squares curve fit of the recovered absorption line shape. Hence, it was considered necessary to account for the effects of these laser modulation parameters on the recovered gas absorption line shape.

5.7 Effect of the Wavelength Modulation Parameters in the Recovery of Gas Absorption Line Shapes

The effects of the DFB laser WM parameters in the recovery of absolute gas absorption line shape using the first harmonic (*1f*) detection techniques (discussed in Section 3.5) such as the PDM or the RAM technique will be discussed in this section, followed by procedures to compensate for these effects.

In the earlier measurements using these *1f* detection techniques [34, 35] the variation of WM-IM phase and tuning coefficient across the current scan was assumed to be insignificant. Hence, the laser WM parameters were measured only at the line centre. Figure 5-27 shows the measured variation in the WM-IM phase lag across the current scan for the 1997 nm DFB-MQW laser, at different diode temperatures. It is noticed that for this DFB laser, there is a significant variation of WM-IM phase lag across the current scan (referred to as the "WM-IM phase walk-off") that affects the recovery of the gas absorption line shape.

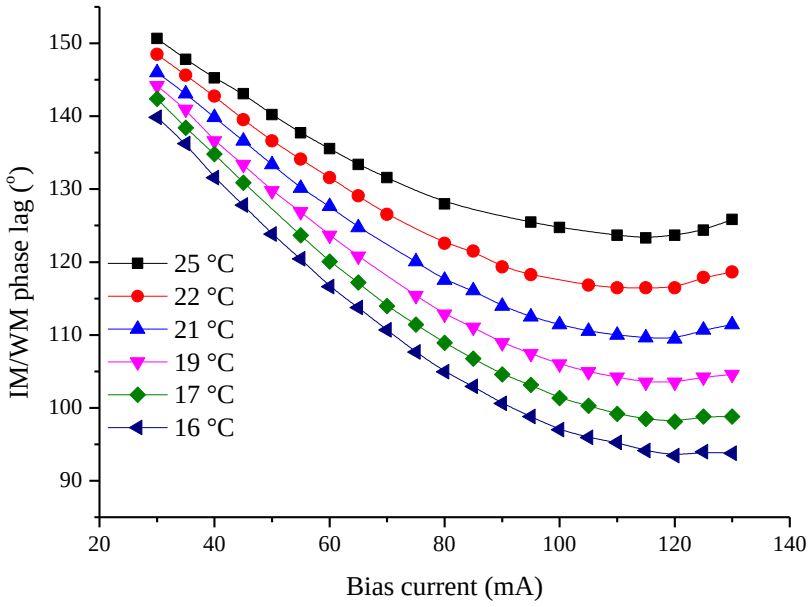

Figure 5-27. WM-IM phase lag measured across the DFB laser current scan range for different diode temperatures at a current modulation frequency of 100 kHz for the 1997 nm DFB-MQW laser.

It can be observed from Figure 5-27 that the variation in WM-IM phase across a current scan range of 30 mA to 120 mA is ~ 22 ° for a diode temperature of 25 °C , while it increases to almost twice the value (~ 45 °) for a cooler diode at a temperature of 16 °C. The theoretical model does not predict this behaviour. One of the reasons for this could be due to the radiative heat loss which was ignored in the model [84]. Radiative heat loss increases with the fourth power of temperature, therefore, at a higher temperature, increased convective heat loss occurs from the laser surface, and consequently the

temperature effect is reduced at higher temperatures resulting in a smaller variation of the WM-IM phase lag across the current scan. Another proposed reason could be the temperature dependence of thermal resistance.

5.8 Correction for WM-IM Phase Walk-off

Figure 5-27 shows that a significant WM-IM phase walk-off across the current scan range was measured for the 1997 nm DFB-MQW laser due to the strong thermal contribution to WM. The measured variation in tuning coefficient across the current scan range was found to be less than 5 %, and hence is not treated in this analysis. For lasers with similar characteristics to the 1430 nm DFB-MQW laser, the variation in tuning coefficient is significant across the current scan. This results in a varying modulation index across the current scan and a varying correction factor has to be applied [34].

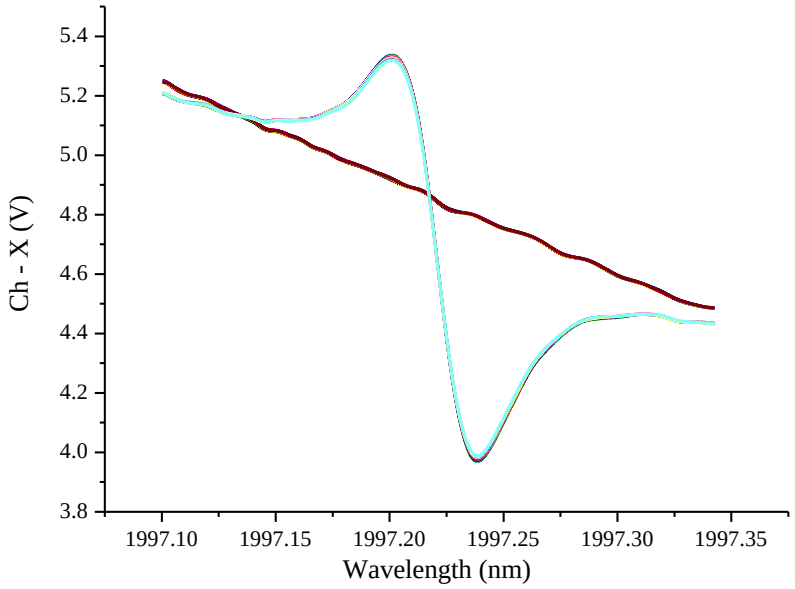

Figure 5-28. The LIA X-channel gas and no-gas measurements for the PDM method with the X-channel gas signals containing the RAM signal and a projection of the FM signal. A 200 mV_{p-p} sinusoidal modulation is applied to the DFB laser giving an *m* value of 0.084 for CO_2 gas, at a temperature of 22 °C and pressure near atmospheric.

For the PDM or RAM techniques, it is required that the entire RAM or the entire FM signal is isolated on one of the orthogonal channels of the LIA. In the PDM, the entire RAM signal is isolated to the X-channel of the LIA, while the Y-channel will contain a pure FM projection. This signal configuration is achieved by obtaining a FM signal with the non-absorbing wings going to zero on the Y-channel output of the LIA. Due to the variation in WM-IM phase across the current scan, it was not possible to obtain a pure FM projection on the Y-channel with the non-absorbing wings lying on zero. For the CO_2 absorption lines, the absence of a non-absorbing baseline complicates the matter further. Hence, several measurements were taken at 0.2° LIA separation, close to the zero baseline on the Y-channel, whereby, a FM signal with a small RAM projection is obtained as shown in Figure 5-29. Figure 5-28 shows the LIA X-channel for these measurements, the signals containing the orthogonal projection of the FM signal and majority of the RAM signal.

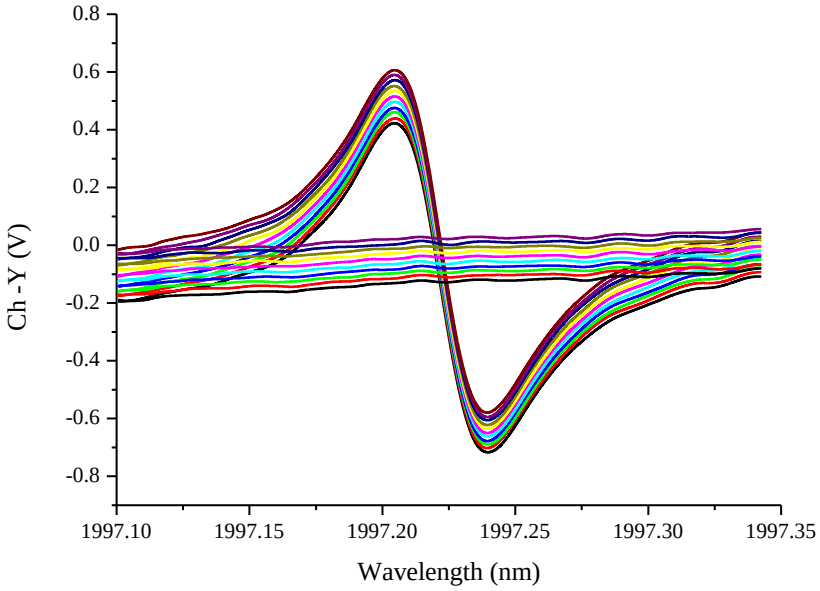

Figure 5-29. Graph showing measurements taken close to the lock-in reference angle which corresponds to a phase arrangement for obtaining a pure FM/WM signal projection on the Y-channel of the LIA. It was not possible to obtain a FM signal with the non-absorbing wings going to zero because of the significant variation in WM-IM phase across the current scan and the absence of a zero-absorption baseline for the CO_2 gas at atmospheric pressure. The corresponding no-gas signals are also shown, which are very small projections of the RAM signal.

The no-gas signals acquired at a 0.2 ° separation are also shown in these two figures which are nothing but small projections of the IM signal with the X-channel containing majority of the IM signal. The sloping background for the no-gas RAM signals indicates that it is not a constant and is of varying phase across the current scan. This is further confirmed during the measurements taken for the linear IM characterisation as mentioned in Section 4.7.2.

Applying the PDM (equation 3.13), with the measured WM-IM phase angle applied at each λ-point across the current scan, to the gas and the no-gas signals, and dividing one by the other gives the recovered gas absorption line shape signals as shown in Figure 5-30. It can be observed that the FM signal is not completely cancelled for all the measurements. The recovered line shape with no FM signal contribution has been identified as the one for which the absorption depth is minimal between the line centre absorption and baseline.

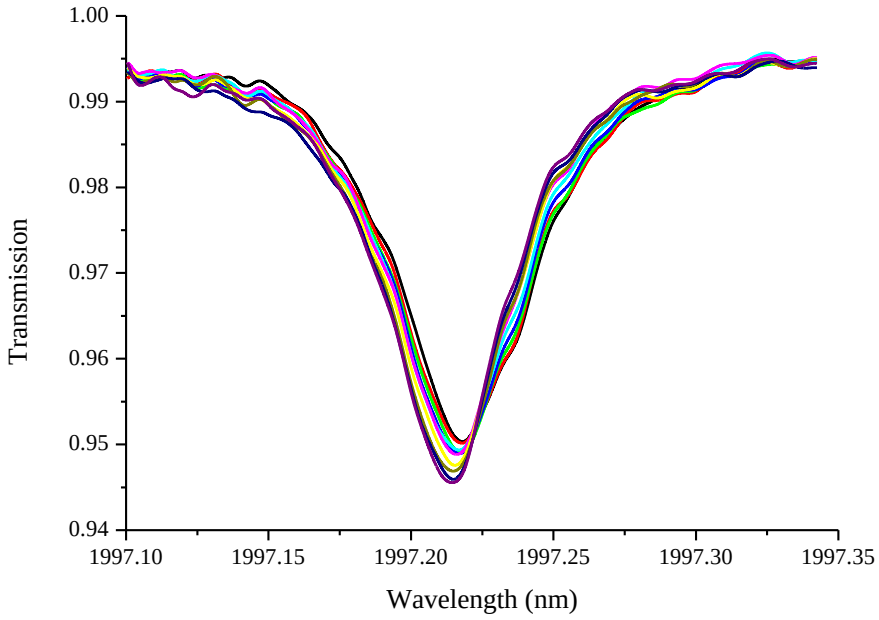

Figure 5-30. The recovered absorption line shapes using the PDM applied to the measurements taken with a 0.2° angle separation of the lock-in amplifier reference signal (shown in Figures 5-28 and 5-29).

The effect of WM-IM phase variation is more pronounced when a larger current scan was used, encompassing two nearby absorbing features. Figures 5-31 (a)-(d) show the

experimentally measured signals for a larger current scan encompassing two nearby absorption lines using the phasor decomposition method.

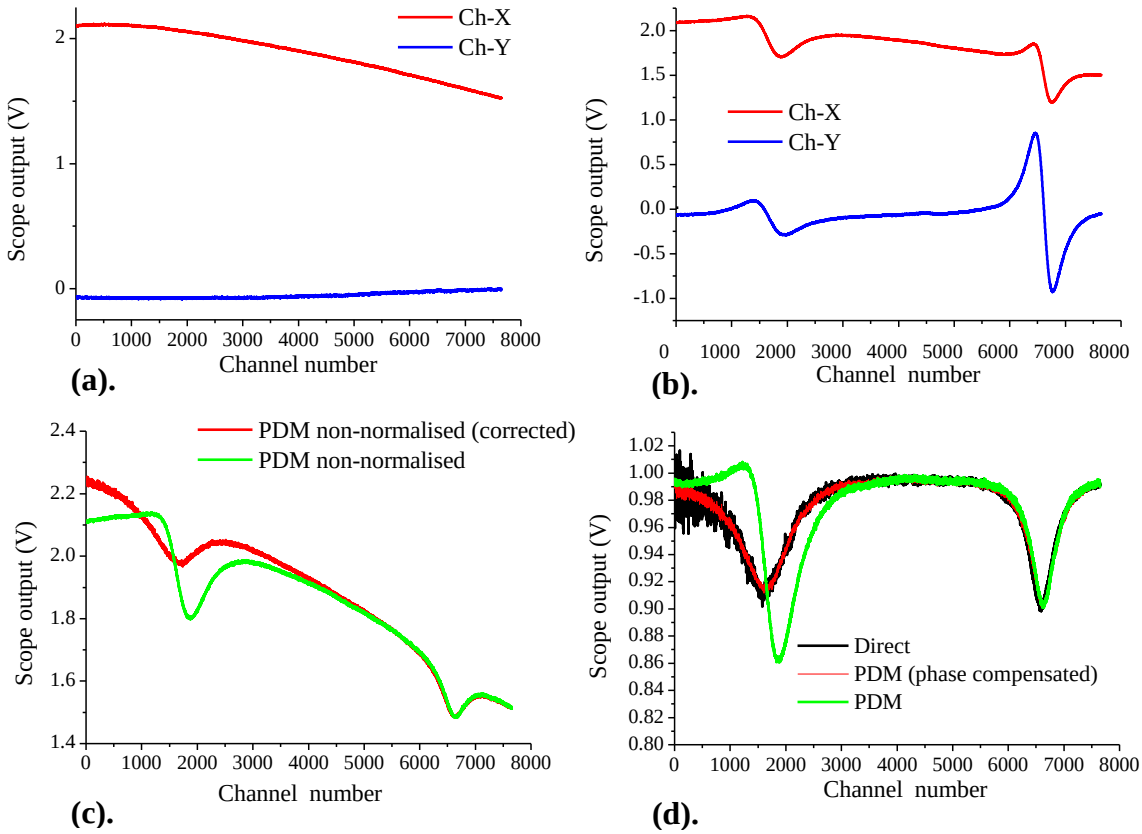

Figure 5-31. PDM method using 100 % CO_2 at a pressure of 1 bar using a 1997 nm DFB-MQW laser. (a)The background RAM signal on the X and Y LIA channels. (b) The Y lock-in amplifier channel contains a projection of the WM gas signal, while the X lock-in amplifier channel contain its orthogonal projection as well as the entire RAM signal. (c) Shows the recovered gas line shape using the PDM method with the phase correction applied (red curve) and not applied (green curve). (d) Shows the recovered gas signals normalised with the background RAM signals compared against the direct gas absorption signal (black curve).

Figures 5-31 (a) and (b) show the measured X and Y channel LIA no-gas and gas signals. The absence of a non-absorbing baseline on the FM signal isolated on the Y-channel was observed (Figure 5-31 (b)). Figure 5-31 (c) shows the PDM signals which are not background normalised, with the correction for phase walk-off applied (red curve) and not applied (green curve), respectively. Incomplete cancellation of the *1f* line shape component is observed when the correction for the phase walk-off is not applied.

Figure 5-31(d) shows the normalised corrected and uncorrected line shapes compared to direct gas absorption signal taken immediately so as not to change the gas conditions.

Another way to isolate a pure RAM signal would have been to use the no-gas measurements and changing the LIA phase to obtain a zero baseline signal on the Y-channel. The X-channel now contains the entire IM signal. For the 1997 nm DFB-MQW laser under test, the amplitude and phase of the "absolute" IM signal was also observed to change across the current scan range, which made this difficult. This is indicated by the sloping no-gas signal on the X and Y channels of the LIA. The "absolute" WM and IM phases were measured with respect to the phase of the applied AC injection current.

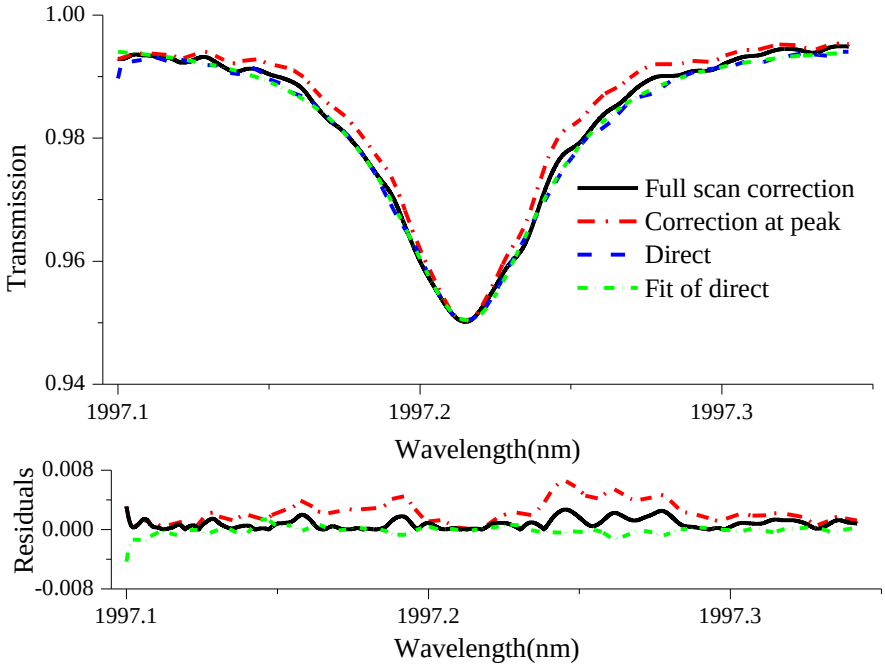

Figure 5-32. The effect of phase walk-off for a single CO_2 absorption line recovered using the PDM. C = 100 %, T = 22 °C, P = 1.013 bar and m = 0.08.

Figure 5-32 shows the recovered gas absorption line shape using PDM, for the R48 absorption line of CO_2 at 1997.2 nm, with the WM-IM phase correction applied only at the line centre (red curve) and the phase correction applied for the entire current scan (black curve). As observed, taking into account the phase walk-off improved the accuracy of the recovered absorption profile, particularly the line width. A least-squares

fitting algorithm (green curve) was used to obtain concentration and temperature values by comparing the corrected and uncorrected PDM signals to a theoretical model. Concentration and temperature measurements of C = 102 % and T = 21.35 °C for the corrected signal, and C = 67.8 % and T = 67.4 °C for the uncorrected signal were calculated, highlighting the importance of taking into account the modulation characteristics of the optical source used in TDLS-WMS applications.

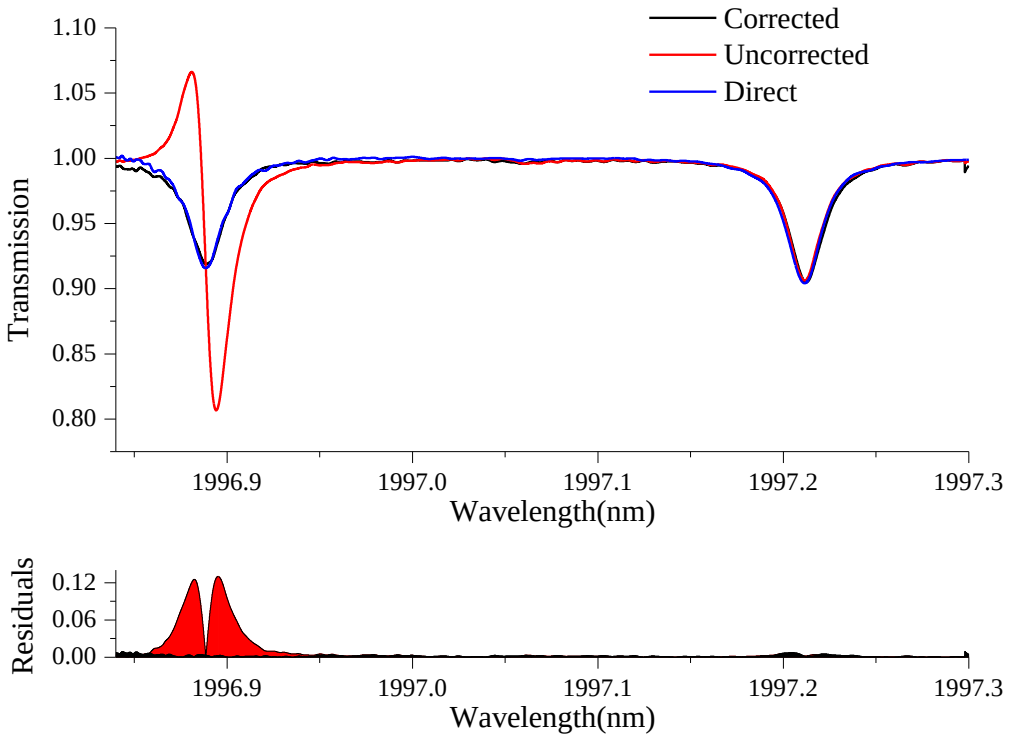

Figure 5-33. Significance of WM-IM phase correction for a larger laser current (wavelength) scan range to span two nearby absorption features. The two absorption features are the R50 and R48 transitions of CO_2, at 1996.8 nm and 1997.2 nm, respectively. An incomplete cancellation of the *1f* line shape component signal is observed for the R50 transition of CO_2.

In twin line absorption thermometry (commonly known as ratio thermometry), the ratio of the peak absorbance or integrated absorbance of two gas transitions with a similar pressure and concentration dependence are used to infer the temperature of the target gas [85]. Use of a single laser source in ratio thermometry is advantageous due to the reduced complexity in the transmitter and receiver hardware, compared to using multiple laser sources to access each absorption line. Moreover, using two nearby

transitions that can be accessed by a larger current scan is preferred in ratio thermometry, due to similar behaviour of their spectral parameters with concentration and pressure, so that the temperature can be inferred from the ratio. Thus, in ratio thermometry, it is advantageous to use two nearby absorption features that can be accessed using a wider current scan range applied to the laser source. As the amplitude of the current scan increases, the WM-IM phase variation across the scan also increases (as shown in Figure 5-27), which makes it necessary to account for it.

Figure 5-33 shows the recovered spectra using PDM, with the laser wavelength being scanned across two nearby absorption lines, where the WM-IM phase variation was measured and applied at each bias point (black curve) and the absorption spectrum recovered using the WM-IM phase values measured using the vector method (red curve) described in Section 4.7.3. The modulation frequency is 50 kHz and $m \sim 0.2$.

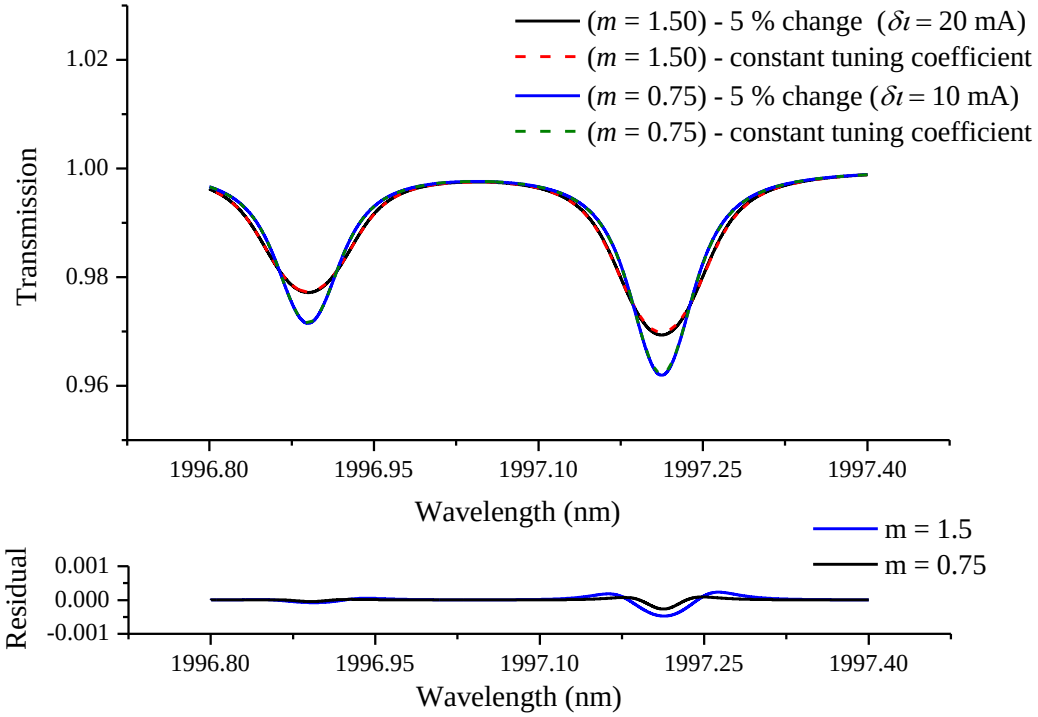

Figure 5-34. Theoretical simulations of the recovered gas absorption signals showing the effect of change in the tuning coefficient across the current scan at different *m* values for the 1997 nm DFB-MQW laser.

It is observed that for the red curve which corresponds to the spectrum with the WM-IM phase values measured at the line centre for the absorption line towards the right of

the spectrum (R48), the *1f* FM component is not completely cancelled using the PDM for the scanned line towards the left end of the spectrum (R50). Applying the measured WM-IM phase values at each bias (λ) point, the recovered absorption line shapes for both lines agree well with the direct measurements with significantly less distortion.

Similar to WM-IM phase lag, the tuning coefficient may vary significantly across the laser current scan range. This causes a variation in the modulation index across the laser scan. The variation in modulation index across the current scan range is approximately 5.2 % for DFB-MQW laser. From modelling, it was found that this variation in the modulation index will become significant only at $m >> 1$ for this laser [60] as shown by the residuals in Figure 5-34.

5.9 Phase Insensitive *1f* Methods

In the PDM, a pure WM/FM signal projection, with no RAM contribution, and hence with the non-absorbing wings going to zero has to be obtained on one of the orthogonal channels of the LIA. On the contrary, in the RAM technique, a projection of a pure RAM absorption signal with no FM contribution has to be obtained on one of the lock-in amplifier channels. These techniques require alignment of the lock-in reference signal phase angle so as to achieve a given orientation of the lock-in amplifier channels/axes with respect to the various *1f* signal components (Sections 3.4-3.5). In situations where the WM-IM phase is varying significantly across the current scan, it would be impossible to isolate the RAM or FM signal to a given lock-in channel, at each point, along the current scan. In the previous section, the absorption line shape was recovered using PDM by using several X and Y channel measurement sets with a small lock-in angle separation (0.02 °), close to the RAM isolation and choosing the measurement set which gives the least contribution from WM when the PDM is applied. This method is inconvenient as it requires multiple measurements sets of the X and Y lock-in amplifier outputs.

Owing to the aforementioned measurement constraints, a computational technique was implemented to extract the absorption line shape using the PDM at an arbitrary lock-in reference angle, with the measured WM-IM phase values applied to each scan point. For an arbitrary orientation (θ_L) of the lock-in amplifier reference signal relative to the first

harmonic signal; the first harmonic detection signal components are depicted in Figure 5-35.

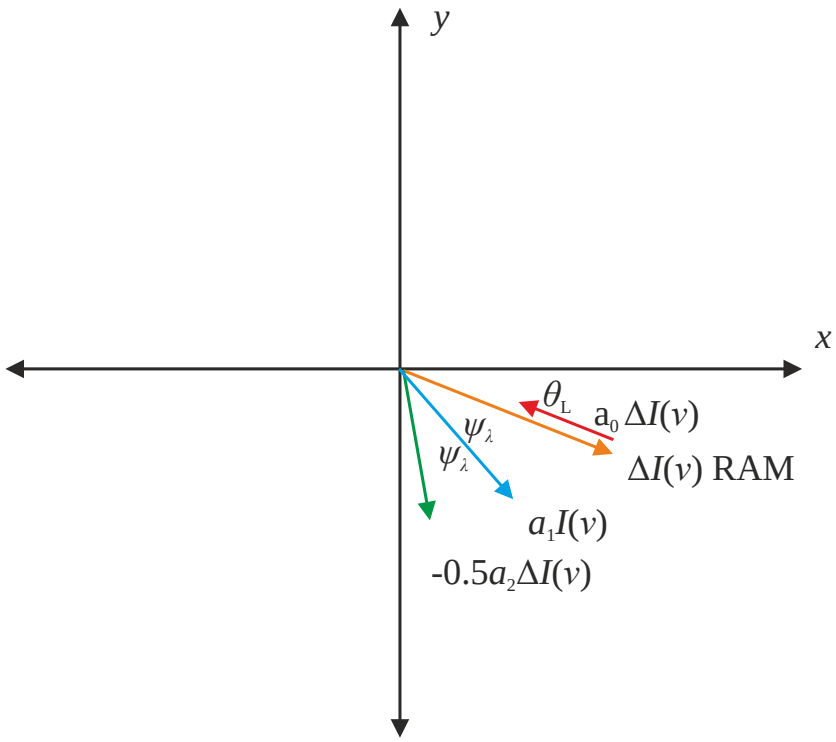

Figure 5-35. The phase invariant PDM.

The *1f* signals in the X and Y channels are now given as:

$$M_x = \Delta I(\nu)(1 + a_0)\cos(\theta_L) + a_1 I(\nu)\cos(\theta_L + \psi_\lambda) + 0.5 a_2 \Delta I(\nu)\cos(\theta_L + 2\psi_\lambda) \quad (5.68)$$

$$M_y = -\Delta I(\nu)(1 + a_0)\sin(\theta_L) - a_1 I(\nu)\sin(\theta_L + \psi_\lambda) - 0.5 a_2 \Delta I(\nu)\sin(\theta_L + 2\psi_\lambda) \quad (5.69)$$

It is noted that ψ_λ in equations (3.15) and (3.16) of Section 3.5 is replaced by $\theta_L + \psi_\lambda$. The processing software then computes the relation:

$$M_x + \frac{M_y}{\tan(\Theta + \psi_\lambda)} \quad (5.70)$$

The value of Θ is iterated from 0 to π until the recovered absorption signal has the least difference between the line centre absorption and wings (zero baseline for gases with non-absorbing spectral wings). At $\Theta = \theta_L$, the WM signal is completely cancelled and the entire RAM absorption signal is recovered.

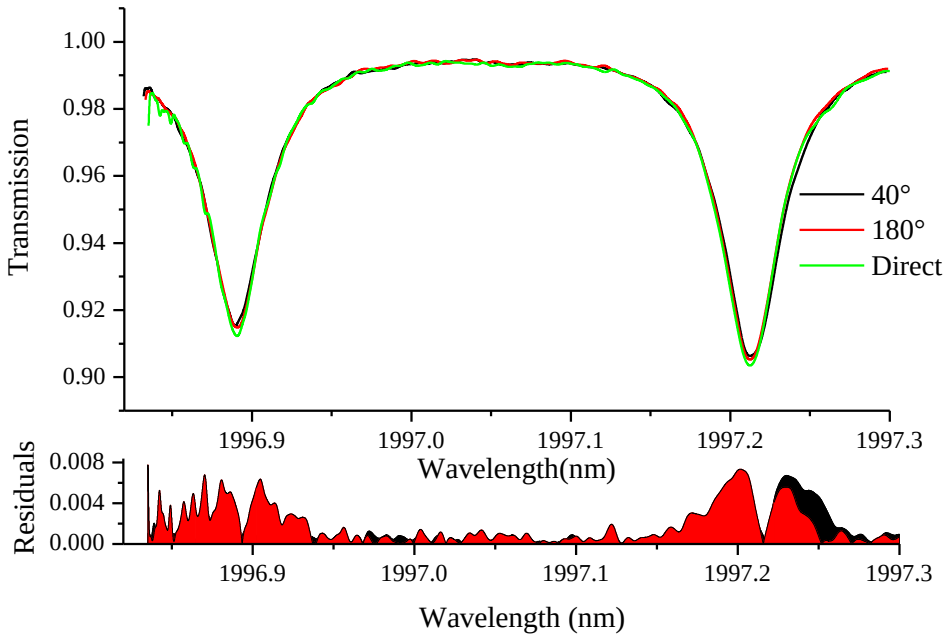

Figure 5-36. Demonstration of the method which recovers the gas absorption signal independent of the phase of the reference signal of the lock-in amplifier relative to the *1f*-WMS signals, corrected for the phase walk-off effect, for the 1997 nm DFB-MQW laser. The residual plots correspond to the difference in the recovered absorption line shape signals (at the two lock- in angles) compared to the direct gas absorption signal (measured without disturbing the system). The similar shapes of the residual plots validate the effectiveness of this approach.

This method is useful in extracting the gas absorption line shape independent of the phase relation between the *1f* signal components and the reference signal of the lock-in amplifier. This method may be extended to *2f* detection for isolation of the prominent *2f* derivative signal using the method similar to Chakraborty et al [38]. This was not pursued due to the other priorities of the project. The symmetric shape of the recovered *2f* derivative line shape could be used to identify the correct LIA reference signal phase.

Figure 5-36 presents the results for the phase invariant method using the 1997.2 nm (R48) absorption line of CO_2, with correction for the WM-IM phase variation across the current scan. Shown in Figure 5-37 is the result using this method for a 1650 nm DFB laser used for accessing the R4 absorption line of methane. This proves that this method can be applied for any laser with the WM-IM phase known.

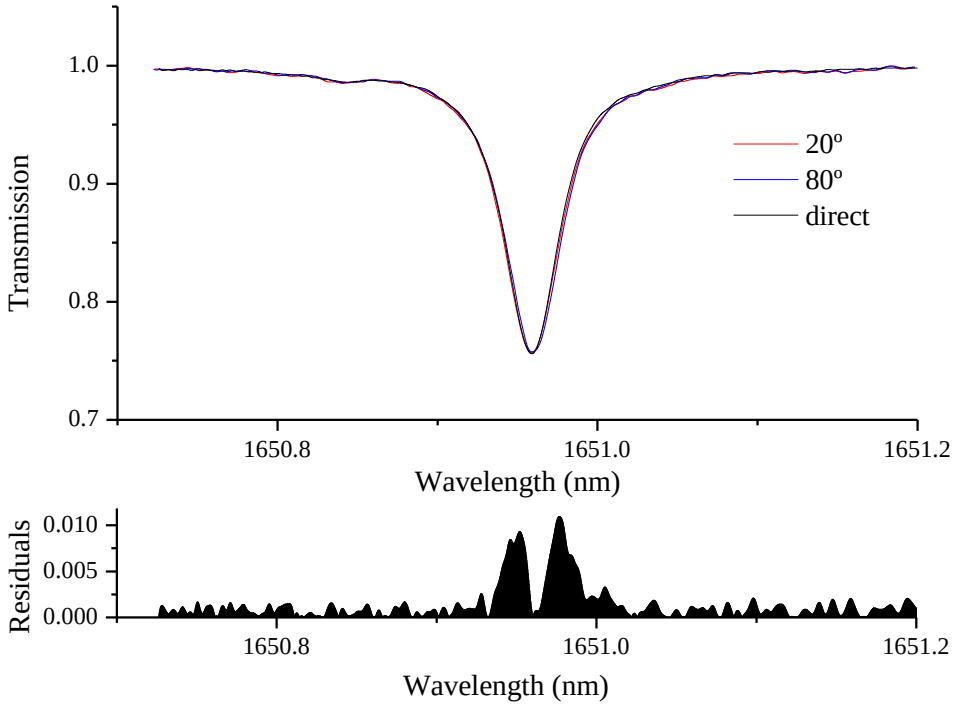

Figure 5-37. The phase insensitive PDM using the R4 Transition of methane at 1650 nm. The recovered gas absorption signals at two arbitrary phase angles (as indicated on the LIA front panel) of the lock-in amplifier reference signal are shown.

5.10 Summary

The wavelength modulation properties of semiconductor DFB lasers and their influence in the recovery of gas absorption line shapes was analysed in this work. Measurement techniques were implemented to completely compensate for the effects of the laser modulation characteristics, such as the WM-IM phase variation across the current scan, in the recovered gas absorption line shapes. Measurement strategies were developed wherein the gas absorption line shape signals could be recovered using the PDM at an arbitrary phase of the lock-in amplifier reference signal, applicable to any DFB laser

with a known WM response. This is important for applications such as FLITES, where it is difficult to align the relative reference signal phases of all the 126 LIAs to the *1f*-WMS signal components.

It has been noted that the WM-IM phase variation is laser dependent. On that account, for the purpose of researchers working in TDLS-WMS it is important that a clear understanding of the WM response of DFB lasers was developed. Hence, semiconductor models were developed to simulate the wavelength modulation characteristics, applicable to DFB lasers. The model shows excellent qualitative agreement with the measured trends of the wavelength modulation characteristics for two DFB lasers. However, it was observed that the model is inadequate in accurately predicting the wavelength modulation characteristics of laser structures with an increased carrier induced WM. Inclusion of the complicated carrier effects such as the spatial hole burning is necessary to accurately describe the wavelength modulation response of such lasers. Moreover, the accuracy can be improved by using a two dimensional heat flow model rather than the laminar heat flow model assumed in this work. This approach is beyond the scope of this project.

Chapter 6

Measurement of Carbon Dioxide in a GTE Exhaust Plume

6.1 Introduction

In this work the most important objective is to develop and implement a suitable WMS technique for the measurement of carbon dioxide concentration and temperature in an aero engine exhaust plume. This is part of a broader work for the FLITES initiative for tomographic measurement of CO_2 concentration and plume temperature in the exhaust of a gas turbine engine. Obtaining accurate tomographic concentration (C) and temperature (T) maps of a GTE exhaust plume necessitates the use of 126 measurement channels in a circular geometry across the plume cross-section [51]. An overview of the FLITES project is given in Section 1.4.

Several TDLS/WMS approaches have been used to measure gas concentration and/or temperature. For example, twin line ratio thermometry has been used to measure the gas temperature, the gas concentration could be extracted from the fit of one of the absorption features [14, 86]. Uncertainty in the temperature measurements using RT can occur if the gas concentration is not known prior to the measurements. In such situations an iterative procedure [2, 87, 88] is used until the recovered concentration coincide with the initial concentration used to obtain the temperature. In ratio

thermometry, to obtain better sensitivity, it is desirable to use gas absorption lines with a significant difference in their lower state energy levels. Hence, it is sometimes desirable to use multiple lasers to access lines with a large difference in their lower state energy levels. This is expensive as it would need twice the amount of laser sources as well as complicated receiver optics or electronics [14]. Consequently, for this work, a measurement strategy was adopted to obtain the gas concentration and temperature values by a least-squares curve fit of theoretically modelled WMS line shape signals to the experimentally measured WMS signal.

The gas turbine exhaust plume is an ideal example of a harsh environment. It has been impossible to obtain direct spectra (especially at slower scan rates) because of the interference from low frequency transmission noise. Hence, phase sensitive detection using wavelength modulation spectroscopy is the preferred measurement method. Due to the absence of a non-absorbing baseline at atmospheric pressure for the CO_2 absorption feature at 1997 nm, a no-gas signal has to be used to normalise direct gas signals or WMS signals. The fluctuating intensity as a result of the varying transmission conditions in an aero engine exhaust plume renders it impossible to cancel the intensity with a no-gas signal taken after the measurement. Upadhyay et al. [46, 89] had made measurements on a gas absorption line of methane at 1650 nm which had non-absorbing spectral wings, from which it was possible to extract the IM signal, at phase quadrature, without the need for pre-characterisation of the intensity modulation characteristics of the laser. However, such a method was not applicable for the chosen CO_2 absorption bands due to the absence of a non-absorbing baseline. In this work a *1f* signal is used to normalise the *2f* gas signal and the technique is known as *2f/1f* WMS. Normalisation by the *1f* signal also compensates for the transmissivity fluctuations expected in harsh engine environments [7]. In most of the earlier measurement approaches using *2f/1f* spectroscopy, the laser modulation parameters were only measured near the absorption line centre [8]. In this work, the laser modulation parameters are measured at each DC bias current across the scan.

Measurements will be made near the detuner (also known as an exhaust muffler or an augmenter tube) which is located at a distance (~ 4 m) from the engine exhaust. The detuner is a large diameter tube which serves to vent and dampen the engine exhaust by

mixing it with the surrounding cooler air (the Venturi effect). The temperature expected in a GTE exhaust plume is in the range of 100-600 °C (this depends mainly on the engine under operation (turbojet or gas turbine (turbofan)). Mixing with the entrained air, the temperature will be further lowered to the range of 100 - 300 °C. To theoretically model the *2f/1f* spectra at these conditions, accurate values of the line strength and line broadening parameters were necessary. The spectral values in the HITRAN 2012 database are valid only for the room temperature measurements. The accuracy of these values for high temperature spectra is limited due to the absence of temperature coefficients of line width and partition functions at higher temperatures. Moreover, HITEMP is only valid at very high temperatures greater than 1000 K. Hot lines are likely to exist at higher temperatures which may not be present in any of these spectral databases. Under these circumstances, laboratory characterisation using the high temperature gas cell was necessary to measure the CO_2 line strength and line width in the temperature ranges expected in an aero engine exhaust plume.

Section 6.7 focusses on the high temperature spectroscopy, where these gas spectral parameters were measured using direct spectroscopy at the higher temperatures (~ 500 °C) expected in a GTE exhaust plume.

A significant part of this work is dedicated to validation of the Fourier model of the WMS signals against the signals measured in the lab. In Section 6.4, the WMS Fourier model is validated by comparing against the experimentally obtained *1f* signals using PDM. This is an excellent starting point as it validates the accuracy of the measured laser modulation parameters using models that are well established in the group. This will be followed by validation of the Fourier model for the *2f/1f WMS* signals. In Section 6.10, the *2f/1f* model is validated at higher temperatures up to 500 °C by comparison with the spectra measured experimentally using a heated optical gas cell, employing the spectral parameters measured at higher temperatures. Section 6.11 explains the optical sensor system to obtain the gas concentration and temperature, validated in a laboratory environment.

Three engine tests were performed at the Rolls-Royce aero engine test facility at East Kilbride. Section 6.13 discusses the results that have been obtained in the initial test campaign, it also gives the optimisation procedures followed to obtain better signal-to-

noise ratios. Section 6.14 provides the results for single channel CO_2 concentration and temperature measurement across the aero engine exhaust plume. To the author's best knowledge, this is the first reported measurement of CO_2 concentration and temperature in an aero engine exhaust plume.

6.2 High Resolution Spectroscopy-Line Selection

The preliminary step in the design of a TDLS/WMS gas sensor is to identify the absorption lines that satisfy the criteria required for a given TDLS-WMS technique and sensor environmental conditions. In WMS, the specific criteria for spectral line selection are as follows:

6.2.1 Optimum Signal-to-noise Ratio

The chosen spectral lines should have sufficient absorption to yield adequate signal-to-noise ratios in the expected temperature and concentration regimes of the sensor environment. It is also desirable that the absorption signals are optically thin ($T(\nu_0)$ >0.95 or $\alpha(\nu_0) < 0.05$) as the fitting algorithm is faster when an optically thin model is used. More importantly, the relationships in WMS are much more straightforward (due to the linearity) if the sample is optically thin [27], though it is not an absolute requirement that the absorbance be within the optically thin limit.

6.2.2 Spectral Isolation

The absorption lines should be spectrally well isolated from other gas lines and neighbouring lines of the same species for the pressures expected in the sensing environment. This reduces the complexity of modelling multiple spectral lines. In this work, high temperature spectroscopic modelling was done using the measured collisional broadening and line strength values for a single absorption feature of CO_2 using the central strong line and the two strong lines on either side, as the nearby lines blended into each other at atmospheric pressure. Water vapour absorption lines are often unavoidable in the measurements, especially since water being one of the by-products of the combustion process.

Figure 6-1 shows the different absorption bands of CO_2 and H_2O in the spectral region from 1000 nm-5000 nm. The line strengths used for modelling the spectrum were obtained using the total internal partition functions calculated for H_2O and CO_2 respectively [25]. At elevated temperatures, spectral absorption lines were identified in the $v_1 + 2v_2 + v_3$ combination band of CO_2 that are well isolated from water vapour lines [90]. As a result, a number of studies were performed in the region around 1997 nm (5005 cm^{-1}) and several well isolated lines in that region have been identified. Many such lines have been reported in literature such as the R56 [90], P16 [91] or R50 [92].

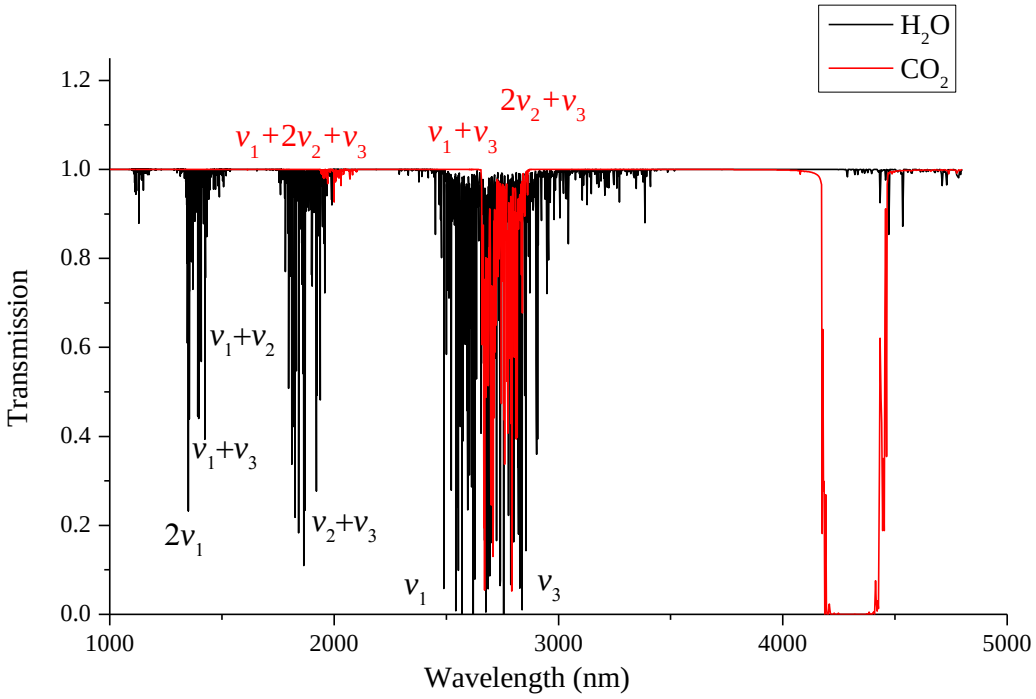

Figure 6-1. The transmission spectra of CO_2 and H_2O molecules modelled using HITRAN 2012 database from 1- 5 μm, at the conditions expected in an aero engine plume (T = 500 °C, l = 80 cm and P = 1 bar, CO_2 concentration = 2 % and H_2O concentration = 1 %).

In another work, Webber et al. [93] had reported the lines R46, R48, R50, R52 and R54 as good candidates for WMS sensors.

6.2.3 Non-absorbing Baseline

An absorption feature with a non-absorbing baseline within the wavelengths accessible by the laser current scan, at the operating pressure, is an additional advantage as normalising signal(s) can be extracted from the non-absorbing spectral wings [7, 46]. For CO_2, it was not possible to obtain absorption lines with a non-absorbing baseline at atmospheric pressure because the rotational bands are closely spaced, and thus blended into each other.

From an in depth spectral survey it was identified that the R48 transition satisfies the two major criteria, i.e. sufficient signal-to-noise ratio within the optically thin limit and spectral isolation. These lines could also be accessed by the commercially available DFB lasers at the time.

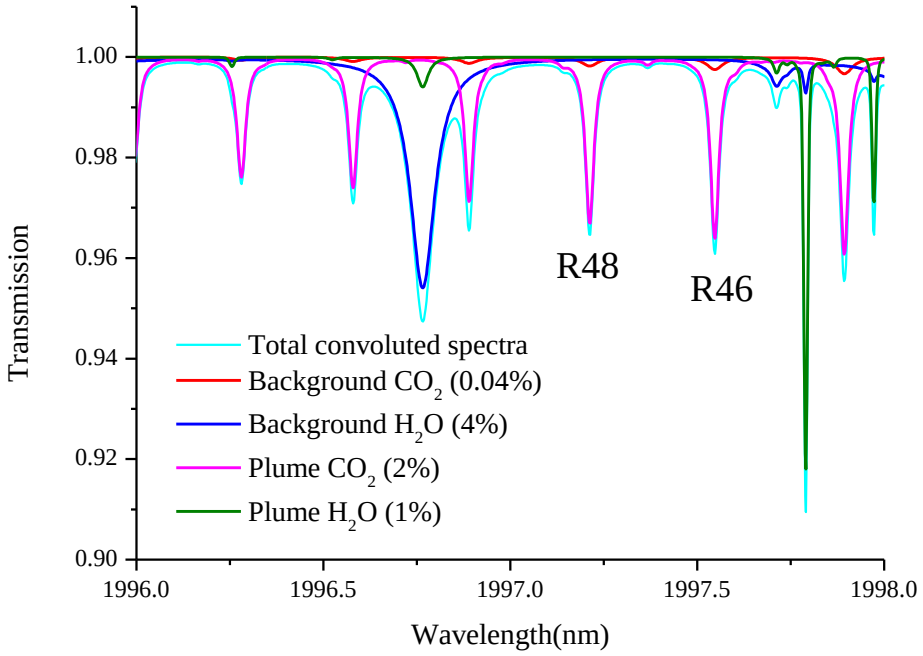

Figure 6-2. The CO_2 spectral lines accessible with the DFB-MQW laser at 2 μm. These lines belong to the 20012→00000 (HITRAN notation - (v_1, v_2, ℓ, v_3, r)) combination band of CO_2. The plume gas concentrations are assumed to be 2 % for CO_2 and 1 % for H_2O. Concentration of background CO_2 is 0.04 % (atmospheric) and the background humidity is assumed to be 4 %.

Figure 6-2 shows the expected spectra for CO_2 and H_2O at 1997.2 nm with approximate assumptions for the gas concentrations, pressures and temperatures for the H_2O and CO_2 species expected in a gas turbine exhaust environment along the laser line of sight (LOS). The dotted curve shows the convoluted spectra. There are two different regions along the laser LOS; the plume with a diameter of 80 cm (for the GTE at East Kilbride) has a higher concentration CO_2 and the ambient air having a lower concentration of CO_2. The plume and ambient air is assumed to have water vapour concentrations of 2 % and 4 % respectively. From Figure 6-2, it may be observed that the spectral line at 1997.2 nm (the R48 rotational transition) has negligible contribution from the water vapour absorption and was chosen for this work.

6.3 Laser Modulation Parameters

In Section 4.7, methodologies were described to measure the various laser modulation parameters for a given DFB laser at a given frequency, across the current scan, using techniques such as measuring the WM-IM phase lag using the non-responsive region of fibre ring resonator transmission or by a second order sinusoidal curve fit of the WM and IM signals.

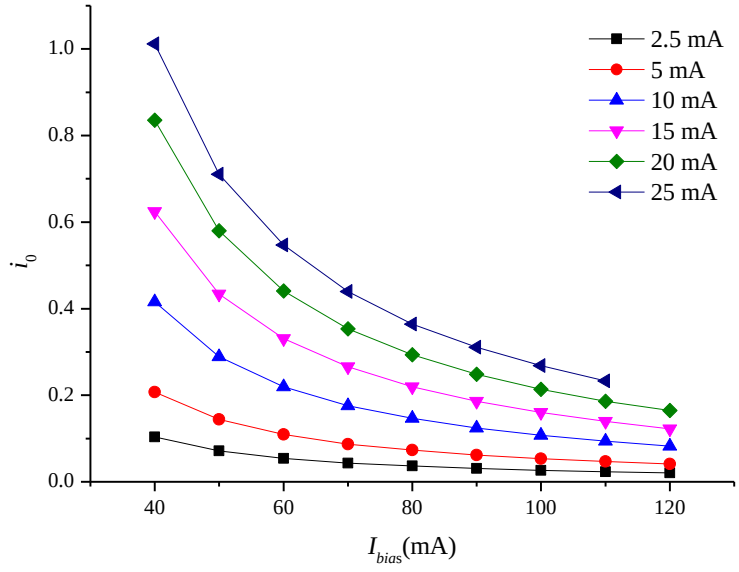

Figure 6-3. The intensity normalised linear IM amplitude measured across the current scan at different modulation amplitudes.

Calibration-free models are developed for the WMS signals using the measured DFB laser modulation parameters. The laser modulation parameters presented in this chapter were measured using the nonlinear curve fit method explained in Chapter 4. The other methods were also tested in this work for consistency, however, the nonlinear curve fit method gave the most repeatable answers (for instance, a standard deviation less than a 0.4° for the measured WM-IM phase lag), and was the preferred measurement method. Recollecting from Chapter 3, the laser modulation parameters required for modelling any WMS signal are the linear and nonlinear intensity modulation amplitudes, the WM-IM phase lag and the wavelength tuning coefficient or modulation amplitude (which is simply the tuning coefficient (GHz/mA) multiplied by the applied current modulation amplitude(mA)).

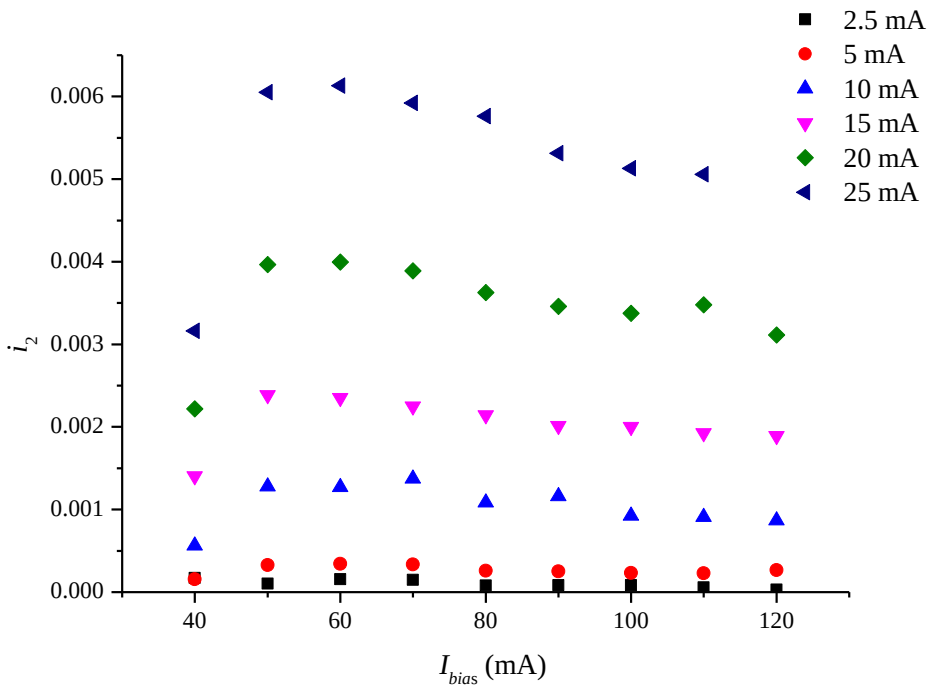

Figure 6-4. The nonlinear intensity modulation amplitude divided by the instantaneous intensity of the laser, measured across the current scan range, at different current modulation amplitudes.

Figures 6-3 and 6-4 show the measured linear and nonlinear intensity modulation amplitudes divided by the instantaneous intensity output from the laser. As mentioned in Chapter 3, it is found that dividing the intensity modulation amplitude with the instantaneous (average) laser intensity makes it a constant for any light transmission

function from the laser source to the detector (exceptions apply as explained further on). Hence, the terms $i_0 = \Delta I/I$ and $i_2 = \Delta I_2/I$ are independent of the transmission fluctuations and are constants at a particular bias current and modulation frequency for a given laser. This was evident from the previous measurement by Dr. Arup Lal Chakraborty [38]. Such an approach was used by several groups [8, 30] for undertaking WMS measurements immune to noise arising from multiplicative transmission fluctuations, which was expected to be a major limiting factor.

As can be seen from Figure 6-3, i_0 follows an inverse relation with the bias current. This is a consequence of the instantaneous laser intensity (I) increasing with the bias current, and also the IM amplitude (ΔI) only slightly decreasing with the bias current due to a small nonlinear response of the intensity-current curve at the given modulation frequency. The nonlinear intensity i_2 also shows a gradual rise with bias current from 40 mA to 50 mA, thereafter, it tends to a constant value, only decreasing slightly at higher bias currents. Again, this is due to a combination of the change in the laser nonlinearity as well as the increasing laser intensity output as a function of the bias current.

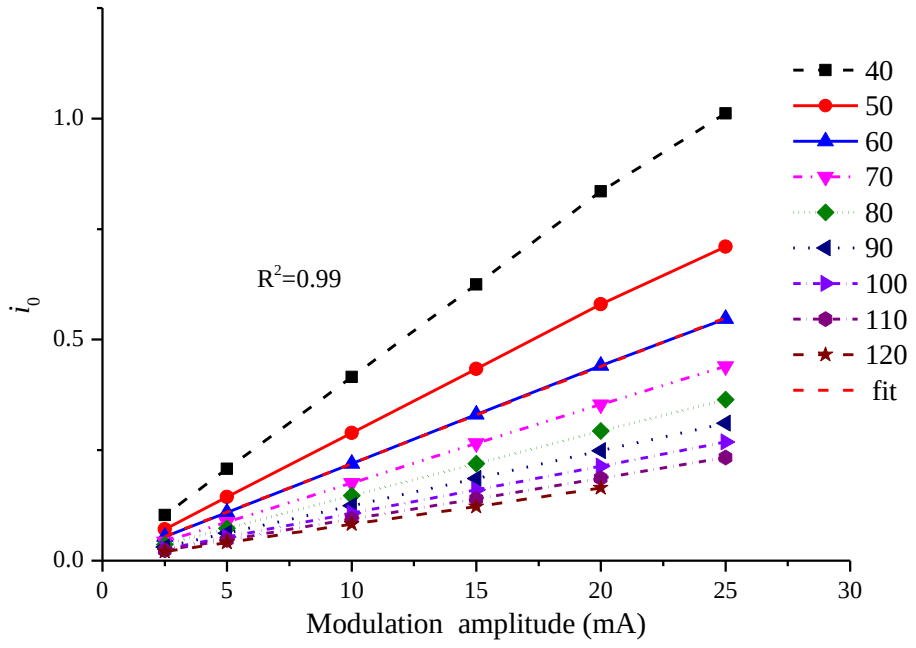

Figure 6-5. i_0 as a function of the applied current modulation amplitude (mA) at different bias currents.

Figure 6-5 shows that the *1f*- IM amplitude i_0 increases linearly as a function of the applied current modulation amplitude. Similarly, Figure 6-6 shows the measured second order intensity modulation amplitude (i_2) as a function of current modulation amplitude. It was observed that the nonlinear intensity modulation amplitude had a 4th order response as a function of the applied current modulation amplitude.

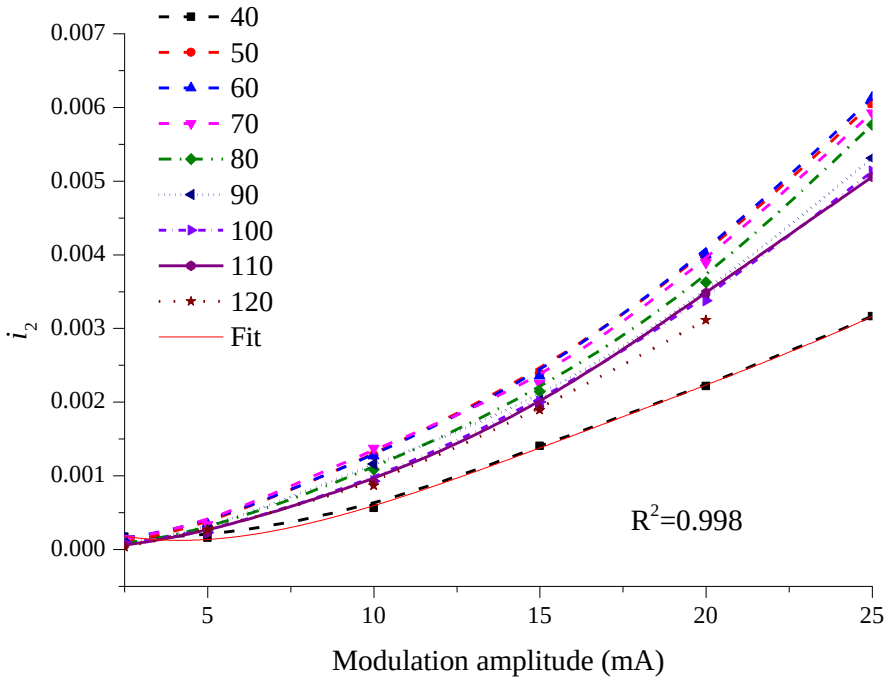

Figure 6-6. i_2 vs. current modulation amplitude, at different bias currents. A best fit is obtained for a 4th order polynomial as shown by the red curve.

The ratio of i_2 to i_0 across the current scan is shown in Figure 6-7 using three different approaches. Firstly, it was measured using a nonlinear curve fit method (round marker plot). Another approach to obtain i_2/i_0, is the ratio of R_{2f}/R_{1f}, that is the ratio of the no-gas resultant signals for *2f* and *1f* detection (dotted lines)(Section 3.9). Yet another way is to calculate ΔI by maximising one of the LIA output channel signals at *1f* detection followed by the measurement of the nonlinear RAM (ΔI_2) by repeating the step for *2f* detection, then dividing latter by the former to give i_2/i_0 (polygon marker plot).The three methods gave closely similar results within the measurement system limitations (etalons in the system and repeatability of measurements).

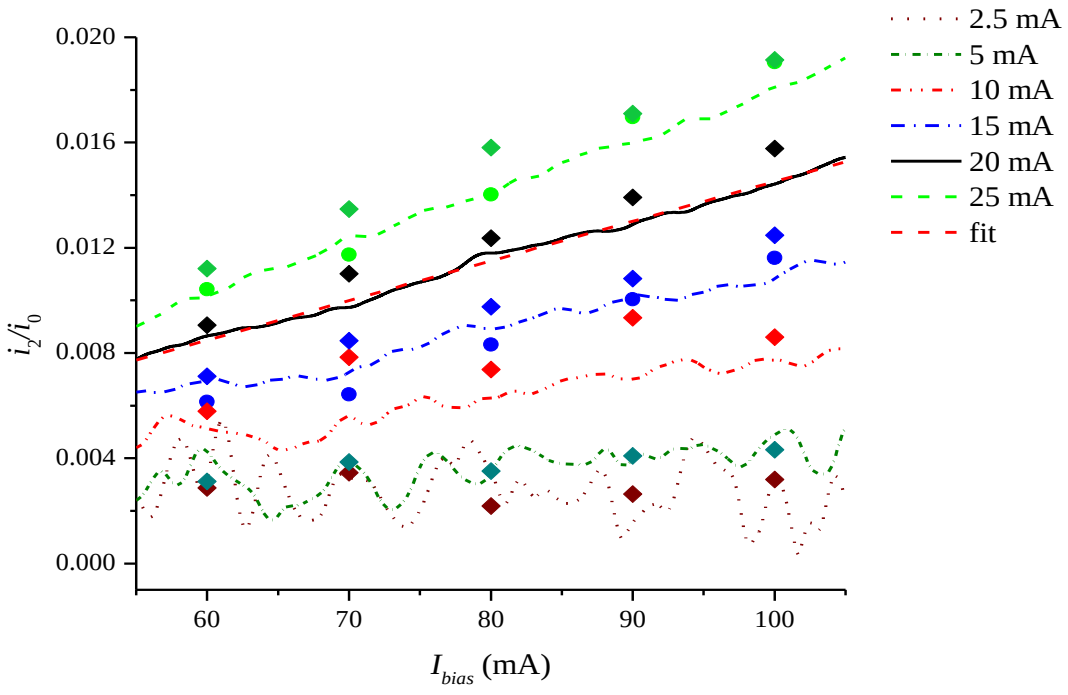

Figure 6-7. Ratio of linear IM to nonlinear IM measured using three different approaches. The round marker plots denote the measurements using the nonlinear curve fit method, the polygon marker plots are for the measurements taken using a simple LIA technique by maximising the *1f* and *2f* LIA signals on one of the orthogonal LIA channels and the dotted lines represent the measurements using the ratio of the LIA resultant signals at *2f* and *1f* across the laser scan.

Figure 6-8 shows the measured WM-IM phase lag (180 ° – (IM-FM phase lag)) across the current scan at a modulation frequency of 200 kHz and laser diode temperature of 21.95 °C (11.45 kΩ), for the 1997 nm DFB-MQW laser. The variation in WM-IM phase across the current scan range was measured to be approximately equal to 15° and was significantly higher than that measured previously for the other DFB lasers. It was discussed in Section 5.7 that the variation in WM-IM phase across the current scan has a significant impact in the recovery of the absorption line shape from the first harmonic signals [37]. Subsequently, it was noted from simulations using the WMS Fourier model that the WM-IM phase variation across the current scan did not have a significant impact on the recovered second derivative WMS line shape at *2f* detection. This is because the distorting components (*1f* and *3f* line shape components) are smaller in

magnitude as well as symmetric with respect to the *2f* line shape component (Section 3.9).

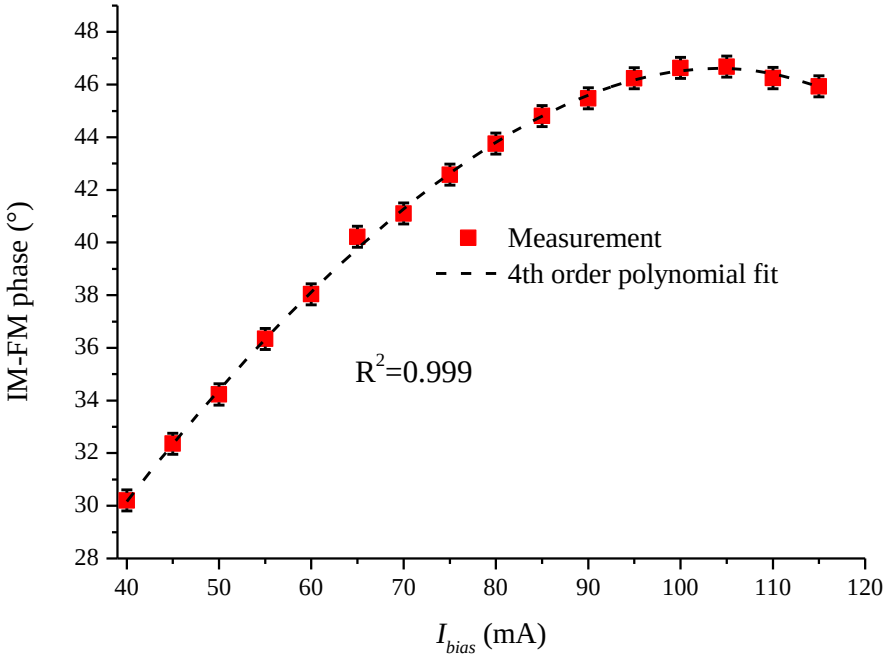

Figure 6-8. Variation of IM-FM phase (180 ° – WM-IM phase) across the current scan at a modulation frequency of 200 kHz and TEC resistance of 11.45 kΩ (21.95 °C). The figure also shows the error bars from five sets of measurements taken over a year.

Figure 6-9 provides the tuning coefficient values measured across the current scan at a modulation frequency of 200 kHz and diode temperature of 21.95 °C to access the absorption feature at 1997.2 nm. The variation in tuning coefficient is found to be approximately 5 % across the current scan. It was demonstrated in Section 5.8 that this variation is insignificant for the phasor decomposition method at low m values. It was noted from simulations that for *2f/1f* spectra as well, the variation in the tuning coefficient for this laser only had a very small effect. The tuning coefficient and WM-IM phase lag is found to be independent of the current modulation amplitude for the 1997.2 nm DFB-MQW laser. It is known that the *2f* line shape signal ($a_2 I$) peaks at m = 2.2 [34]. For typical DFB laser diodes, the tuning coefficient decreases rapidly with the modulation frequency. This causes the modulation index to drop significantly at

higher modulation frequencies. Hence, the majority of the DFB lasers are operated at modulation frequencies less than 100 kHz to obtain sufficient signal amplitudes.

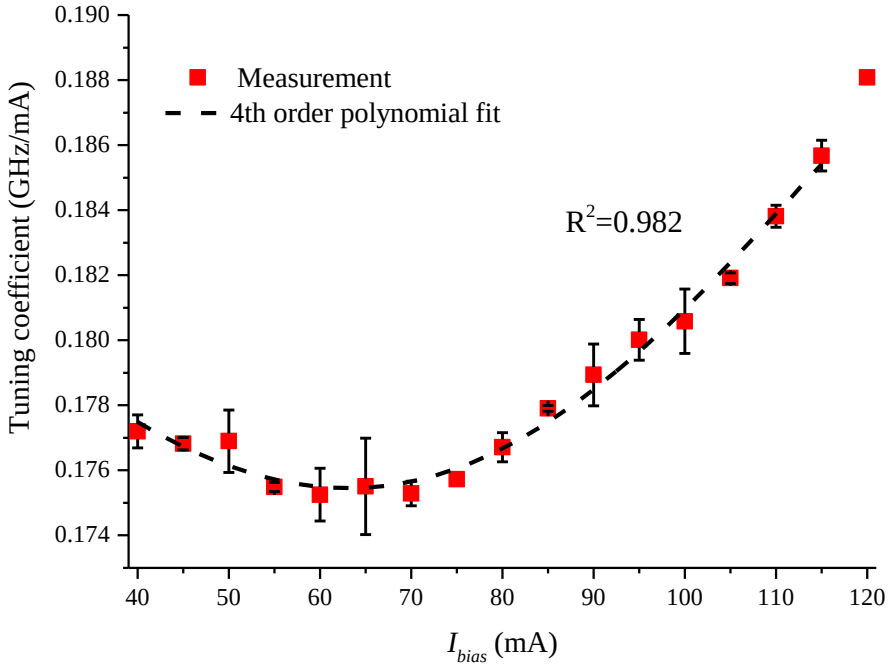

Figure 6-9. Tuning coefficient measured across the current scan for a modulation frequency of 200 kHz and laser diode temperature of 21.95 °C. The error bars depict the deviation for five measurement sets taken over a year.

It can be observed from Figure 5.18 that the tuning coefficient increased as a function of the frequency of applied current modulation, for the 1997.2 nm DFB-MQW laser. This particular property of this laser makes it suitable for operation at higher modulation frequencies (several hundred kHz) without a significant reduction in the modulation index, and hence the signal size.

6.4 Validation of the Fourier Model for *1f* Techniques

The WMS techniques used in this work are described in Chapter 3. Accurate modelling of the WMS signal output from the LIA relies on the Fourier modelling of these signals. The output signals from the lock-in amplifier can be accurately modelled only if the

laser modulation parameters such as the linear and nonlinear intensity modulation amplitudes, WM-IM phase lag, wavelength modulation amplitude and the gas spectral parameters are measured accurately. In this section the Fourier model is validated and accuracy of the measured laser modulation parameters verified using the *1f* demodulation technique viz. the phasor decomposition method described in Section 3.5. The spectral parameters from HITRAN were used since the measurements were taken at room temperature.

Figure 6-10 shows the recovered gas absorption line shape signals using the PDM technique at three distinct modulation index values. The blue and red curves show the experimental and theoretical direct absorption line shapes. The magenta curve shows the recovered gas absorption line shape using the PDM technique. It can be seen that at high *m* values, the recovered absorption line shape becomes distorted. This is due to the $\Delta I a_2$ component superimposed on the RAM absorption signal as shown in Figure 3.2. Bain et al. [60] had implemented a correction function method to compensate for the distorting effects of this *2f* line shape signal. The correction function was calculated from the ratio of the absorption maxima for the undistorted and the distorted gas signals or it was modelled theoretically using the second order Fourier coefficient (a_2) [34, 41] with the *m* value assumed to be known beforehand (from a known laser tuning coefficient, gas temperature and pressure). The recovered gas absorption line (distorted) was multiplied by the correction function to obtain the undistorted absorption line shape which could be used to infer the gas parameters when fit to a theoretically modelled direct absorption line shape. Here, instead of correcting for the distorted line shape, it is modelled using the laser modulation characteristics and the HITRAN 2012 spectral parameters.

The black curves show the absorption signals obtained using the Fourier model. The Fourier model matches the recovered absorption spectra at different modulation indices. This proves that the measured tuning coefficient and WM-IM phase values are accurate.

The recovered absorption signal is a function of only two laser modulation parameters, viz. the laser modulation amplitude (or the tuning coefficient) ($\Delta\nu$) and the WM-IM phase lag (ψ_λ).

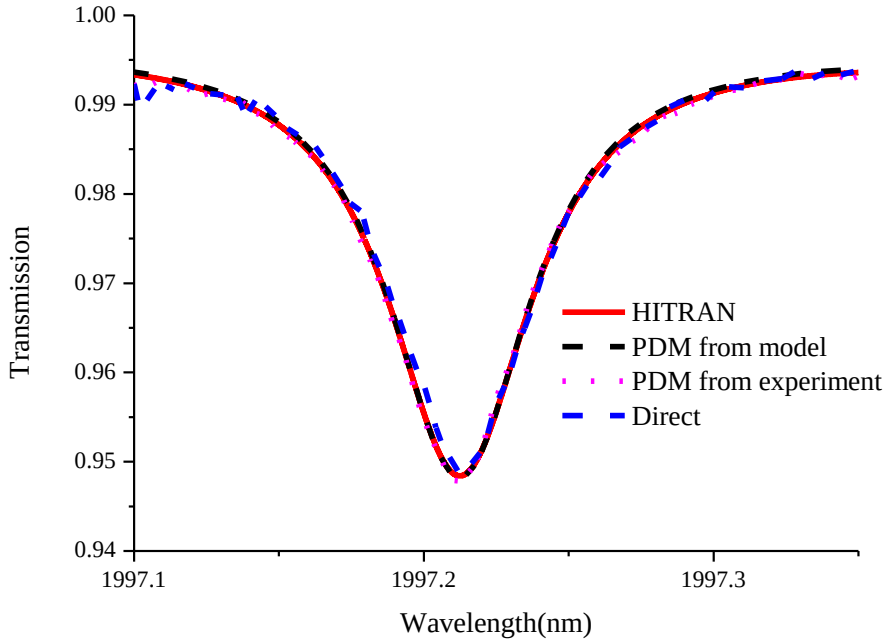
1.00
0.99
0.98
0.97
0.96
0.95
0.94
Transmission
1997.1
1997.2
1997.3
Wavelength(nm)
HITRAN
PDM from model
PDM from experiment
Direct

(A)

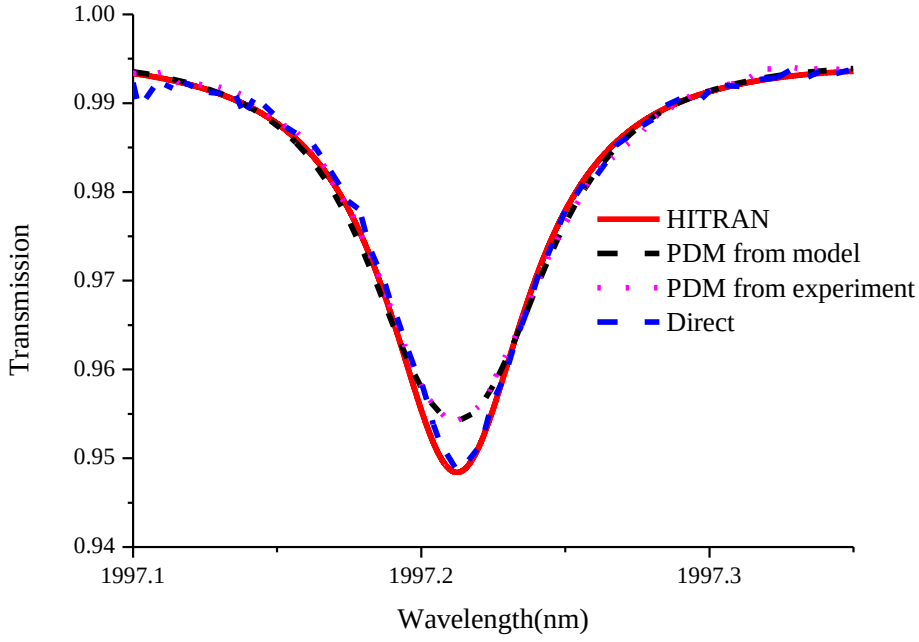
1.00
0.99
0.98
0.97
0.96
0.95
0.94
Transmission
1997.1
1997.2
1997.3
Wavelength(nm)
HITRAN
PDM from model
PDM from experiment
Direct

(B)

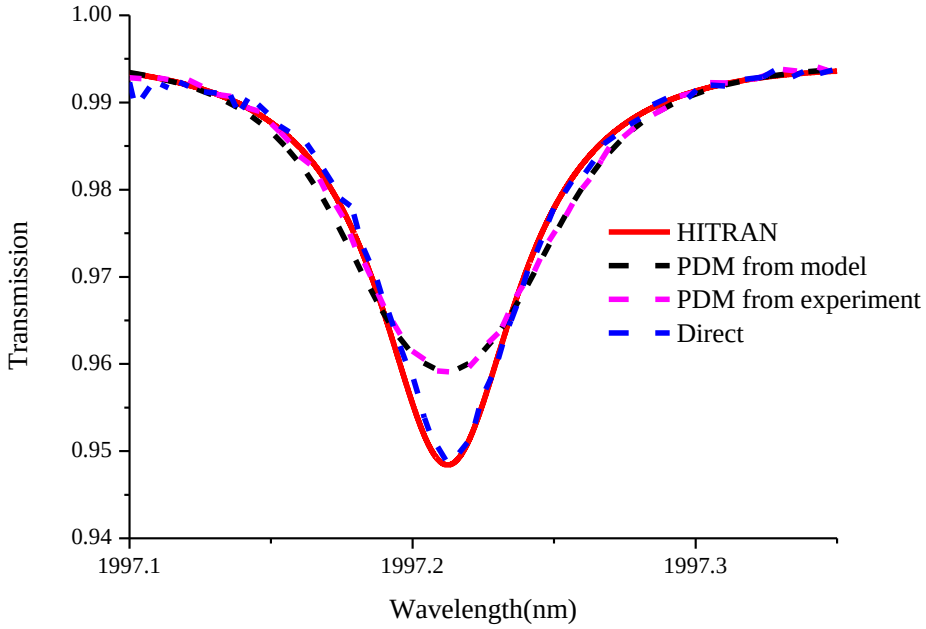

(C)

Figure 6-10. Figure shows the recovered gas absorption line shape signals using PDM at a pressure of 1 bar, T = 25 °C, C = 100 % and l = 6.1 cm, for different modulation amplitudes. The direct spectrum (red) matched the theoretical transmission obtained using the HITRAN 12 spectral values. The pink curve is the PDM signal recovered at m = 0.2 (A), 0.4 (B) and 1.24 (C). The black curve represents the recovered line shape using the PDM modelled using the laser modulation parameters viz. the tuning coefficient and WM-IM phase lag.

To obtain a signal dependent on i_0, the FM isolated Y-channel (equation 3.11) is divided by the FM isolated Y-channel background to obtain a WMS line shape signal that depends on i_0, $\Delta\nu$ and ψ_λ. The signal has a first derivative line shape as shown. The background signal was obtained by taking a no-gas signal without disturbing the system. Figure 6-11 shows the recovered signals using the above method compared to the theoretical WMS signals using the Fourier model.

A small wavelength shift due to the nonlinear heating effect of the laser diode (as explained in Chapter 5) is expected and corrected for. There is a slight mismatch in the wings. This might be due to inadequacies in the HITRAN 2012 spectral data or etalons in the gas cell windows.

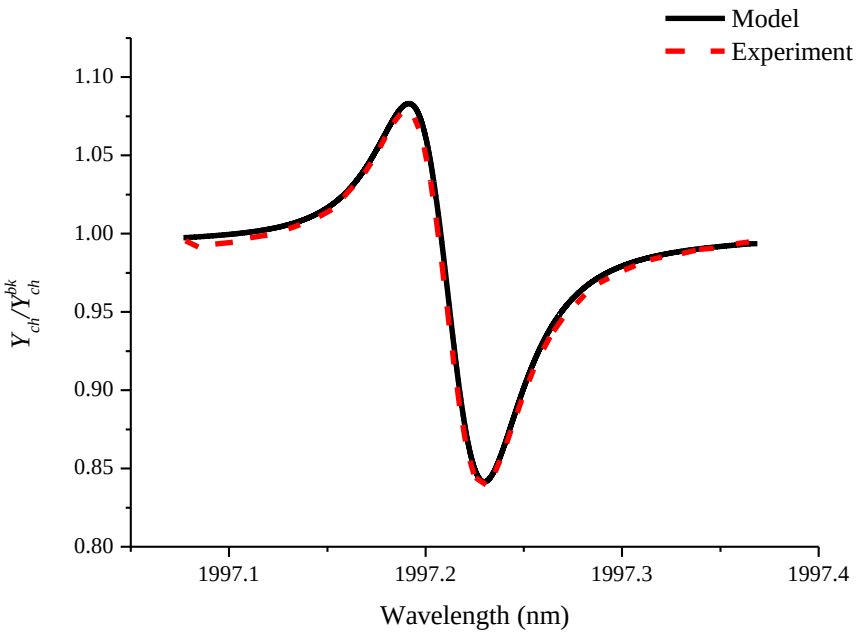

(A)

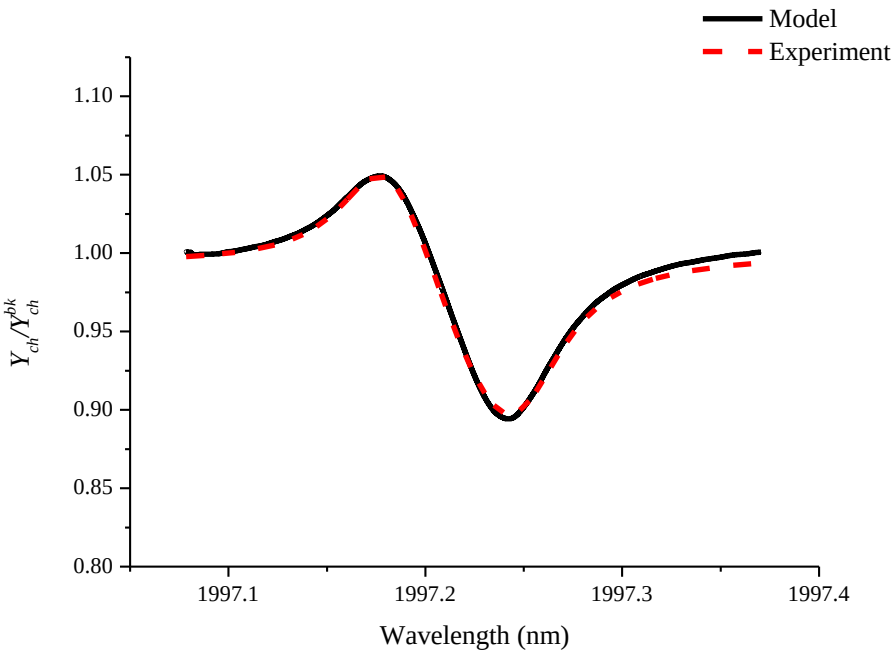

(B)

Figure 6-11. Figures (A) and (B) show the experimental (red curve) $Y_{channel}\ /Y_{channel}^{bk}$ signals at modulation amplitudes of 5 mA (m = 0.4) and 15 mA (m = 1.2), compared against the Fourier model output (black curve).

In this section, the Fourier model has been validated by comparison with the experimentally recorded *1f* line shape signals and it was confirmed that the HITRAN 12 spectral parameters are adequate for accurately modelling the WMS spectra at room temperatures. This work was carried out as a prelude to validation of the complex spectral models as described in the subsequent sections.

6.5 *2f/1f* Spectroscopy

Section 6.4 discussed how the Fourier model was used to accurately model the *1f*-WMS signals. As stated in Chapter 3, *1f*-WMS calibration-free approaches such as the PDM and the RAM technique cannot be used in an environment with varying transmission fluctuations especially since a non-absorbing baseline is absent as for the CO_2 spectra in the near-infrared. Moreover, the signal-to-noise ratio of the *1f* signals was found to be insufficient even at very high modulation frequencies due to the *1f*-FM component signals being buried in the noise on the high RAM background signals. As stated in Section 6.2, the CO_2 absorption line chosen for this work is the R48 line at 1997.2 nm. This CO_2 absorption feature lacks a non-absorbing baseline as shown in Figure 6-12. Hence, the RAM signal cannot be extracted from a polynomial fit of the non-absorbing baseline.

In environments where the transmission is rapidly fluctuating, *1f* signal and the *2f* signal to a lesser extent are severely distorted by the multiplicative transmission noise which convolutes with the WMS signals within the LIA pass band. One way to cancel the transmissivity is to divide the *2f* signal by the *1f* signal. This method is known as *1f* normalised *2f* spectroscopy and is immune to transmissivity fluctuations in harsh environments. This method was used by several research groups [7, 8] for optical metrology of concentration and temperature in harsh environments. In addition, a background subtraction procedure was followed using equation (3.29) to cancel the nonlinear RAM signal and to reduce the effects of the temporally stable etalons as well as contributions from gas absorption outside the measurement path.

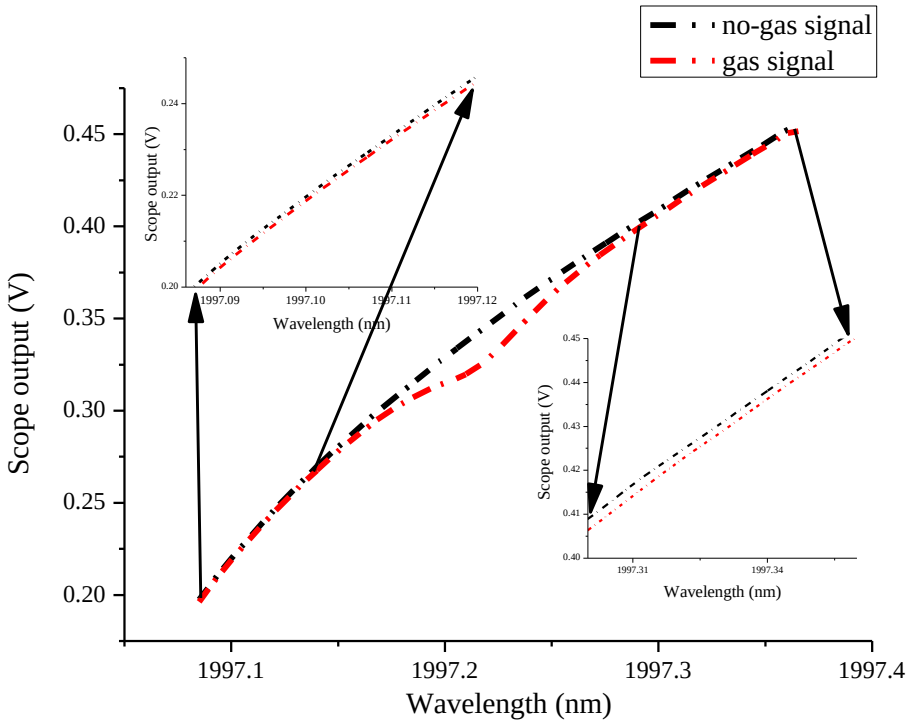

Figure 6-12. Absence of non-absorbing baseline signal for the R48 Transition of CO_2 at 1997.2 nm. T = 50 °C, C = 100 %, P = 1 bar and l = 5.5 cm.

6.6 Experimental Methodology

Figure 6-13 shows the measurement setup used in this work to obtain the *1f* normalised *2f* signals. Two Perkin Elmer digital lock-in amplifiers are used to demodulate the input signal at the *2f* and *1f* harmonics of the modulation frequency. The input gain and output sensitivity of the LIA is adjusted to give the maximum signal-to-noise ratio for the *2f* and *1f* signals, without overloading the input A/D converter. Three signals are required for the WMS *1f* normalised *2f* method, viz. the *2f* X-channel (X_{2f}), the *2f* Y- channel (Y_{2f}) and the magnitude of the *1f* signal (R_{1f}).

For some of the preliminary measurements, all the WMS signals viz. the *2f* X-channel and the *2f* Y-channel, followed by the *1f*-R signal were extracted from a single lock-in amplifier in succession as it had only two output ports. Care was taken so that there was no change in the signals over the duration of the measurement. Such a measurement strategy will not be feasible in an engine environment due to the rapidly varying

transmission conditions, and hence all the above mentioned signals need to be recorded simultaneously which necessitated the use of two lock-in amplifiers.

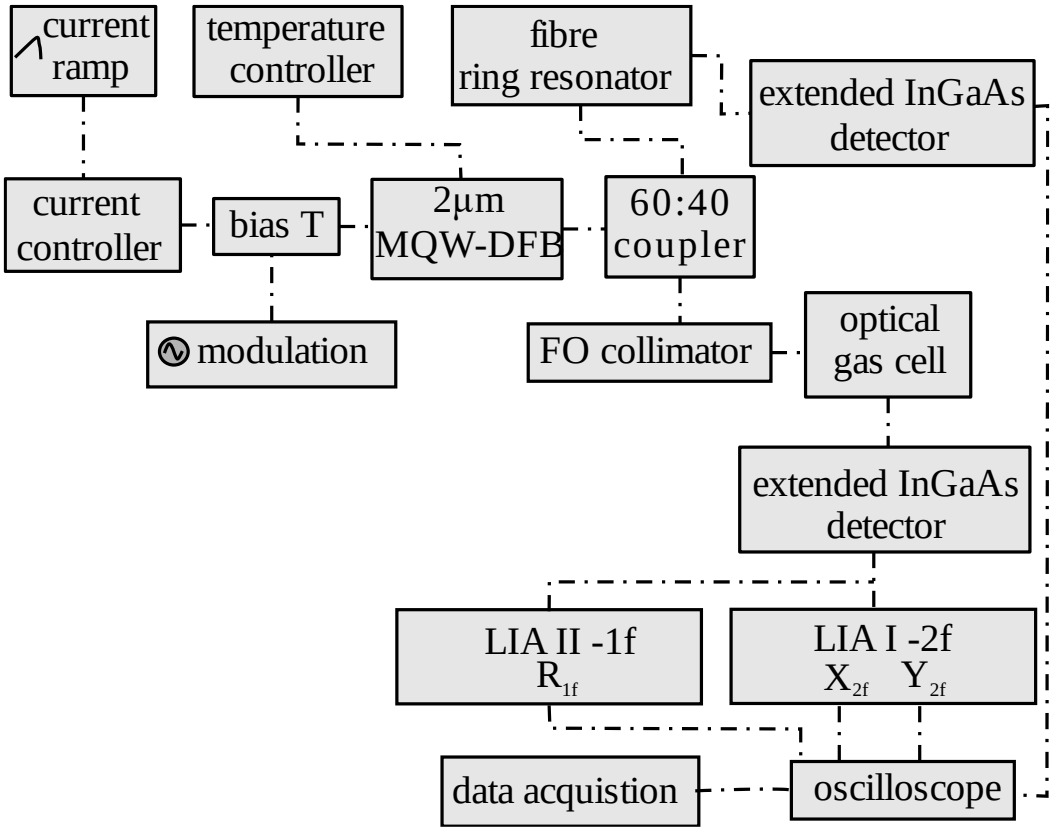

Figure 6-13. Experimental setup for the *1f* normalised *2f* method using two lock-in amplifiers.

Figures 6-14 (A) and (B) show the WMS gas and no-gas; R_{1f} and the R_{2f} signals from the two Perkin Elmer LIAs. It was observed that the *1f* signal output from both the lock-in amplifiers were identical as shown in Figure 6-14 (A). However, the *2f* signals had an offset on one of the lock-in amplifiers (Figure 6-14 (B)). This instrumental offset could be due to the non-ideal filtering effects of the LIA. Subtraction of the *2f*/*1f* background signal according to equation (3.29) was used to solve the problem of instrumental offsets. The background subtraction also removes the nonlinear IM as well as any common absorption signals or any static etalons.

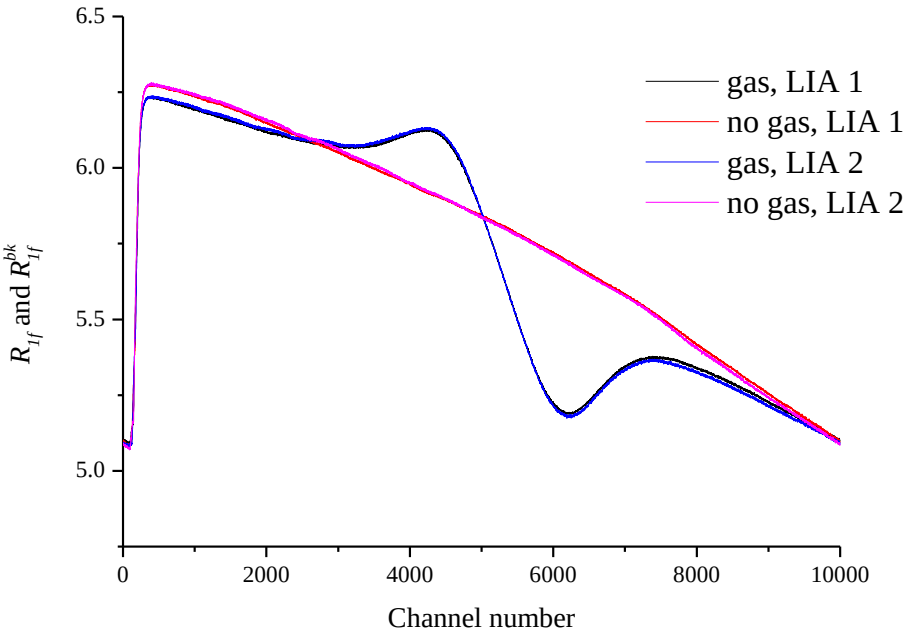

(A)

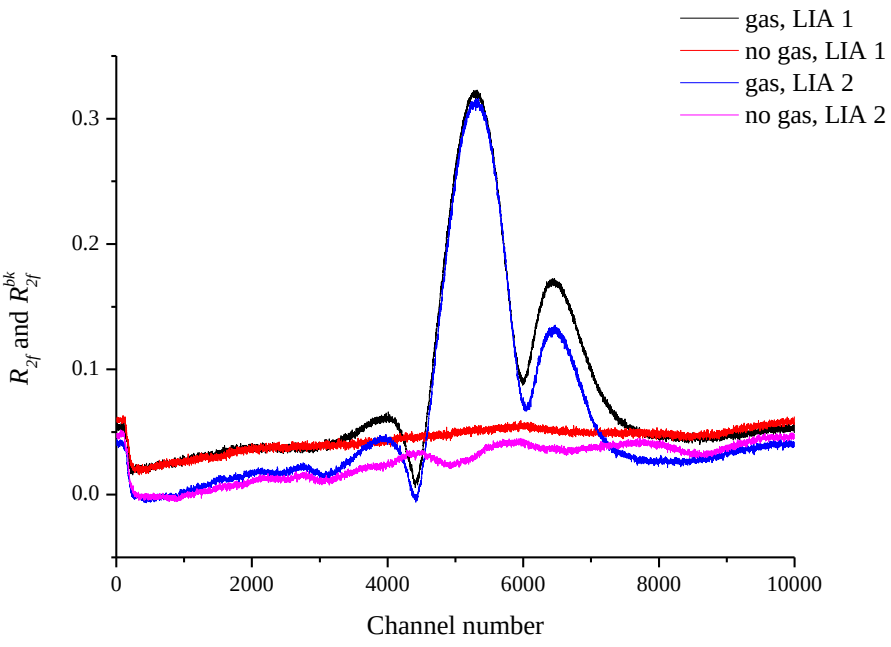

(B)

Figure 6-14. The gas and background *2f* and *1f* signal outputs from the individual lock-in amplifiers, measured in succession.

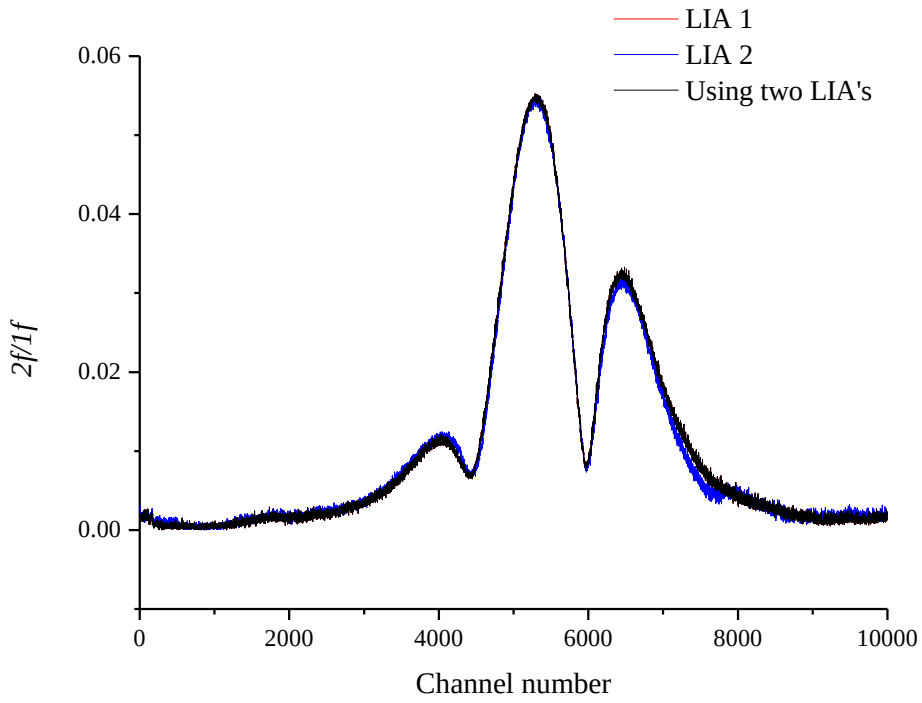

Figure 6-15. The background-subtracted *1f* normalised *2f* signals using both the lock-in amplifiers (black curve) together as well as using the individual lock-in amplifiers (red and blue curves) by extracting the *2f* and *1f* signals in succession.

Figure 6-15 shows the background-subtracted signals using the individual lock-in amplifiers (red and blue curves) by measuring X_{2f} and Y_{2f}, followed by measuring the R_{1f} signal in succession and using both the lock-in amplifiers (black curve) referred to as the dual lock-in amplifier arrangement, where the X_{2f} and Y_{2f} signals were measured from one LIA and R_{1f} was measured from the other. The order of the LIAs in the dual lock-in arrangement was reversed for consistency. It can be observed that there is no significant difference in the signal outputs using a single lock-in amplifier, or a dual-lock-in amplifier arrangement or with the LIA order reversed in the dual setup. This demonstrates that the dual lock-in amplifier arrangement with background subtraction can be used in measurement scenarios when a time multiplexed signal acquisition was not possible.

More sophisticated off-the-shelf lock-in amplifiers have an in-built multi-harmonic detection feature. Another alternative was to implement a PXI-e board based lock-in

amplifier in LabVIEW, as was done later on in this work with the help of fellow group members. However, this method is limited to lower modulation frequencies at present due to the higher sampling rates that are needed to demodulate the high frequency signals at the detector output (at least five times the modulation frequency) without aliasing.

6.7 Validation of the *2f/1f* Spectroscopic Model

The *1f* normalised *2f* model is validated for the spectral parameters (γ_L,ν_0 and $S'(T)$) from the HITRAN 2012 spectral database, and the measured laser wavelength modulation and intensity modulation parameters (i_0, i_2, ψ_1, ψ_2 and $\Delta\nu$). HITRAN values are verified to be accurate for room temperature measurements by comparison of the experimental and theoretically modelled direct spectra at ambient temperatures.

Initially, it was thought that an optically thin assumption can be used as the difference in the modelled direct spectrum was negligible for an optically thick and an optically thin case, for the conditions expected in a GTE plume. Subsequently, it was noticed that, for the WMS signals, an optically thin assumption would be inaccurate at the gas conditions expected in the plume. Figure 6-16 shows the difference in the theoretically modelled background-subtracted *1f* normalised *2f* spectra for an optically thin and thick case using a Voigt line shape profile. It was inferred that, even if the optically thin model was sufficient for modelling the direct signals, it fell short for accurately representing the WMS signals. This is attributed to the different sensitivities of the direct and WMS signals to the various spectral parameters. Hence, it can be concluded that, in the temperature ranges used in this work, especially for the laboratory measurements with higher concentrations of CO_2, an optically thick model is necessary to obtain accurate results.

The Lorenzian line shape function is inaccurate at high temperatures because the Doppler broadening effect becomes significant. As explained in Section 2.9, the Voigt line shape function accounts for the Doppler broadening as well. Figure 6-17 shows the difference in the theoretically modelled *2f*/*1f* spectra using the Lorentzian and Voigt line shape functions at, 500 °C. It can be inferred that an appropriate line shape function is necessary for accurate spectral modelling.

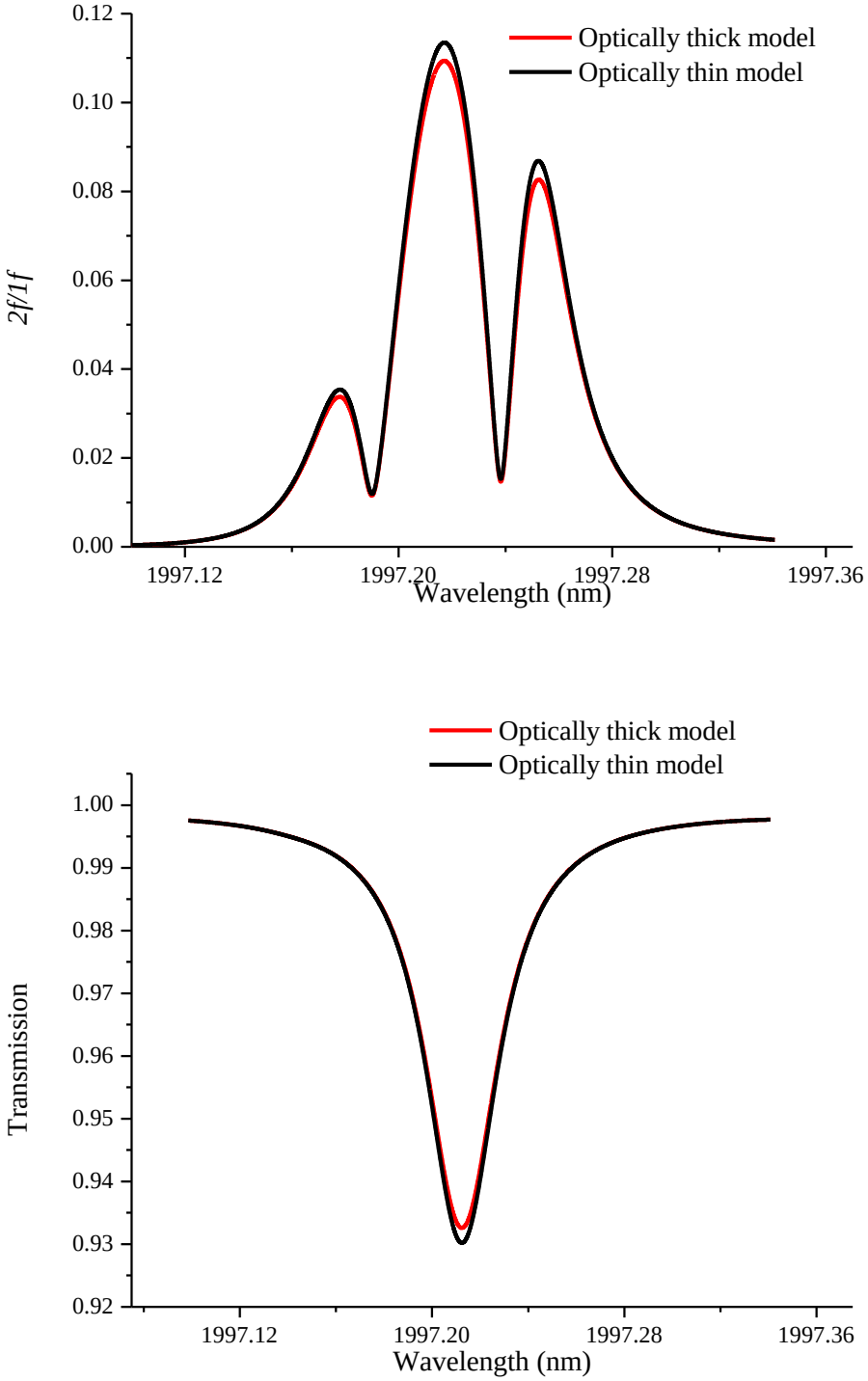

Figure 6-16. Difference in the theoretically modelled *2f/1f* spectra (left) and direct spectra (right) for optically thin and thick assumptions. Temperature = 250 °C, pressure = 1.014 bar, concentration = 4 % and path length = 80 cm.

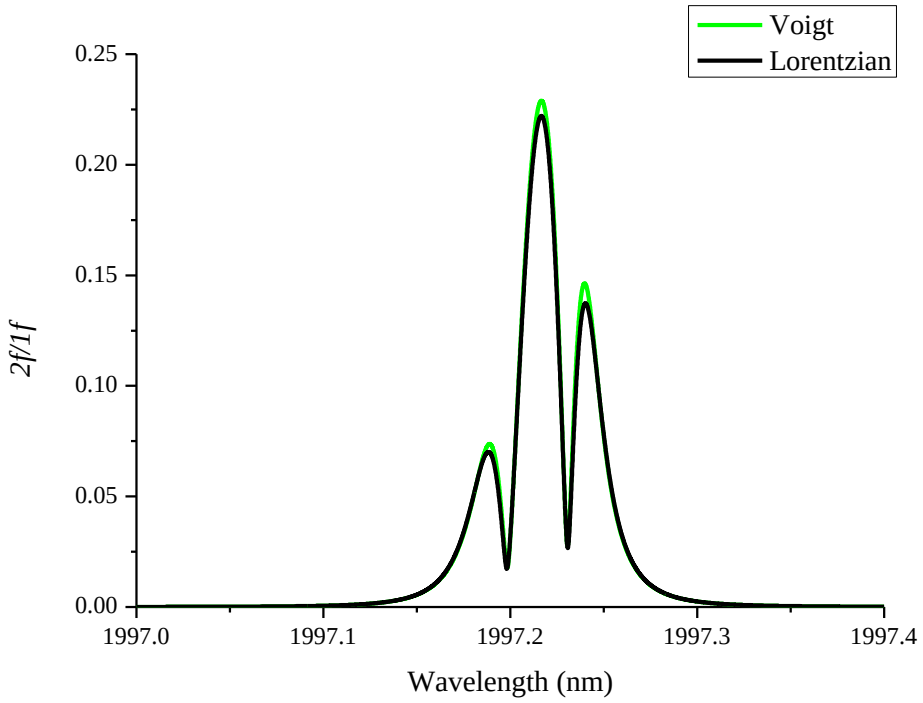

Figure 6-17. Theoretically modelled *2f/1f* spectra using Lorentzian and Voigt line shape functions at T = 500 °C, P = 1.013 bar, l = 5.5 cm, C = 100 % and m = 1.6328 (δi =10 mA). It can be seen that there is a significant difference in the peak heights for the two.

For example, at high pressures, the mean free path of the molecule can be less than the wavelength of the radiative transition, the molecule may change its direction several times during an absorption or emission of a photon, resulting in an averaging over the Doppler states, thus causing the line width to be narrower [94]. This is known as Dicke narrowing effect modelled using line shape functions such as the Galatary (velocity of the colliding species before and after collision are uncorrelated) or the Rautian Sobel'sman function [95] (which assumes correlated velocities before and after collision). The collisional narrowing effect is characterised by a gull-wing shaped residual.

The experimental and theoretical *2f/1f* signals are compared side by side in Figure 6-18 (A) to (D) corresponding to current modulation amplitudes of 10 mA, 15 mA, 20 mA and 25 mA, respectively. The line strength and line broadening parameters used were those from the HITRAN 2012 spectroscopic database.

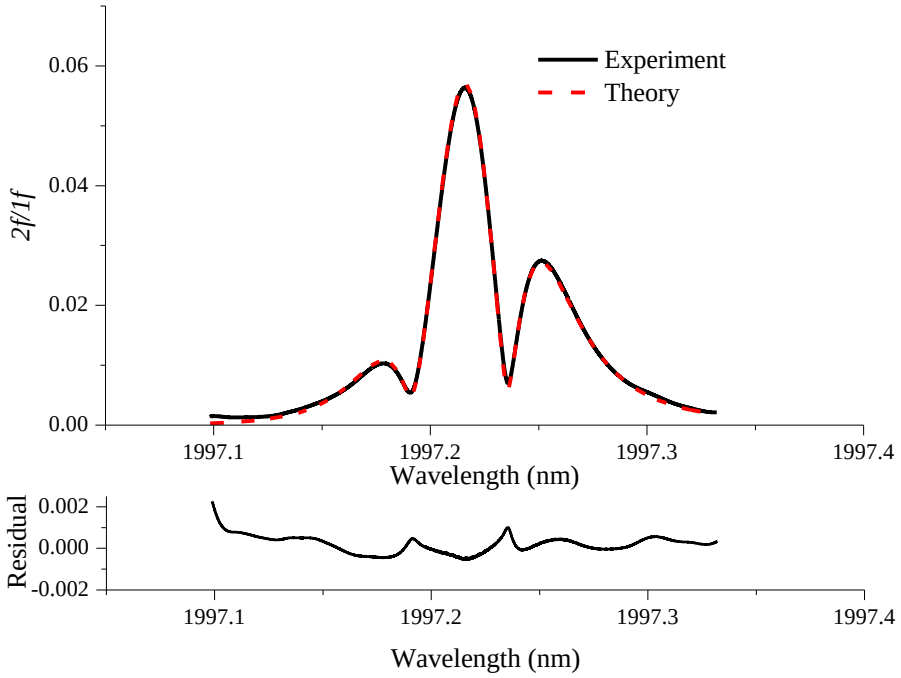
Experiment
Theory
2f/1f
0.06
0.04
0.02
0.00
1997.1
1997.2
1997.3
1997.4
Wavelength (nm)
Residual
0.002
0.000
-0.002
1997.1
1997.2
1997.3
1997.4
Wavelength (nm)

(A)

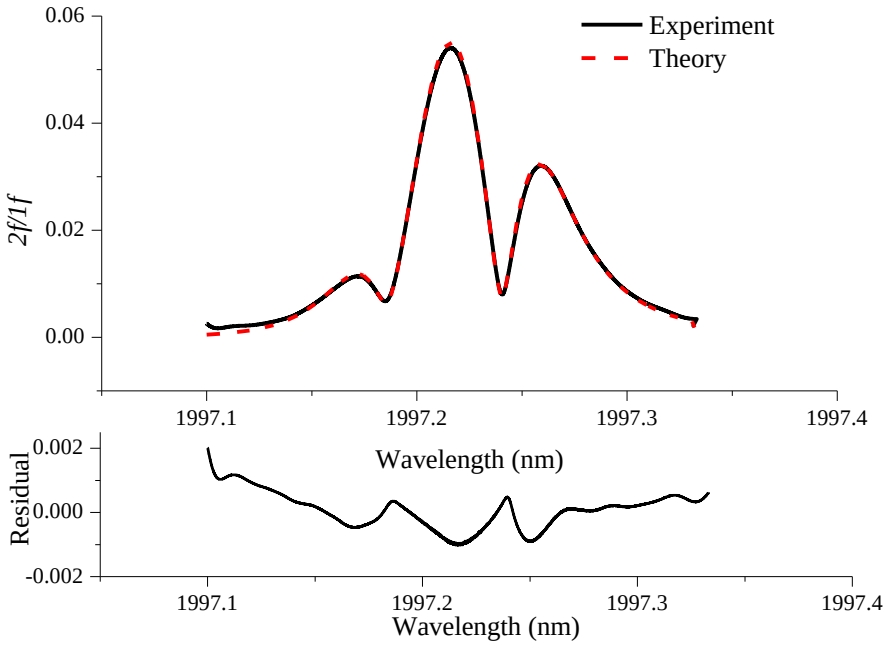
Experiment
Theory
2f/1f
0.06
0.04
0.02
0.00
1997.1
1997.2
1997.3
1997.4
Wavelength (nm)
Residual
0.002
0.000
-0.002
1997.1
1997.2
1997.3
1997.4
Wavelength (nm)

(B)

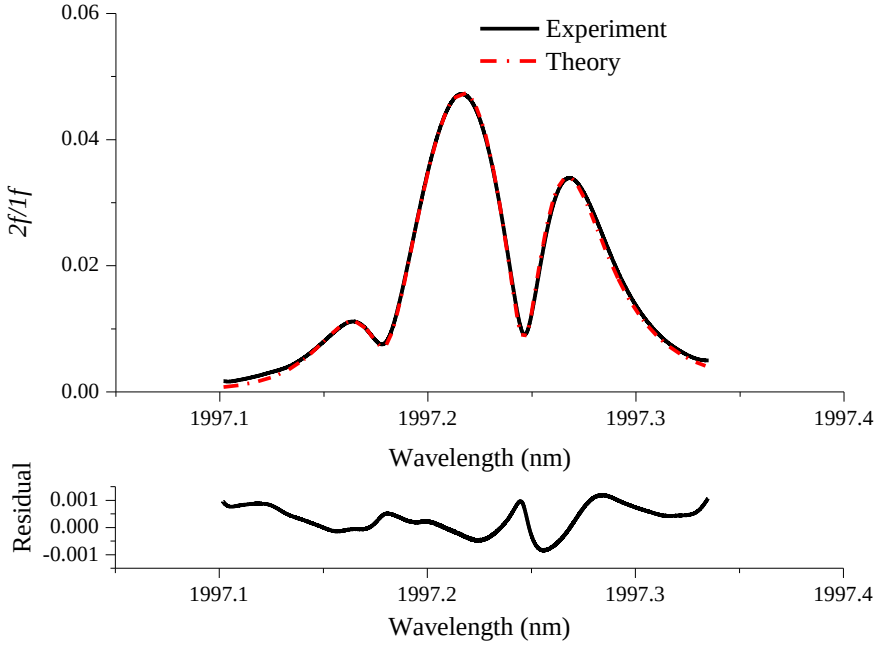

(C)

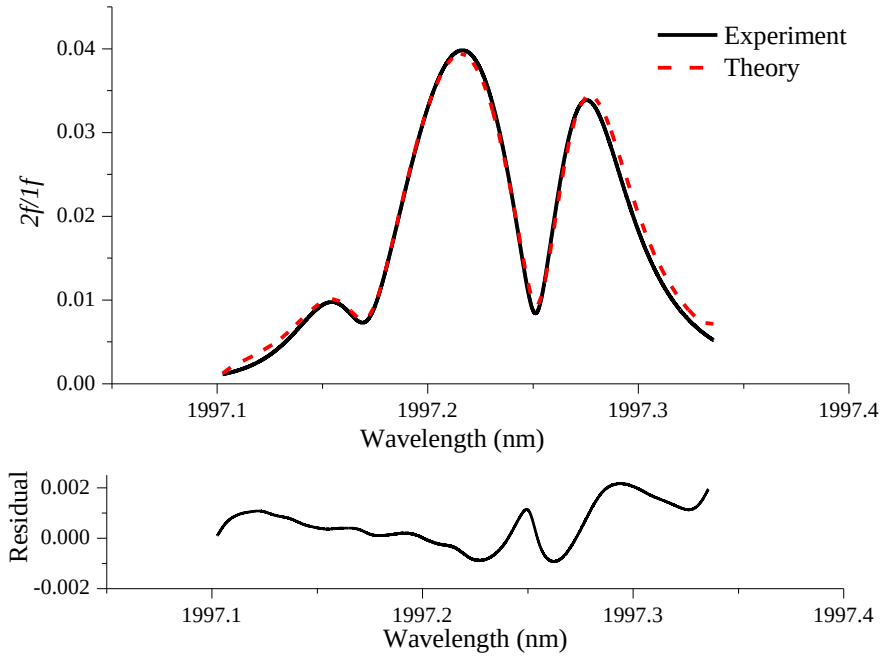

(D)

Figure 6-18. Experimental *2f /1f* spectra compared to the theoretical *2f/1f* spectra at T = 16 °C, P = 0.9995 bar, l = 5.5 cm, CO_2 concentration = 100 %, at modulation indices of (A) m = 0.8 ($\delta i = 10\ mA$), (B) m = 1.2091 (δi = 15 mA), (C) m = 1.6121 ($\delta i =$ 20 mA) and (D) m = 2.05 ($\delta i =$ 25 mA).

In the WMS model, the measured tuning coefficient, WM-IM phase values and intensity modulation amplitudes ($i_0$and i_2) are applied at each point of the current scan by interpolating these laser modulation parameters measured at discrete current steps. It was observed that the wings start to deviate from the model at higher modulation indices.

The centre wavelength of the laser was observed to shift as a function of the applied current modulation amplitude and needs to be accounted for. From the theory of wavelength modulation of DFB lasers formulated in the previous chapter, it is inferred that this phenomenon occurs as a result of the nonlinear heating effect of the applied current modulation, due to a finite electrical resistance of the laser diode.

From the theory of DFB lasers described in the previous chapter, the expression for the shift in the DFB laser centre wavelength is derived as:

$$\Delta\lambda = \frac{\Delta\lambda}{\Delta T} R_T \left\{ \frac{r_s i_m^2}{2} \right\} \tag{6.1}$$

For the 1997.2 nm DFB-MQW laser, $\frac{\Delta\lambda}{\Delta T} = 0.11\ \text{nm}/^\circ\text{C}$, the thermal resistance $R_T = 30$ °C/ W and the series resistance is approximately equal to $5\ \Omega$ (measured using high frequency electrical probes). Applying these values to equation (6.1), the shift in the central wavelength of the DFB laser due to an applied current modulation amplitude (i_m) is calculated as:

$$\Delta\lambda = 9.6 \times 10^{-6} i_m^2 \text{ (nm)} \tag{6.2}$$

The measured wavelength shift and the calculated wavelength shift, as a function of the applied current modulation amplitude is presented in Figure 6-19.

The wavelength shift was measured relative to the direct signal, by using the centre wavelength as one of the parameters in the nonlinear least-squares fitting algorithm as explained in Section 6.10.

Figure 6-19 shows that the theory developed in Chapter 5 successfully estimates the shift in the centre wavelength of the DFB laser due to an applied current modulation. This wavelength shift has a significant impact on the magnitude and shape of the

theoretical *2f/1f* spectra; consequently, the centre wavelength of the laser is used as a fitting parameter for measurement of the gas concentration and temperature from the experimental *2f/1f* line shape using the least-squares curve fit algorithm.

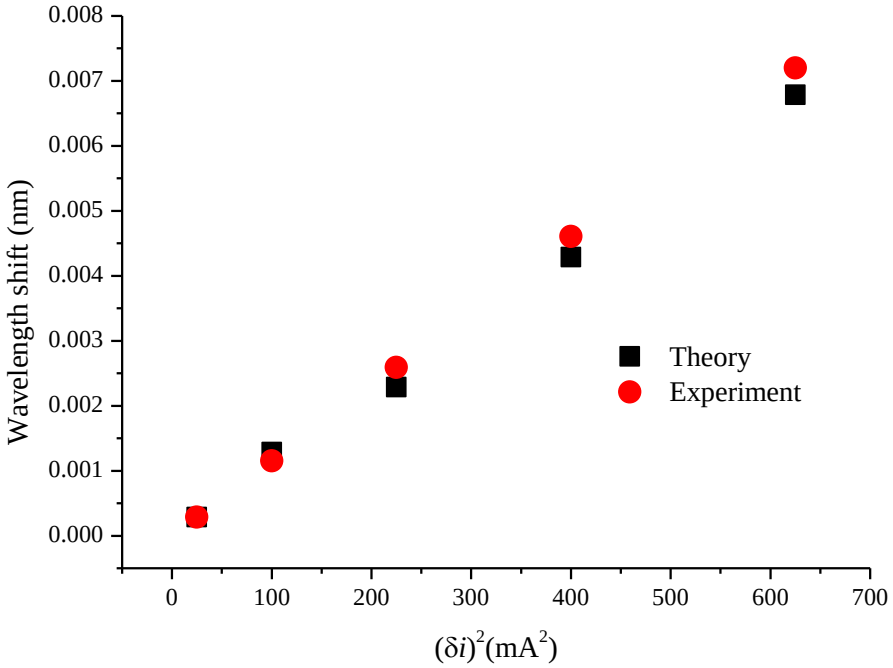

Figure 6-19. Wavelength shift as a function of the applied current modulation amplitude plotted for the experimental measurements and from the RC heat transfer model, for the 1997.2 nm DFB-MQW laser.

From these sections the two important conclusions are the validation of the *2f/1f* WMS model at ambient temperatures and analysis of the shift in centre wavelength of the DFB laser due to an applied current modulation. The following two sections are dedicated to the measurement of the spectral parameters at higher temperatures and their verification using the high temperature *2f/1f* spectra. The challenges in modelling the high temperature spectra are also discussed.

6.8 High Temperature Spectroscopy

Availability of an accurate spectroscopic database for the line width and line strength is important for modelling WMS signals. As mentioned in Section 2.12, the HITRAN database is accurate for modelling the measurements taken close to the ambient

temperatures while the HITEMP database is only accurate for spectral modelling at very high temperatures of the order of 1000 K. The expected temperature range near the detuner is approximately in between these values, i.e. from 50 to 600 °C. Hence, it was necessary to measure these spectral parameters in the laboratory.

In order to measure the line strength and line width experimentally, different approaches were used [90, 92, 96]. In this work, a least-squares fit of the theoretical Voigt absorption line shape to the measured direct spectra is used to infer these parameters [97].

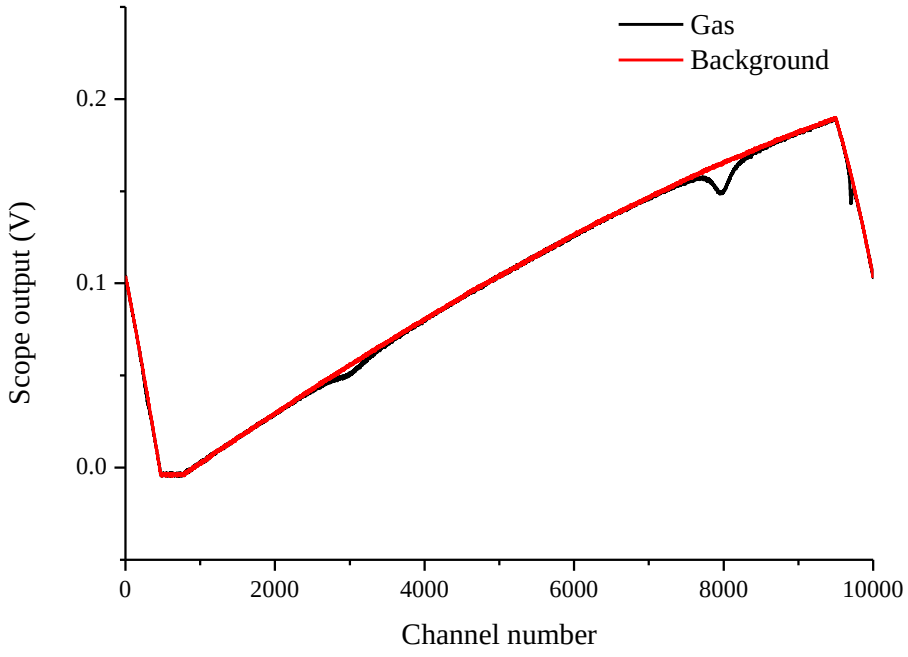

Figure 6-20. The current scan amplitude and centre bias point is adjusted so that the lower part of the current scan (95 % symmetry) goes below the threshold current of the DFB laser.

Direct spectra were measured by dividing a gas signal, with a no-gas signal obtained by purging the test gas out of the cell using a vacuum pump. In the direct measurements, it was important to subtract the offsets due to the dark voltage and varying ambient light levels. In addition to the dark voltage offset, there is also an offset from the scope as a function of the scope vertical resolution. After measuring the gas and no-gas signals, the offsets due to dark current, the stray light and the scope were measured by taking a

detector voltage measurement after blocking the laser beam or turning off the DFB laser. Even though this method compensated for the scope offsets, it might not completely mitigate the detector dark voltage and stray light offsets, which can fluctuate over time with the temperature as well as ambient lighting. For *in-situ*, simultaneous, subtraction of the dark current, the ambient light and scope offsets an easier method is to scan the DFB laser below its threshold current value, where there is no stimulated emission output from the laser and take the scope output reading below the threshold as the net offset (Figure 6-20). Amplified spontaneous emission (ASE) can occur below threshold, and hence may create errors as it is not present in the above threshold signal. For the DFB lasers, ASE is found to be very small and can be ignored.

A larger current scan was used to probe the absorption line and also sweep the current lower than the threshold value for the laser. For example, to measure the two nearby CO_2 absorption lines a current scan amplitude of 57.5 mA was applied to the DFB-MQW laser, at a bias point of 70 mA and TEC temperature corresponding to 12.2 kΩ (Figure 6-20). This scans the laser wavelength from 12.5 mA to 127.5 mA. It is observed from Figure 4-5 that the threshold current for this laser lies in the range of 20-25 mA, hence, for the lower part of the current scan, the laser is biased below threshold and gives no stimulated emission output.

The collisional broadening parameter is usually represented per atmosphere. To reduce the errors in the measurement, the collisional broadening parameter was measured at different pressures from 0-500 mbar and a linear fit of the γ-P graph gave a precise measurement of the collisional broadening parameter. Moreover, working at lower pressures reduced the blending of absorption lines, and hence spectral parameters of each line can be measured accurately, independent of the nearby absorption lines. A custom made optical gas cell (described in Section 4.4) was used to measure the spectral parameters at higher temperatures (0-600 °C) and lower pressures (1 mbar to 4000 mbar).

For a given value of the collisional broadening parameter, the area under the absorption curve (integrated absorbance) can be used to infer the gas line strength if the pressure, mole fraction and optical path length are known:

$$\mathcal{A} = P\chi lS(T) \tag{6.3}$$

The collisional broadening parameter is initially fixed to a given value and the experimental transmission curve is fit for the line strength with the pressure, temperature, mole fraction and optical path length known. Then the value of the collisional broadening parameter is changed and the fitting procedure repeated. This process is iterated until a best fit of the absorption line shape is obtained. The incremental value of the collisional broadening parameter is changed in the loop by a value comparable to its minimum percentage error reported in literature, HITRAN, as well as knowledge from previous measurements. The HITRAN values were used as the starting values in the fitting routine.

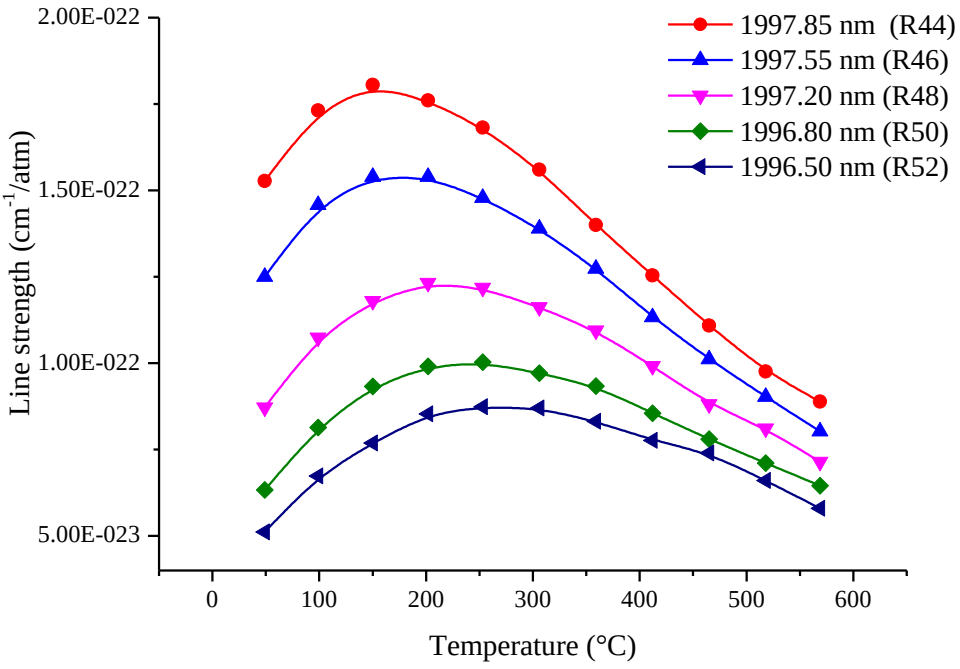

Figure 6-21. The line strength values (per molecule) measured for the different CO_2 spectral lines at 1997.2 nm.

The Doppler broadening HWHM was calculated theoretically using the formula, $\gamma_G = \nu_0\sqrt{2\ ln2\ kT/Mc^2}$, and applied to the Voigt line shape function.

Collisional line width values plotted at different temperatures were used to obtain the temperature coefficient (Δ) of collisional broadening using slope of the logarithmic plot; the y-intercept gave the collisional line width at 296 K (γ_0):

$$\gamma_L = \gamma_0 (\frac{P}{P_0}) \left(\frac{T_0}{T}\right)^{\Delta} \quad (6.4)$$

Measurements were repeated several times and the average values were taken for improved accuracy. This method is equivalent to the earlier approaches where the area under the absorption curve was used to measure the line strength and this value used in a nonlinear curve fit of the absorption line shape to infer the collisional line width, with the pressure, concentration, temperature and path length known (measured) beforehand.

Figure 6-21 shows the measured line strength values as a function of the temperature for the different transitions of CO_2 that could be accessed with this laser. It was noticed that the similar slope for the curves makes it difficult to achieve good temperature sensitivities using these lines in RT applications. It is observed that the line strength peaks at a temperature of approximately 250 °C. This can be related to the population density behaviour of the lower state energy levels.

Figure 6-22 shows a comparison of measured line strength values for the chosen R48 line compared to HITRAN 2012 spectral database. It is noticed that the line strength values coincide at lower temperatures.

The actual composition of an aero engine plume will be a mixture of several gas molecules. The net broadening is determined by the concentration of the target gas as well as the other gas molecules present in the GTE plume. The net collisional line width is given as a sum of the broadening coefficient for each gas molecule multiplied by its concentration. The broadening coefficient due to the target gas species is referred to as the self-broadening coefficient and other species is referred to as the cross-broadening coefficients. Spectral modelling using the air-broadening coefficients is expected to bring the collisional width closer to the actual value in the plume. HITRAN usually gives the air-broadening coefficient. The self-broadening and air-broadening coefficients were also measured in the lab at higher temperatures.

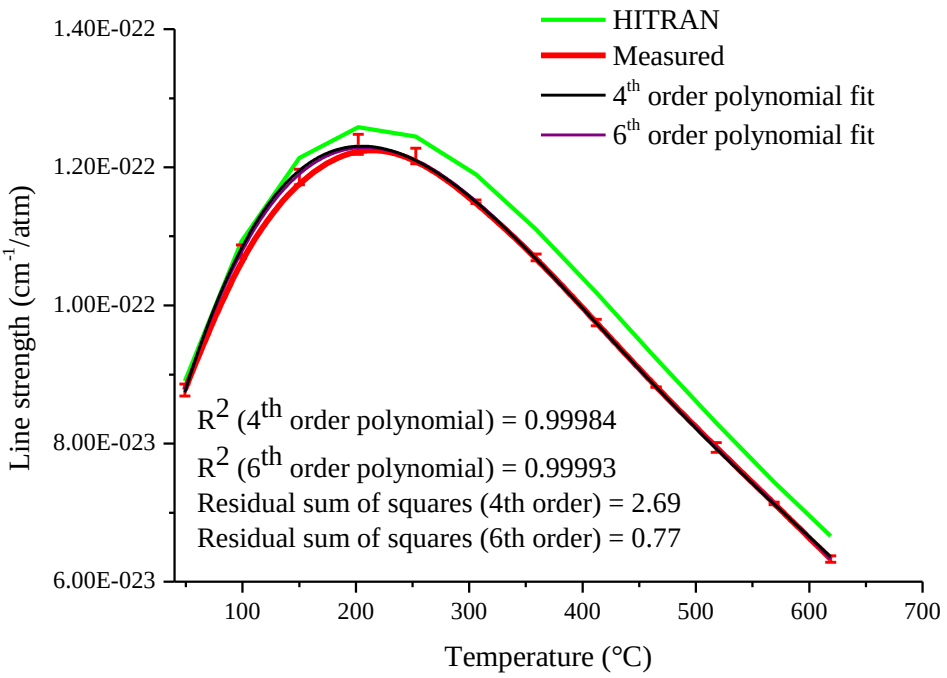

Figure 6-22. Measured and HITRAN line strength values vs. temperature, for the R48 rotational-vibrational transition of CO_2. A 6th order polynomial fit of the line strength vs. temperature for R48 absorption line will be used in the fitting algorithm to obtain the concentration and/or temperature.

A comparative analysis was done against the spectral databases such as HITEMP, Carbon Dioxide Spectral Database (CDSD) (contains spectral parameters for temperatures up to 2000 °K) and HITRAN ,and also the data published on CO_2 by Rieker et al. [93]. It could be observed that the measured γ_0 and Δ values are close to the values given in the HITRAN 2012 and CDSD databases. However, the measured line strength values showed a relatively larger variation from the values given in the various spectral databases. In subsequently recorded direct spectra at different conditions of pressures, temperatures and concentrations, the theoretical direct absorption line shapes gave a good match to the experimentally obtained direct absorption line shapes, as shown in Figure 6-23 for one of the measured direct traces. The results obtained using high temperature direct measurements (Figure 6-23) justified that the measured spectral parameters were accurate. Figure 6-23 indicates that the spectral parameters measured in this work gave a far better fit to the experimental absorption feature compared to the

spectrum modelled using the HITRAN 2012 values. In Section 6.9, these parameters are further validated using the *2f*/*1f* WMS signals.

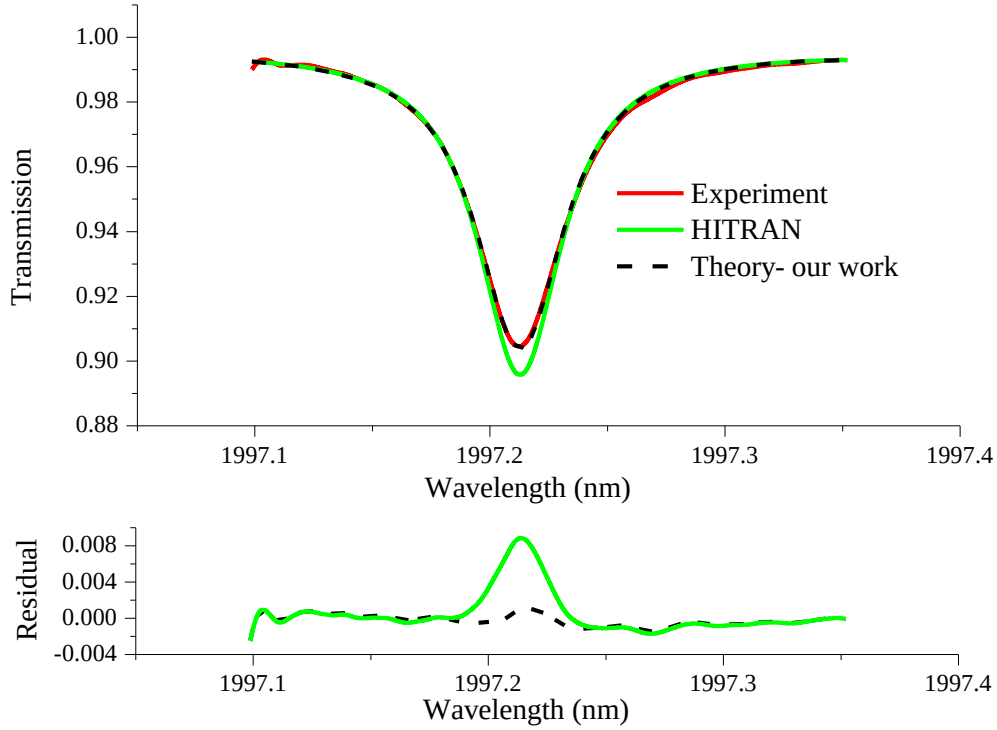

Figure 6-23. Experimental direct transmission compared against theoretical transmission spectrum, calculated using the measured as well as HITRAN line strength and collisional broadening parameters. P = 1 bar, T = 518 °C, C = 100 % and l = 5.5 cm. Absence of any structure in the residual proves that the Voigt line shape accurately models the R48 absorption line of CO_2.

6.9 High Temperature WMS Modelling

The measured spectral parameters at high temperatures are further validated by applying these values to the *2f*/*1f* WMS model described in Chapter 3. The laser modulation parameters such as the tuning coefficient, the linear and nonlinear IM amplitudes, the linear and nonlinear WM-IM phase lags, DC laser scan wavelength etc. were measured at each point of the current scan and used in the WMS model. These parameters were measured with an empty gas cell or measured directly from the laser output via. an attenuator (to prevent detector saturation) and a detector.

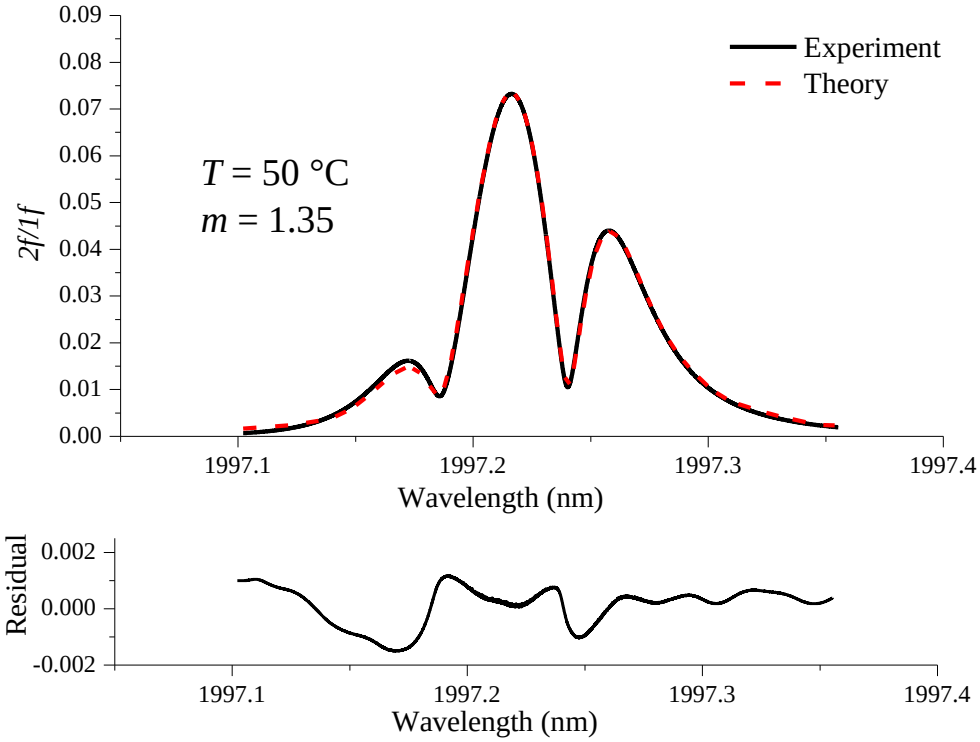
Experiment
Theory
T = 50 °C
m = 1.35
2f/1f
0.09
0.08
0.07
0.06
0.05
0.04
0.03
0.02
0.01
0.00
1997.1
1997.2
1997.3
1997.4
Wavelength (nm)
Residual
0.002
0.000
-0.002
1997.1
1997.2
1997.3
1997.4
Wavelength (nm)

(A)

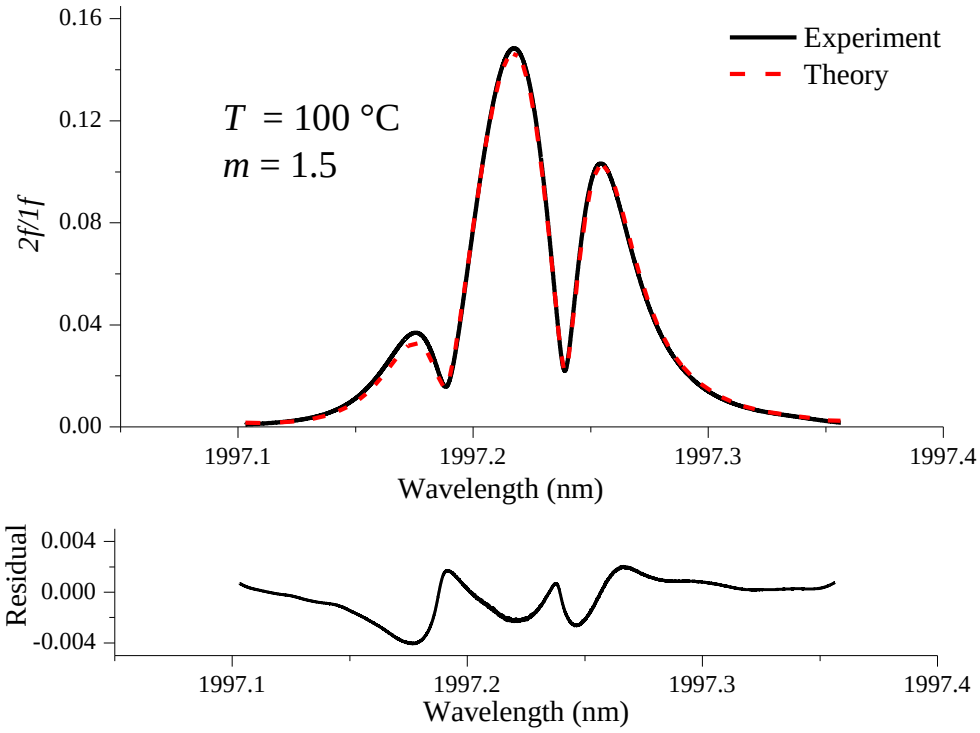
Experiment
Theory
T = 100 °C
m = 1.5
2f/1f
0.16
0.12
0.08
0.04
0.00
1997.1
1997.2
1997.3
1997.4
Wavelength (nm)
Residual
0.004
0.000
-0.004
1997.1
1997.2
1997.3
1997.4
Wavelength (nm)

(B)

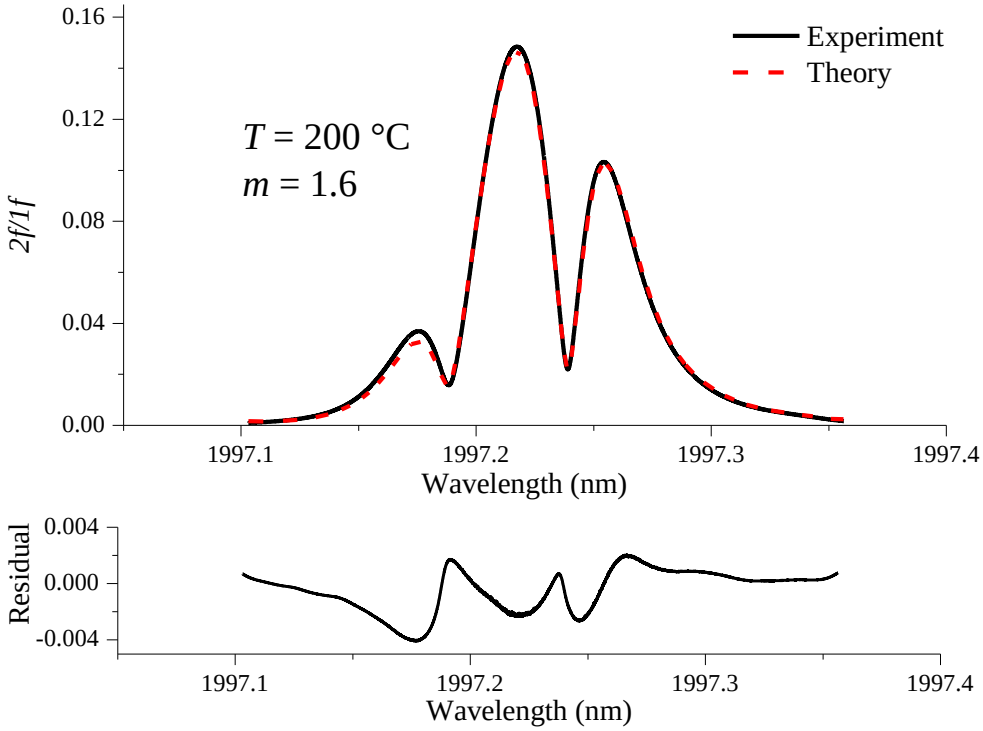
Experiment
Theory
T = 200 °C
m = 1.6
2f/1f
0.16
0.12
0.08
0.04
0.00
1997.1
1997.2
1997.3
1997.4
Wavelength (nm)
Residual
0.004
0.000
-0.004
1997.1
1997.2
1997.3
1997.4
Wavelength (nm)

(C)

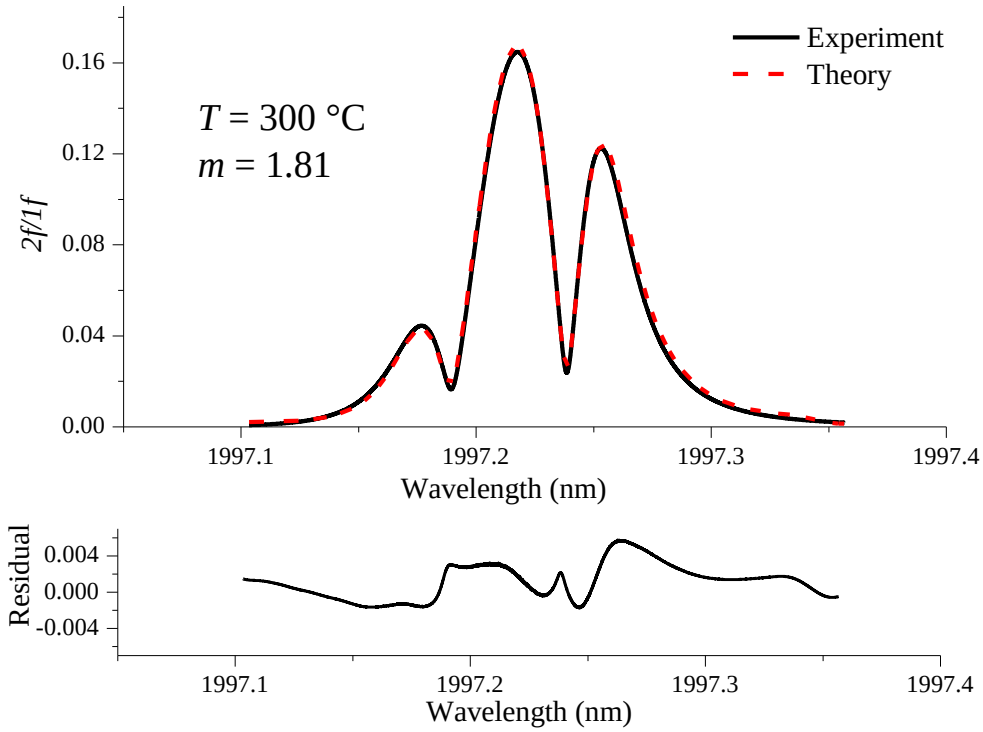
Experiment
Theory
T = 300 °C
m = 1.81
2f/1f
0.16
0.12
0.08
0.04
0.00
1997.1
1997.2
1997.3
1997.4
Wavelength (nm)
Residual
0.004
0.000
-0.004
1997.1
1997.2
1997.3
1997.4
Wavelength (nm)

(D)

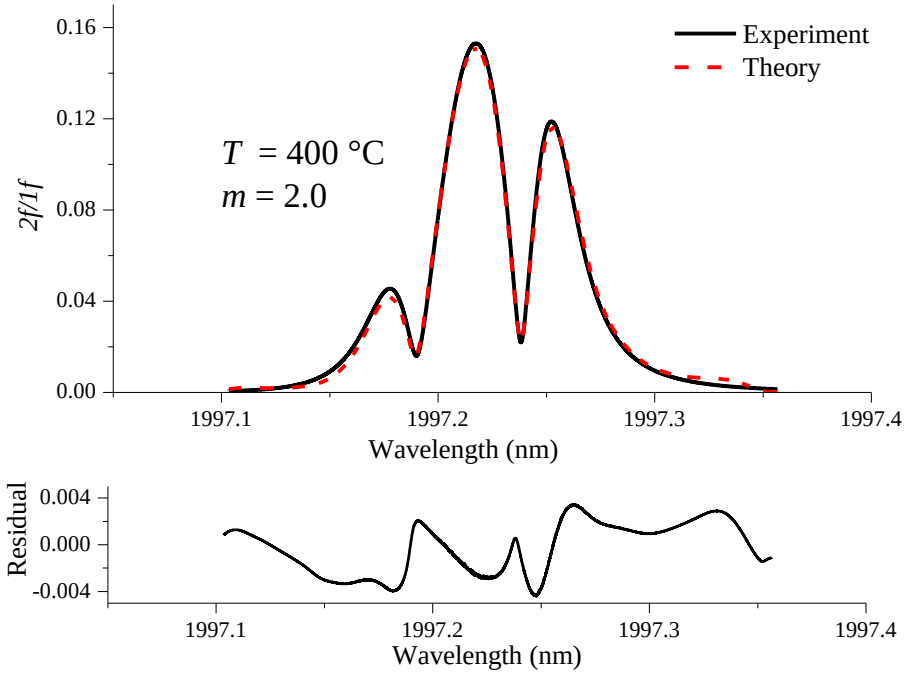

(E)

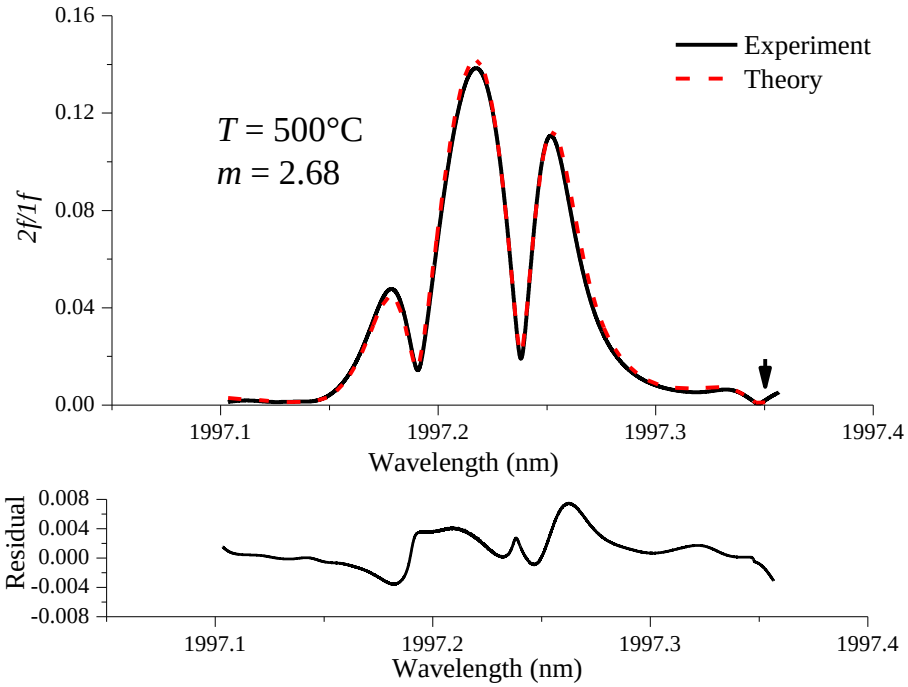

(F)

Figure 6-24. Measured *2f/1f* spectra of CO_2 compared to theoretical WMS models at a pressure of 1.029 bar, concentration = 100 %, path length = 5.5 cm and at temperatures ranging from 50 °C to 500 °C (A-F). The arrow at 500 °C corresponds to a hot line of CO_2.

The DC laser wavelength scan is measured after the laser has reached a steady state (approximately 30-45 minutes for DFB lasers). The gas cell was heated and CO_2 gas was allowed to flow through it at atmospheric pressure. The no-gas signals were obtained by flowing N_2. It was inferred that the gas flow took approximately 5 minutes to stabilise in temperature from the readout of the in-cell thermocouples. The drift in the *2f*/*1f* signal over time was negligible.

Figures 6-24 (A)-(F) show the measured *2f*/*1f* spectra at temperatures from 50 °C to 500 °C, compared to WMS Fourier model. It can be seen that all experimental WMS spectra match well with the theory. For high temperature measurements, it was important to include the nearby CO_2 lines in HITRAN. There is a slight mismatch at the wings and the two side lobes which could be due to several reasons; for example, it could be due to the inaccurate spectral modelling in the wings, there could be several lines missing in the HITRAN 2012 database (a strong $C^{13}O_2$ absorption line is observed towards shorter wavelengths). Moreover, numerous hot lines of CO_2 could be observed at higher temperatures. Another possible reason could be an etalon in the system, not completely cancelled by the background subtraction.

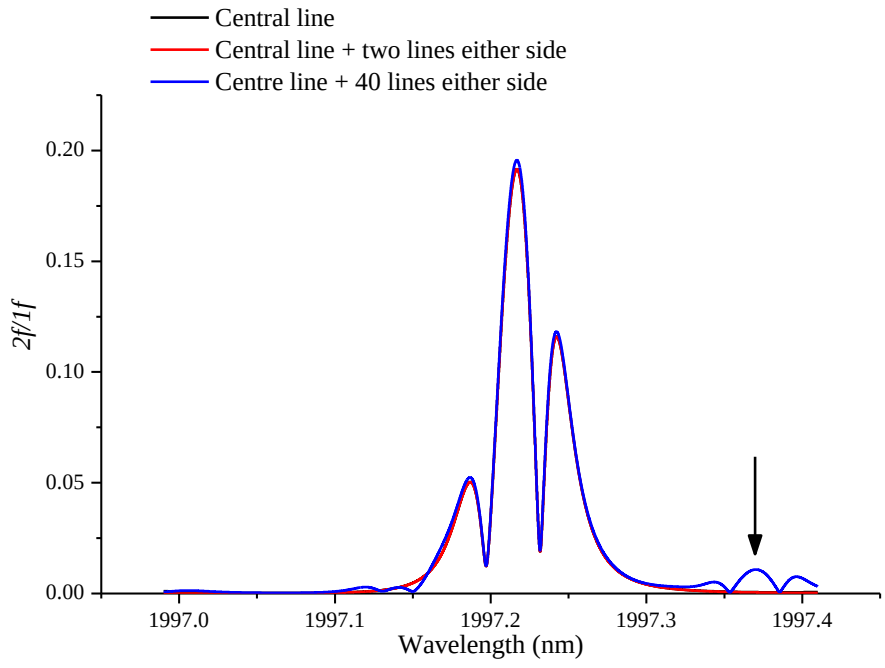

Figure 6-25. Theoretical modelling shows the hot lines of CO_2 that begin to appear at higher temperatures. The spectra is modelled for T = 500 °C, P = 1 bar, l = 5.5 cm and C = 100 %.

For the measurements at higher temperatures up to 400 °C, only the central strong line of CO_2 and the two strong lines either side were necessary to model the CO_2 absorption feature at 1997.2 nm. At 500 °C, several hot lines of CO_2 were observed and including the nearby lines in HITRAN was necessary to accurately model the *2f*/*1f* spectral feature, even to accurately model its peak. The hot lines are not apparent from Figure 6-24 as a smaller current scan was used. When a large current scan was used, it was observed that hot lines of CO_2 started to appear, that cannot be excluded from the spectral modelling. This is depicted in Figure 6-25 for a temperature of 500 °C, where the strong line and 80 weaker lines from HITRAN were used to model the spectrum.

While modelling direct spectra, including the nearby prominent spectral transitions was important, as it will affect the peak and wings of the spectra. Whereas, for the *2f*/*1f* method, it is found that the central strong line is sufficient to accurately model the absorption feature. This is due to the lower sensitivity of the *2f*/*1f* spectra to the integrated absorbance (concentration and temperature) and slightly increased sensitivity to line width, at $m = 1.06$, compared with the direct spectra [31]. This is shown in Figure 6-26. Due to this, while modelling the *2f*/*1f* spectra it was only required to use a single strong line for representing the spectra with sufficient accuracy. As mentioned before, an exception for this is at higher temperatures of the order of 500 °C where several hot lines start to appear and the spectra can no longer be modelled with the prominent CO_2 absorption lines. This is indicated in Figure 6-25, which shows a theoretical simulation using the HITRAN database at 500 °C. It can be seen that small CO_2 absorption lines start to appear. Hence, to accurately model the experimental *2f*/*1f* spectra at 500 °C, the nearby smaller lines from HITRAN database had to be included in the model. This theoretically modelled hot line (black arrow) is also highlighted in the experimental data in Figure 6-24 (F). It is to be noted that, including more spectral lines increase the execution time of the model for the fitting algorithm. This can be important in the FLITES measurement system where nearly 630 (126 channels x 5 Hz) spectral acquisitions are generated per second, which requires faster processing speeds. Hence, a balance has to be established between the spectral modelling accuracy and the time for execution. Including two nearby lines was sufficient to obtain the required accuracy and precision for the concentration and temperature values.

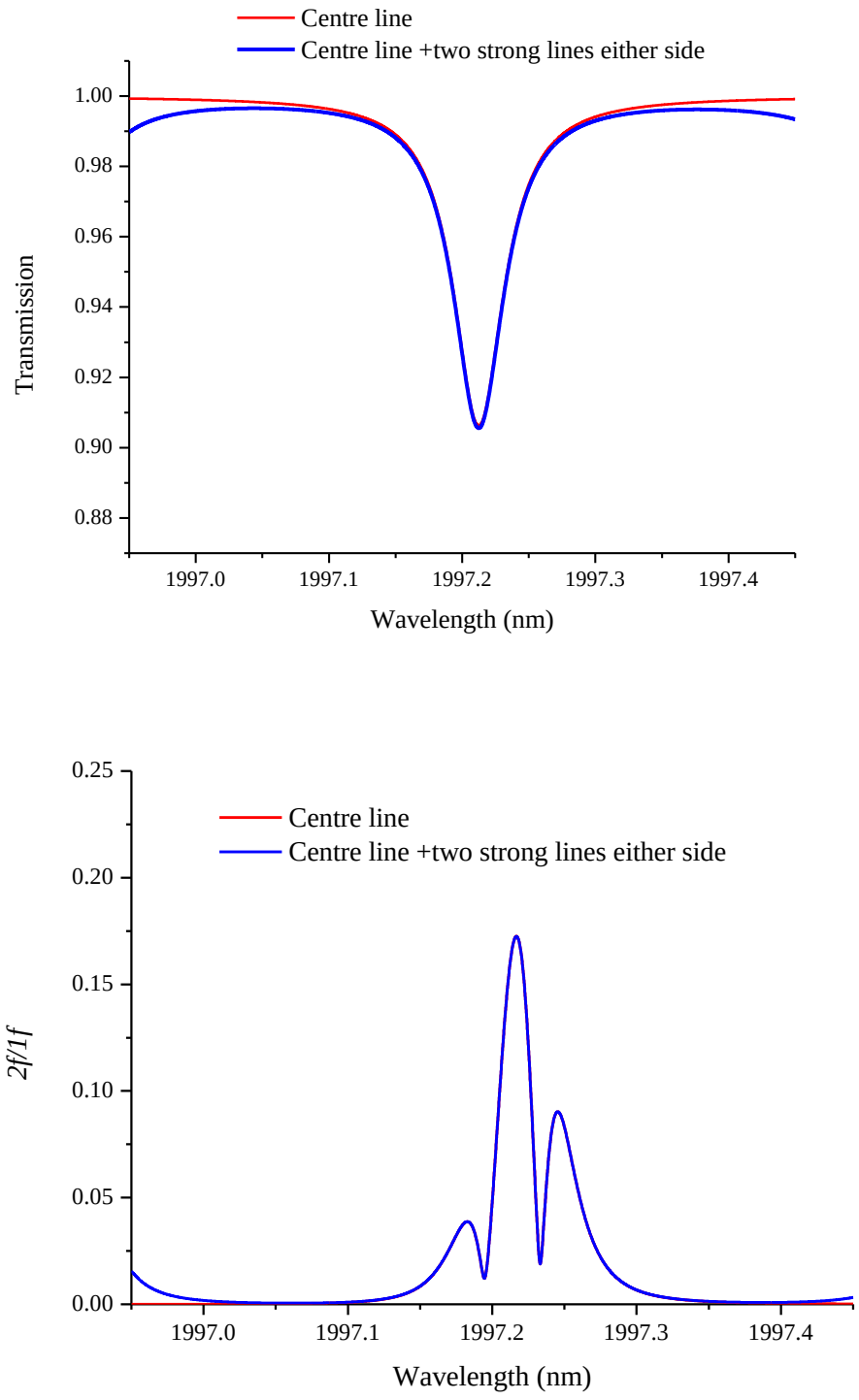

Figure 6-26. Variation in the wings for *2f/1f* spectra and direct spectra modelled using only the strong transition (R48) and by using the two strong transitions (R46 and R50) on either side of R48. T = 20 °C, P = 1.013 bar, C = 100 %, l = 5.5 cm, m = 1.06. It can be seen that the *2f/1f* spectra is less sensitive to the overlapping lines, especially at the line centre and part of the spectra near the two side lobes.

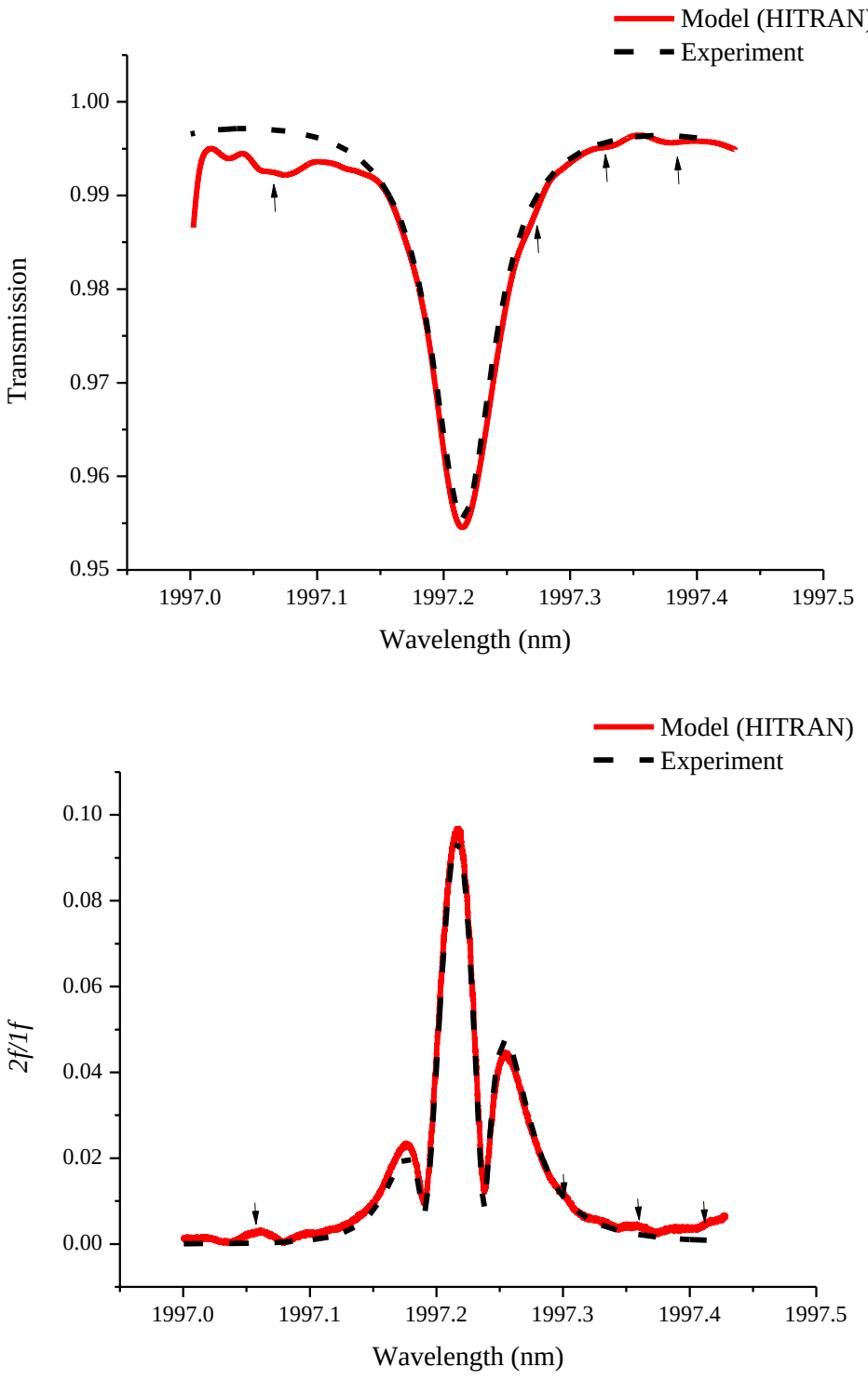

Figure 6-27. RTP measurements using another 2 μm InGaAsP multi-quantum well laser diode with a different WM response. Frequency = 100 kHz, pressure = 1.016 bar, path length = 5.5 cm, concentration = 100 %, temperature = 19 °C and modulation index = 0.86 (corresponding to a 10 mA current modulation amplitude). The direct spectrum is also shown for consistency of the results.

Small water vapour lines can interfere with the *2f*/*1f* spectra near the far-wings. These lines were due to the moisture present in the outer gas cell. Nonetheless, it is important to account for these lines as they will be present in the actual measurements as water vapour is one of the by-products of combustion.

Figure 6-27 shows the *2f*/*1f* spectra measured using a different InGaAsP multi-quantum well DFB laser (Eblana Photonics) emitting at the same wavelength, measured at a current modulation frequency of 100 kHz. The laser was manufactured with a similar structure, but was 200 μm shorter in chip length compared to the other laser. This caused it to have an increased nonlinear intensity response, as well as different wavelength modulation characteristics. This topic is not discussed further, however, the theoretical *2f*/*1f* spectra showing excellent correlation with the experimental spectra for this laser emphasises the applicability of approach to a wide variety of DFB lasers with distinct modulation characteristics. These measurements were taken using a different gas cell. It can be seen that the spectra are different in the wings owing to a large etalon formed in the glass cell windows, with an FSR comparable to the line width of the gas absorption feature.

It is concluded that inadequate spectral modelling of CO_2 mainly affects wings of the modelled WMS signals. Hence, the spectral information away from the two side lobes was not used to infer the gas thermodynamic state variables of concentration and temperature or pressure.

6.10 CO_2 Concentration Sensor

In this section, the development of a concentration sensor is discussed, operating at ambient and elevated temperatures expected in a GTE exhaust plume. Concentration measurements obtained from the fit of the peak values of the absorption line shape (WMS or direct) or fit of the entire absorption line shape has been implemented by several groups, with the temperature already measured using other methods such as RT. Fitting using the line centre absorption is useful if the line shape is poorly modelled using the spectral parameters or the line shape function, whereas, fitting the entire absorption line shape would give increasingly accurate results for a noisy signal. In this work, concentration values are measured in the lab using a fit of the *2f*/*1f* line shape at

room temperature and at high temperatures, with the pressure and temperature known beforehand. The centre wavelength of the laser was seen to drift over time. This is in addition to a shift in the centre wavelength, caused due to the nonlinear heating effect of the current modulation. Moreover, it was not possible to incorporate a fibre ring resonator into the rig for wavelength referencing each measurement, due to the temperature and mechanical stability issues faced by the fibre optical ring resonator. Hence, the centre laser wavelength was also used as fitting parameter in the algorithm.

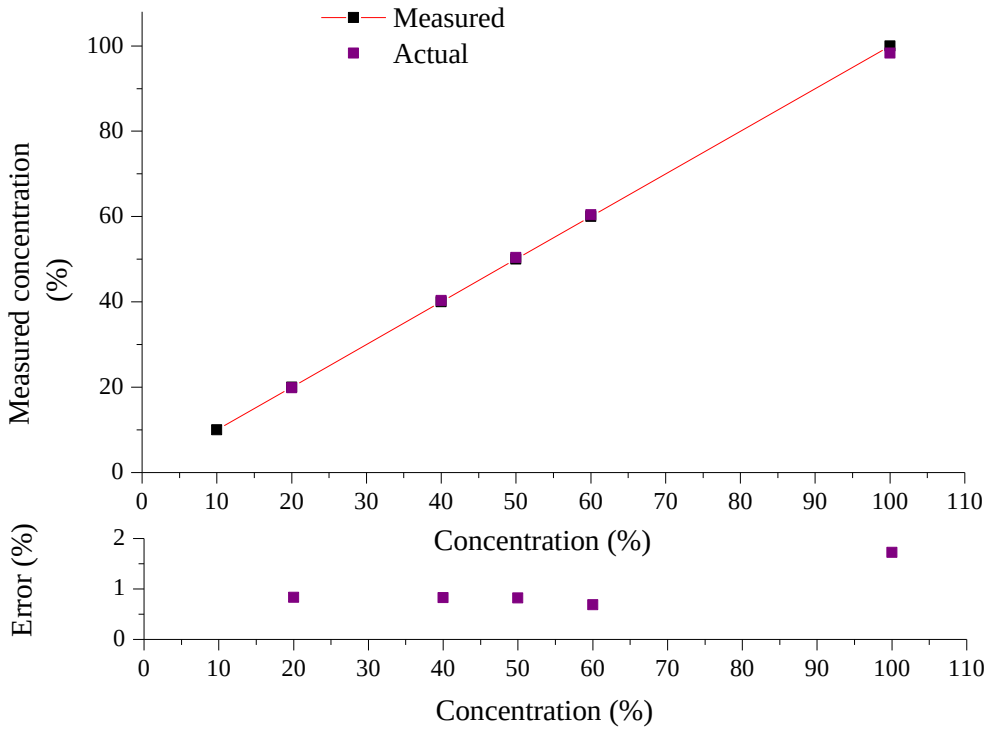

Figure 6-28. Measured CO_2 concentrations at a temperature of 17 °C and pressure of 0.9995 bar, for calibrated mixtures of CO_2 in N_2. Modulation index is equal to 0.8.

Initially, the concentration sensor is validated at ambient temperatures and pressures. The pressure is measured using a gauge attached to the cell inlet and the temperature is measured *in-situ* using four K-type thermocouples placed at different positions along the cell as described in Section 4.4. A gas mixture with a given concentration of CO_2 was obtained by flowing CO_2 and N_2 at predetermined flow rates. For example, a 50 % CO_2 mixture is obtained by flowing CO_2 and N_2 at equal flow rates (~50 ml/min) using a mass flow controller. Figure 6-28 shows the measured concentration values from *2f*/*1f*

spectra for calibrated gas mixtures at ambient temperature and pressure. The line strength and line width values of the HITRAN 2012 database were observed to be accurate near room temperatures, and hence used in the fitting algorithm.

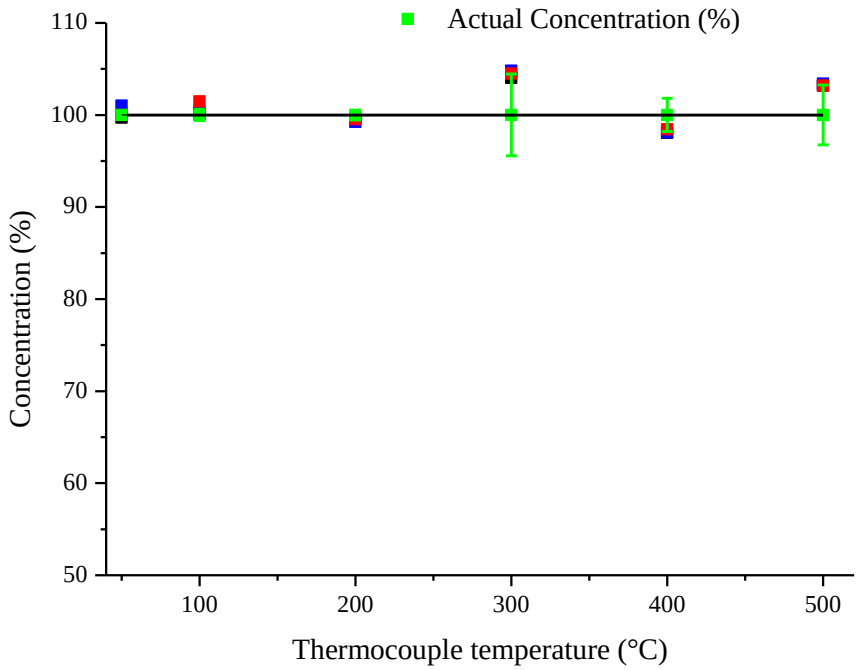

Figure 6-29. Concentration values measured at high temperature for pure CO_2. C = 100 %, P = 1.029 bar, and m values vary from 0.8 to 2.1.

The average error between the measured and the actual concentrations was found to be 0.97 % for room temperature measurements and 1.81 % for the concentration measurements at higher temperatures.

Concentration values are also measured at high temperatures with pure gaseous CO_2 (100 %) at ambient pressure. The line strength and line width parameters used to model the theoretical *2f/1f* signals were experimentally measured as described in Section 6.8. Figure 6-29 shows the recovered concentration values at different temperatures. The average error is found to be approximately equal to 2 %, with a standard deviation of 2.9 %. These values are found to be within the error bars that had previously been reported using analogous *2f/1f* WMS techniques [27, 47]. The nonphysical concentration values greater than 100 % resulted from the number density (N_g) values exceeding the

actual value corresponding to that particular gas temperature and pressure. The above results demonstrate that it was possible to accurately obtain the CO_2 concentration values (with the temperature and pressure known) by a nonlinear least-squares curve fit of the *2f*/*1f* absorption line shape. Fitting approach using the peak values of the *2f*/*1f* line shape also give similar results, however, it may have an increased susceptibility to noise for the field measurements.

6.11 Concentration and Temperature Determination

Section 6.10 has described how a least-squares nonlinear curve fit of the theoretical model to experimental *2f*/*1f* line shape could be used to extract the gas concentration with the temperature, pressure, all the other laser modulation and spectral parameters known.

This is an ideal situation, however, in most practical gas sensing scenarios, the temperature of the probed region is unknown, as is the case for the GTE exhaust plume. Hence, it was envisaged that it would be useful to measure the CO_2 concentration and temperature, simultaneously, by a nonlinear curve fit of the entire CO_2 absorption line shape (excluding the wings far from the two side lobes due to the reasons outlined in Section 6.9). Three unknowns were used in the fitting routine viz. the concentration, temperature and centre wavelength of the DFB laser. This is similar to the approach very recently implemented by Qu et al. [2, 87], where two nearby strong absorption lines are used to simultaneously fit for concentration, temperature and wavelength modulation amplitude using the spectroscopic parameters from the HITRAN 2012 database. Even though two strong absorption features, could improve the accuracy as it fits for more information, in this work, only a single absorption feature has been used to simplify the data post processing for FLITES, as well as, not to go into the complexities of high temperature spectral characterisation of multiple lines (though, the two strong lines either side have been used in the WMS fitting algorithm using their spectral values given in HITRAN). Furthermore, spectra encompassing multiple absorption lines may have interference from water vapour; the longer path length in an aero engine plume will enhance the intensity of the water vapour lines in the spectrum, which can be difficult to model. Another way this method differs from the approach by Qu et al. as well as the

methodologies used by Goldstein [27] and Sun [98], is that the laser IM and WM parameters are measured beforehand.

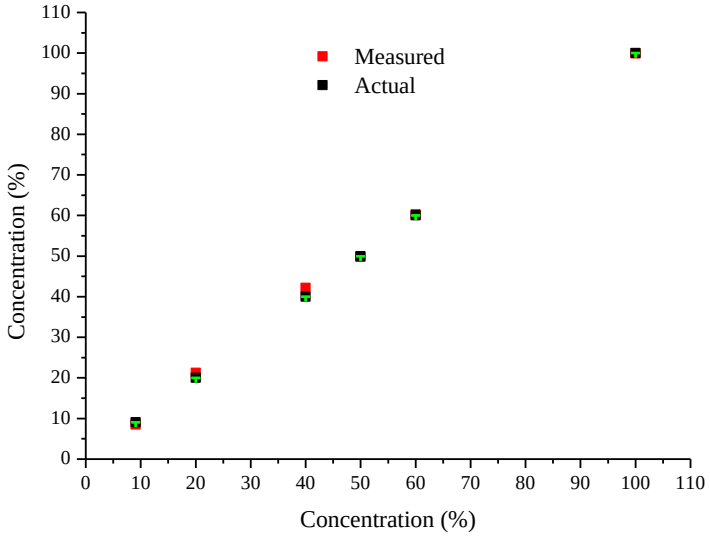

Figure 6-30. Concentration values obtained by a multi-parameter fit of room temperature WMS-*2f/1f* spectra. The concentration, temperature and the laser centre wavelength were used as the fitting variables in the least-squares algorithm. The error bars indicate the difference in the measured values from the actual values (calculated from the flow rates of CO_2 and N_2 (buffer)).

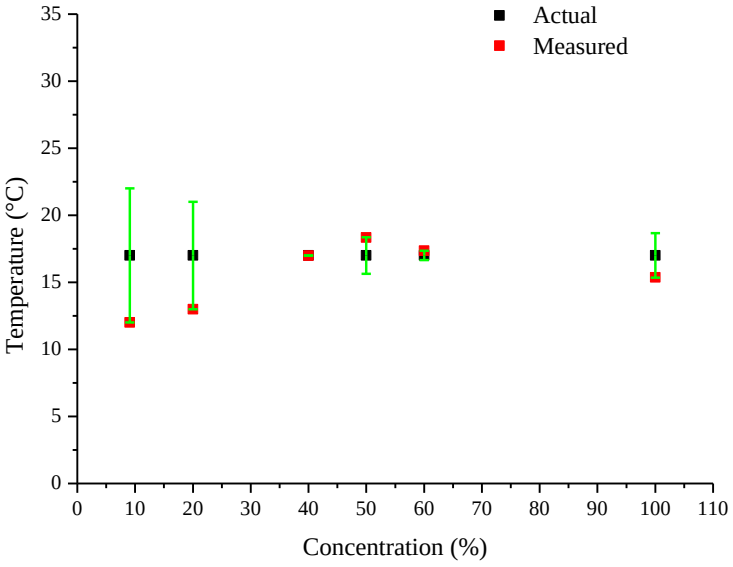

Figure 6-31. Temperature values obtained by a multi-parameter fit of the room temperature *2f/1f* spectra.

Using a single absorption feature also has the advantage of reducing the signal processing overhead, important for the FLITES project. Moreover, scanning the laser to encompass two absorption features could create difficulties in accurate spectral modelling due to a larger gradient in the wavelength modulation parameters for some lasers, especially if these wavelength modulation parameters are prone to drift over time. For example, when the laser was transferred to the test cell at INTA, Madrid, due to the change of temperature in the test cell, the laser modulation characteristics were observed to drift from the values measured in the lab, which necessitated an *in-situ* recalibration.

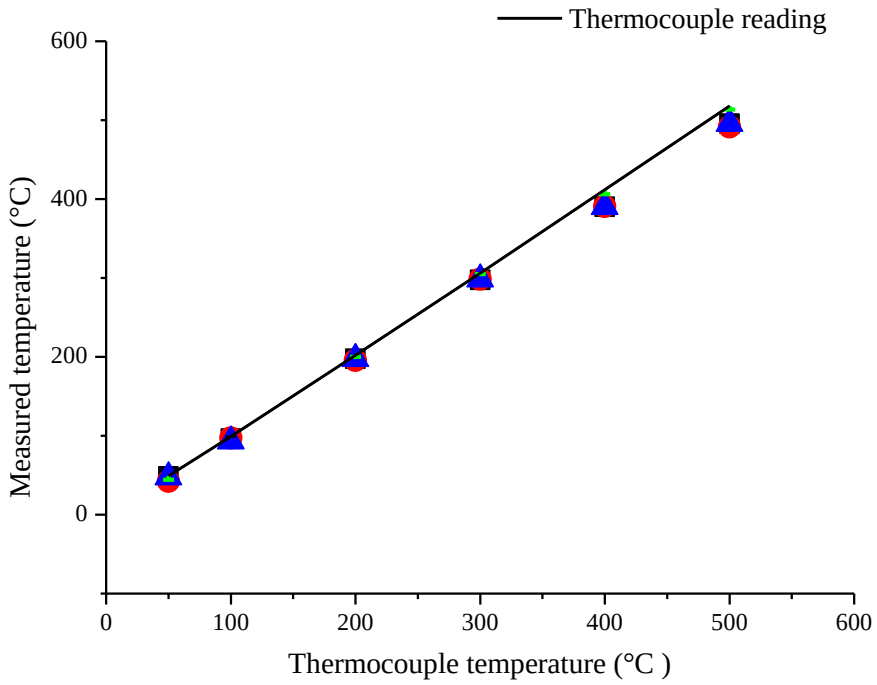

Figure 6-32. Recovered temperatures values by a multi-parameter fit of the spectra measured using the heated optical gas cell (Section 4.4).

Figures 6-30 and 6-31 show recovered concentration and temperature values using calibrated mixtures of CO_2 at RTP by a nonlinear least-squares fit. Similar to Section 6.10 , the HITRAN 2012 spectral values were used. The recovered concentration values were accurate, with an average error of 1.629 % and a standard deviation of 2.75 %.

The measured temperature values showed more inaccuracy; with an average error of 4.94 % and standard deviation of 7.3 % (excluding the two values at lower concentrations).

The measurements taken at higher temperatures using the measured line strength and line width values are shown in Figures 6-32 and 6-33.

The temperature was calibrated using four K-type thermocouples along the gas cell as described in Section 4.4. The results were close to the expected values; having an average error of 3.39 % for concentration and 3.72 % for temperature, with a standard deviation of 3.9 % and 2.05 %, respectively.

The *lsqnonlin* function in Matlab® was used to implement a Levenberg Marquardt algorithm based least-squares curve fit, with the functional tolerance set to 10^{-4}. The increased error at higher temperatures could be reduced by including the nearby hot lines of CO_2 in the model, as depicted in Figure 6-25.

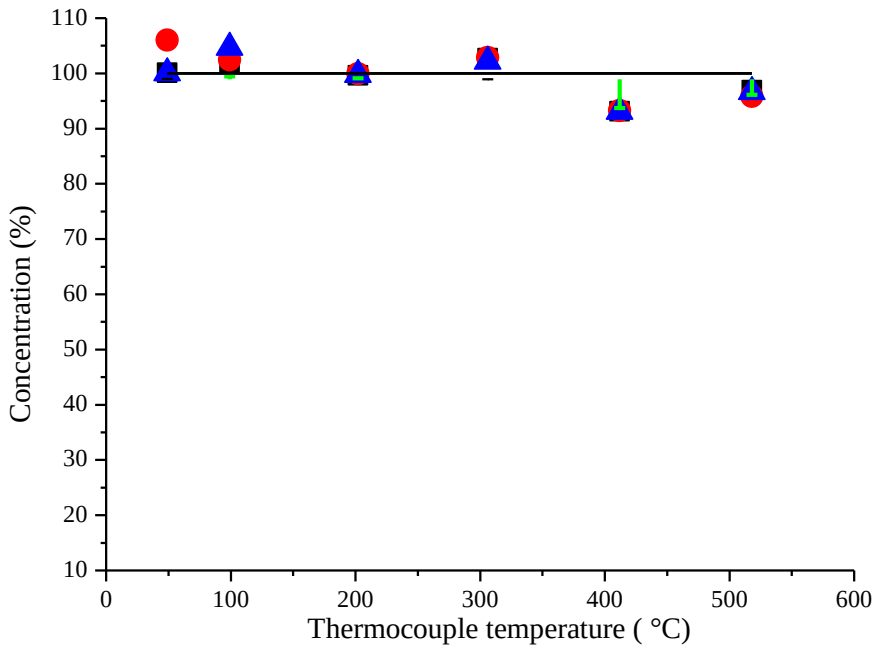

Figure 6-33. Recovered concentrations by a multi-parameter fit, using a heated optical gas cell. The black line indicates the actual concentration of CO_2 which in this case is 100%.

These results validate the WMS sensor methodology in the laboratory for simultaneous measurement of CO_2 concentration and temperature by a least-squares curve fit of the absorption feature at 1997.2 nm. This technique was used for the aero engine measurements in the Rolls-Royce test bed at East Kilbride and will be used for the multi-channel measurements for tomographic imaging in a GTE exhaust plume at INTA.

6.12 Measurement Rig at the Rolls-Royce Test Facility

Before performing the multi-channel measurements for optical tomography, it is necessary to test the *1f* normalised *2f* WMS technique for a single channel measurement of CO_2 concentration and temperature across an aero engine exhaust plume.

A measurement rig for single channel measurement was set up at the Rolls-Royce test facility located in East Kilbride, Scotland, UK. The CO_2 measurements across the aero engine exhaust plume were taken at the detuner, located 4 m away from the engine exhaust. The on-site measurement setup is similar to the rig set up in the lab. The transmission side consists of the 2 mW 1997.2 nm DFB-MQW laser which is attached to a fibre coupled collimator (Thorlabs) using long telecommunication grade single mode optical fibre (SMF-28®) cables coupled to each other using two removable mechanical connectors (total length ~30 m). The SMF-28 fibre maintained single mode operation at 2 μm which could be inferred from the V parameter calculated to be around 2.2 for that wavelength (V < 2.405 for single mode propagation through an optical fibre). Single mode operation has several advantages such as reduced modal noise, fibre losses etc. A 2 μm fibre coupled collimator was used because the standard telecommunications grade fibre collimator at 1550 nm was measured to have a significantly higher beam divergence at 2 μm. Even though the *1f* normalised *2f* technique is independent of the intensity of the beam falling on the detector, it is preferable to get as much signal through as possible without saturating the detectors. From the detector responsivity, it was estimated that the detector saturates at a power of about 1 mW. Furthermore, too much optical power causes the detector to work in a nonlinear response regime which can cause it to have different intensity modulation characteristics (i_0 and i_2) as a

function of the bias current, different from the characterised values, and must be avoided. The receiver side consists of a short focal length (= 5 cm) aspherical mirror with a detector at its focal point. The transmitter and receiver optics are mounted in two heavy steel boxes bolted down to the detuner ring. The heavy steel plates ensure minimal mechanical disturbance of the optical components. The measurement rig is shown in Figures 6-34 and 6-35. Figure 6-34 shows the launch and receive electronics rig.

The temperature of the laser is controlled by a PID controller (TED 2000). The laser is driven by a 5 Hz current ramp and a 200 kHz sinusoidal current modulation, using two signal generators and a bias-T network (Section 6.5). The detector output is connected via long BNC cables (~30 m) to a trans-impedance amplifier for impedance matching; the output of the trans-impedance amplifier is connected to two Perkin Elmer 7280 lock-in amplifiers, with one lock-in amplifier detecting at *2f* and the other at *1f*. The lock-in amplifiers outputs the X_{2f} and Y_{2f} signals from the former and R_{1f} from the latter. The sensitivity and gain of the of the lock-in amplifiers are adjusted to give the maximum signal-to-noise ratio for the *2f* and the *1f* signals.

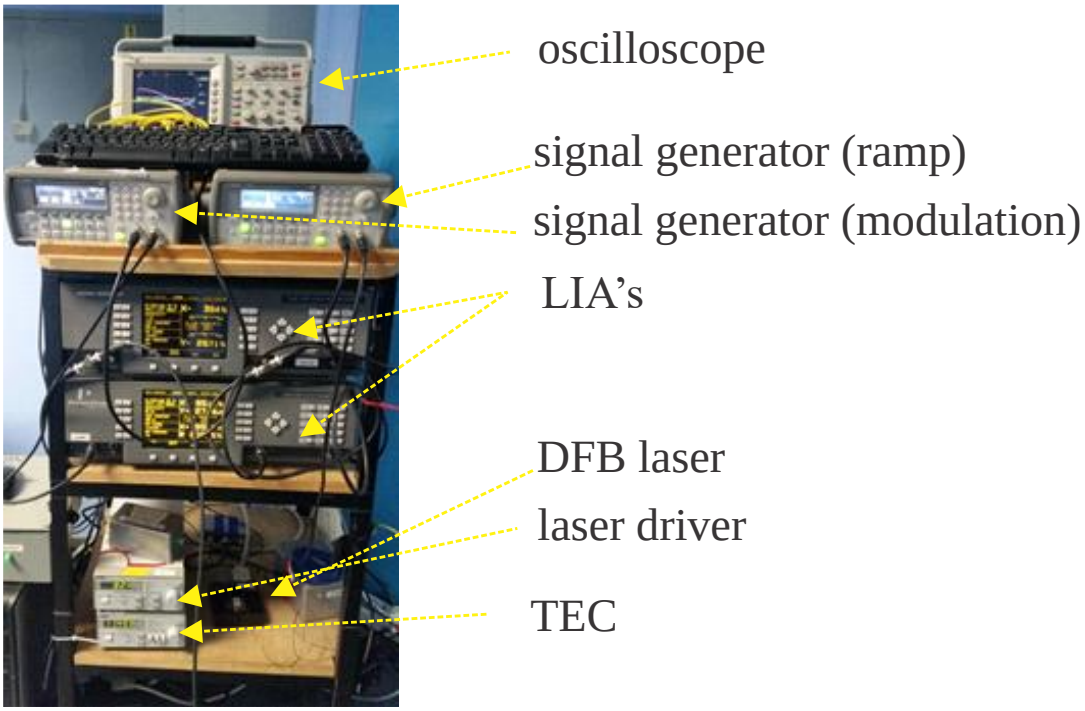

Figure 6-34. The launch and receive electronics rig at the Rolls-Royce test bed.

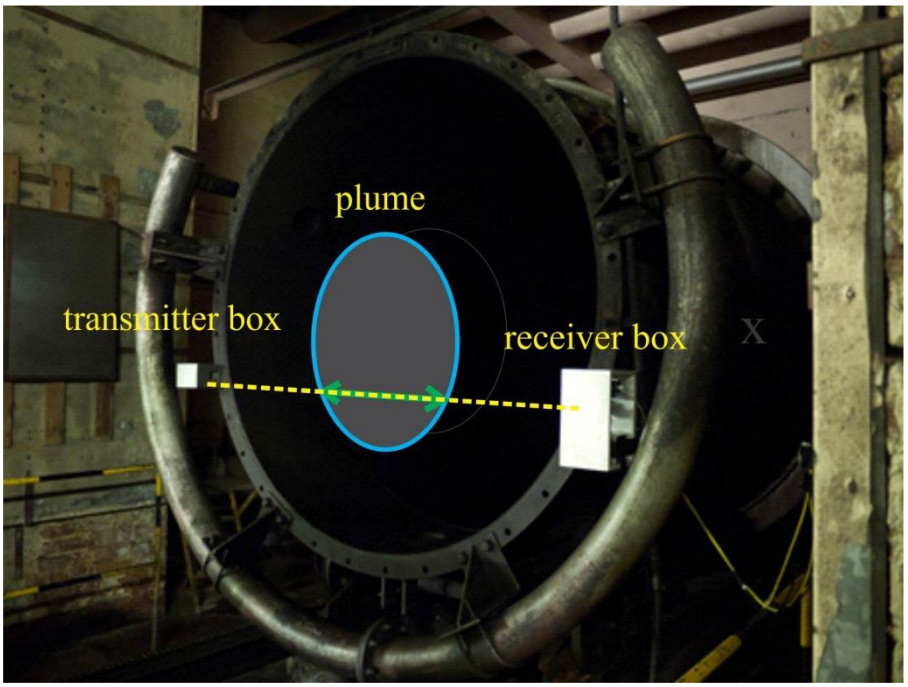

Figure 6-35. The launch and receive optics.

The plume diameter was estimated as 80 cm from the diameter of the exhaust nozzle by Bain et al. [41], while the total optical path length was measured to be approximately 2 m. The FLITES project consists of 126 beams in a circular dodecagon geometry. The mirror arrangement was not suitable for the FLITES measurement setup. Procuring 126 2 μm fibre coupled collimators is costly (~ £400 per unit). Hence, in the final measurement system for FLITES, a single lens collimator will be used in the transmission side with a collimated beam output, collected using a second lens with the detector at its focal point (Appendix C) [51]. The collimated, mid-plume focussed and moderately divergent arrangements will be tested for noise performance characteristics by alternating these arrangements for the measurement channels, on one of the six optical launch plates (Appendix C).

6.13 Initial Test Results on an Aero Engine

This section summarises the results and conclusions from TDLS-WMS measurements taken during the initial test campaign. The initial measurements gave significant insights into the feasibility of the different techniques as well as providing opportunities for system optimisation.

6.13.1 Signal Noise and Losses

The aero engine exhaust plume is an environment with many strong noise sources which distort the optical signal. Noise can be categorised as either additive noise or multiplicative noise. The lock-in amplifier excludes the low frequency additive noise (e.g. the relative intensity (RIN) noise, Johnson noise etc.) from the measured signals but not the multiplicative noise (transmissivity fluctuations, etalons etc.). Hence, the noise in phase sensitive detection primarily refers to the multiplicative noise. The distortions of an optical beam on passing through a GTE plume can be categorised as due to plume induced divergence and wander, scintillation and pointing errors [13, 51]. All these optical effects induce noise in the measured WMS signals.

The prominent sources of noise are categorised as follows [51]:

1. Mechanical vibrations (vibration of the transmitter and receiver optics).
2. Scattering by particulates.
3. Beam divergence, wander, scintillation, etc.
4. Electrical interference.
5. Transient etalons.
6. Speckle noise.

It was possible to get an estimate of the pointing errors from mechanical vibrations of the mounting structure using forced vibration simulations in the test cell at INTA. The maximum vibrational amplitude is <<1 mm and the maximum bandwidth of mechanical vibrational noise was less than 10 kHz from the simulations done for the INTA test bed, using the mounting structure built for tomographic imaging.

The soot in the plume or the unburnt fuel can scatter the beam, and hence create additional noise. Propagation of a light beam through a turbulent medium introduces wave-front distortions which lead to beam scintillations, wander, as well as beam divergence. Due to the high plume velocity and short turbulence scales, wave-front correction methods cannot be implemented.

For the FLITES system, the maximum plume induced divergence of the beam was estimated to be 250 μrad rms [17, 51]. A speckle patterned beam output from an optical fibre occurs due to the interference of the various modes propagating in a fibre. Fibre speckle noise is expected to be minimal because a single mode fibre was used. Speckle

patterns, could nonetheless occur due to other phenomena such as scattering and propagation in the turbulent plume. Moreover, since wavelength chirp is inherent in WMS, dynamic speckle patterns are inescapable. The speckle pattern is wavelength dependent (as interference is wavelength dependent), and hence if part of the beam is not detected; it could create a wavelength dependent intensity variation.

The beam wander effect is expected to be less significant (150 μrad rms). The effective spreading of the beam was calculated to be around 300 μrad rms which corresponds to a 7 mm (pk-pk) beam expansion at the detector [51]. The approach to reduce the noise from pointing errors was to overfill the detector, but the random speckle patterns will cause increased scintillations. The best choice is aperture averaging using a large area lens or a mirror focussed onto a large area detector, which can reduce the effects such as beam steering, divergence, scattering and speckle [51]. However, the large area detectors required for aperture averaging impose a limitation on the bandwidth.

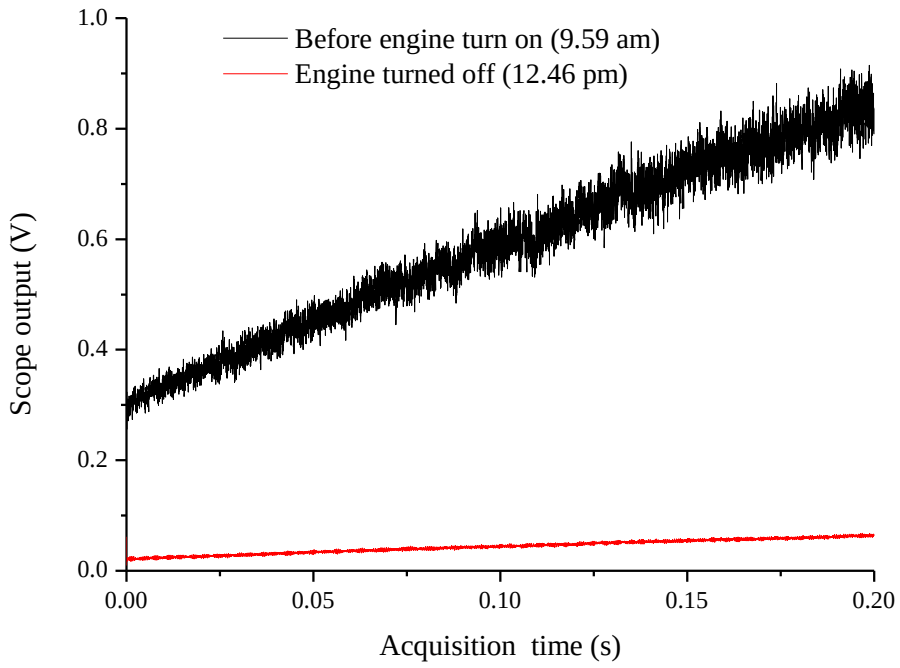

Figure 6-36. A 5 Hz ramp signal (55-105mA) measured before engine was on (black plot) and after the engine had stopped running (red plot). The total power lost is the ratio of both. Optical interference noise is seen on the signal which increases with the laser intensity.

The background-subtracted *2f*/*1f* signals are not immune to transient etalons; hence, any time varying etalons along the measurement path, with an FSR comparable to the gas absorption line width will appear as a distortion/noise in the *2f*/*1f* signals. In addition to the noise, the optics may become covered by unburnt fuel and soot causing the signal power to drop at the detector. Hence, periodic cleaning of the optics was necessary.

It is difficult to identify the individual contributions from each of these effects, however, to estimate the total power lost from the mechanical misalignment losses, as well as dirty optical components, a ramp was taken before and after measurement, as shown in Figure 6-36. It was observed that the total power lost from mechanical misalignment losses as well as fowling of the optics was approximately 6 dB (4 times power lost). Also, it was observed that the noise level in the direct signal makes it unsuitable for the measurement process. Optical interference noise is observed which increases with the intensity. Additionally, the noise sources in the aero engine also make it difficult to measure direct absorption signals, especially at slower ramp rates.

6.13.2 Optimum Modulation Frequency, Signal Amplitude and Averaging

Selection of a modulation frequency away from the system noise bandwidth is important for measurements using a lock-in amplifier. In the previous measurements by Bain et al., it was observed that noise spectrum gets extended up to very high modulation frequencies of several hundreds of kHz [99].

It was also interesting to note that the noise spectrum showed a cut-off frequency which varied from 100 kHz to 200 kHz. Also, the noise spectrum was random, i.e. at a given frequency, the magnitude of the noise was not a constant. This was inferred by averaging the noise spectra and comparing it with a non-averaged case [99]. Using a higher ramp frequency and a higher modulation frequency could effectively mitigate the noise arising from the low frequency transmissivity fluctuations. Averaging signals prior to the LIA is equivalent to using a comb filter in the frequency domain and is useful for removing the high frequency transmissivity fluctuations [7]. Previously, attempts were made to reduce the beam steering noise by using a particular optical geometry, for example, by focusing the laser beam onto a large area detector (aperture averaging).

Using a small focal length mirror with a detector at its focal point could mitigate the angular deviations up to 3° in beam steering. Another way is to overfill the detector area using a diffuser plate [41]. The effectiveness of different optical geometries was investigated for the engine tests at INTA by using different optical arrangements on one of the launch-receive dodecagon edge plates. To analyse the effect on the beam cross-section after travelling through a turbulent high temperature gas, image of the beam through a heated furnace was taken using an infrared camera. The beam cross-section showed relatively lower intensity fluctuations (scintillations) and speckle patterns after passing through the heated turbulent air in the furnace [51]. Three different geometries were tested, a collimated arrangement, a moderately divergent and a mid-plume focussed arrangement [51] (Appendix C). The results of the test on the thermal medium was not conclusive, and therefore provision for focal adjustment has been incorporated into the FLITES measurement system to test these three geometries with light propagating through the plume [51]. On the contrary, normalisation by the *1f* is a powerful technique which can be used to remove noise from transmissivity fluctuations [30].

To analyse the noise at different modulation frequencies, WMS signals were measured at different modulation frequencies. The initial measurements were taken using a Stanford Research Systems (SR830) lock-in amplifier with a square-wave reference having the maximum bandwidth of detection limited to 100 kHz (100 kHz for *1f* detection and 50 kHz for *2f* detection). Figures 6-37 and 6-38 show the *1f* and *2f*-WMS signals taken at modulation frequencies from 10 kHz to 100 kHz.

Measurements indicate that modulation frequencies above 100 kHz have to be used to obtain appreciable signal-to-noise ratio. These measurements were performed to test feasibility of the phase invariant PDM technique to recover the gas absorption signals. The phase invariant PDM technique is useful for field applications as described in Chapter 5.

A major obstacle faced while implementing the phasor decomposition method was that the R48 CO_2 absorption line does not have a non-absorbing baseline. In an environment with a fluctuating transmission, it was impossible to obtain a no-gas PDM signal to normalise the PDM gas signals. As observed from the measurements at higher

modulation frequencies shown in Figure 6-40, it was apparent that the *2f* detection is less susceptible to noise compared to the *1f* detection.

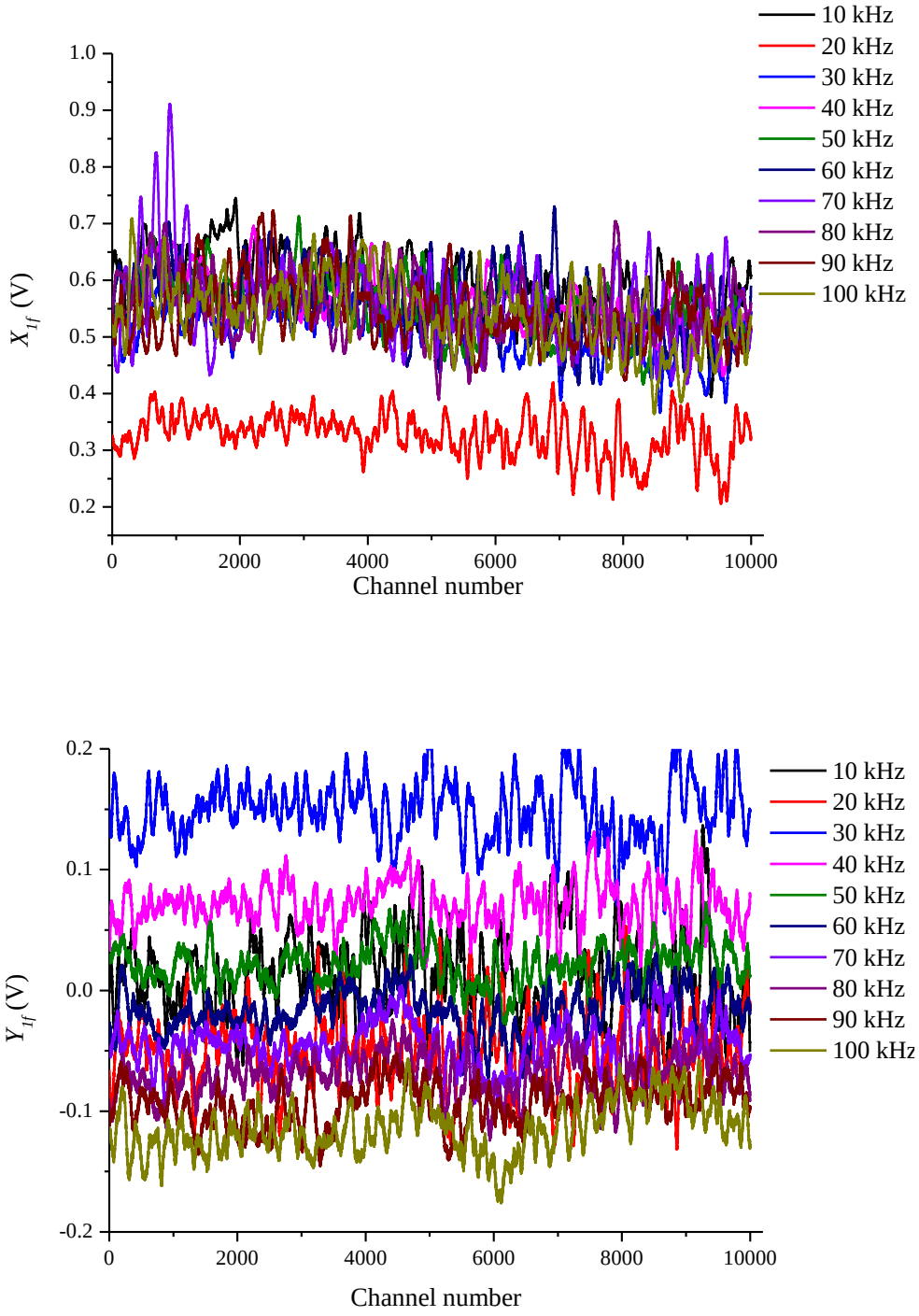

Figure 6-37. *1f*-X and *1f*-Y channel signals detected at modulation frequencies from 10 kHz to 100 kHz. The above spectra are useful to gain an insight into the noise characteristics of optical aero engine measurements.

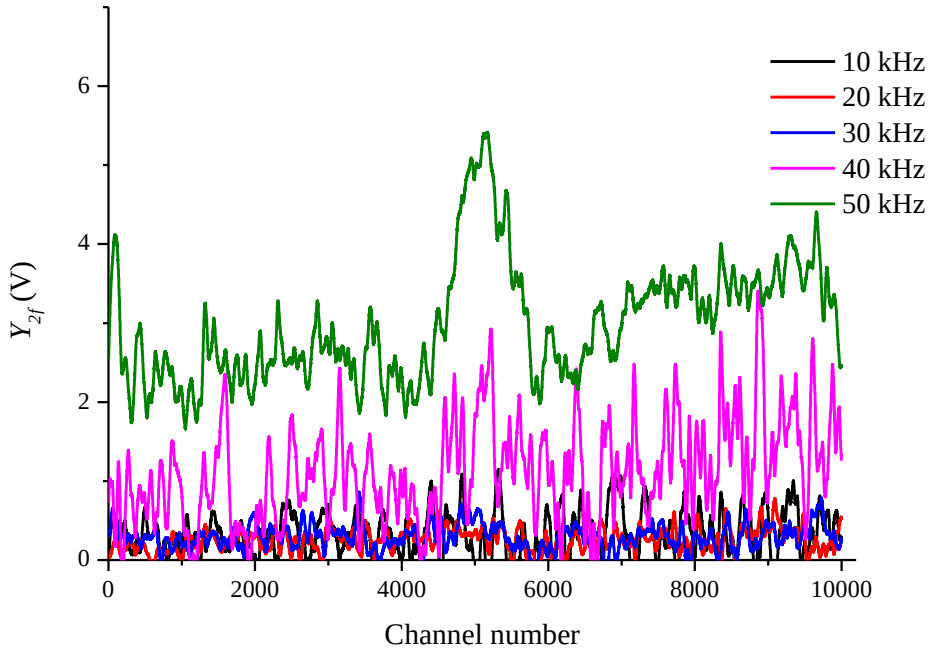

Figure 6-38. *2f* signals measured at modulation frequencies ranging from 10 kHz to 50 kHz (limited by the bandwidth of the SR830 lock-in amplifier).

Even if the normalisation RAM signal could be obtained from a baseline fit of the *1f*-X and *1f*-Y channels, the large noise levels on the *1f* signal compared to the *2f* signal would create a significant error in the recovered concentration and temperature values. The *2f* signal on the other hand is less prone to noise and much more sensitive to concentration and temperature than the *1f* signals. These points can be inferred from Figure 6-39 where the *2f* and *1f* signals are compared for two different concentrations of CO_2 and plume temperatures. It was observed that the nonlinear *2f*-RAM background is almost two orders of magnitude (80 times) smaller than the *2f* signal peak, while the linear *1f*-RAM is of comparable magnitude to the signal. This is one of the advantages of *2f* detection. Even though the *2f* signal is demodulated at a higher modulation frequency (400 kHz in the example below) compared to the *1f* signals (200kHz), from the noise spectrum and the *1f*-measurements at higher modulation frequencies shown in Figure 6-40, it was apparent that *2f* detection is less susceptible to noise compared to the *1f* detection. Hence, it can be inferred that the *2f* detection is better suited for

measurements in harsh environments such as in an aero engine exhaust plume. Nonetheless, it is important to emphasise that the line shape recovery techniques such as the PDM or the RAM technique can be implemented if the RAM nulling approach was used similar to the approach used by Bain el al. [41] using the Hobbs electronic auto-balanced receiver.

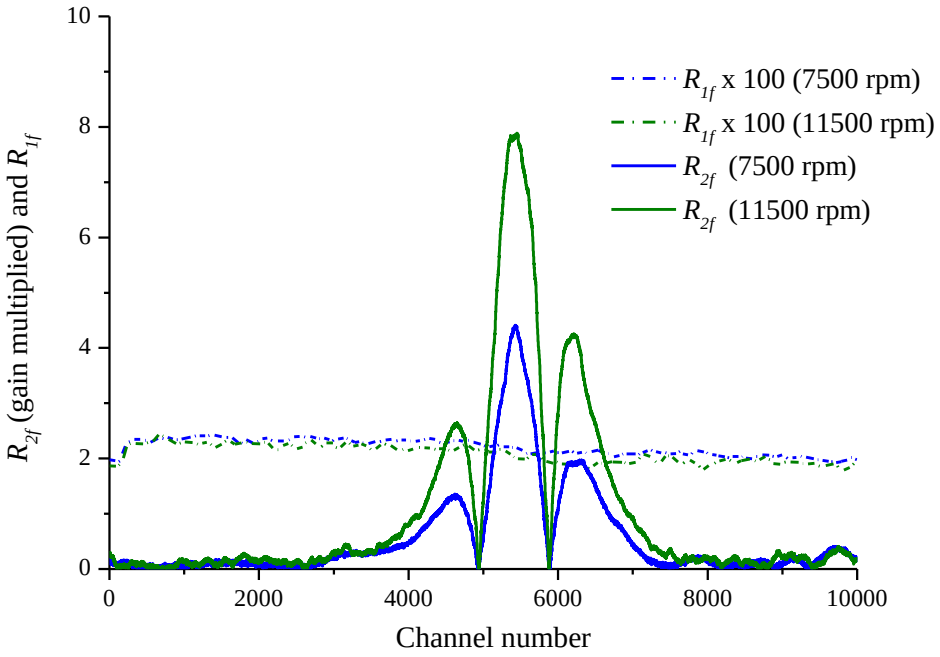

Figure 6-39. *2f* detection has an increased sensitivity compared to *1f* detection. Measurements were taken at 200 kHz with current modulation amplitude of 10 mA.

Dividing the *2f* signal by the *1f* signal further improves the noise characteristics by cancelling the effects of optical transmission fluctuations.

Figure 6-40 shows the advantage of *2f* detection over *1f* detection in terms of noise immunity. These measurements were taken when the engine was idling (constant thrust).

Figure 6-41 shows the *2f*/*1f* spectra at different modulation frequencies. It was stated in [8] that the signal-to-noise ratio of the *2f*/*1f* signal increases ten-fold compared to the *2f* signal. Such a dramatic increase in the SNR was not observed. This could be due to different noise sources and the signal levels in both the experiments. Also, it can be

understood that the additive noise spectra is flat from 100 kHz (as the *2f/1f* spectra mainly cancels the multiplicative noise [7]).

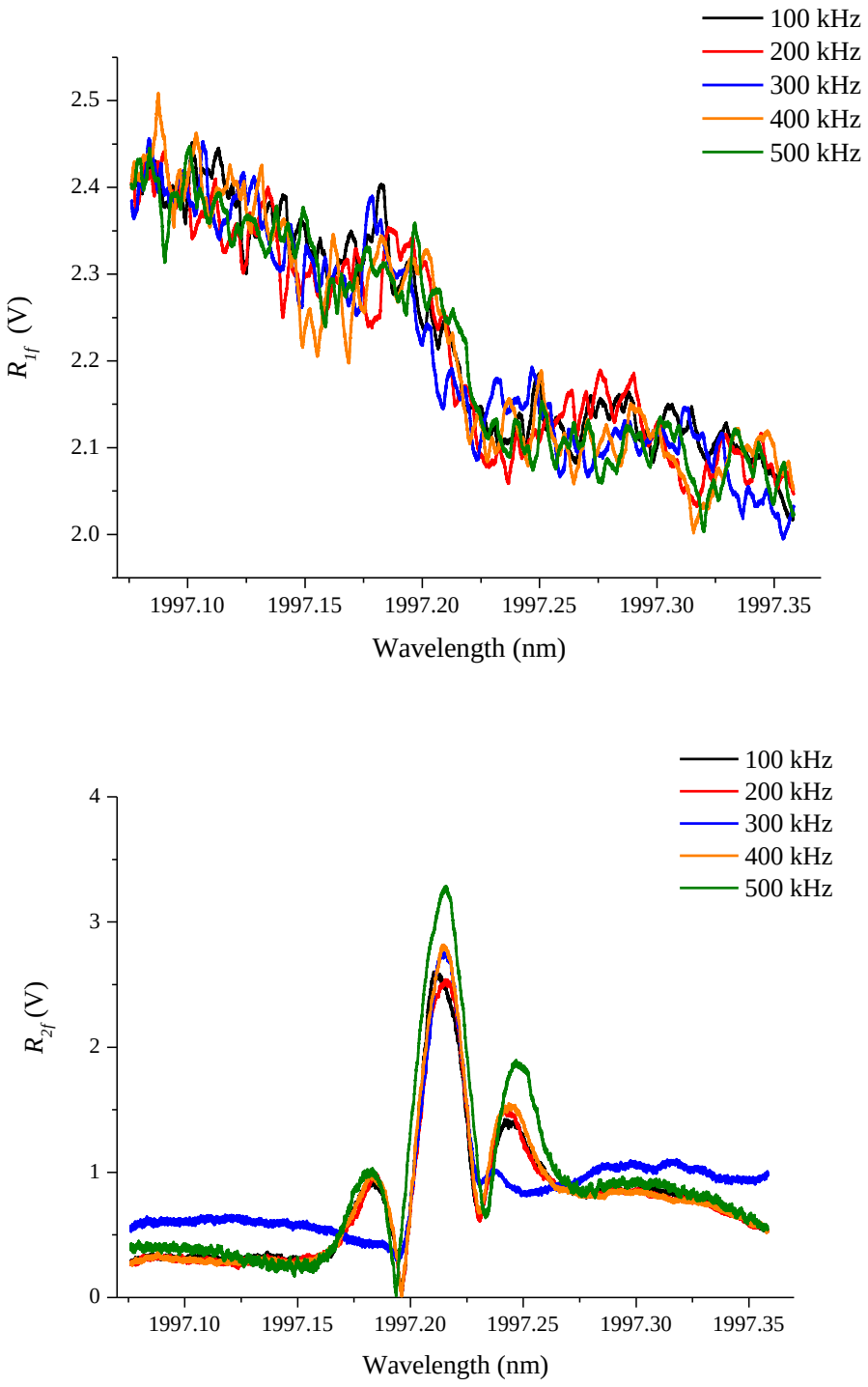

Figure 6-40. R_{2f} and R_{1f} signals measured at modulation frequencies from 100 kHz to 500 kHz with the engine operating in a constant condition.

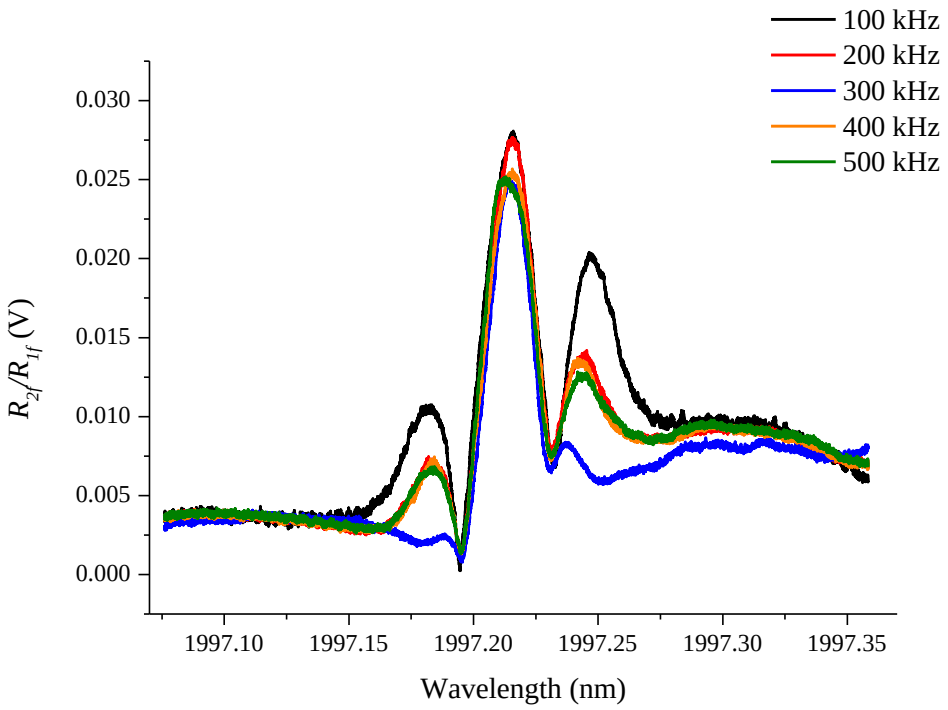

Figure 6-41. *2f/1f* spectra (with no-background subtraction) measured at different modulation frequencies.

It was expected that the signal-to-noise ratio should increase with larger modulation amplitudes. Figure 6-42 shows the *2f* and *1f* signal magnitudes at different modulation amplitudes. It can be seen that increasing modulation amplitude does not decrease the noise levels markedly for the *2f* or *1f* WMS signals. Such behaviour is characteristic of multiplicative transmission noise [100].

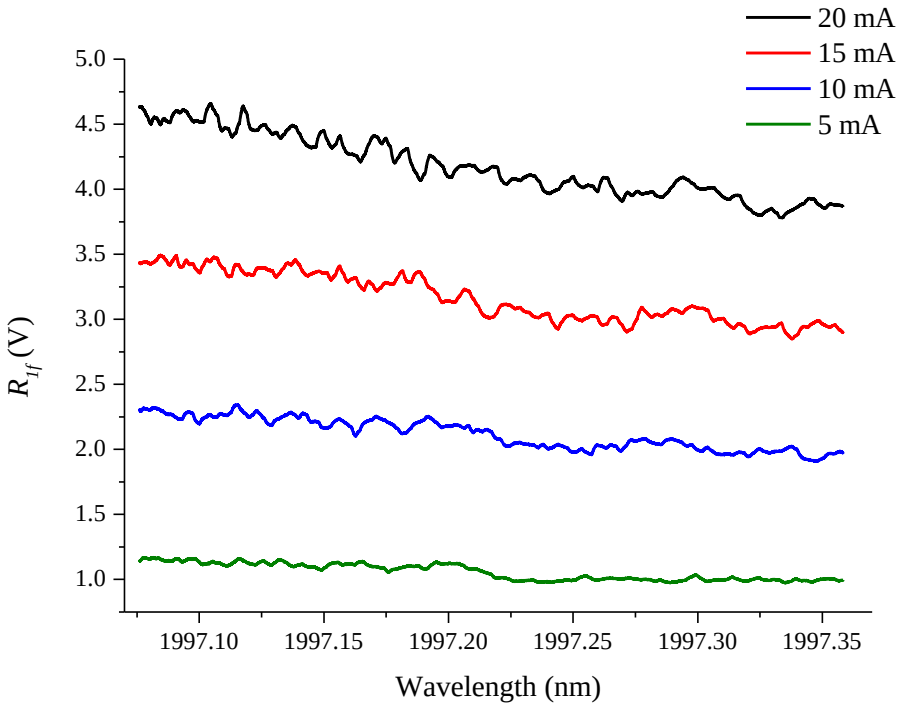
20 mA
15 mA
10 mA
5 mA
5.0
4.5
4.0
3.5
3.0
2.5
2.0
1.5
1.0
R_{1f} (V)
1997.10
1997.15
1997.20
1997.25
1997.30
1997.35
Wavelength (nm)

(A)

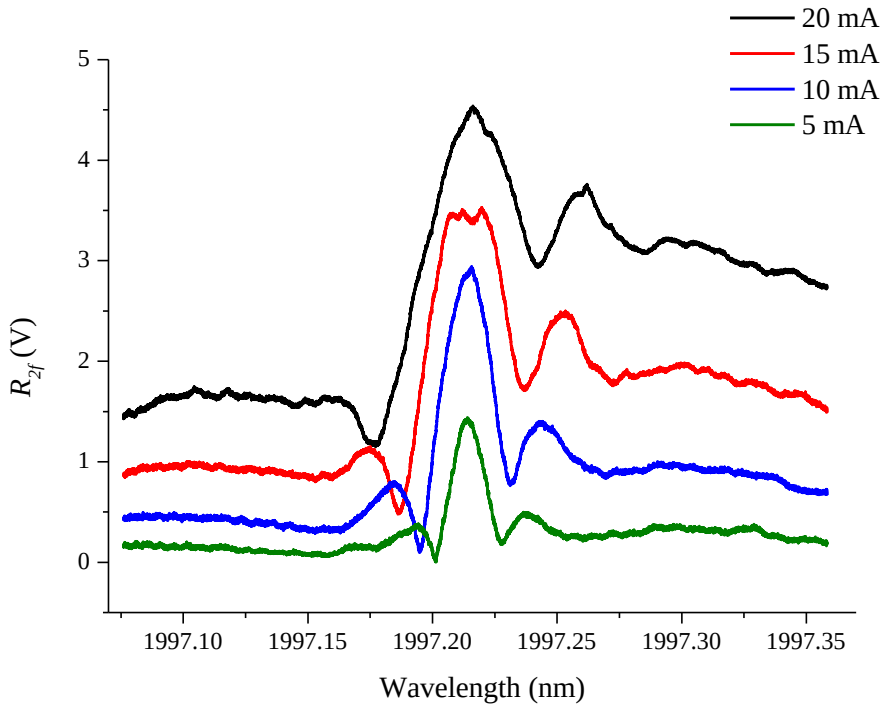
20 mA
15 mA
10 mA
5 mA
5
4
3
2
1
0
R_{2f} (V)
1997.10
1997.15
1997.20
1997.25
1997.30
1997.35
Wavelength (nm)

(B)

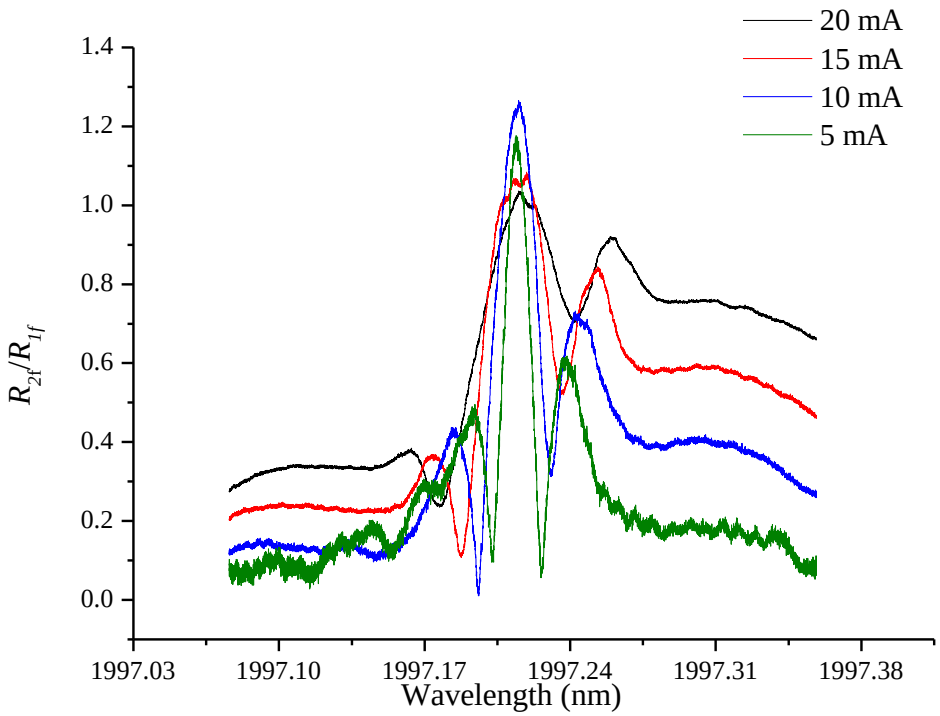

(C)

Figure 6-42. Comparison of (A)$R_{2f,}$(B) R_{1f} and (C) R_{2f}/R_{1f} signals at different modulation amplitudes (*m* value approximately changing from 0.64 to ~ 2.5). It has to be borne in mind that the *2f* signal maximises at *m* = 2.2, the *1f* signal at *m* = 2 and the *2f/1f* signal at *m* = 1.1.

However, for the *2f*/*1f* signals, the noise levels on the signals were found to decrease for higher modulation amplitudes as shown in Figure 6-42 (C). This was due to the cancellation of the multiplicative transmission noise. On the other hand, any static or transient etalons with a comparable FSR (~3GHz) to the gas absorption line along the measurement channel will have a distorting effect on the WMS signals. From approximate calculations it is expected that path lengths from shorter cavities (through silica) less than 2 mm or longer cavities greater than 10 cm have reduced impact on the WMS signal noise. These cavity lengths are expected to be slightly greater for free space propagation (due to a smaller refractive index). Since most of the cavity lengths (fibre adapters, free space propagation through the plume etc.) in the measurement system

were outside this range, it is expected that the noise from static etalons on the WMS signals would be negligible.

Background subtraction is useful in substantially reducing the contributions from temporally stable etalons which are unavoidable in the optical measurement path.

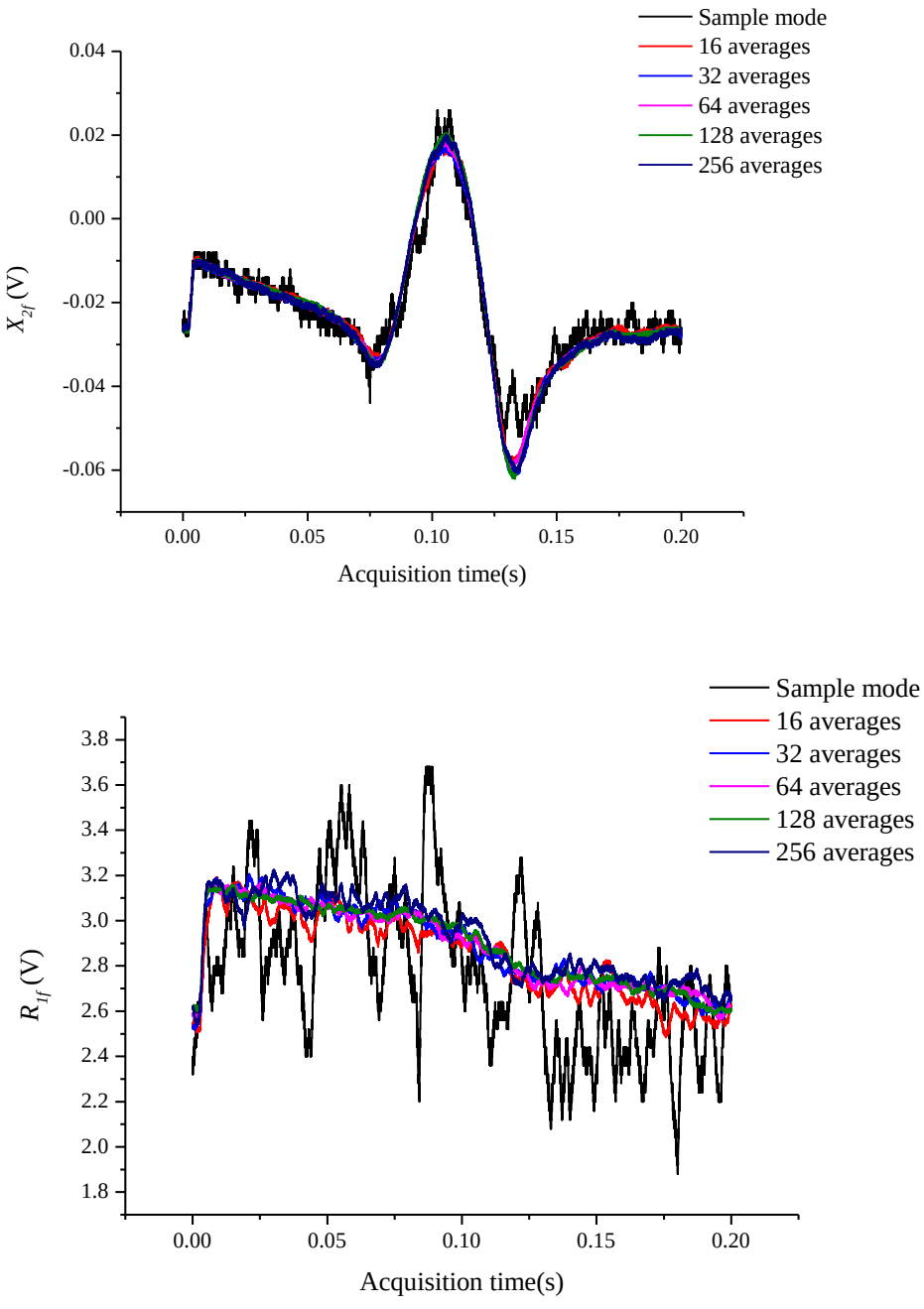

Figure 6-43. Effect of post-averaging on the *2f* and *1f* signals. The DFB laser is scanned at 5 Hz, which implies that to acquire 256 scans, it took approximately 50 seconds. All the *1f* and *2f* signals were acquired serially over a duration of two minutes.

Averaging WMS signals is equivalent to applying a low pass filter and can be useful to reduce the noise from various sources in the system. Post-averaging the signals stored in the buffer of the oscilloscope is valid as long as the signal does not drift over the time period of averaging. Figure 6-43 shows the results for the lock-in amplifier output signals acquired in the averaging mode (with number of the scans averaged during an acquisition varying from 16 to 256) and sampling mode of the oscilloscope.

The effect of post-averaging more than 16 samples is minimal for the *2f* and *1f* signal. It can be observed that the *2f* and *1f* signals did not fluctuate in magnitude over the duration of approximately two minutes as the engine was idling (constant thrust), and hence emitting a constant volume of CO_2. Therefore, it was deduced that moderate noise reduction will be observed with averaging 16 acquisitions, however, subsequent averaging has little noticeable effect on the signal-to-noise ratio.

6.13.3 Selection of Optimum Modulation Index

The modulation amplitude, and thereby the modulation index determines the signal-to-noise ratio in WMS systems [31].

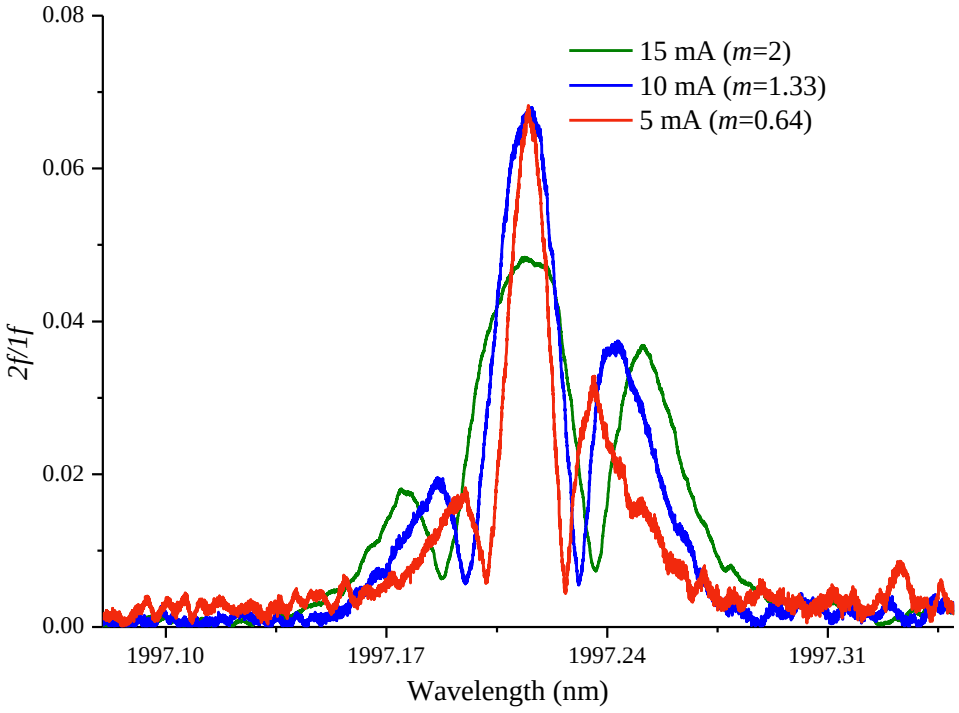

Figure 6-44. The background-subtracted *2f*/*1f* signals having modulation amplitudes of 5 mA, 10 mA and 15 mA.

The choice of the modulation index determines the signal size. The modulation index to obtain a maximum background-subtracted *2f*/*1f* signal was calculated to be around *m* = 1.1 [27, 101]. Figure 6-44 shows the background-subtracted *2f*/*1f* signals with different modulation amplitudes that were measured when the engine was idling (at constant thrust). The temperature and concentration of CO_2 in the exhaust plume was measured using the nonlinear curve fit algorithm and was found to be 1.9 % and 250 °C. The background-subtracted *2f*/*1f* signal with a 5 mA modulation amplitude peaked at the same value as a signal with a 10 mA modulation amplitude (twice).

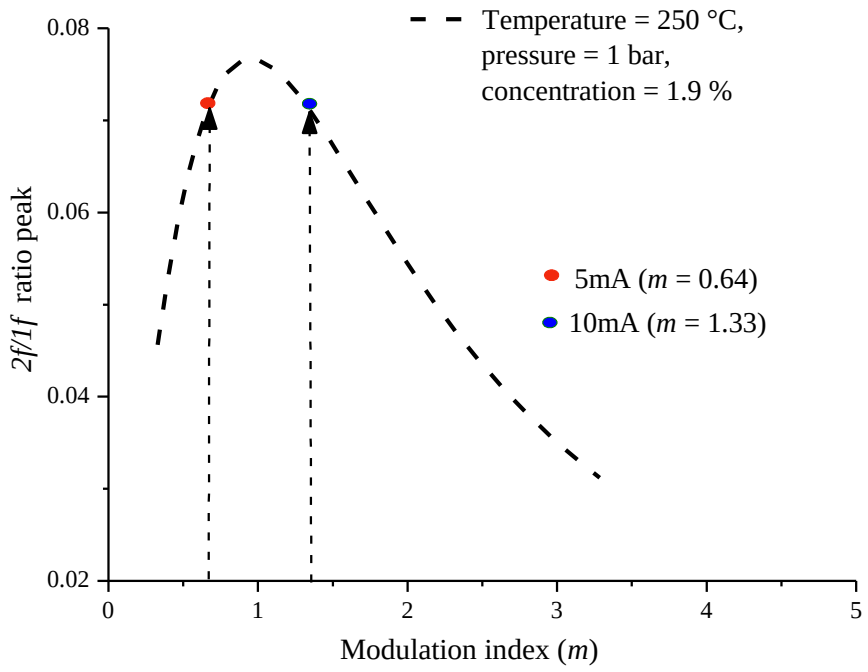

Figure 6-45. The peak of the background-subtracted *2f*/*1f* signal plotted as a function of modulation index. The peaks of the *2f*/*1f* signals with modulation amplitudes of 5 mA (red marker) and 10 mA (blue marker) are also shown.

This is expected from the dotted graph shown in Figure 6-45 which shows the peak size of the *2f*/*1f* signal as a function of modulation index for a pressure of 1 bar, temperature of 250 °C and 1.9 % concentration, where increasing the modulation index (amplitude) reduces the *2f*/*1f* signal size beyond *m* ~ 1.1.

Increasing the modulation amplitude also reduces the interference from transient and

static etalons.

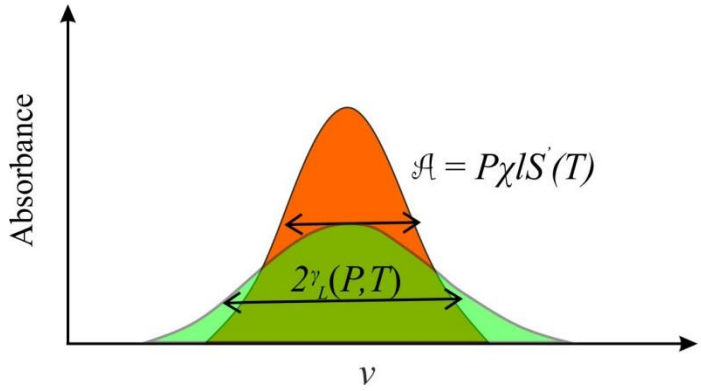

Figure 6-46. The integrated absorbance is sensitive to concentration, pressure and temperature, while the line width is dependent on the temperature (to a lesser extent) and pressure. The sensitivity of the *2f/1f* signal absorbance (area under the curve) is independent of the modulation amplitude; the recovered concentration and temperature can be made less sensitive to the line width (or pressure) by increasing the modulation amplitude.

Also, increasing the modulation amplitude greater than the absorption line width can decrease the sensitivity of the *2f/1f* line shape to the collisional line width as illustrated in Figure 6-46. It has been reported in several works [27, 85] that the sensitivity of the line shape towards pressure uncertainties could be reduced at higher modulation indices.

6.13.4 Conclusion

From the initial test campaign, it was clear that the *1f* detection techniques are not suitable for the measurements on the aero engine exhaust plume as the *1f*-gas absorption signal was submerged in the noise on the RAM background signal. The *2f* detection was suitable for the measurements due to the smaller nonlinear RAM background. A brief review is given on the noise sources in an aero engine test environment and the optical designs to mitigate their effects on the measured signals. It was observed that increasing the modulation frequency above approximately 100 kHz had no marked effect on the noise levels in the signal. Increasing the current modulation amplitude increased the IM signal size at the detector, but had no effect on the noise levels on the *2f* and *1f* signals due to the presence of multiplicative noise on these signals. On the contrary the *2f/1f* signals showed reduced noise levels with an increase in the IM amplitude due to the cancellation of the multiplicative transmission noise in these signals. The optimum

modulation index for maximum signal size of the *2f/1f* signals was identified as $m = 1.1$. The results presented in this section were used to optimise the experimental parameters such as the modulation frequency, modulation amplitude, ramp frequency, signal averaging as well as the optical and electronic design for the subsequent measurements on an aero engine platform.

6.14 Single Channel Measurements of Concentration and Temperature in a GTE Exhaust Plume

Single channel measurements of concentration and temperature using *2f/1f* WMS were undertaken at the East Kilbride (EK) test bed of Rolls-Royce. The R48 transition of CO_2 at 1997.2 nm was probed using a 2 μm DFB-MQW laser source as discussed in this chapter. The optical path length through the plume is estimated to be 80 cm (l). Any error in the optical path length will manifest as an error in the measured path integrated concentration, i.e. χl. The ambient absorption by CO_2 (0.04 %) was found to be negligible. The water vapour concentration in the atmosphere can vary from 0-4 %; however, the interference of the water vapour spectra on the CO_2 spectra was found to be insignificant (Figure 6-2) at 1997.2 nm. Figure 6-47 shows the measurement system at EK. As observed in Figure 6-47, three signals were required, the X_{2f}, Y_{2f} and R_{1f}.

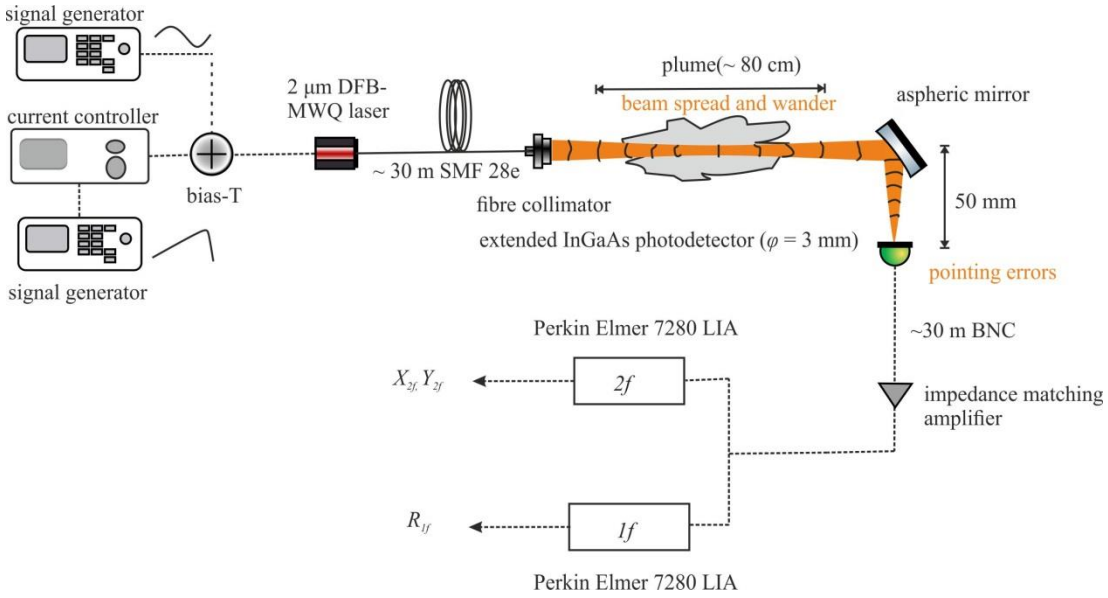

Figure 6-47. Measurement rig for the East Kilbride engine tests.

All the measurements at the test bed were done on Rolls-Royce Tay engines, which are high-bypass gas turbine engines. Two tests were conducted in succession on the same day with the engine being operated under different thrust configurations. Temperature of the engine core was simultaneously recorded using the temperature sensors installed by Rolls-Royce. A background *2f*/*1f* signal was taken before or after the experiment, to be subtracted from the gas signals.

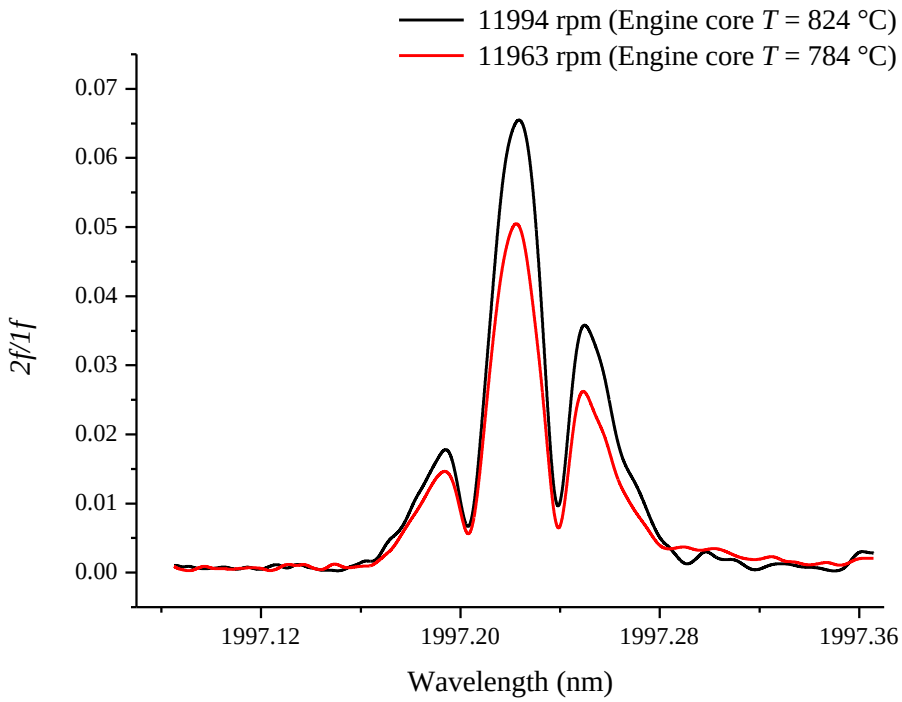

Figure 6-48. Two background-subtracted *2f*/*1f* engine measurements at different engine thrusts. Modulation frequency = 200 kHz, δi= 10 mA.

The modulation frequency was chosen as 200 kHz from knowledge of the noise spectra in earlier measurements (Section 6.13.2). Figure 6-48 shows the background-subtracted *2f*/*1f* signals corresponding to two different engine thrusts.

For analysis, three sets of measurements were taken as shown in Figure 6-49 to 6-51. The first signal (black curve) was measured when the engine was turned off and is taken as the background signal. The blue and red curves depict signals measured at different engine thrusts. Increased noise levels (from vibrating optics, transient etalons, beam steering etc.) are expected at higher engine thrusts. The noise in the *1f* signal was higher

compared to the noise in the *2f* signal, which is evident from the signal-to-noise ratio and is attributed to the large background RAM signal. As mentioned before, this is an advantage of the *2f* technique over other methods, and hence the *2f* signal alone may be used to determine the gas properties.

From Figure 6-49, it can be inferred that a background subtraction could be done for the *2f* signals owing to the small fluctuation of the nonlinear RAM in the *2f* gas signals taken during engine run, relative to the nonlinear RAM in the *2f* signals taken when the engine is turned off. One of the disadvantages of using only a *2f* signal can be that the temporally stable etalons can cause a false absorption signal. Though, subtracting a background *2f* signal reduces the effects of these non-time varying etalons, the signal-to-noise in the *1f* normalised *2f* WMS technique is expected to improve compared to *2f* signals due to the cancellation of transmissivity fluctuations.

A nonlinear curve fit algorithm was implemented to simultaneously recover the concentration and temperature values from the experimental gas signals, as explained in Section 6.11.

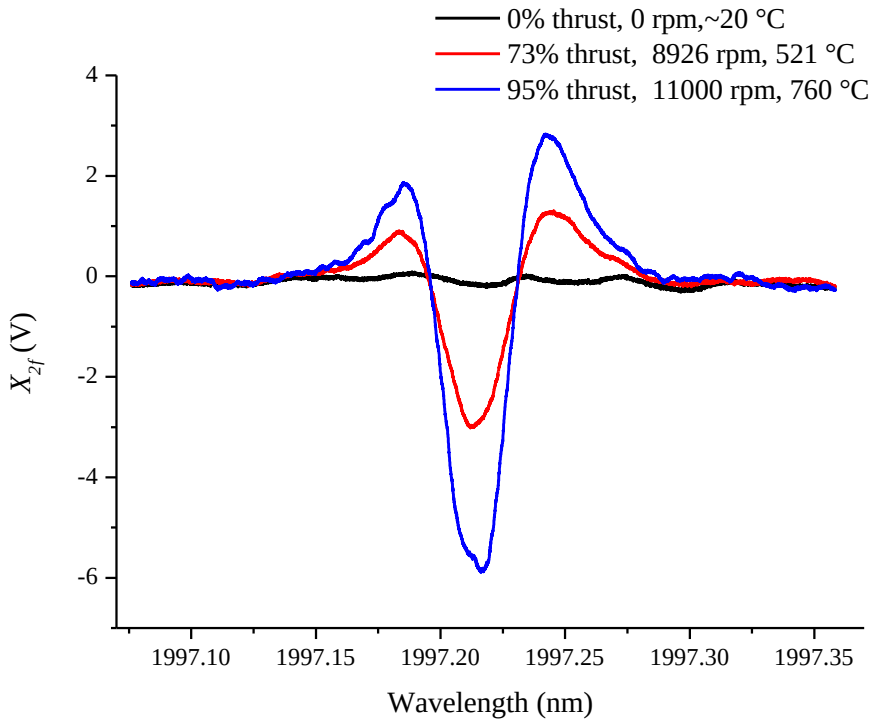

(A)

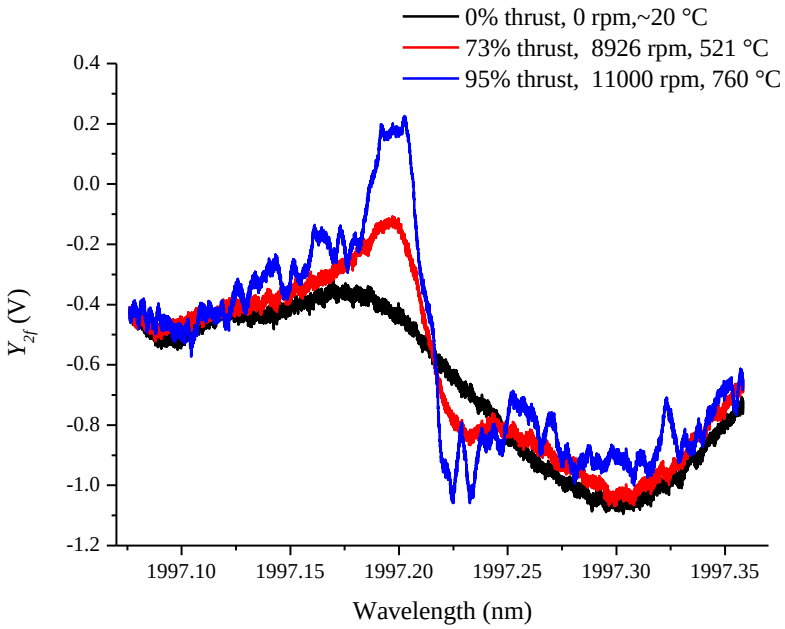

(B)

Figure 6-49. (A) The *2f* X-channel and (B) Y-channel signals at different engine thrusts (0-11000 rpm).

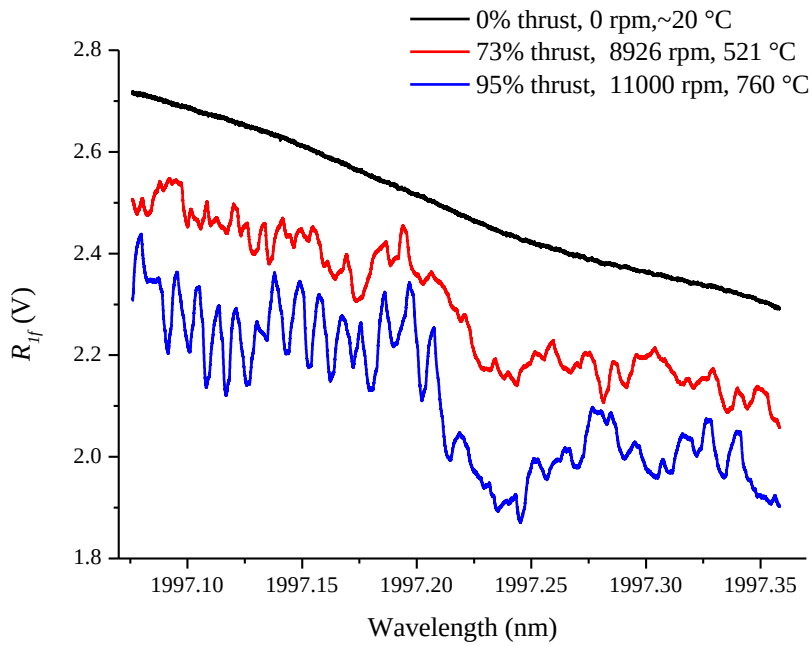

Figure 6-50. The *1f* magnitude signals measured with the engine thrust changing from 0-11000 rpm.

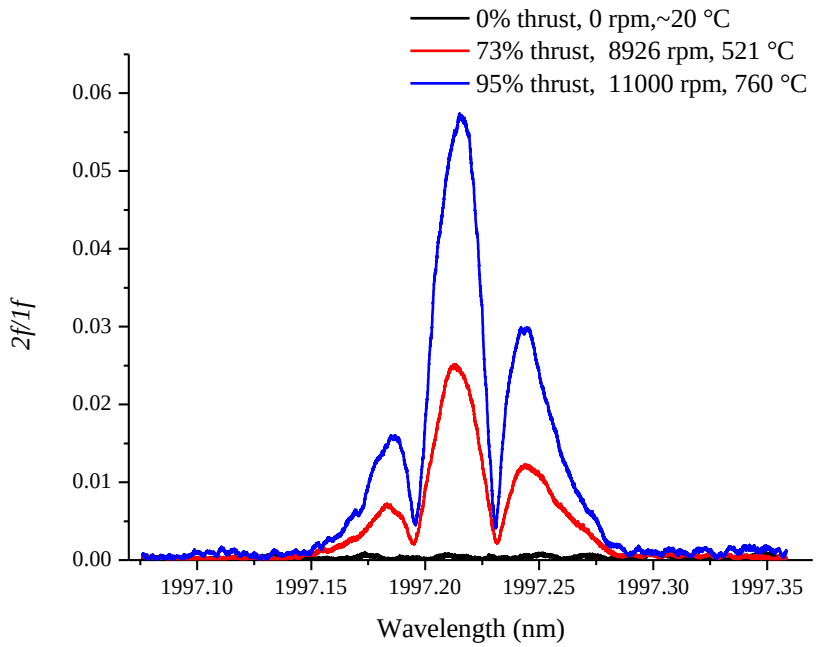

Figure 6-51. Background-subtracted *1f* normalised *2f* signals at different engine thrusts (0-11000 rpm). Modulation frequency = 200 kHz and δi = 10 mA.

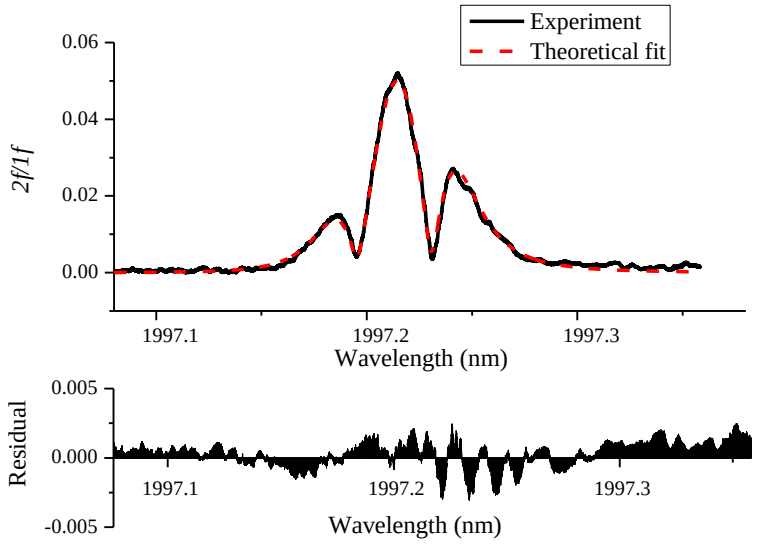

Figure 6-52. Nonlinear least-squares curve fit of a background-subtracted *2f/1f* spectrum of CO_2 acquired in the aero engine plume. Using the least-squares curve fit algorithm the concentration was measured as 1.4 % and the temperature as 238 °C; for a path length assumed to be equal to 80 cm, pressure assumed to be atmospheric (= 1.023 bar) and modulation index = 1.2 (calculated).

To improve the accuracy of the measurements, the measured air-broadening parameters have to be applied to the *2f*/*1f* WMS model. The pressure of the plume is close to atmospheric because the pressure exerted by the surrounding atmosphere on the plume at any cross-section is equal to the pressure exerted by plume on the surrounding atmosphere and an equilibrium is maintained, unless the plume velocity is greater than the speed of sound, which would be the case with the turbojet engines. All the experimental signals measured from the aero engine gave good fits to the theoretical *2f*/*1f* model as shown in Figure 6-52, with small residuals of 2-3 %.

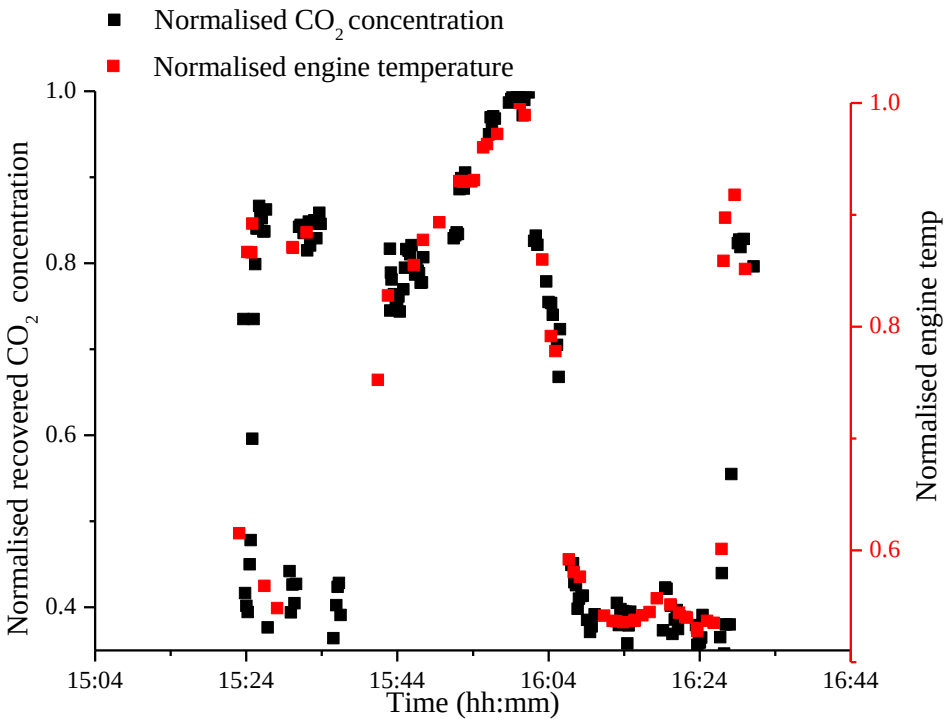

(A)

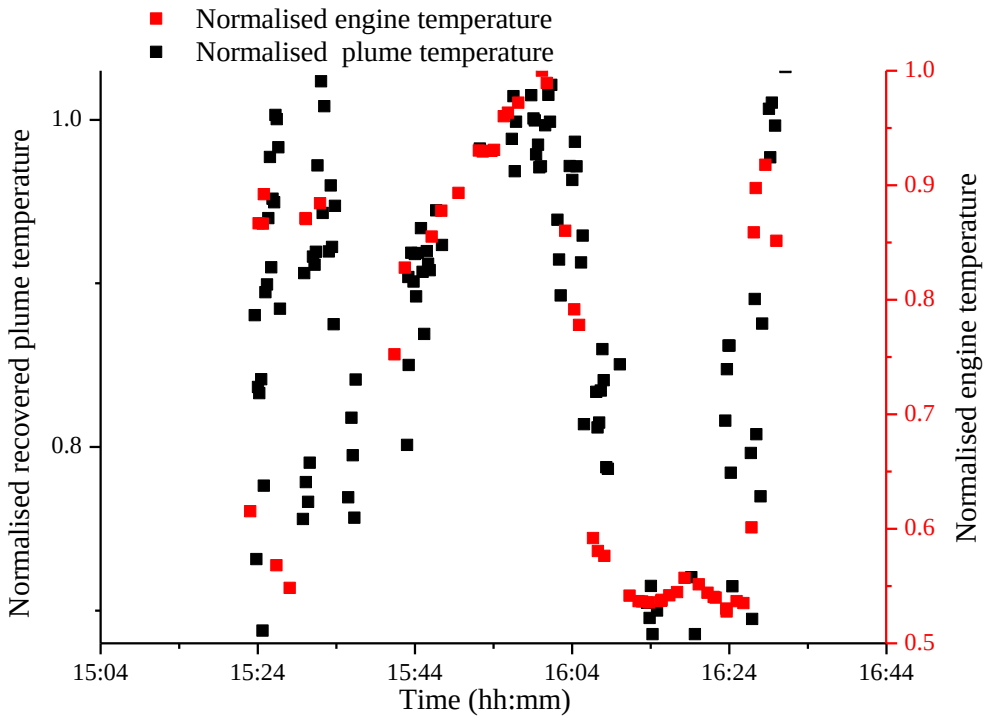

(B)

Figure 6-53. (A) Relative variation in the concentration of CO_2 measured in an aero engine exhaust plume using the *2f/1f* WMS technique compared to the temperature of the engine core. (B) The measured relative variation in temperature of the plume near the detuner compared to the measured temperature of the engine core. The actual values are not shown due to a non-disclosure agreement with Rolls-Royce.

Figures 6-53 (A) and (B) show the measurements using the *2f/1f* signals for the relative variation in CO_2 concentration and plume temperature values, compared against the relative temperature variation of the engine core as measured by Rolls-Royce. The temperature of the engine core is an indicator (proportional) of the engine thrust. The recovered trends in relative concentration and temperature variations showed excellent correlation with the engine core temperature. The concentration of CO_2 at the combustion core is expected to be 2 % at idle thrust, which goes up to 4.5 % at full throttle. Concentration at the detuner depends on how much dilution of engine output has occurred at the detuner entrance. The minimum dilution ratio due to the high bypass ratio of the Tay engine is approximately 3.1:1 [102], plus a bit more due to the entrained

air. Analysing these factors, the expected concentration at the detuner should be close to 0.64 % at engine idle state and about 1.4 % at full throttle. Also, since the Tay engine is a high-bypass engine where the colder bypass is designed to mix with the hot compressed air from the core; the temperature at the detuner is expected to be around 100-200 °C [103].

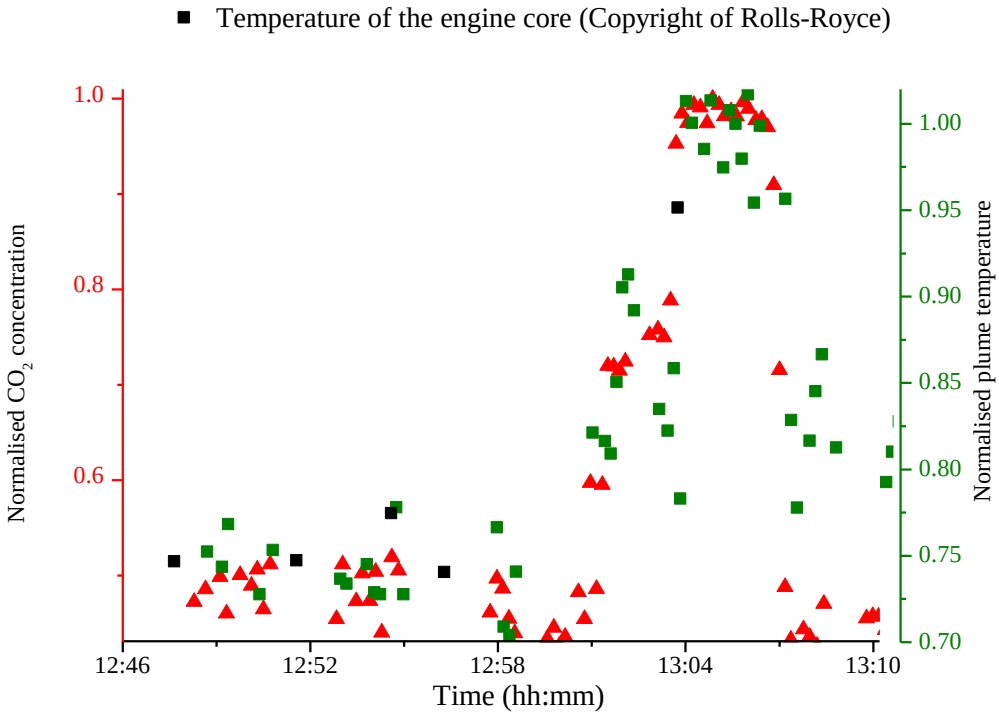

Figure 6-54. Relative variation in CO_2 concentration and plume temperature values measured in the gas turbine exhaust at the detuner entrance. The actual values are not shown due to a non-disclosure agreement with Rolls-Royce.

This compares well with the results shown in Figure 6-53, where the concentration and temperature are approximately within the expected range (the actual values are not shown due to a non-disclosure agreement with Rolls-Royce).

The standard deviation of the concentration and temperature values were calculated from the measurements taken when the engine was at a constant thrust and is found to be 2.1 % and 5 %, respectively.

Similarly, Figure 6-54 shows the measured relative variations in concentration and temperature from another engine test, with the engine operated in a different fashion.

The engine was in the idling state for a longer duration, from 12.46 p.m. to 12.58 p.m., gradually increased to a maximum thrust by 13.04 p.m., where it was kept for almost 4 minutes, after which it was brought back to idling state and turned off. The measured temperature and concentration values were seen to vary approximately within the expected bounds, between the engine idling and the engine going to full throttle.

Figures 6-53 and 6-54 show that the measured concentration and temperature values are well correlated to the engine thrust/core temperature. Hence, it was inferred that the sensor accurately measures the CO_2 concentration and plume temperature values and is suitable for combustion research and related applications.

6.15 Summary

The aim of this project was to develop and implement a suitable spectroscopic methodology for non-invasive measurement of CO_2 concentration and temperature in the exhaust plume of a gas turbine engine, which can easily be scaled to a multi-channel measurement system for FLITES.

After an exhaustive spectral survey to identify a rotational-vibrational transition of CO_2 in the near-IR, with sufficient signal-to-noise ratio and independent of interference from water vapour absorption lines, the R48 transition was chosen at 1997.2 nm, which could be accessed by a DFB-MQW laser. Calibration-free measurements in WMS involved comparing the experimental WMS signals to theoretical WMS signals modelled using the laser modulation and gas spectral parameters. The initial step was to validate the WMS models by testing their accuracy in representing the experimentally measured WMS signals. The various laser modulation parameters were measured across the current scan range and applied to the model. Initially, the Fourier model is validated for the WMS-*1f* detection techniques, for room temperature measurements, using the measured laser modulation parameters and spectral parameters given in the HITRAN 2012 database. For the engine measurements the background-subtracted *1f* normalised *2f* technique was the preferred method due to the cancellation of low frequency transmission fluctuations and the absence of a non-absorbing baseline for the chosen CO_2 absorption feature. The *1f* normalised *2f* technique is validated in the lab at different modulation indices.

Chapter 6 - Measurement of Carbon Dioxide in a GTE Exhaust Plume- Summary

The temperature of a gas turbine exhaust plume near the detuner is expected to be around 500 °C. Accurate spectroscopic data are not available in this temperature range from the known spectral databases such as HITRAN or HITEMP. Hence, a high temperature gas cell was built and an accurate high temperature spectroscopic database developed, by simultaneously measuring the collisional line width and absorption line strength by a least-squares fit of the direct spectra. The WMS-*2f*/*1f* technique is validated for the temperature range of 0-500 °C using a heated gas cell. Presence of hot CO_2 lines was observed at higher temperatures, which had to be included in the fitting model.

A CO_2 concentration sensor is demonstrated in the lab by fitting theoretical *2f*/*1f* WMS spectra to experimental *2f*/*1f* WMS spectra measured using a gas cell heated from ambient to higher temperatures (~500 °C), with the temperature measured using a thermocouple. HITRAN spectral parameters were found to be accurate for the room temperature measurements, while the measured high temperature spectral database was indispensable for concentration measurements at higher temperatures.

In an aero engine plume, since the temperature is unknown, it was required to simultaneously measure the concentration and temperature. The pressure of the plume is considered to be atmospheric. Previous attempts to measure concentration and temperature in aero engines or fuel cells employed multiple gas lines for measurement of temperature using ratio thermometry, followed by the extraction of concentration by a least-squares curve fit of one of the absorption lines (with the temperature now known). Another method was to scan the laser bias current across two strong nearby transitions to extract the concentration and temperature, as more information is obtained from a nonlinear curve fit of two strong absorption lines. In this work a sensor was developed to simultaneously measure the temperature and concentration of CO_2 by a least-squares fit of a single strong *2f*/*1f* absorption feature at 1997.2 nm. Accurate measurement of concentration and temperature could be made at high temperatures limited only by etalons in the system as well as uncertainties in the measured laser modulation or gas spectral parameters.

Finally, single channel measurements were conducted in the exhaust plume of a Tay engine, at the detuner entrance. The results showed excellent correlation to engine

operating conditions and the measured concentration and temperature values were close to the predicted values. These results constitute the first reported measurement of CO_2 concentration and temperature in the exhaust plume of an aero engine.

Chapter 7

Conclusions and Future Work

7.1 Conclusions

The primary aim of this work was to develop a calibration-free TDLS-WMS technique for the measurement of gas concentration and temperature in the exhaust plume of a GTE, scalable to a multi-channel tomographic measurement system for FLITES. The first objective to achieve this was initially to build an accurate mathematical model of the recovered signals based on the Fourier series expansion of the absorption line shape, taking account of the measured laser modulation and spectral parameters of the target gas (the latter measured over an extensive range of higher temperatures). This model was then fit to experimentally measured WMS signals to extract the gas concentration and temperature or pressure. The second objective was to establish techniques to correct for the effects of laser modulation parameters such as WM-IM phase walk-off on the *1f* line shape recovery techniques such as the phasor decomposition method. The third objective was to develop a suitable WMS technique in the laboratory for accurate measurement of gas concentration (and temperature) followed by validation of the technique in the harsh environment of a GTE exhaust plume. The key outcomes of this project are summarised in this chapter.

7.1.1 Improvement to PDM for Varying WM Parameters and Adaptation for FLITES

The laser modulation parameters were measured and their effect on line shape recovery using *1f* demodulation techniques was corrected for. It was observed that for the 2 μm DFB-MQW laser, the WM-IM phase lag changed significantly across the current scan. This distorted the absorption spectra recovered using *1f* measurement schemes such as phasor decomposition method or the RAM technique. The measured variation in the tuning coefficient across the current scan range was small for this laser and only had negligible effects on the recovered spectra. The effect of WM- IM phase variation across the current scan was corrected to accurately recover the absorption line shape. This significantly improved the accuracy of the measured concentration and/or temperature values obtained from the curve fit of modelled absorption line shapes to the experimentally recovered absorption line shape signals. The recovered concentration measurements validated the accuracy of the Fourier model of the *1f* (and by inference the *2f*) WMS signals, the laser characterisation methods, their accuracy and the fitting algorithm to yield concentration. Previously, the phasor decomposition method required adjustment of the reference signal of the lock-in amplifier to be in phase with the residual amplitude modulation component of the signal. This requirement was considered as a major impediment in field applications. Hence, a computational technique was developed by which the absorption line shape could be recovered independently of the phase of the LIA reference signal relative to the WMS signals. This method increases the processing speed, and also is useful for multi-channel measurement applications such as optical tomography (establishing the signal phases and setting up the reference phases of the LIAs for all 126 channels would have been otherwise impossible). Finally, it was noticed that the phase of the RAM component is sensitive to the etalons in the system. This method is useful in such a situation.

7.1.2 Analytical Model for the Wavelength Modulation Properties of DFB Lasers

A multi-quantum well DFB laser was used throughout this work for high resolution measurement of the CO_2 spectral absorption feature at 1997.2 nm. It was observed that,

unlike conventional DFB lasers, DFB-MQW lasers in general or vertical cavity surface emitting lasers (VCSELs), the wavelength modulation amplitude for the specific 2 μm DFB-MQW laser used here increased as a function of the applied current modulation frequency. Also, a significant WM-IM phase walk-off was measured across the current scan range. Understanding these phenomena was considered important as it would help in the optimisation of laser modulation parameters for the WMS experiments as well as aid in laser design or selection for WMS applications. Hence, a theoretical model was developed to study the modulation characteristics of semiconductor DFB lasers. The measured wavelength modulation characteristics showed good concurrence with the model. The model successfully identified all the major issues associated with the wavelength modulation characteristics of semiconductor DFB lasers. The model accuracy was observed to be limited in DFB lasers with a higher carrier contribution to WM as the complicated spatial hole burning [61, 66, 67] effects are not accounted in the model.

7.1.3 Calibration-free WMS Techniques for Simultaneous Concentration and Temperature Measurements

Calibration-free WMS techniques use a least-squares curve fit algorithm wherein a theoretically modelled WMS signal is fitted to the experimentally measured signal to recover the gas concentration and temperature or pressure. Similar to most sensing environments, in an aero engine exhaust plume the temperature and concentration values are not known *a-priori*. Hence, the focus of this work was to use calibration-free techniques to simultaneously measure the concentration and temperature from the WMS signals.

A Fourier expansion model was implemented for the gas WMS signals recovered at *2f* and *1f* detection, under the influence of wavelength and intensity modulation. The Fourier formalism forms the core of the calibration-free TDLS-WMS technique and was validated to some extent in the *1f* measurements as may be noted from Section 6.1.2.

2f and *1f* demodulation schemes, with normalisation of the *2f* signal by the *1f*, have been implemented in this work as it provides for cancellation of the transmission fluctuations as well as provides for signal normalisation due to the broadened and blended spectra of CO_2 lacking a zero-absorption baseline, even for atmospheric

pressure measurements. It was shown that an optically thick model was required to accurately model the CO_2 gas absorption measurements taken at EK over an 80 cm plume with expected concentrations and temperatures in the range of 2-4 % and 50-500 °C, respectively. The *2f*/*1f* WMS model was validated at room temperature using the spectral parameters from the HITRAN 2012 database. The model was further validated against measurements taken over a wide range of modulation indices (current modulation amplitudes).

The full *2f*/*1f* model was also validated for two lasers, both at 1997 nm, but from separate manufactured batches having different chip lengths resulting in dissimilar wavelength modulation behaviour.

The spectral parameters such as line strength and collisional line broadening are important for accurately modelling the *2f*/*1f* WMS signals. The line strength and collisional broadening parameters available from spectral databases such as HITRAN 2012 or HITEMP are inaccurate over the temperature ranges expected in a GTE exhaust plume. Hence, these spectral parameters were characterised in the laboratory using direct spectroscopy in a heated optical gas cell at temperatures up to 500 °C and pressures less than 500 mbar. These measured spectral parameters were validated by the lower residuals (< 3 %) obtained in the curve fit of the theoretical *2f*/*1f* signals to the experimental signals. Hot lines of CO_2 were observed at higher temperatures and had to be included into the spectral model.

The demonstration of the final concentration sensor was performed in the laboratory with calibrated mixtures of CO_2 and N_2, with the pressure and temperature measured beforehand using a manometer and thermocouple. The HITRAN 2012 spectral parameters were used in the calibration-free WMS model for room temperature measurements. The spectral parameters obtained by extensive characterisation of direct spectra during the course of this project were used for the concentration measurements at higher temperatures. Concentration values were recovered with an average error of 0.97 % for room temperature measurements and 2 % at higher temperatures up to 500 °C.

As mentioned before, in majority of the gas sensing scenarios, the temperature of the probed region is not known *a-priori,* which was the case with the aero engine exhaust plume. Therefore, spectral algorithms were implemented which facilitated the

concentration and temperature values to be measured simultaneously in carefully controlled laboratory experiments by a least-squares curve fitting of the theoretical *2f*/*1f* WMS line shape at 1997.2 nm, to the experimentally measured *2f*/*1f* WMS line shape. As done previously for the concentration measurements, the spectral parameters from HITRAN 2012 were used for room temperature measurements and the spectral data measured in this work were used for modelling the *2f*/*1f* WMS spectra measured at higher temperatures. For the room temperature measurements, concentration and temperature could be recovered with an average error of 1.6 % and 4.9 %, respectively, and for the high temperature measurements, the concentration and temperature values could be recovered with an average error of 3.39 % and 3.72 %, respectively. These error bars are comparable with other works [2, 31, 90] and satisfy the requirement of a maximum measurement error of 4 % in concentration for optical tomography. A similar measurement strategy was recently demonstrated by Qu et al. [87] using two nearby H_2O lines accessible by a 1.4 μm DFB laser [2, 87] for simultaneous concentration and temperature measurements in a reactor for temperatures as high as 2000 K, with an accuracy of 50 K (2 %) for temperature and less than 1 % for H_2O concentration.

The precision and accuracy of concentration and temperature measurements validated the Fourier model of the WMS signals, the laser characterisation methods, the accuracy of the measured gas spectral parameters and the fitting algorithm. Finally, these measurements procedures will be used for the determination of gas concentration and temperature in the exhaust plume of a GTE to obtain tomographic images of these parameters.

7.1.4 CO_2 Measurements in a GTE Exhaust Plume

A series of measurements were conducted at the Rolls-Royce test bed in East Kilbride. Owing to the high noise levels expected in the measurements due to pointing errors arising from vibrations of the mechanical launch/receive mounts, beam wander and divergence due to turbulence in the plume [13, 51]; different optical access strategies were investigated [17, 105]. In these tests a beam was collimated across the exhaust plume and focussed onto a large area detector using an aspheric mirror. This arrangement with a large aperture allowed for reduced beam scintillation caused by wander, spread and speckle [105].

In these measurements, the engine was operated in various thrust cycles. The concentration and temperature values obtained from a least-squares curve fit of the theoretical *2f*/*1f* signals to the experimental signals followed the changes in the engine operation, viz. the thrust and the temperature of the engine core. The results obtained validated the background-subtracted *2f*/*1f* technique as suitable for measurements in an aero engine exhaust plume. Extension of this technique to the TFLAS-WMS measurements using the TDFA required no additional characterisation of the TDFA, with the excess *2f*-RAM induced in the TDFA cancelled by subtraction of a background *2f*/*1f* signal. This result will be presented in a future piece of work.

Measurements were conducted at INTA, Madrid, with the ring being placed horizontally with paella burners placed inside the ring to create a known concentration and temperature distributions (test phantoms). The initial images of the CO_2 phantoms reconstructed using optical tomography employing the spectral absorbance values measured by the backgrounds subtracted *1f* normalised *2f* spectroscopy, for the 126 measurement channels, gave promising results.

7.2 Future Work

7.2.1 Signal Processing Improvements for FLITES

An approach was recently developed [30, 31, 46, 98] in which a raw background intensity signal is multiplied with a theoretical gas absorption signal and subsequently demodulated using lock-in amplifiers in the software domain to generate the theoretical WMS signals. These signals could be compared with the experimental WMS signals measured through the same LIA. This method is equivalent to the WMS Fourier modelling approach used in this work but does not have the complications of modelling the IM characteristics as this information is embedded in the background signals used to simulate the theoretical WMS model. It was proposed by Goldstein et al. [31] that this methodology can be used for measuring all the gas thermodynamic state variables, viz. the pressure, concentration and temperature using two absorption lines. This approach was used recently by Qu et al. [2, 87]. with the capability of simultaneous measurement of concentration and temperature by using a nonlinear curve fitting algorithm using two well-known water vapour lines at 1430 nm that were used in the works by former CMP

group members [41] for measuring water vapour concentration and temperature in aero engine exhausts.

Background subtraction can be disadvantageous in situations when the signal is comparable to the noise level. The approach mentioned in this section does not require background subtraction as the etalons and the background absorption signals are embedded in the raw scanned and modulated intensity signal used to simulate the WMS signal.

Implementation in software domain also gives the opportunity to use advanced signal processing strategies. For example, it was suggested by Sun et al. [98] that using higher harmonics (*3f, 4f* etc.) could improve the measurement technique due to improved sensitivities and lower RAM contributions. Recently, a method was suggested for *in-situ* measurement of the collisional broadening parameter (or pressure) using the ratio of the peaks of *4f* and *2f* WMS signal magnitudes. This method can be useful for *in-situ* measurement of line width due to the unknown concentration of collisional species in the aero engine exhaust plume, especially at higher pressures [31, 98].

There is a trade-off between noise and the maximum scan frequency due to the finite bandwidth of the low pass filter. If a higher scan frequency is to be used, a higher bandwidth (smaller time constant, encompassing all the frequency components of the scan) was required (lest the signals be distorted). A higher bandwidth could make the measurement susceptible to noise. A technique known as digital fast scanned WMS (DFS-WMS) [30] was used where an equivalent demodulation scheme has been implemented using a narrow bandwidth comb filter and a super-Gaussian filter. This method is useful in improving the signal-to-noise ratio of the WMS signals by cancelling the effects of high frequency multiplicative transmission fluctuations with similar or higher frequency characteristics compared to the intensity scan. The *2f/1f* method could still be used to cancel the low frequency noise. This could be an alternative to the *2f/1f* measurement strategy presented in this thesis for measurements in harsh environments similar to an aero engine exhaust plume, for improved signal-to-noise ratios.

7.2.2 Effect of Etalons / Wavelength Dependent Transmission

Owing to the narrow line width of the DFB lasers, the coherence length is usually tens of meters, and hence optical interference effects occur in TDLS measurements. Sensitivity of TDLS measurements is majorly limited by these optical interference fringes rather than the detector noise. In TDLS measurements, Fabry-Perot etalons are often formed between reflecting or scattering surfaces such as mirrors, lenses, windows of the gas cell, optical coatings, fibre end surfaces, damaged fibre, fibre connectors, optical feedback to the laser diodes etc.

It was observed during the course of this work that etalons [106, 107] cause errors in the measured laser modulation parameters/WMS signals. This is due to the FM (WM) to AM conversion process where the FM (WM) induced AM component at a given phase adds to the RAM component. This can cause an error in the magnitude and phase of IM measured during the characterisation process and can fundamentally limit the Fourier model based fitting approach from being applied to certain measurement systems. Even though background subtraction can remove the effect of etalons to some extent, it is not possible to entirely remove the effect of etalons with FSR comparable to the line width of the absorption feature (~3 GHz). It was observed that the direct absorption signals were severely distorted by the etalons, however, the *2f*/*1f* signals were only distorted by etalons with FSR comparable to the gas absorption feature. Moreover, it was observed that static etalons with a larger FSR affected the background-subtracted *2f*/*1f* signals to a lesser extent. Transient etalons which are present only in the measurements were difficult to remove even though large FSR etalons are always supressed by the WMS signals [31].

Apart from etalons, any multiplicative wavelength dependent transmission function along the measurement path, due to optical coatings, fibre amplifier gain etc. may cause FM to AM conversion and affect the measured laser IM modulation characteristics, and hence the acquired concentration and temperature measurements. A large etalon was formed in the output bulk optical isolator of the TDFA, and consequently the isolator had to be replaced. A small etalon still persisted indicated by a change in the IM phase and amplitude relative to the DFB laser. The IM phase of the TDFA also changed as a function of the pump power which strongly suggests a contribution from other

wavelength dependent phenomena. Therefore, it is proposed that in the future FLITES measurement campaigns, the TDFA be characterised *in-situ* to account for the variations in the IM characteristics across the optical path length.

7.2.3 *In-situ* Characterisation of the Laser Modulation Parameters and Baseline Fitting Approaches

In this section *in-situ* characterisation techniques are described for obtaining the laser intensity modulation (i_0 and i_2) parameters. The potential of this approach was not fully utilised in this work. The wavelength modulation parameters can be characterised using the techniques described in Section 4.7. The instantaneous laser intensity can be obtained by low pass filtering the detector signal. For the background signal, this can be done relatively easily with a filter passband containing the major frequency components of the intensity sweep (ramp). For a 5 Hz ramp, a 500 Hz bandwidth low pass filter (Butterworth or elliptical) was used. The intensity modulation amplitudes can be obtained by *1f* and *2f* lock-in amplifier detection on the raw intensity signals; the magnitude of the *1f* and *2f* signals gives the magnitude of the linear and nonlinear intensity modulation amplitudes.

In a system with temporally stable etalons along the optical measurement path, an *in-situ* characterisation approach is a good measurement strategy.

If the effect of etalons can be neglected, the instantaneous intensity and the IM amplitudes can be obtained in-line from a baseline fit of the non-absorbing spectral regions along the wavelength scan. *In-situ* characterisation techniques could be important for FLITES to compensate for the effects of long term drifts and wavelength dependent transmission effects such as etalons along the optical measurement channel.

7.2.4 NO Measurement System

NO (nitric oxide) is another gas molecule targeted in the FLITES project. In the future, the measurement methodologies developed in this work for CO_2 will be extended to a single channel measurement system for NO at 5.2 μm. A DFB-QCL laser will be used with a thermoelectrically cooled MCT detector. A high quality solid-state Ge etalon will be used for characterisation of the WM parameters. The NO band at 5.2 μm was chosen for optical sensing using a quantum cascade DFB laser (DFB-QCL). It was inferred

from the engine measurements that it is advantages to use modulation frequencies higher than 100 kHz for improved noise isolation. Previously, measurements were reported at 5.2 μm using an external cavity QCL at a frequency of 10 kHz using the *1f* normalised WMS methodology, in a coal fired power plant, by Chao et al. [10]. The FM bandwidth of commercially available QCLs are, however, limited to several tens of kHz which may limit the signal-to-noise ratio of WMS signals for the aero engine measurements. Long path length solid-state Ge etalons will have to be used for characterisation of WM properties which are expensive (£10,000). The *1f* WMS LIA technique described in Section 4.7.3 can be an alternative choice for the measurement of the laser WM characteristics. Recently, difference frequency generation (DFG) lasers have shown promise for this application [108].

7.2.5 The FLITES System and FLITES II

The techniques developed in this work are to be applied to the FLITES tomographic measurement system to obtain gas species concentration and temperature distributions across the exhaust plume of a GTE with state of the art spatio-temporal resolution.

Figure 7-1. Paella burners at the centre of the dodecagon mounting ring placed horizontally, for the phantom tests at INTA (Courtesy of the FLITES consortium).

The tomographic concentration and temperature measurements will be used for engine diagnostics applications as well as research into alternate fuels. For example, a blocked burner nozzle can be easily detected in the output concentration/temperature map. An

asymmetry in the measured plume concentration distribution is an indicator of non-optimal engine operation.

Tests are currently being conducted using TFLAS combined with optical tomography, with the ring placed horizontally, on known test phantoms created by placing paella burners (with CO_2 pumped into the flame to enhance its concentration) at various locations inside the ring cross-section as shown in (Figure 7-1). The initial results look promising. Future work will constitute tests using modern aero engines such as the Trent 1000 XWB with multiple burners. Different optical access geometries will be tested for susceptibility to beam wander, divergence and pointing effects [13].

Comparison with other intrusive techniques such as multi-aperture sampling rakes [1] will be done in future measurements. The final measurements will also be used for validating the results obtained using computational fluid dynamics (CFD) models.

In the exhaust plume of the turbofan engines, the pressure is usually atmospheric, however, in other engines such as scramjets, the pressure might be several atmospheres, which necessitates the measurement of pressure as well.

The initial aim of the FLITES consortium was to obtain only the images of concentration. The presently used tomographic reconstruction algorithms employing smoothing methods (applying smoothing functions on the basis using *a-priori* knowledge [28, 50]) and positivity, assume a top hat temperature profile across the GTE exhaust plume and were capable of reconstructing only the concentration images of the plume. The recovered concentration data from the fitting algorithm were transferred to the Agile Tomography group at Edinburgh, who used these to calculate the absorbance for the 126 measurement channels, assuming a top hat temperature profile, to reconstruct the concentration distribution by solving the inverse mathematical problem. It would be useful to gain information about the temperature distributions as well. This would require re-analysis of the tomographic inverse problem and may require that Strathclyde works together with Edinburgh. Recently, a proof of concept was demonstrated for tomographic reconstruction employing the *2f/1f* WMS technique by Cai et al. [109] and is an important step forward. In their work, multiplexed (implies using several wavelengths to probe the imaging space, which relaxes the requirement on the number of measurement channels) tomography was proposed for simultaneous

measurement of concentration and temperature using *2f/1f* WMS signals. These problems will be addressed in the FLITES II project.

Bibliography

[1] K. Schäfer, J. Heland, D. H. Lister, C. W. Wilson, R. J. Howes, R. S. Falk, E. Lindermeir, M. Birk, G. Wagner, P. Haschberger, M. Bernard, O. Legras, P. Wiesen, R. Kurtenbach, K. J. Brockmann, V. Kriesche, M. Hilton, G. Bishop, R. Clarke, J. Workman, M. Caola, R. Geatches, R. Burrows, J. D. Black, P. Hervé, and J. Vally, "Nonintrusive optical measurements of aircraft engine exhaust emissions and comparison with standard intrusive techniques," *Appl. Opt.*, vol. 39, no. 3, pp. 441–455, 2000.

[2] Z. Qu, R. Ghorbani, D. Valiev, and F. M. Schmidt, "Calibration-free scanned wavelength modulation spectroscopy – application to H_2O and temperature sensing in flames," *Opt. Express*, vol. 23, no. 12, p. 16492, 2015.

[3] J. Chen, A. Hangauer, R. Strzoda, and M. C. Amann, "Laser spectroscopic oxygen sensor using diffuse reflector based optical cell and advanced signal processing," *Appl. Phys. B Lasers Opt.*, vol. 100, no. 2, pp. 417–425, 2010.

[4] G. B. Rieker, J. B. Jeffries, and R. K. Hanson, "Calibration-free wavelength-modulation spectroscopy for measurements of gas temperature and concentration in harsh environments," *Appl. Opt.*, vol. 48, no. 29, pp. 5546–5560, 2009.

[5] D. T. Cassidy and J. Reid, "High-sensitivity detection of trace gases using sweep integration and tunable diode lasers," *Appl. Opt.*, vol. 21, no. 14, pp. 2527–2530, 1982.

[6] V. Ebert, K. Pleban, and J. Wolfrum, "*In-situ* oxygen-monitoring using near-infrared diode lasers and wavelength modulation spectroscopy," *OSA 1998 Tech. Dig. Ser. Vol 3 Laser Appl. to Chem. Environ. Anal. Pap. LWB3*, vol. 209, pp. 206–209, 1998.

[7] T. Fernholz, H. Teichert, and V. Ebert, "Digital, phase-sensitive detection for in situ diode-laser spectroscopy under rapidly changing transmission conditions," *Appl. Phys. B Lasers Opt.*, vol. 75, no. 2–3, pp. 229–236, 2002.

[8] H. Li, G. B. Rieker, X. Liu, J. B. Jeffries, and R. K. Hanson, "Extension of wavelength-modulation spectroscopy to large modulation depth for diode laser

absorption measurements in high-pressure gases," *Appl. Opt.*, vol. 45, no. 5, pp. 1052–1061, 2006.

[9] "Private communications - Dr. Michael Lengden, Dr. Ian Armstrong, Dr. James Bain, Prof. Walter Johnstone and Prof. George Stewart, University of Strathclyde."

[10] X. Chao, J. B. Jeffries, and R. K. Hanson, "Wavelength-modulation-spectroscopy for real-time, in situ NO detection in combustion gases with a 5.2 μm quantum-cascade laser," *Appl. Phys. B Lasers Opt.*, vol. 106, no. 4, pp. 987–997, 2012.

[11] Rolls-Royce, "Rolls Royce Trent 700 image." [Online]. Available: http://www.rolls-royce.com/products-and-services/civil-aerospace/products/civil-large-engines/trent-700/trent-700-infographic.aspx.

[12] M. G. Allen, "Diode laser absorption sensors for gas-dynamic and combustion flows," *Meas. Sci. Technol.*, vol. 9, no. 4, pp. 545–562, 1998.

[13] M. Henriksson, D. Seiffer, L. Sjöqvist, R. Deron, and R. Schleijpen, *Study of jet engine plume phenomena on laser beam pointing and tracking*, 1st ed. Information Systems, Swedish Defence Research Agency (FOI), 2009.

[14] J. Liu, G. Rieker, J. Jeffries, M. Gruber, C. Carter, T. Mathur, and R. Hanson, "Near-infrared diode laser absorption diagnostic for temperature and water vapor in a scramjet combustor," *Appl. Opt.*, vol. 44, no. 31, pp. 6701–6711, 2005.

[15] A. Griffiths and F. Houwing, "Diode laser absorption spectroscopy of water vapor in a scramjet combustor," *Appl. Opt.*, vol. 44, no. 31, pp. 6653–6659, 2005.

[16] C. Sky, "Clean Sky 2 : developing new generations of greener aircraft," 2014. [Online]. Available: www.cleansky.eu.

[17] P. Wright, N. Terzija, J. L. Davidson, S. Garcia-Castillo, C. Garcia-Stewart, S. Pegrum, S. Colbourne, P. Turner, S. D. Crossley, T. Litt, S. Murray, K. B. Ozanyan, and H. McCann, "High-speed chemical species tomography in a multi-cylinder automotive engine," *Chem. Eng. J.*, vol. 158, no. 1, pp. 2–10, 2010.

[18] L. S. Rothman, I. E. Gordon, Y. Babikov, a. Barbe, D. Chris Benner, P. F. Bernath, M. Birk, L. Bizzocchi, V. Boudon, L. R. Brown, a. Campargue, K. Chance, E. a. Cohen, L. H. Coudert, V. M. Devi, B. J. Drouin, a. Fayt, J. M. Flaud, R. R. Gamache, J. J. Harrison, J. M. Hartmann, C. Hill, J. T. Hodges, D.

Jacquemart, a. Jolly, J. Lamouroux, R. J. Le Roy, G. Li, D. a. Long, O. M. Lyulin, C. J. Mackie, S. T. Massie, S. Mikhailenko, H. S. P. Müller, O. V. Naumenko, a. V. Nikitin, J. Orphal, V. Perevalov, a. Perrin, E. R. Polovtseva, C. Richard, M. a H. Smith, E. Starikova, K. Sung, S. Tashkun, J. Tennyson, G. C. Toon, V. G. Tyuterev, and G. Wagner, "The HITRAN2012 molecular spectroscopic database," *J. Quant. Spectrosc. Radiat. Transf.*, vol. 130, pp. 4–50, 2013.

[19] N. Jacquinet-Husson, L. Crepeau, R. Armante, C. Boutammine, A. Chédin, N. A. Scott, C. Crevoisier, V. Capelle, C. Boone, N. Poulet-Crovisier, A. Barbe, A. Campargue, D. Chris Benner, Y. Benilan, B. Bézard, V. Boudon, L. R. Brown, L. H. Coudert, A. Coustenis, V. Dana, V. M. Devi, S. Fally, A. Fayt, J. M. Flaud, A. Goldman, M. Herman, G. J. Harris, D. Jacquemart, A. Jolly, I. Kleiner, A. Kleinböhl, F. Kwabia-Tchana, N. Lavrentieva, N. Lacome, L. H. Xu, O. M. Lyulin, J. Y. Mandin, A. Maki, S. Mikhailenko, C. E. Miller, T. Mishina, N. Moazzen-Ahmadi, H. S. P. Müller, A. Nikitin, J. Orphal, V. Perevalov, A. Perrin, D. T. Petkie, A. Predoi-Cross, C. P. Rinsland, J. J. Remedios, M. Rotger, M. A. H. Smith, K. Sung, S. Tashkun, J. Tennyson, R. A. Toth, A. C. Vandaele, and J. Vander Auwera, "The 2009 edition of the GEISA spectroscopic database," *J. Quant. Spectrosc. Radiat. Transf.*, vol. 112, no. 15, pp. 2395–2445, 2011.

[20] F. Schreier, "Optimized implementations of rational approximations for the Voigt and complex error function," *J. Quant. Spectrosc. Radiat. Transf.*, vol. 112, no. 6, pp. 1010–1025, 2011.

[21] A. McLean, C. Mitchell, and D. Swanston, "Implementation of an efficient analytical approximation to the Voigt function for photoemission lineshape analysis," *J. Electron Spectros. Relat. Phenomena*, vol. 69, no. 2, pp. 125–132, 1994.

[22] C. Banwel, *Fundamentals of molecular spectroscopy*, 2nd ed., vol. 1, no. 1. 1966.

[23] G. Herzberg, *Molecular spectra and molecular structure. Vol.1: Spectra of diatomic molecules*, 1st ed. 1950.

[24] W. Demtröder, *Laser spectroscopy volume 1 : basic principles*, 2nd ed. 2008.

[25] R. R. Gamache, S. Kennedy, R. Hawkins, and L. S. Rothman, "Total internal partition sums for molecules in the terrestrial atmosphere," *J. Mol. Struct.*, vol. 517–518, no. Feb 2000, pp. 407–425, 2000.

[26] L. S. Rothman, I. E. Gordon, R. J. Barber, H. Dothe, R. R. Gamache, A.

Goldman, V. I. Perevalov, S. A. Tashkun, and J. Tennyson, "HITEMP, the high-temperature molecular spectroscopic database," *J. Quant. Spectrosc. Radiat. Transf.*, vol. 111, no. 15, pp. 2139–2150, 2010.

[27] C. S. Goldenstein, C. L. Strand, I. a Schultz, K. Sun, J. B. Jeffries, and R. K. Hanson, "Fitting of calibration-free scanned-wavelength-modulation spectroscopy spectra for determination of gas properties and absorption lineshapes," *Appl. Opt.*, vol. 53, no. 3, pp. 356–67, 2014.

[28] "Private communications - Dr.Nick Polydorides, Agile Tomography Group, University of Edinburgh."

[29] G. Schulze, A. Jirasek, M. M. L. Yu, A. Lim, R. F. B. Turner, and M. W. Blades, "Investigation of selected baseline removal techniques as candidates for automated implementation," *Appl. Spectrosc.*, vol. 59, no. 5, pp. 545–574, 2005.

[30] A. Klein, O. Witzel, and V. Ebert, "Rapid, time-division multiplexed, direct absorption- and wavelength modulation-spectroscopy," *Sensors*, vol. 14, no. 11, pp. 21497–21513, 2014.

[31] C. S. Goldenstein, C. L. Strand, I. A. Schultz, K. Sun, J. B. Jeffries, and R. K. Hanson, "Fitting of calibration-free scanned-wavelength-modulation spectroscopy spectra for determination of gas properties and absorption lineshapes.," *Appl. Opt.*, vol. 53, no. 3, pp. 356–67, 2014.

[32] A. L. Chakraborty, K. Ruxton, W. Johnstone, M. Lengden, and K. Duffin, "Elimination of residual amplitude modulation in tunable diode laser wavelength modulation spectroscopy using an optical fiber delay line," *Opt. Express*, vol. 17, no. 12, pp. 9602–9607, 2009.

[33] W. Johnstone, A. J. McGettrick, A. Cheung, and G. Stewart, "Tunable diode laser spectroscopy for industrial process applications: system characterization in conventional and new approaches," vol. 8, no. 7, pp. 1079–1088, 2008.

[34] J. R. P. Bain, S. Member, W. Johnstone, K. Ruxton, G. Stewart, and M. Lengden, "Recovery of absolute gas absorption line shapes using tunable diode laser spectroscopy with wavelength modulation—part I: theoretical analysis," *Light. Technol. J.*, vol. 29, no. 6, pp. 811–821, 2011.

[35] K. Duffin, A. J. McGettrick, W. Johnstone, G. Stewart, and D. G. Moodie, "Tunable diode-laser spectroscopy with wavelength modulation: A calibration-

free approach to the recovery of absolute gas absorption line shapes," *J. Light. Technol.*, vol. 25, no. 10, pp. 3114–3125, 2007.

[36] K. Ruxton, A. L. Chakraborty, W. Johnstone, M. Lengden, G. Stewart, and K. Duffin, "Tunable diode laser spectroscopy with wavelength modulation: Elimination of residual amplitude modulation in a phasor decomposition approach," *Sensors and Actuators, B: Chemical*, vol. 150, no. 1. pp. 367–375, 2010.

[37] T. Benoy, M. Lengden, G. Stewart, and W. Johnstone, "Recovery of absorption line shapes with correction for the wavelength modulation characteristics of DFB lasers," *IEEE Photonics J.*, vol. 8, no. 3, pp. 1–17, 2016.

[38] A. L. Chakraborty, K. Ruxton, and W. Johnstone, "Suppression of intensity modulation contributions to signals in second harmonic wavelength modulation spectroscopy," *Opt. Lett.*, vol. 35, no. 14, pp. 2400–2402, 2010.

[39] X. Zhu and D. T. Cassidy, "Electronic subtracter for trace-gas detection with InGaAsP diode lasers," *Appl. Opt.*, vol. 34, no. 36, pp. 8303–8308, 1995.

[40] P. C. Hobbs, "Ultrasensitive laser measurements without tears," *Appl. Opt.*, vol. 36, no. 4, pp. 903–920, 1997.

[41] J. R. P. Bain, "Advances in tunable diode laser spectroscopy for aero engine research -thesis," University of Strathclyde, 2012.

[42] J. T. C. Liu, J. B. Jeffries, and R. K. Hanson, "Large-modulation-depth 2f spectroscopy with diode lasers for rapid temperature and species measurements in gases with blended and broadened spectra," *Appl. Opt.*, vol. 43, no. 35, pp. 6500–6509, 2004.

[43] J. Reid and D. Labrie, "Second-harmonic detection with tunable diode lasers - Comparison of experiment and theory," *Appl. Phys. B*, vol. 26, no. 3, pp. 203–210, 1981.

[44] R. Arndt, "Analytical line shapes for lorentzian signals broadened by modulation," *J. Appl. Phys.*, vol. 36, no. 8, 1965.

[45] J. Henningsen and H. Simonsen, "Quantitative wavelength-modulation spectroscopy without certified gas mixtures," *Appl. Phys. B Lasers Opt.*, vol. 70, no. 4, pp. 627–633, 2000.

[46] A. Upadhyay and A. L. Chakraborty, "Calibration-free 2f WMS with in situ real-time laser characterization and 2f RAM nulling," *Opt. Lett.*, vol. 40, no. 17, pp. 4086–4089, Sep. 2015.

[47] G. B. Rieker, H. Li, X. Liu, J. B. Jeffries, R. K. Hanson, M. G. Allen, S. D. Wehe, P. a Mulhall, and H. S. Kindle, "A diode laser sensor for rapid, sensitive measurements of gas temperature and water vapour concentration at high temperatures and pressures," *Meas. Sci. Technol.*, vol. 18, no. 5, pp. 1195–1204, 2007.

[48] L. S. Chang, J. B. Jeffries, and R. K. Hanson, "Mass flux sensing via tunable diode laser absorption of water vapor," *Aiaa J.*, vol. 48, no. 11, pp. 2687–2693, 2010.

[49] K. Sun, X. Chao, R. Sur, C. S. Goldenstein, J. B. Jeffries, and R. K. Hanson, "Analysis of calibration-free wavelength-scanned wavelength modulation spectroscopy for practical gas sensing using tunable diode lasers," *Meas. Sci. Technol.*, vol. 24, no. 12, p. 125203, 2013.

[50] N. Polydorides and H. McCann, "FLITES technical report," pp. 1–17, 2014.

[51] M. Johnson, E. Fisher, P. Wright, D. McCormick, K. Ozanyan, M. Johnson, J. Black, E. Fisher, A. Chighine, N. Polydorides, H. McCann, Y. Feng, K. Khan, P. Bastock, F. Jia, D. Hewak, J. Nilsson, M. Lengden, D. Wilson, I. Armstrong, T. Benoy, and W. Johnstone, "Progress towards non-intrusive optical measurement of gas turbine exhaust species distributions," *IEEE Aerosp. Conf. Proc.*, vol. 2015-June, 2015.

[52] W. Cai and C. F. Kaminski, "A tomographic technique for the simultaneous imaging of temperature, chemical species, and pressure in reactive flows using absorption spectroscopy with frequency-agile lasers," *Appl. Phys. Lett.*, vol. 104, no. 3, 2014.

[53] A. J. McGettrick, W. Johnstone, R. Cunningham, and J. D. Black, "Tunable diode laser spectroscopy with wavelength modulation: Calibration-free measurement of gas compositions at elevated temperatures and varying pressure," *J. Light. Technol.*, vol. 27, no. 15, pp. 3150–3161, 2009.

[54] "Perkin Elmer 7280 lock in amplifier-manual."

[55] S. Osterman, S. Diddams, M. Beasley, C. Froning, L. Hollberg, P. MacQueen, V. Mbele, and A. Weiner, "A proposed laser frequency comb-based wavelength reference for high-resolution spectroscopy," *Proc. SPIE*, vol. 6693, p. 66931G–66931G–9, 2007.

[56] S. Osterman, G. G. Ycas, S. A. Diddams, F. Quinlan, S. Mahadevan, L. Ramsey, C. F. Bender, R. Terrien, B. Botzer, S. Sigurddson, and S. L. Redman, "A near infrared frequency comb for Y+J band astronomical spectroscopy," *arXiv.org*, vol. 1209, p. 3295, 2012.

[57] S. Schilt and L. Thevenaz, "Experimental method based on wavelength-modulation spectroscopy for the characterization of semiconductor lasers under direct modulation," *Appl. Opt.*, vol. 43, no. 22, pp. 4446–4453, 2004.

[58] S. Kobayashi, Y. Yamamoto, M. Ito, and T. Kimura, "Direct frequency modulation in AlGaAs semiconductor lasers," *IEEE Trans. Microw. Theory Tech.*, vol. 30, no. 4, pp. 428–441, 1982.

[59] L. A. Coldren and S. W. Corzine, *Diode lasers and photonic integrated circuits*. 1995.

[60] J. R. P. Bain, W. Johnstone, K. Ruxton, G. Stewart, M. Lengden, and K. Duffin, "Recovery of absolute gas absorption line shapes using tunable diode laser spectroscopy with wavelength modulation-Part II: Experimental investigation," *J. Light. Technol.*, vol. 29, no. 7, pp. 987–996, 2011.

[61] P. Vankwikelberge, F. Buytaert, A. Franchois, R. Baets, P. I. Kuindersma, and C. W. Fredriksz, "Analysis of the carrier-induced FM response of DFB lasers: Theoretical and experimental case studies," *IEEE Journal of Quantum Electronics*, vol. 25, no. 11. pp. 2239–2254, 1989.

[62] C. H. Henry, "Theory of the linewidth of semiconductor lasers," *Quantum Electron. IEEE J.*, vol. 18, no. 2, pp. 259–264, 1982.

[63] R. S. Tucker, "High speed modulation of semiconductor lasers," *IEEE JLT*, vol. LT-3, no. 6, pp. 1180–1191, 1989.

[64] C. A. Green, N. K. Dutta, and W. Watson, "Linewidth enhancement factor in InGaAsP/InP multiple quantum well lasers," *Appl. Phys. Lett.*, vol. 50, no. 20, pp. 1409–1410, 1987.

[65] S. Melnik, G. Huyet, and A. Uskov, "The linewidth enhancement factor α of quantum dot semiconductor lasers," *Opt. Express*, vol. 14, no. 7, p. 2950, 2006.

[66] R. Schatz, "Dynamics of spatial hole burning effects in DFB lasers," *IEEE J. Quantum Electron.*, vol. 31, no. 11, pp. 1981–1993, 1995.

[67] J. Kinoshita, "Modelling of high-speed DFB lasers considering the spatial holeburning effect using three rate equations," *IEEE J. Quantum Electron.*, vol. 30, no. 4, pp. 929–938, 1994.

[68] T. L. Koch and J. E. Bowers, "Nature of wavelength chirping in directly modulated semiconductor lasers," *Electron. Lett.*, vol. 20, no. 25, pp. 1038–1040, 1984.

[69] M. Ito and T. Kimura, "Stationary and transient thermal properties of semiconductor laser diodes," *IEEE J. Quantum Electron.*, vol. 17, no. 5, pp. 787–795, 1981.

[70] P. Correc, O. Girard, and I. F. de Faria, "On the thermal contribution to the FM response of DFB lasers:Theory and experiment.," *IEEE J. Quantum Electron.*, vol. 30, no. 11, pp. 2485–2490, 1994.

[71] M. J. Steinmann, R. J. S. Pedersen, and Y. Kotaki, "Experimental and theoretical analysis of the carrier induced red-shifted FM-response of W4-shifted MQW DFB LD.," pp. 172–173, 1990.

[72] H. Yamazaki, M. Yamaguchi, M. Kitamura, and I. Mito, "Analysis on FM efficiency of InGaAs / InGaAsP SCH-MQW LD's taking injection carrier transport into account," vol. 4, no. 4, pp. 396–398, 1993.

[73] "Thermal conduction," 2016. [Online]. Available: https://en.wikipedia.org/wiki/Thermal_conduction.

[74] MIT, "Thermal electrical analogue." [Online]. Available: http://web.mit.edu/16.unified/www/FALL/thermodynamics/notes/node118.html.

[75] H. S. Carslaw, *Conduction of heat in solids*. Clarendon press, 1959.

[76] A. Hangauer, R. Strzoda, and M. C. Amann, "The frequency modulation response of vertical-cavity surface-emitting lasers: experiment and theory," *IEEE*

J. Sel. Top. Quantum Electron., vol. 17, no. 6, pp. 1584–1593, 2011.

[77] W. B. Joyce and R. W. Dixon, "Thermal resistance of heterostructure lasers," *J. Appl. Phys.*, vol. 46, no. 2, pp. 855–862, 1975.

[78] G. Soundra Pandian and S. Dilwali, "On the thermal FM response of a semiconductor laser diode," *IEEE Photonics Technol. Lett.*, vol. 4, no. 2, pp. 130–133, 1992.

[79] G. Soundra Pandian and S. Dilwali, "Transfer function of thermal FM, FSK step response and the dip in the FM response of laser diodese," *Opt. Quantum Electron.*, vol. 24, pp. 661–676, 1992.

[80] S. Sujecki, *Photonics modelling and design*, 1st ed. 2014.

[81] R. Phelan, J. O'Carroll, D. Byrne, C. Herbert, J. Somers, and B. Kelly, "In 0.75Ga 0.25As/InP multiple quantum-well discrete-mode laser diode emitting at 2 μm," *IEEE Photonics Technol. Lett.*, vol. 24, no. 8, pp. 652–654, 2012.

[82] J. I. Kinoshita and K. Matsumoto, "Transient chirping in distributed feedback lasers: effect of spatial hole-burning along the laser axis," *IEEE J. Quantum Electron.*, vol. 24, no. 11, pp. 2160–2169, 1988.

[83] Tien-Pei Lee, *Current trends in integrated optoelectronics*. World Scientific, 1994.

[84] "Private communications - Prof. George Stewart, University of Strathclyde."

[85] G. B. Rieker, H. Li, X. Liu, J. B. Jeffries, R. K. Hanson, M. G. Allen, S. D. Wehe, P. A. Mulhall, and H. S. Kindle, "A diode laser sensor for rapid, sensitive measurements of gas temperature and water vapour concentration at high temperatures and pressures," *Meas. Sci. Technol.*, vol. 18, no. 5, pp. 1195–1204, 2007.

[86] J. T. C. Liu, J. B. Jeffries, and R. K. Hanson, "Wavelength modulation absorption spectroscopy with 2f detection using multiplexed diode lasers for rapid temperature measurements in gaseous flows," *Appl. Phys. B Lasers Opt.*, vol. 78, no. 3–4, pp. 503–511, 2004.

[87] Z. Qu and F. M. Schmidt, "Low-cost TDLAS sensor for real-time *in-situ*

temperature and H2O measurements in biomass combustion applications CF-WMS method biomass flame," vol. 125203, p. 125203, 2013.

[88] G. B. Rieker, J. B. Jeffries, and R. K. Hanson, "Calibration-free wavelength-modulation spectroscopy for measurements of gas temperature and concentration in harsh environments.," *Appl. Opt.*, vol. 48, no. 29, pp. 5546–5560, 2009.

[89] A. Upadhyay and A. L. Chakraborty, "Residual amplitude modulation method implemented at the phase quadrature frequency of a 1650-nm laser diode for line shape recovery of methane," *IEEE Sens. J.*, vol. 15, no. 2, pp. 1153–1160, 2015.

[90] R. M. Mihalcea, D. S. Baer, and R. K. Hanson, "Diode-laser absorption measurements of CO2 near 2.0 μm at elevated temperatures," *Appl. Opt.*, vol. 37, no. 36, p. 8341, 1998.

[91] R. M. Mihalcea, R. M. Mihalcea, M. E. Webber, M. E. Webber, D. S. Baer, D. S. Baer, R. K. Hanson, R. K. Hanson, G. S. Feller, G. S. Feller, W. B. Chapman, and W. B. Chapman, "Diode-laser absorption measurements of CO_2 , H_2O, N_2O, and NH_3 near 2.0 μm," *Appl. Phys. B Lasers Opt.*, vol. 67, no. 3, pp. 283–288, 1998.

[92] R. M. Mihalcea, D. S. Baer, and R. K. Hanson, "Advanced diode laser absorption sensor for in situ combustion measurements of CO_2, H_2O, and gas temperature," *Symp. Combust.*, vol. 27, no. 1, pp. 95–101, 1998.

[93] M. E. Webber, S. Kim, S. T. Sanders, D. S. Baer, R. K. Hanson, and Y. Ikeda, "*In-situ* combustion measurements of CO_2 by use of a distributed-feedback diode-laser sensor near 2.0 μm," *Appl. Opt.*, vol. 40, no. 6, p. 821, 2001.

[94] W. Demtroder, *Laser spectroscopy volume 1*. 2008.

[95] R. K. Hanson, M. R. Spearrin, and C. S. Goldenstein, *Spectroscopy and optical diagnostics for gases*. 2001.

[96] M. E. Webber, "Diode laser measurements of NH_3 and CO_2 for combustion and bioreactor applications," 2001.

[97] C. Corsi, F. D'Amato, M. De Rosa, and G. Modugno, "High-resolution measurements of line intensity, broadening and shift of CO_2 around 2μm," *Eur. Phys. J. D - At. Mol. Opt. Phys.*, vol. 6, no. 3, pp. 327–332, 1999.

[98] K. Sun, "Utilization of multiple harmonics of wavelength modulation absorption spectroscopy for practical gas sensing-thesis," University of Stanford, 2013.

[99] J. Bain, "FLITES project report," 2012.

[100] P. C. D. Hobbs, *Building electro-optical systems : making it all work*, 2nd ed. 2009.

[101] K. Sun, R. Sur, X. Chao, J. B. Jeffries, R. K. Hanson, R. J. Pummill, and K. J. Whitty, "TDL absorption sensors for gas temperature and concentrations in a high-pressure entrained-flow coal gasifier," *Proc. Combust. Inst.*, vol. 34, no. 2, pp. 3593–3601, 2013.

[102] "Bypass ratio." [Online]. Available: https://en.wikipedia.org/wiki/Bypass_ratio.

[103] "Private comminucations - Dr.Mark Johnson, Rolls- Royce plc."

[104] P. Wright, D. McCormick, J. Kliment, K. Ozanyan, M. Johnson, J. Black, S. A. Tsekenis, E. Fisher, H. McCann, M. Lengden, D. Wilson, W. Johnstone, V. Archilla, Á. González-Núñez, Y. Feng, and J. Nilsson, "Implementation of non-intrusive jet exhaust species distribution measurements within a test facility," *2016 IEEE Aerosp. Conf.*, pp. 1–14, 2016.

[105] L. C. Andrews and R. L. Phillips, *Laser beam propagation through random media*, 2nd ed. 2005.

[106] J. Cao, Z. Wang, K. Zhang, R. Yang, and Y. Wang, "Etalon effects analysis in tunable diode laser absorption spectroscopy gas concentration detection system based on wavelength modulation spectroscopy," *2010 Symp. Photonics Optoelectron.*, no. 3, pp. 1–5, 2010.

[107] A. Lidgard and N. A. Olsson, "Generation and cancellation of second-order harmonic distortion in analog optical systems by interferometrie FM-AM conversion," *IEEE Photonics Technology Letters*, vol. 2, no. 7. pp. 519–521, 1990.

[108] J. J. Scherer, J. B. Paul, H. J. Jost, and M. L. Fischer, "Mid-IR difference frequency laser-based sensors for ambient CH_4, CO, and N_2O monitoring," *Appl. Phys. B Lasers Opt.*, vol. 110, no. 2, pp. 271–277, 2013.

[109] W. Cai and C. F. Kaminski, “Multiplexed absorption tomography with calibration-free wavelength modulation spectroscopy,” *Appl. Phys. Lett.*, vol. 104, no. 15, p. 154106, 2014.

Publications

Journal Publications

[1] T. Benoy, M. Lengden, G. Stewart, and W. Johnstone, "Recovery of absorption line shapes with correction for the wavelength modulation characteristics of DFB lasers," *IEEE Photonics J.*, vol. 8, no. 3, pp. 1–17, 2016.

[2] T. Benoy, M. Lengden, D. Wilson, I. Armstrong, W. Johnstone, and G. Stewart, "Measurement of CO_2 concentration and temperature in an aero engine exhaust plume using wavelength modulation spectroscopy"- Submitted.

Conferences

[1] T. Benoy, M. Lengden, I. Armstrong, D. Wilson, G. Stewart, and W. Johnstone, "Near-IR tunable diode laser spectroscopy for aero engine research," *International Conference on Field Laser Applications in Industry and Research*, Florence, Italy, 2014.

[2] Y. Feng, J. Nilsson, S. Jain, T. C. May-Smith, J. K. Sahu, F. Jia, T. Benoy, D. Wilson, M. Lengden, and W. Johnstone, "LD-seeded thulium-doped fibre amplifier for CO_2 measurements at 2 μm," in *Europhoton*, Neuchatel, Switzerland, *2014*.

[3] M. Lengden, D. Wilson, I. Armstrong, T. Benoy, and W. Johnstone, "Fibre Laser Imaging of Gas Turbine Exhaust Species - A review of CO_2 aero engine imaging," in *Advanced Photonics 2015*, 2015, p. JM3A.37.

[4] P. Wright, D. McCormick, K. Ozanyan, M. Johnson, J. Black, E. Fisher, A. Chighine, N. Polydorides, H. McCann, Y. Feng, K. Khan, P. Bastock, F. Jia, D. Hewak, J. Nilsson, M. Lengden, D. Wilson, I. Armstrong, T. Benoy, and W. Johnstone, "Progress towards non-intrusive optical measurement of gas turbine exhaust species distributions," *IEEE Aerosp. Conf. Proc.*, vol. 2015-June, 2015.

[5] T. Benoy, M. Lengden, D. Wilson, and W. Johnstone, "Fibre laser imaging of gas turbine exhaust species – A review of CO_2 aero engine imaging," in *University of Glasgow Aerospace Symposium 2015: The Aerospace Ecosystem*, 2016.

In preparation

[1] T. Benoy, G. Stewart, M. Lengden, and W. Johnstone, “Preliminary studies into the frequency chirp properties of DFB lasers at sub-MHz modulation frequencies”.

[2] T. Benoy, G. Stewart, M. Lengden, W. Johnstone, G. Humphries, D. Wilson, “WMS using a thulium doped fibre amplifier”.

Appendix A

```
 % Master code to find the phase and tuning coefficient from the fit method
% Copyright
% Thomas Benoy , Dr.Micahel lengden
% CMP, Strathclyde
% This code read files by their creation time and finds out the phase and
% tuning coeffcient from the input data.
% It calculates file by file and outputs the data to an excel file and  appends it.
% assumes that the file is in the tronix format of Uber Control

% input file format
% time     % AM wave  % Resonator Trace
% data     %data      %data
%%%%      %%%%%%%%   %%%%%%%%%%%%%%%
%%%%
%
% Warning: careful selection of the resonator peaks required(do not select the
% peaks in the non-responsive region. % make sure it is symmetric
% Warning: apply filter to the resonator trace if too noisy...

clc;
clear all;
close all;
format long;

in = 1;                                                 % file number (keep appending
it for accessing the subsequent files)
% Enter your frequency in Hz
freqq = [100];

freqqq = freqq(1);                                      % to facilitate multi
plotting(ignore)
% Enter your bias Current range(mA)
Ib = [40:5:120];
Power =[0];                                             % Specify for the TDFA if
used
% Enter FSR of your Fibre Ring Resonator(GHz)
FSR = 0.1234;                                           % characterised at 2000 nm
% FSR = 0.4275;


%  Enter peak to peak applied curret sine to calculate tuning coefficient(rough)-mA
di_p2p = 20;

% Enter the output file name and location in xls format
output_file_name = '../Char_0.1238_res_output.xls';
file_head = {['Eblana II FSR =0.1234 ']};

%%%%%%%%%%%%Read in the AM and resonator files%%%%%%%%%%%%%%%%%%%%%%%%%%%%%%%%%%%%
```

```
file_loc ='T:\Thomas Benoy\27-04-2016\Eblana 2\Direct\Char_0.1238_res\AM';
cd(file_loc);
d = dir([file_loc '\*.csv']);

sync_offset_file = csvread('T:\Thomas Benoy\27-04-
2016\Dark_current_covered_cell_det.csv'); % offset for AM-important
sync_off = sync_offset_file(:,1);

file = csvread(d(in).name);
time = file(:,1);
sync = file(:,2);
res = file(:,3);
%%%%%%%%%%%%%%%%%%%%%%%%%%%%%%%%%%%%%%%%%%%%%%%%%%%%%%%%%%%%%%%%%%%%%%%%%%%%%%%%%%%%%%
%
sync = sync-sync_off;                                                        %
subtract AM offset


figure(1);
plot(sync,'r');
hold on;
frequency = freqqq*1000;                                                     % in kHz

G = @(g,time) g(1)+ g(2).*cos((g(3).*time)+(g(4)))+ g(5).*cos((2*g(3).*time)+g(6));
% fit to a second order nonlienar equation
G1 = @(g,time) g(1)+g(2)*cos(g(3)*time+g(4));
% fit to a first order nonlinear equation

H = @(h,time) h(1)+h(2)*cos(2*h(3)*time+h(4));
% to fit the residual to 2f sinusoid
g0 = [0 -1 frequency*2*pi 0 1e-3 0];
% initiliasition values
g10 = [0 -1 frequency*2*pi 0 ];
h0 = [0 -1 frequency*2*pi 0 ];
options  =optimset('MaxFunEvals',100000,'TolFun',1e-15,'MaxIter',100000,'TolX',1e-
15);       % lsqcurvefit optimisation values


%%%%%%%%%%%%%%%%% curve fitting %%%%%%%%%%%%%%%%%%%%%%%%%%%%%%%
[g1,resnorm,~,exitflag,output] = lsqcurvefit(G1,g10,time,sync,[-10 -10 (frequency-
10)*2*pi -pi ],[10 10 (frequency+10)*2*pi pi],options);
[g,resnorm,~,exitflag,output] = lsqcurvefit(G,g0,time,sync,[-10 -10 (frequency-
10)*2*pi -pi -.1  -pi ],[10 10 (frequency+10)*2*pi pi .1  pi],options);
%%%%%%%%%%%%%%%%%%%%%%%%%%%%%%%%%%%%%%%%%%%%%%%%%%%%%%%%%%%%%%%%

sync_1x_2x = G(g,time);                                       % 1f and 2f fit
sinusoid
sync_1x  =G1(g1,time);                                        % 1f only fit sinusoid

% fitting the residual to a 2f sinusoid
[h,~,~,exitflag,output] = lsqcurvefit(H,h0,time,sync-sync_1x,[-10 -5 (frequency-
10)*2*pi -pi  ],[10 5 (frequency+10)*2*pi pi ],options);

sync_2x = H(h,time);                                          % 2f sinusoid fit
```

```
figure;
subplot(2,1,1);plot(sync);
hold;plot(sync_1x,'g');
subplot(2,1,2);plot(sync-sync_1x);hold;
plot(g(5).*cos((2*g(3).*time)+g(6)),'k');
plot(sync_2x,'r');
legend('1f Residual','Standard model fit','residual fit');

% parameters from 1f fit
I0_1x = g1(1);                          % Instantaneous laser intensity
amp_AM_1x = abs(g1(2));                 % 1f AM
psi_1x = g1(4);                         % 1f AM phase
ps1_1x_d = psi_1x.*180/3.14;            % 1f AM phase in degrees
i0_1x = g1(2)./g1(1);                   % i0

% all parameters from the complete model(2f and 1f fit)

I0 = g(1);                              % Instaneous laser intensity
amp_AM_1f = abs(g(2));                  % 1f AM
i0 = abs(g(2)./g(1));                   % i0
psi_1 = g(4);                           % 1f AM phase
psi_1_d = psi_1.*180./3.14;             % 1f AM phase in degrees

amp_AM_2f = abs(g(5));                  % 2f AM
i2 = abs(g(5)./g(1));                   % i2
psi_2 = g(6);                           % 2f AM phase
psi_2_d = psi_2.*180/3.14               % 2f AM phase in degrees

% parameters from 2f cosine fit of 1f residaul
amp_AM_2x = abs(h(2));                    % 2f AM
I0_2x = h(1);                             % not used(garbage value)
i2_2x = abs(h(2)./h(1));                  % i2
psi_AM_2x = h(4);                         % 2f AM phase
psi_AM_2x_d = psi_AM_2x.*180/3.14;        % 2f AM phase in degrees



figure;
hold on;
plot(t,res);

% adjust this for noise in resonator trace
[b1 a1] = ellip(2,0.006,60,0.01);
% adjust this for noise in AM wave(not ideally done)
[b22 a22] = ellip(2,0.02,60,0.002);
sync = filtfilt(b22,a22,sync);
res = filtfilt(b1,a1,res);
plot(t,res,'r');
title('Resonator trace with filtering and without filtering');

%%%%%%%%%%%%%%%%%%%%%%%%%%%%%%%%%%%%%%%%%%%%%%%%%%%%%%%%%%%%%%%%%%%%%%%%%%%%%%%
%Peak Detection
%%%%%%%%%%%%%%%%%%%%%%%%%%%%%%%%%%%%%%%%%%%%%%%%%%%%%%%%%%%%%%%%%%%%%%%%%%%%%%%
```

```
%peak detection
[aa bb]= peakdet(res,0.0005);                                          %[peak x
and y , trough x and y = peakdet(vector,threshold)
peak = aa(:,1);                                                        %peak x
value
resonator_peak = aa(:,2);                                              %peak y
value


% Plot the Resonator scan and show the identified peaks
figure;
hold;
subplot(2,1,1);
plot(peak,resonator_peak,'or');
plot(res,'r');
title('peak identification');

[x_in y_in]= ginput;                                                   %input
the coordinates  of peak selection graphically
x_in = round(x_in);
%rounding for index value
mat = [];

%loop for getting the graphically selected peak values
for i = 1:2:length(x_in)-1

    temp = find(peak>x_in(i) & peak<x_in(i+1))
    mat = [mat peak(temp)'];
    clear temp;
end

clear peak resonator_peak;
%clearing the old resonator peak x and y coordinates
peak = mat;                                                            % save
the selected peaks
resonator_peak = res(peak);                                            %
selected peak coordinates
subplot(2,1,2);
hold;
plot(peak,resonator_peak,'or');
plot(res,'r');
xlabel('\bf Time Index')
ylabel('\bf Photodiode Voltage (V)')
title('\bf Plot of graphically selected peaks')



for n = 1:length(peak)-1
   z(n) = abs(peak(n)-peak(n+1));                                     %z is the
distance between consequtve peaks
end

figure;
plot(z);
```

```
title('To select the threshold for peak selection');

%%%%%%%%%%%%%%%%%%%%%%%%%%%%%%%%%%%%%%%%%%%%%%%%%%%%%%%%%%%%%%%%%%%%%%%%%%%%%%%%%%%
val1=(peakdet(z,150));                 % determine the threshold (=150) from the
above figure
%%%%%%%%%%%%%%%%%%%%%%%%%%%%%%%%%%%%%%%%%%%%%%%%%%%%%%%%%%%%%%%%%%%%%%%%%%%%%%%%%%%%%
%%

% To indetify the turning points in the FM wave
val  =  min(val1(:,2));
x = find(z>=val);
n = 1;
count=1;

while n <= x(1)
    freq(n) =FSR-( n*FSR);                                          % building the FM
wave using the FSR
    n = n+1;
end


m = n;
for i = 2:length(x)

while m <= x(i)
    freq(m) = freq(n-1) + (-1)^i*(FSR*(m-n));
    m = m+1;
end
count=count+1;
n = m;
end



z1 = length(peak);

while n <= z1
    freq(n) = freq(m-1)-(-1)^count*(FSR*(n-m));
    n = n+1;
end


freq_t = t(peak);                                                 % get the time
index of the peaks

min_sync = AM_maxormin(1);                                        % select the first
trough of the AM wave
max_sync = AM_maxormin(2);                                        % select the first
peak of the AM wavel
%


%************************************************************************************
%*********************Fitting the FM wave to second order
cosine***********************
```

```
F=@(x,freq_t) x(1)+ x(2).*cos((x(3).*freq_t)+(x(4)))+
x(5).*cos((2*x(3).*freq_t)+x(6));
x0=[-7 7 frequency*2*pi 120/180*pi  .0001 0];
% initial values uses for fitting
options=optimset('MaxFunEvals',100000,'TolFun',1e-15,'MaxIter',100000,'TolX',1e-15);
% lsqnonlin paramters

%%%%%%%%%%%%%%%%%%%%%%%%%%%%%nonlinear curve fit of the FM
wave%%%%%%%%%%%%%%%%%%%%%%%%%%%%%%%%%%%%%%
[x,resnorm,~,exitflag,output] = lsqcurvefit(F,x0,freq_t,freq',[-10 -10 (frequency-
100)*2*pi -pi -10 -pi ],[10 10 (frequency+100)*2*pi pi  10 pi ],options)
%%%%%%%%%%%%%%%%%%%%%%%%%%%%%%%%%%%%%%%%%%%%%%%%%%%%%%%%%%%%%%%%%%%%%%%%%%%%%%%%%%%%%%
%%%%

%%%%%%%%%%%%%%%%%%%%%%%%%%%%%%%%%%%%%%%%%%
y2 = F(x,t);                    % fitted FM wave
FM_dc = x(1);                   % random value DC tuning value
psi_FM = x(4);                  % phase of FM
psi_FM_d = psi_FM.*180/3.14;    % phase of FM degrees
amp_FM_1f = abs(x(2));          % amplitude of FM
amp_FM_2f = abs(x(5));          % second order amplitude of FM
phi_FM_2f = x(6);               % phase of 2f FM
phi_FM_2f_d = phi_FM_2f.*180/3.14; % phase of 2f FM degrees

%*************************************************************************************
%***********************************************************************************

%rescaing for comparison
sync_norm = sync-sync(1);
figure;
sync_norm_s =((sync_norm)*(max(res)/max(sync_norm)))
subplot(2,1,1);plot(freq_t,freq,'rx'); hold; plot(time,y2,'r')

%Rescaling%%%%%%%%%%%%%%%%%%%%%%%%%%%%%%%%%%%%%%%%%%%%%%%%%%%%%%%%%%%%%%%%%%%%%%%%%%%%
%
a = max(y)-min(y);
b = max(sync_norm_s)-min(sync_norm_s);
yi = y*b/a;
yshift = min(yi)-min(sync_norm_s);
yi  =yi-yshift;
%%%%%%%%%%%%%%%%%%%%%%%%%%%%%%Selecting the peaks of the FM
wave%%%%%%%%%%%%%%%%%%%%%%%%%%%%%%%%%%%%%
[MAXF MINF] = peakdet(y,.01)
max_freq = MAXF(2,1);
max_freq = round(max_freq);
%%%%%%%%%%%%%%%%%%%%%%%%%%%%%%%%%%%%%%%%%%%%%%%%%%%%%%%%%%%%%%%%%%%%%%%%%%%%%%%%%%%%%%
%
subplot(2,1,2);plot(time,yi,'g');hold; plot(time,sync_norm_s);legend('FM','IM');
plot(time(max_freq)*ones(1,10),linspace(-.5,.5,10),'-');
plot(time(max_sync)*ones(1,10),linspace(-.5,.5,10),'-');

xlabel('\bf Time (\mus)')
ylabel('\bf Intensity/Frequency modulation amplitude (a.u.)')
title('\bf Plot of intensity modulation and frequency modulation')
```

```
diff_T = abs(t(max_freq)-t(max_sync));                                  % time
delay between FM and AM

phase = (diff_T./(2*abs(t(max_sync)-t(min_sync))))*360;                 % time
delay converted to phase delay

phase_from_fit=(180/pi)*abs(psi_FM-psi_1);                              %FM-AM
phase from fit method
phase_2_from_fit = (180/pi)*abs(psi_FM-psi_2);                          %FM-
2f(AM) phase from fit method
Tuning_Coeffcient=2*amp_FM_1f/di_p2p;                                   %Tuning
coefficient(GHz/mA) from fit method


% Writing the results ,in order, to an excel file
offset=1;
xlswrite(output_file_name, file_head, 2, sprintf('A%d',offset));
A = {'Power(A)','Freq(kHz)','Ib(mA)','Intensity(V)-model', '1f-amplitude(V)-model'
,'i0-model','psi_1(rad)-model','psi_1(deg)-model','amp_AM_2f(V)-model','i2-
model','psi_2(rad)-model','psi_2(deg)model','','','Intensity(V)-1f fit','1f-
amplitude(V)-1f fit','i0-1f fit','psi_1(rad)-1f-fit','psi_1(deg)-1f
fit','','','Intensity(V)-2f resid ','amp_AM_2f(V)-2f resid','i2-2f
resid','psi_2(rad)-2f resid','psi_2(deg)-2f resid','','','FM DC(GHz)','FM
amplitude(1x)(GHz)','FM phase 1x(rad)','FM phase 1x(deg)','FM amplitude(2x)(GHz)','FM
phase 2x(rad)','FM phase 2x(deg)','phase(from peak)(deg)','phase(psi_1) from
Fit(deg)','phase(psi_2) from Fit(deg)','Tuning Coeff(GHz/mA) from  fit)'};
xlswrite(output_file_name, A, 2, sprintf('A%d',offset+3));
AA=[Power(1) freqq(1) Ib(1) I0 amp_AM_1f i0 psi_1 psi_1_d amp_AM_2f i2 psi_2 psi_2_d
0 0 I0_1x amp_AM_1x i0_1x psi_1x ps1_1x_d 0 0 I0_2x amp_AM_2x i2_2x psi_AM_2x
psi_AM_2x_d 0 0 FM_dc amp_FM_1f psi_FM psi_FM_d amp_FM_2f phi_FM_2f phi_FM_2f_d phase
phase_from_fit phase_2_from_fit Tuning_Coeffcient];
xlswrite(output_file_name, AA, 2, sprintf('A%d',offset+4+in));
```

Published with MATLAB® R2014a

Appendix B

```
% Fourier model for WMS signals for an optically thin and optically thick case
% Copyright 2016
% Thomas Benoy, Dr. Michael Lengden
% This code calculates the thortical direct spectra and WMS spectra (for
% the optically thin and thick cases)
% Wavelength referencing will be required if the signals are experimental
% WMS paramters such as tuning coefficient and phase are measured and
% applied in the model.
% Note: This code is not optimised for speed, please contact Dr. Micahel
% Lengden(michael.lengden@strath.ac.uk) or
% myself(thomas.benoy@strath.ac.uk) for future correspondences

close all;clc;clear all;format long;

%%%%%%%%%%%%%%%%%%%%%%%%%%%%%%%%%%%%%%%%%%%%%%%%
%%%Gas parameters(Enter the gas parameeters here
pressure = 1.018 ;                                  % Pressure
methane_concentration = 1;                          % Gas is assumed to be methane(can
be any gas)
degreeT = 200;                                      % Temperature in degree celcius
degreeT =  HT_Cell_temp_calibration( degreeT );     % Function for calibrating the
temperature to the values measured using the thermcouple
L = 5.5 ;                                           % Length of gas cell used
%%%%%%%%%%%%%%%%%%%%%%%%%%%%%%%%%%%%%%%%%%%%%%%%%%%%%%%%%%%%%%%%%%%%%%%%%%%%
%Define modulation prameters(From experiment)
%%%%%%%%%%%%%%%%%%%%%%%%%%%%%%%%%%%%%%%%%%%%%%%%%%%%%%%%%%%%%%%%%%%%%%%%%%%%

frequency = 200e3;                                                          %Enter the
frequency you are operating at
omega = 2*pi*frequency;
%Converting to rad
bias_point = 80;                                                            %bias
point in mA on LDC
voltage_ramp_pp = 0.6;                                                      %Ramp
Voltage peak to peak
conversion_factor_LDC = 100;                                                %Voltage
to current conversion in mA/1V
current_ramp_amp = (conversion_factor_LDC.*voltage_ramp_pp)./2;
%Converting Vpp into current amplitude
ac_modulation_voltage_pp = 3;                                               %sine
Voltage peak to peak
conversion_factor_bias_T = 10;
%conversion factor =10mA/1V for bias-T, 20 for bias-T with high Z
ac_current_amp = (ac_modulation_voltage_pp*conversion_factor_bias_T)*0.5;
%mA(AMPLITUDE in mA)
additional_plots =1;
[b1 ,a1] = ellip(2,0.001,90,0.01);                                          %filtering
values of ellip filter
```

```
trunc_noise = 1000:9000;
%truncating for noise(only for experiment)
lag_index = 1;                                                          %define
lag index for the LIA due to its time constant(only for experiment)
%%%%%%%%%%%%%%%%%%%%%%%%%%%%%%%%%%%%%%%%%%%%%%%%%%%%%%%%%%%%%%%%%%%%%%%
%Defining wavelength range
%%%%%%%%%%%%%%%%%%%%%%%%%%%%%%%%%%%%%%%%%%%%%%%%%%%%%%%%%%%%%%%%%%%%%%%

lower_lambda = 1997.2-.21;
upper_lambda = 1997.2+.21;
vsteps = 10000;
wavelength = linspace(lower_lambda,upper_lambda,vsteps);
wavelength =wavelength(trunc_noise);
% %%%%%%%%Experimental Laser Parameters - Tuning Coefficient, phase

x = linspace(50,110,10000);
x_act = x;
x = x(trunc_noise);
Ib_new = [40  45 50 55 60 65 70 75  80 85 90 95 100 105 110 115 ];
nu_exp = [0.177710305 0.177009156 0.175938965 0.175630548 0.17444415 0.176989803
0.174907779 0.175732423 0.177159599 0.177994394 0.179883709 0.180642704 0.181567168
0.182067708 0.183475439 0.186151153 ];
psi_1_exp = [30.168  32.4 34.272 36.36 38.088 40.104 41.16753299 42.552 43.776 44.856
45.504 46.224 46.656 46.584 46.224 45.936];
pp = polyfit(Ib_new,nu_exp,4);
nu_fit = polyval(pp,x_act);
p=polyfit(Ib_new,psi_1_exp,4);
psi_1=polyval(p,x_act);

if additional_plots
figure;
plot(x_act,nu_fit);
hold;
plot(Ib_new,nu_exp,'r*');

figure;
plot(x_act,psi_1);
hold;
plot(Ib_new,psi_1_exp,'r*');
end

% nu_fit = - 0.00017*x.^2 + 0.047.*x - 0.53

nu_fit = nu_fit(trunc_noise);
nu_fit =  nu_fit.*1e9./(3e8*100);%(cm-1/mA);


psi_1 =psi_1(trunc_noise);

% Intensity modulation paramters
Ib = [ 40 50 60 70 80 90 100 110  120  ];
aaa = [0.624359977     0.433842772     0.330563467     0.265698043     0.219611327
        0.185863324     0.160314002     0.139695255     0.122372065
0.001403776     0.002386297     0.002351958     0.002250411     0.002142873
        0.002012942     0.00200021      0.001924821     0.00189044
```

```
1.110947098    1.358612516    1.366551669    1.358763363    1.355477055
        1.380246793    1.337843058    1.323071707    1.371147999];

i0_1 =aaa(1,:);
i0_2 = aaa(2,:);
psi_21 = aaa(3,:);

xx = polyfit(Ib,i0_1,5);
i0 = polyval(xx,x);
xx1 = polyfit(Ib,i0_2,5);
i2 = polyval(xx1,x);
xx2 = polyfit(Ib,psi_21,6);
psi_2 = polyval(xx2,x);
psi_2 = psi_2*180/pi;                                                              %
converting to degrees

if additional_plots
figure;
plot(Ib,i0_1,'r*');
hold;
plot(x,i0);
figure
plot(Ib,i0_2,'r*');
hold;
plot(x,i2);
end


%%%%%%%%%%%%%%%%%%%%%%%%%%%%%%%%%%%%%%%%%%%%%%%%%%%%%%%%%%%%%%%%%%%%%%%%%%%%%%%%%%%%%%%%%%%%
%%%%%%%%%%%%%%%%%%
% Modelling direct spectra
%%%%%%%%%%%%%%%%%%%%%%%%%%%%%%%%%%%%%%%%%%%%%%%%%%%%%%%%%%%%%%%%%%%%%%%%%%%%%%%%%%%%%%%%%%%%
%%%%%%%%%%%%%%%%%%
methanelines = csvread('C:\Users\isb12205\My Documents\CO2
mick\CO2_FLITES_hit08_trim.csv');
partition = csvread('C:\Users\isb12205\My Documents\CO2
mick\CO2partitionfunctions.csv'); %Hitran data
z = length(methanelines);
k = 1.3806503e-23; %Boltzmann
M = 44; % for CO2
c = 299792458e2; %speed of light
h = 6.626e-34; %Planck
v = 1e7./wavelength;

% Defining temperature
T_0 = 296; % Reference Temperature in Kelvin
T_K = 273.15; %0 degrees celcius in Kelvin
T = degreeT+T_K; %Converting to Kelvin

%  Defining Start Concentrations
nitrogen_concentration = 1-methane_concentration;
% Calculation of individual line strengths
% Reading in pressure and converting from bar to atm
total_pressure = pressure*0.986926; %atm
index1 = find(partition(:,1) == T_0);
```

```
Q_T0 = partition(index1,2);

deltaT = abs(partition(:,1)-T);
minT = min(deltaT);
index2 = find(deltaT == minT);
Q_T = partition(index2,2);

S1 = 1-exp(-(h*c.*methanelines(:,1))/(k*T));
S2 = (1-exp(-(h*c.*methanelines(:,1))/(k*T_0)));
S3 = S1./S2;
S4 = Q_T0./Q_T;
S5 = T_0/T;
S6 = exp((-h*c*methanelines(:,5)/k)*((1/T)-(1/T_0)));

S7 = S3.*S4.*S5.*S6;



S_T = S7.*methanelines(:,2); %Total linestrength

S_T_save = S_T(53);
% Overwriting with experimentally measured linestrength values
%**********************************************************************
T_exp = [49    99     150    202    253    306    359    412    465    518    569
       619];
S_T_exp = [8.78E-23   1.08E-22      1.19E-22      1.24E-22      1.22E-22
       1.15E-22      1.07E-22      9.75E-23      8.82E-23      7.94E-23
       7.14E-23      6.33E-23];

p_S_T=polyfit(T_exp,S_T_exp,4);

S_T_interp =polyval(p_S_T,50:650);

if additional_plots
figure(2000)
plot(T_exp,S_T_exp,'*');
hold on;
plot(50:650,S_T_interp);
hold off;
end

S_T(53)=polyval(p_S_T,degreeT);

%**********************************************************************

%  Gaussian Broadening
gammag = 7.1625e-7.*methanelines(:,1).*(T/M)^0.5;
gammag = gammag';

%  Air-broadening parameter
air_broadening_parameter = methanelines(:,3).*(T_0/T).^methanelines(:,6); %
calculated as average of trasistion 10-16 in 2008 Database

 % Lorentzian Broadening
self_broadening_parameter = methanelines(:,4).*(T_0/T).^methanelines(:,6);
```

```
%  Overwriting with experimental measured collissional broadening value
self_broadening_parameter(53) = (0.0729755)*(T_0/T).^(0.612975);
% Lorentzian Broadening(FWHM)
gammal =
2*total_pressure.*((air_broadening_parameter*nitrogen_concentration)+(self_broadening
_parameter*methane_concentration));
gammal = gammal';

X = zeros(length(v),z);

% X values for Voigt Profile
for j = 1:z
X(:,j) = 2*sqrt(log(2))*(v-methanelines(j,1))./gammag(j);
end


% A-D values for Voigt Profile
A = [-1.2150 -1.3509 -1.2150 -1.3509];
B = [1.2359 0.3786 -1.2359 -0.3786];
C = [-0.3085 0.5906 -0.3085 0.5906];
D = [0.0210 -1.1858 -0.0210 1.1858];


% Final voigt Y-value
Y = (gammal./gammag)*sqrt(log(2));

for j = 1:z
    for i = 1:4
        V_top(i,:)= (C(i)*(Y(j)-A(i)))+(D(i)*(X(:,j)-B(i)));
        V_bottom(i,:) = (Y(j)-A(i))^2+(X(:,j)-B(i)).^2;
    end
V = V_top./V_bottom;
Vfinal(:,j) =
(2/gammag(j))*(log(2)/pi)^0.5*methane_concentration*(7.339e21/T_0)*S_T(j)*sum(V);
end

% Final spectral absorption coefficient
kv = pressure * sum(Vfinal'); % absorbance

% Final fractional transmission
Tv = exp(-kv.*L);

Tv = Tv';
figure(100);
plot(wavelength,Tv);hold on;
plot(wavelength,1-kv.*L,'r');
legend('Optically Thick','Optically thin');


%%%%%%%%%%%%%%%%%%WMS Fourier Transform Model (optically thick model including all
the lines)%%%%%%%%%%%%%%%%%%%%%%%%%%%%%%%%%%%%%%%%
vsteps = length(wavelength);
theta_j = ones(50,vsteps);
Vfinal_0_exp = zeros(50,vsteps);       %Initialising arrays for the 0th,1st, 2nd and
4th order Fourier coefficients
```

```
Vfinal_1_exp = zeros(50,vsteps);
Vfinal_2_exp = zeros(50,vsteps);
Vfinal_3_exp = zeros(50,vsteps);
Vfinal_4_exp = zeros(50,vsteps);

a0_exp = zeros(1,vsteps);
a1_exp = zeros(1,vsteps);
a2_exp = zeros(1,vsteps);
a3_exp = zeros(1,vsteps);
a4_exp = zeros(1,vsteps);

S_T = (7.339e21/T_0).*S_T;                % notation given in this work

lines = [53];                            % insert all the lines you want to include in
the model

XX = zeros(50,vsteps);
multiplier_1 = linspace(1,1,vsteps);
multiplier_2 = linspace(1,1,50);      % this value is set to 50(no of theta steps),
can be lowered down to 25 for increased speed
theta = linspace(-pi,pi,50);
theta_j = theta';
theta_j = theta_j*multiplier_1;
delta_nu =nu_fit.*ac_current_amp;

delta_nu = delta_nu'*multiplier_2;
delta_nu = delta_nu';
Absorbance = total_pressure .*methane_concentration .*L;
%Pressure in bar, gas conc on mole fraction, length in cm( note this is not the
formula for absorbance)

% Mclean's coefficients as for direct transmission
A = [-1.2150 -1.3509 -1.2150 -1.3509];
B = [1.2359 0.3786 -1.2359 -0.3786];
C = [-0.3085 0.5906 -0.3085 0.5906];
D = [0.0210 -1.1858 -0.0210 1.1858];

   for kk = 1:50        % summation over theta

for ii=(lines)          % summation over all the lines


% modulation_index_guide =
% delta_nu(round(length(nu_fit)/2))./(.5*gammal(ii));% rough guide of the
% modulation indes


     delta = (v- methanelines(ii,1)-(methanelines(ii,7).*total_pressure));
     delta_j = delta'*multiplier_2;
     delta_j = delta_j';

% Defing X parameters
       XX = 2*sqrt(log(2))*(delta_j+delta_nu.*cos(theta_j))./gammag(ii);

       X=XX(kk,:);
```

```
       Y = (gammal(ii)./gammag(ii))*sqrt(log(2));

 for i = 1:4
        V_top(i,:)= (C(i)*(Y-A(i)))+(D(i)*(X-B(i)));
        V_bottom(i,:) = (Y-A(i))^2+(X(:)-B(i)).^2;
 end
V_dir = V_top./V_bottom;
Vfinal = (2/gammag(ii)).*sqrt(log(2)/pi)*sum(V_dir);


Vfinal_0_exp(kk,:) = Vfinal_0_exp(kk,:) + (S_T(ii).*Vfinal);
Vfinal_1_exp(kk,:) = Vfinal_1_exp(kk,:) + (S_T(ii).*Vfinal);
Vfinal_2_exp(kk,:) = Vfinal_2_exp(kk,:) + (S_T(ii).*Vfinal);
Vfinal_3_exp(kk,:) = Vfinal_3_exp(kk,:) + (S_T(ii).*Vfinal);
Vfinal_4_exp(kk,:) = Vfinal_4_exp(kk,:) + (S_T(ii).*Vfinal);
% v_trap(kk) =  trapz(v,Vfinal_1(kk,:));  % to see if normalised to 1.


end

Vfinal_0_exp(kk,:) = exp(-Vfinal_0_exp(kk,:).*Absorbance);
Vfinal_1_exp(kk,:) = exp(-Vfinal_1_exp(kk,:).*Absorbance).*cos(theta(kk));
Vfinal_2_exp(kk,:) = exp(-Vfinal_2_exp(kk,:).*Absorbance).*cos(2.*theta(kk));
Vfinal_3_exp(kk,:) = exp(-Vfinal_3_exp(kk,:).*Absorbance).*cos(3.*theta(kk));
Vfinal_4_exp(kk,:) = exp(-Vfinal_4_exp(kk,:).*Absorbance).*cos(4.*theta(kk));

   end

a0_exp = (1./(2*pi)).*trapz(theta,(Vfinal_0_exp));
a1_exp = (1./(pi)).*trapz(theta,(Vfinal_1_exp));
a2_exp = (1./(pi)).*trapz(theta,(Vfinal_2_exp));
a3_exp = (1./(pi)).*trapz(theta,(Vfinal_3_exp));
a4_exp = (1./(pi)).*trapz(theta,(Vfinal_4_exp));

% redudant step(kept for Historical reasons)
H0_exp = a0_exp;
H1_exp = a1_exp;
H2_exp = a2_exp;
H3_exp = a3_exp;
H4_exp = a4_exp;
%*****************************


X_2f_v_exp = H2_exp + .5*i0.*(H1_exp+H3_exp).*cosd(psi_1) +
i2.*(H0_exp+.5*H4_exp).*cosd(psi_2);
Y_2f_v_exp = -1*(0.5.*i0.*(H1_exp-H3_exp).*sind(psi_1) +i2.*(H0_exp-
.5*H4_exp).*sind(psi_2));
X_2f_0_v_exp = i2.*cosd(psi_2);
Y_2f_0_v_exp = -i2.*sind(psi_2);
R_1f_v_exp = sqrt((H1_exp + i0.*(H0_exp+.5*H2_exp).* cosd(psi_1)+0.5.*i2.*
(H1_exp+H3_exp).*cosd(psi_2)).^2 + (i0.*(H0_exp-.5*H2_exp).*sind(psi_1)+0.5.*i2.*
(H1_exp-H3_exp).*sind(psi_2)).^2);
R_1f_0_v_exp = i0;
f2_1f_v_exp = sqrt( (X_2f_v_exp./R_1f_v_exp-X_2f_0_v_exp./R_1f_0_v_exp).^2 +
```

```
(Y_2f_v_exp./R_1f_v_exp-Y_2f_0_v_exp./R_1f_0_v_exp).^2 );
% Some useful equations worth checking out
% f2_1f_exp = sqrt( (I_chX_2f./sqrt(I_chX_1f.^2+I_chY_1f.^2) -
I_chX_bk_2f./sqrt(I_chX_bk_1f.^2+I_chY_bk_1f.^2)).^2 +
(I_chY_2f./sqrt(I_chX_1f.^2+I_chY_1f.^2) -
I_chY_bk_2f./sqrt(I_chX_bk_1f.^2+I_chY_bk_1f.^2)).^2 );
% f2_1f_exp_no_bk_sub = sqrt( (I_chX_2f./sqrt(I_chX_1f.^2+I_chY_1f.^2) ).^2 +
(I_chY_2f./sqrt(I_chX_1f.^2+I_chY_1f.^2)).^2 );
% f2_1f_linear_v = sqrt( (X_2f_linear_v./R_1f_linear_v).^2 +
(Y_2f_linear_v./R_1f_linear_v).^2 );



%%%%%%%%%%%%%%%%%%%%%%%%%%%%%%%%WMS- thin model%%%%%%%%%%%%%%%%%%%%%%%%%%%%%%%%%%
theta_j = ones(50,vsteps);
Vfinal_0 = zeros(50,vsteps);
%Initialising arrays for the 0th,1st .... fourier coefficients
Vfinal_1 = zeros(50,vsteps);
Vfinal_2 = zeros(50,vsteps);
Vfinal_3 = zeros(50,vsteps);
Vfinal_4 = zeros(50,vsteps);

a0 = zeros(1,vsteps);
%Initialising arrays for the 0th,1st second and 3drd order fourier coefficients
a1 = zeros(1,vsteps);
a2 = zeros(1,vsteps);
a3 = zeros(1,vsteps);
a4 = zeros(1,vsteps);
delta_nu = nu_fit.*ac_current_amp;
modulation_index_guide = delta_nu(round(length(nu_fit)/2))./(.5*gammal(53));

Abs = total_pressure .*methane_concentration .*L   ;
%Pressure in bar, gas conc on mole fraction length in cm


multiplier_1 = linspace(1,1,vsteps);
multiplier_2 = linspace(1,1,50);
theta = linspace(-pi,pi,50);
delta = (v- methanelines(ii,1)-(methanelines(ii,7).*total_pressure));
theta_j = theta';
theta_j = theta_j*multiplier_1;

delta_nu = delta_nu'*multiplier_2;
delta_nu =delta_nu';

delta_j = delta'*multiplier_2;
delta_j = delta_j';
% Defing X parameters
XX = zeros(50,vsteps);
XX = 2*sqrt(log(2))*(delta_j+delta_nu.*cos(theta_j))./gammag(ii);
% Iterate over ii if here adding each a0,a2,...a4 values into each other in
% each loop

for ii = lines
    for kk = 1:50
```

```
X=XX(kk,:);
Y = (gammal(ii)./gammag(ii))*sqrt(log(2));
A = [-1.2150 -1.3509 -1.2150 -1.3509];
B = [1.2359 0.3786 -1.2359 -0.3786];
C = [-0.3085 0.5906 -0.3085 0.5906];
D = [0.0210 -1.1858 -0.0210 1.1858];

    for i = 1:4
        V_top(i,:) = (C(i)*(Y-A(i)))+(D(i)*(X-B(i)));
        V_bottom(i,:) = (Y-A(i))^2+(X(:)-B(i)).^2;
    end
V = V_top./V_bottom;
Vfinal_0(kk,:) = S_T(ii).* (2/gammag(ii))*(log(2)/pi)^0.5*sum(V);
Vfinal_1(kk,:) = S_T(ii).*(2/gammag(ii))*(log(2)/pi)^0.5*sum(V).*cos(theta(kk));
Vfinal_2(kk,:) = S_T(ii).* (2/gammag(ii))*(log(2)/pi)^0.5*sum(V).*cos(2*theta(kk));
Vfinal_3(kk,:) = S_T(ii).*(2/gammag(ii))*(log(2)/pi)^0.5*sum(V).*cos(3*theta(kk));
Vfinal_4(kk,:) = S_T(ii).*(2/gammag(ii))*(log(2)/pi)^0.5*sum(V).*cos(4*theta(kk));

    end

% Fourier coefficients
a0 = a0+ (1./(2*pi)).*trapz(theta,Vfinal_0);        % a0+ previous values if
iterating over all lines
a1 = a1+ (1./(pi)).*trapz(theta,Vfinal_1);
a2 = a2+ (1./(pi)).*trapz(theta,Vfinal_2);
a3 = a3+ (1./(pi)).*trapz(theta,Vfinal_3);
a4 = a4+ (1./(pi)).*trapz(theta,Vfinal_4);

end

%Kept for historical reasons
H0 = -Abs.*a0;
H1 = -Abs.*a1;
H2 = -Abs.*a2;
H3 = -Abs.*a3;
H4 = -Abs.*a4;

% to find the effect of i2 on the signal
% linear model doesnt include the nonlinear IM term
X_2f_linear_v = H2 + .5.*i0.*(H1+H3).*cosd(psi_1);
Y_2f_linear_v = -0.5.*i0.*(H1-H3).*sind(psi_1);

R_2f_linea_v = sqrt( X_2f_linear_v.^2+Y_2f_linear_v.^2);

X_2f_v = H2 + .5*i0.*(H1+H3).*cosd(psi_1) + i2.*(1+H0+.5*H4).*cosd(psi_2);

Y_2f_v = -1*(0.5.*i0.*(H1-H3).*sind(psi_1) +i2.*(1+H0-.5*H4).*sind(psi_2));

R_2f_v = sqrt (X_2f_v.^2 + Y_2f_v.^2);
X_2f_0_v = i2.*cosd(psi_2);
Y_2f_0_v = -i2.*sind(psi_2);
R_2f_0_v = sqrt ( X_2f_0_v.^2 + Y_2f_0_v.^2);

S_2f_v = sqrt( (X_2f_v-X_2f_0_v).^2 +  (Y_2f_v-Y_2f_0_v).^2 );
S_2f_linear_v = sqrt( (X_2f_linear_v).^2 +  (Y_2f_linear_v).^2 );
```

```
R_1f_linear_v = sqrt((H1 + i0.*(1+H0+.5.*H2).* cosd(psi_1)).^2 + (i0.*(1+H0-
.5*H2).*sind(psi_1)).^2);
R_1f_v = sqrt((H1 + i0.*(1+H0+.5*H2).* cosd(psi_1)+0.5.*i2.* (H1+H3).*cosd(psi_2)).^2
+ (i0.*(1+H0-.5*H2).*sind(psi_1)+0.5.*i2.* (H1-H3).*sind(psi_2)).^2);


R_1f_0_v = i0;
f2_1f_v = sqrt( (X_2f_v./R_1f_v-X_2f_0_v./R_1f_0_v).^2 +  (Y_2f_v./R_1f_v-
Y_2f_0_v./R_1f_0_v).^2 );
f2_1f_linear_v = sqrt( (X_2f_linear_v./R_1f_linear_v).^2 +
(Y_2f_linear_v./R_1f_linear_v).^2 );

figure;

plot(wavelength,f2_1f_v);
hold;
plot(wavelength,f2_1f_v_exp,'r');
legend('Optically thin model','Optically thick model');
```

Published with MATLAB® R2014a

Appendix C

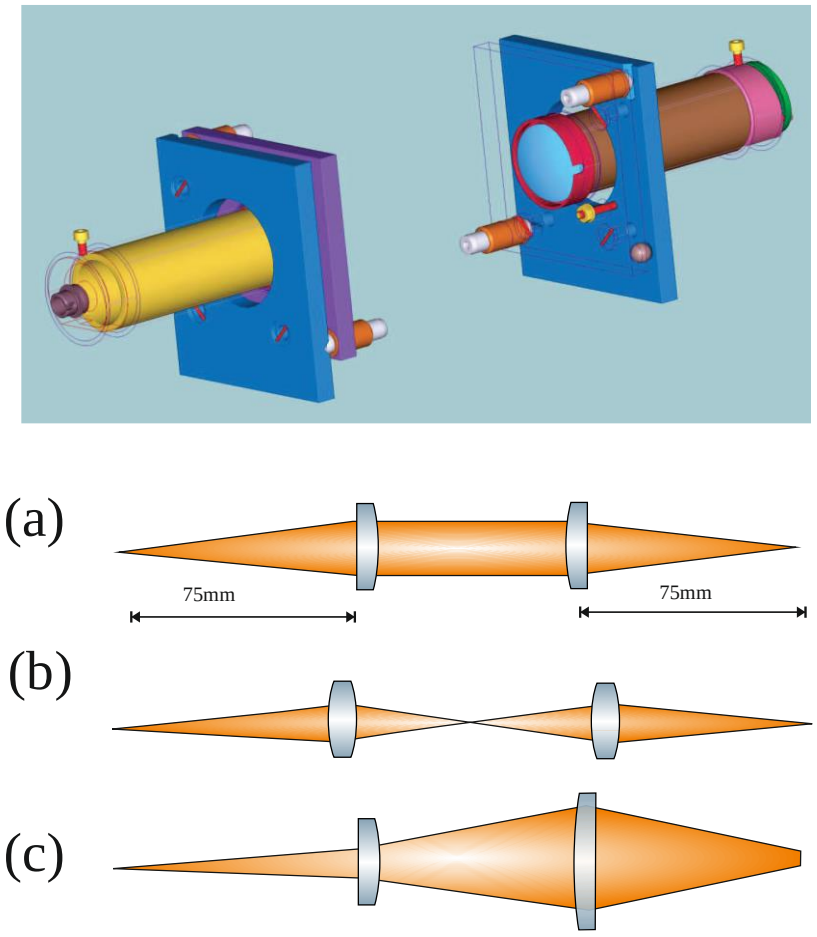

Figure C-1. The launch and receive optics (top image) and the three optical configurations (bottom image) tested in the FLITES system [51]: (a) collimated (b) mid-plume focussed and (c) moderately divergent.

List of Symbols

k_s	Spring constant
r	Displacement
r_{eq}	Equilibrium internuclear distance
$\bar{\omega}_{osc}$	Oscillation wave number
c	Speed of light in vacuum
μ	Effective mass
E_v	Discretised vibrational energy
v	Vibrational quantum number
D_{eq}	Dissociation energy
a	Constant factor
χ_e	Anharmonicity constant
E_{rot}	Rotational energy
B	Rotational constant
D	Centrifugal distortion constant
I_B	Rotational moment of inertia (about bond axis)
h	Planks constant
J	Rotational quantum number
α	Spectral absorbance
I_{in}	Incident laser intensity
I_t	Transmitted laser intensity
N_g	Number of gas molecules per unit volume
$\sigma(v)$	Absorption cross-section
l	Optical path length
$S(T)$	Line strength per molecule
ϕ	Line shape function
T	Temperature (°C)
P	Pressure (atm)
χ	Mole fraction
t	Time
ħ	$h/2\pi$
$f_{L-N}(v)$	Natural broadened line shape
γ_N	Natural broadening linewidth (HWHM)
v_0	Line-centre frequency
A_{kl}	Spontaneous decay rate
$f_L(v)$	Collisionally broadened line shape
γ_L	Collisional broadening linewidth (HWHM)
P_0	Reference pressure (1 atm)
T_0	Reference temperature (296°K)
Δ	Temperature coefficient of line width
γ_0	Collisional line width at the temperature T_0 and pressure P_0
γ_L^{ii}	Self-broadening coefficient
γ_L^{ij}	Cross- broadening coefficient
$f_G(v)$	Gaussian line shape function for thermal broadening
γ_G	Doppler broadening line width (HWHM)
M	Molecular mass
k_B	Boltzmann constant
$f_v(v)$	Voigt line shape function
$K(x,y)$	Voigt function normalised to $\sqrt{\pi}$
n_i	Population density of upper energy level *i*
n_t	Overall population density
g_i	Degeneracy of energy level *i*
E_i	Energy of level *I*

List of Symbols

$Q(T)$	Total internal partition function (TIPS)
B_{21}	Einstein's *B* coefficient for stimulated emission
B_{12}	Einstein's *B* coefficient for stimulated absorption
$\bar{\nu}_0$	Characteristic molecular absorption wave number
ζ	Isotopic abundance
$\|R_t\|^2$	Einstein's *A* Coefficient
n_L	Population density of the lower energy state
$a, \mathcal{b}, c\,.d$	Coefficients of TIPS
V	Volume occupied by the gas
$\mathcal{R}$	Ideal gas constant
N_A	Avogadro's constant
n_g	Number of moles of the gas
$S'(T)$	Different definition of line strength
E"	Lower state energy
δ	Pressure induced line shift
I_l	Laser output intensity
I	Instantaneous laser intensity
ΔI	Linear IM
ΔI_2	Nonlinear IM
ω	Angular modulation frequency
ψ_2	Phase difference between nonlinear IM and FM
ν_1	Centre (average) frequency of the laser
$\Delta\nu$	Amplitude of the applied WM/FM
ψ_1	Phase difference between IM and FM
I_{out}	Intensity transmitted through gas
θ	$\omega t - \psi_1$
n	Detection harmonic
θ_L	Orientation angle of the LIA
a_n	Fourier coefficients
ψ_λ	WM-IM phase lag
I_{det}^{ω}	Detector components at frequency ω
M_y	Y- channel of the LIA
M_x	X-channel of the LIA
m	Modulation index
γ_{HWHM}	Half width at half maximum of the absorption line
$\in$	Tuning coefficient
i_0	Intensity normalised IM amplitude
i_2	Intensity normalised nonlinear IM amplitude
$\mathcal{G}$	LIA gain
X_{2f}	*2f* X-channel
Y_{2f}	*2f* Y-channel
R_{2f}	Resultant *2f* signal
X_{1f}	*1f* X-channel
Y_{1f}	*1f* Y-channel
R_{1f}	Resultant *1f* signal
X_{2f}^{bk}	*2f* X-channel - background signal
Y_{2f}^{bk}	*2f* Y-channel - background signal
R_{2f}^{bk}	Resultant *2f* signal - background signal
R_{1f}^{bk}	Resultant *1f* signal - background signal
$T_{heat\ sink}$	Heat sink temperature
$R_{thermistor}$	Resistance of the thermistor
X_L	Inductive reactance
L	Inductance
f	Applied modulation frequency
X_C	Capacitive reactance
$\mathcal{C}$	Capacitance
f_L	Bias-T lower cut-off frequency
R_{AC}	Impedance as seen from the AC arm
f_H	Bias-T upper cut-off frequency
R_{DC}	Impedance as seen from the DC arm

List of Symbols

Φ	Phase of the bias-T
V_{Sig}	Signal amplitude
V_{LIA}	Amplitude of the LIA reference signal
$\emptyset$	Arbitrary phase of the LIA reference signal with respect to the input signal
n_e	Effective refractive index
L_{ring}	Ring cavity length
n_{peak}	Number of peaks
Δt	Time delay
y_{FM}	FM amplitude on y axis
ν_c	Unmodulated laser frequency (arbitrary)
$\Delta\nu_2$	Nonlinear FM amplitude
ϕ_{FM}	FM (linear) phase(w.r.t. current modulation)
ϕ_{2FM}	FM (nonlinear) phase (w.r.t. current modulation)
y_{AM}	IM y-axes
ϕ_{IM}	IM (linear) phase (w.r.t. current modulation)
ϕ_{2IM}	IM (linear) phase (w.r.t. current modulation)
ψ	IM/FM phase lag
ψ_λ	WM-IM phase lag
$\lvert Y_1\rvert$	Maximum of FM signal projection on Y- channel.
$\lvert Y_2\rvert$	Minimum of FM signal projection on Y- channel.
X_1	Maximum of FM signal projection on X- channel.
X_2	Minimum of FM signal projection on X- channel.
η_i	Internal/injection efficiency
q	Charge in coulombs
N	Number of charge carriers per unit volume
V	Volume of the active region
R_{nr}	Nonradiative recombination rate per unit volume
R_{sp}	Spontaneous emission rate per unit volume
$R_{sp}{}'$	Spontaneously emitted photons coupled back into the laser cavity per unit volume
R_{21}	Stimulated emission rate per unit volume
S	Cavity photon density
V_p	Optical mode volume.
η_o	Output coupling efficiency
τ_p	Cavity photon lifetime
τ_N	Carrier lifetime
v_g	Group velocity
$G(N,S)$	Gain of the laser
Γ	Mode confinement volume
β'_{sp}	Fraction of spontaneous emission coupled to the laser mode
G_{0N}	Empirical gain coefficient
N_{tr}	Transparency carrier density
ϱ	Differential gain
N_s	Curve fitting parameter
ϵ	Gain compression factor
ω_m	Current modulation angular frequency
N_0	Steady state carrier density
S_0	Steady state photon density
G_0	Steady state gain
δN	Carried density perturbation
δS	Photon density perturbation
δG	Gain perturbation
n_r	Real part of the refractive index
$\bar{m}$	Cavity mode number
$\not{f}$	Laser frequency
L_c	Optical length of the cavity
n_{gr}	Group refractive index
v_g	Group velocity
$\bar{\alpha}$	Line width enhancement factor

List of Symbols

n_i	Imaginary part of the refractive index
f_m	Applied current modulation frequency
I_{th}	Threshold current
δP	Change in optical power
C_T	Thermal capacitance
R_T	Thermal resistance
P_{el}	Electrical power
v_f	Forward voltage
i_f	Forward current
P_{opt}	Optical power
r_s	Series resistance of the laser diode
V_j	Junction voltage of the laser diode
η	Slope efficiency
I_{bias}	Laser bias current
I_{th}	Laser threshold current.
i_m	Current modulation amplitude
P_{DC}	DC electrical heat dissipated
A_1	Amplitude of the AC heat dissipated in the active layer
φ_1	Thermal phase lag
τ_{th}	Thermal time constant
$\Delta\lambda$	Change in wavelength
α_l	Temperature expansion coefficient
α_n	Refractive index coefficient
λ_0	Central (average) laser wavelength
A_2	Nonlinear AC electrical heating amplitude
H_0	DC thermal tuning.
C_f	Carrier induced FM
ω_c	Thermal cut-off frequency
κ	Thermal diffusivity
d_s	Substrate thickness
C_λ	Carrier induced WM
$T_a(t)$	Time dependent active layer temperature
$\tilde{T}_a$	Amplitude of active layer temperature
T_{ss}	Steady state temperature
$\vec{q}$	Heat flux
c_h	Heat capacity
c_p	Specific heat capacity
K	Thermal conductivity
ρ	Density
$H_s(t)$	Heat flowing from the active region into the substrate layer
$H_b(t)$	Heat flowing from the active region into the barrier layer
C_a	Thermal capacity of the active layer
d_b	Thickness of the barrier layer
C_b	Thermal capacity of the barrier layer
C_s	Thermal capacity of the substrate layer
d	Thickness of the laser chip
ω_{cs}	Thermal cut-off frequency - substrate layer
ω_{cb}	Thermal cut-off frequency - barrier layer
ω_{ca}	Thermal cut-off frequency - active layer
d_a	Thickness of the active layer
d_w	Width of the laser strip
ℓ	Length of the laser strip
Θ	Iteration angle
C	Concentration (%)
$\mathcal{A}$	Integrated absorbance